Ollscoil na Gaillimhe
University of Galway

An Experimental and Computational Investigation of the Corrosion Behaviour and Mechanical Performance of a Bioabsorbable medical grade Magnesium alloy

by

Kerstin van Gaalen, M.Sc

May 26, 2023

Supervisor of Research: Dr. Ted J. Vaughan

Co-Supervisor of Research: Prof. Peter E. McHugh

Industry Supervisor: Dr. Ing. Alexander Kopp

A thesis submitted to Ollscoil na Gaillimhe - University of Galway as fulfilment of the requirements for the Degree of Doctor of Philosophy

Discipline of Biomedical Engineering,

College of Engineering and Informatics,

Ollscoil na Gaillimhe - University of Galway.

2023

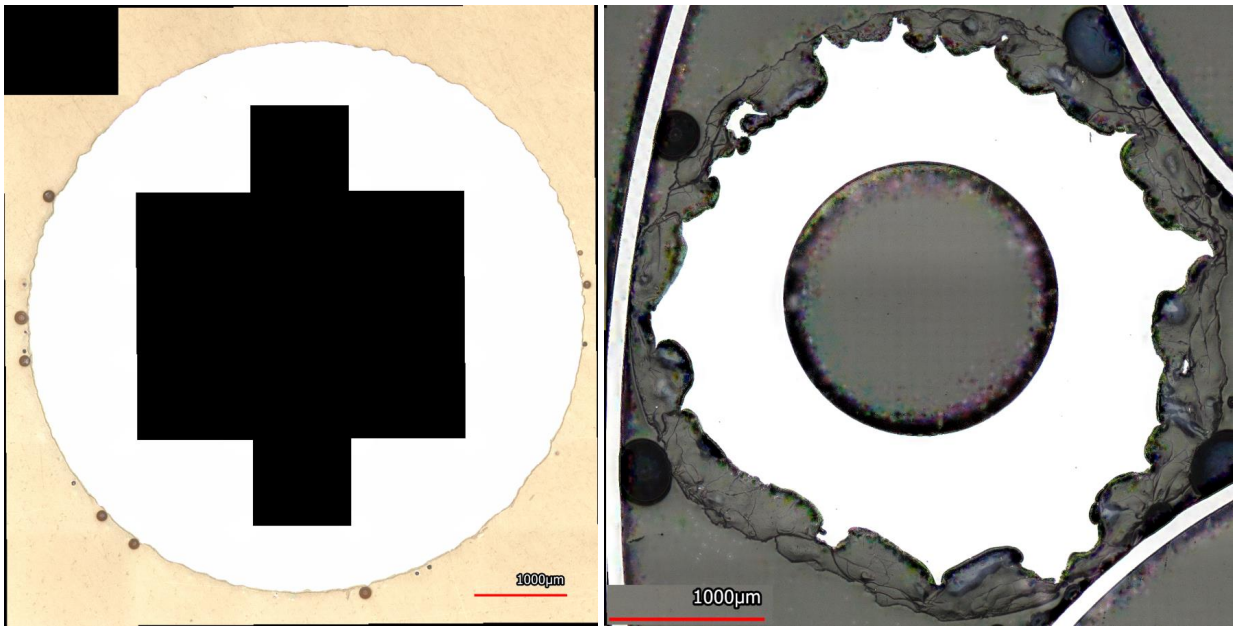

Felix Benn. Danke!

I declare that the work presented in this thesis is my own.

Kerstin van Gaalen

2023

Abstract

Magnesium-based medical implants have the potential to overcome several complications that arise with permanent metallic implants. Magnesium-based implants are biodegradable such that they can undergo absorption once their load-bearing function has been completed, thereby avoiding a secondary removal surgery. However, several challenges must be overcome as non-uniform and highly localised pitting corrosion mechanisms can lead to early failure of implants. Despite this, the majority of experimental studies to date tend to consider bulk measures of corrosion by measuring mass loss, while the role of localised surface corrosion mechanisms have been largely ignored, or evaluated using qualitative approaches. As a consequence, there is limited quantitative understanding on how pit formation (e.g. severity and spatial distribution) affects the overall mechanical performance of magnesium-based alloys. The objective of this thesis is to investigate the relationship between spatial corrosion performance with the corresponding mechanical integrity of a magnesium WE43 alloy for orthopaedic implants by means of an experimental and numerical approach.

In this thesis, a three-dimensional automated detection framework, '*PitScan*' was developed to systematically evaluate the extent and morphology of surface-based pitting corrosion of cylindrical magnesium specimens undergoing corrosion through in-vitro immersion. *PitScan* used a Python-based approach to analyse micro-computed tomography images (µCT) of cylindrical specimens undergoing corrosion. It was used to establish relationships between local pitting parameters and mechanical performance, which was determined through uniaxial mechanical testing. Additionally, a finite element surface-based degradation model was implemented to further explore the correlation between the severity of localised corrosion mechanisms and mechanical integrity. These experimental and computational approaches were then used to investigate the influence of a plasma electrolytic oxidation (PEO) surface treatment on the corrosion performance of a Magnesium alloy. Finally, the degradation model was utilised to demonstrate its potential within the design development chain of degradable implants.

The *Pitscan* algorithm was able to systematically identify pitting morphology on the corroding surface, enabling full spatial characterisation of pitting parameters, including pit density, pit size, pit depth as well as pitting factor according to ASTM G46-94. It was found that bulk measures of mass loss during corrosion were not suitable predictors of the mechanical integrity of corroding magnesium specimens. Instead, PitScan showed that features linked to the reduction of the cross-sectional area seem to be the best predictors for the remaining strength. This thesis also provides the first quantitative evidence that a surface-based non-uniform corrosion model could capture both the geometrical and mechanical features of a magnesium alloy undergoing corrosion. By considering a wide range of corrosion scenarios, it was demonstrated that parameters described in ASTM G46-94 showed weaker correlations to the mechanical integrity of corroding specimens, compared to parameters determined by *Pitscan*. Similar to experimental observations, the minimal cross-sectional area parameter was the strongest predictor of the remaining mechanical strength ($R^2 = 0.98$), with this relationship being independent of the severity or spatial features of localised surface corrosion. It was also shown that uniform degradation models are not suitable to predict the mechanical performance of samples undergoing corrosion. This thesis also demonstrated that PEO

surface treatment on the magnesium alloy continued to protect the samples from corrosion throughout the entire corrosion process, and not just in the early stages of corrosion. Furthermore, the phenomenological surface features were used to calibrate the surface-based corrosion model to fully predict the mechanical performance of both unmodified and PEO surface modified magnesium WE43. Finally, the surface-based corrosion model was used to demonstrate how simulated design adaptations could optimize material usage, while maintaining similar mechanical integrity during corrosion. Overall, this provides significant technical advances and enhances the scientific understanding of corrosion in magnesium alloys, and could inform future work in this area.

List of Publications

Journal Articles

The following publication have arise from the work presented in this thesis:

- **van Gaalen, K.**, Gremse, F., Benn, F., McHugh, P. E., Kopp, A., Vaughan, T. J. (2022) 'Automated ex-situ detection of pitting corrosion and its effect on the mechanical integrity of rare earth magnesium alloy-WE43', Bioactive Materials. 8, p. 545-558. doi:10.1016/j.bioactmat.2021.06.024.

- **van Gaalen, K.**, Quinn, C., Benn, F., McHugh, P.E., Kopp, A., Vaughan, T.J. (2023) 'Linking the effect of localised pitting corrosion with mechanical integrity of a rare earth magnesium alloy for implant use', Bioactive Materials. 21, p. 32-43. doi: 10.1016/j.bioactmat.2022.08.004

- **van Gaalen, K.**, Quinn, C., Weiler, M., Gremse, F., Benn, F., McHugh, P.E., Kopp, A., Vaughan, T.J. 'Predicting localised corrosion and mechanical performance of a PEO surface modified rare earth magnesium alloy for implant use through in-silico modelling', *Bioactive Materials. 26, p. 437-451. doi:10.1016/j.bioactmat.2023.03.009*

International Conference Proceedings

- **van Gaalen, K.**, Gremse, F., Kopp, A., Vaughan, T.J., 'Standardized Detection of Pitting Behaviour of a Magnesium Alloy with Automated Image Recognition of µCT Scans', Updates in Bioabsorbable Metals 2020 – Virtual Workshop, August 2020.

- **van Gaalen, K.**, Gremse, F., Benn, F., McHugh, P.E., Kopp, A., Vaughan, T.J. 'Phenomenological Tracking of Pitting Corrosion and the Mechanical Integrity of a Magnesium Rare Earth Alloy', 13th Biometal Conference, August 2021, Virtual Conference.

- **van Gaalen, K.**, Gremse, F., Benn, F., McHugh, P.E., Kopp A., Vaughan, T.J. 'Phenomenological ex-situ tracking of pitting corrosion and the mechanical integrity of a

WE43 magnesium alloy', Poster Presentation, 31st Annual Conference of the European Society for Biomaterials (ESB 2021), September 2021.

- **van Gaalen, K.**, Quinn, C., McHugh, P.E., Kopp, A., Vaughan, T.J. 'On the Mechanical Performance of a Magnesium Alloy Undergoing Corrosion: In-vitro Testing and Finite Element Analysis', 11th European Solid Mechanics Conference, July 2022, Galway, Ireland.

- **van Gaalen, K.**, Quinn, C., Benn, F., McHugh, P.E., Kopp, A., Vaughan, T.J. 'Linking geometrical degradation phenomena with the mechanical integrity of rare earth magnesium alloy for implant use', 14th Biometal Conference, August 2022, Alicante, Ireland.

Acknowledgments

This thesis was written during my work as Marie-Curie Early Stage Researcher within the BioimplantITN project. Here, I worked at the University of Galway, Ireland as well as at Meotec GmbH, Germany. I would like to take this opportunity to thank all the people who contributed to the success of this work.

Foremost, I would like to thank my supervisor Dr. Ted Vaughan for is consistent support, having always the bigger picture in mind throughout the past 3.5 years, and the weekly *Ted Talks*. Thank you for all the revisions, your expertise and always having a sympathetic ear. I would also like to thank Prof. Peter McHugh for his guidance and extraordinary expertise. Dr. Alexander Kopp, functioning as CEO of Meotec, thanks a lot for your tireless support and the freedom I enjoyed working at the facilities of Meotec and all the samples I was allowed to degrade and damage throughout my work. Thank you for all the fruitful discussions and your high expertise on magnesium.

I wish to acknowledge my funding source, the European Union's Horizon 2020 research and innovation programme under the Marie Skłodowska-Curie grant agreement No 813869 and all people who were involved in this project.

I would also like to thank all former and active colleagues who helped me with my work on certain machines and supported me during the various tests. From the University of Galway, I thank Conall Quinn for introducing me into the modelling of magnesium corrosion, and for using his proposed adaptions within my work. From Meotec, I would like to thank especially Felix Benn for all the discussions about magnesium and the hundreds of coffees we had together. Also thanks to Igor Schestakow and Toni Mommertz for helping me to perform the lab work.

A big thank you goes to my family and friends who supported me. In particular, I would like to thank my parents, Hermine and Peter van Gaalen, who have supported and encouraged me throughout my life and education. Aunt Jutta, Uncle Jaco thank you so much for always supporting me at crucial moments throughout my studies. Finally, to my husband Kai Schelthoff, who encouraged me even to start a PhD. Thank you for your unconditional love, always being there for me and being able to see more in me than I do myself.

Abbreviations

CDM	Continuum-based damage mechanics
DMEM	Dulbecco's Modified Eagle Medium
EDX	Energy-dispersive X-ray spectroscopy
EIS	Electro impedance spectroscopy
FBS	Fetal bovine serum
FSP	Friction stir processing
FE	Finite element
FEA	Finite element analysis
FEM	Finite element method
FTIR	Fourier-transform infrared spectroscopy
HBSS	Hank's Balanced Salt Solution
MEM	Minimum Essential Medium
OPC	Open Circuit Potential
PDP	Potentiodynamic polarisation
PLA	Polylactic acid
PEO	Plasma electrolytic oxidation
RH	Relative humidity
SEM	Scanning electron microscope
SBF	Simulated body fluid
UTS	Ultimate tensile strength
XRD	X-Ray diffraction analysis
XPS	X-ray photoelectron Spectroscopy
YS	Yield strength

Table of Contents

Chapter 1

Introduction

1.1 Orthopaedic implants

1.1.1 Conventional implants

Each year, there are almost 200 million bone fracture events across the world [1, 2]. Many of these traumatic fractures require surgical intervention, whereby a variety of orthopaedic fixation devices are implanted to stabilise the fracture region to ensure healing. Currently, the majority of orthopaedic implants are made of Titanium or Stainless steel, which exhibit mechanical properties that provide sufficient support to the surrounding tissue during the healing phase. However, these permanent metallic implants can cause issues in later stages of healing as their high stiffness compared to the native bone can result in stress shielding, whereby loading is directed through the implant, leading to unwanted resorption of the surrounding bone tissue [3]. As a consequence, implant removal may be necessary through a second surgical procedure. This removal of fixed-metallic implants is the most common orthopaedic procedure in industrial countries, accounting for approximately 5 % of orthopaedic surgeries and contributing to an estimated annual cost of over 250 million Euro in Germany alone [2, 4–6]. Biodegradable implants have the potential to form the basis for the next generation of orthopaedic fixation implants, as they can reduce the need for removal surgeries [7] and avoid certain late-stage issues associated with conventional permanent implants.

1.1.2 Biodegradable implants

Biodegradable materials are a category of biomaterial that gradually degrade once implanted in a biological environment. There has been increasing interest in biodegradable materials over the last number of decades to provide alternative materials for both orthopaedic and vascular implant applications. Polymer- and metal-based biodegradable implant materials have been developed, with the specific aim to provide structural support to the fractured region during the healing process, with the device subsequently degrading fully, once healing has been completed and the functional role of the implant is no longer needed [8]. Compared to permanent metallic implants (e.g. titanium, stainless steel, nitinol), this eliminates the need for an additional removal surgery, which reduces the risk on the patient and overall cost burden on health systems.

The target functional properties of biodegradable orthopaedic implants presents a difficult balancing act between (i) providing enough structural support in the first number of months and (ii) minimising subsequent absorption time to reduce the possibility of late-stage events. Figure 1.1 shows the optimal degradation performance for a biodegradable implant, whereby its degradation process is carefully synchronised with the natural growth and healing timescales of the surrounding tissue. During the initial phase, the load at the fracture site is carried by the implant until both the inflammatory and soft callus phases of healing have completed. As the hard callus begins to form, the tissue increases in stiffness and load can be transferred to the tissue again. [9].

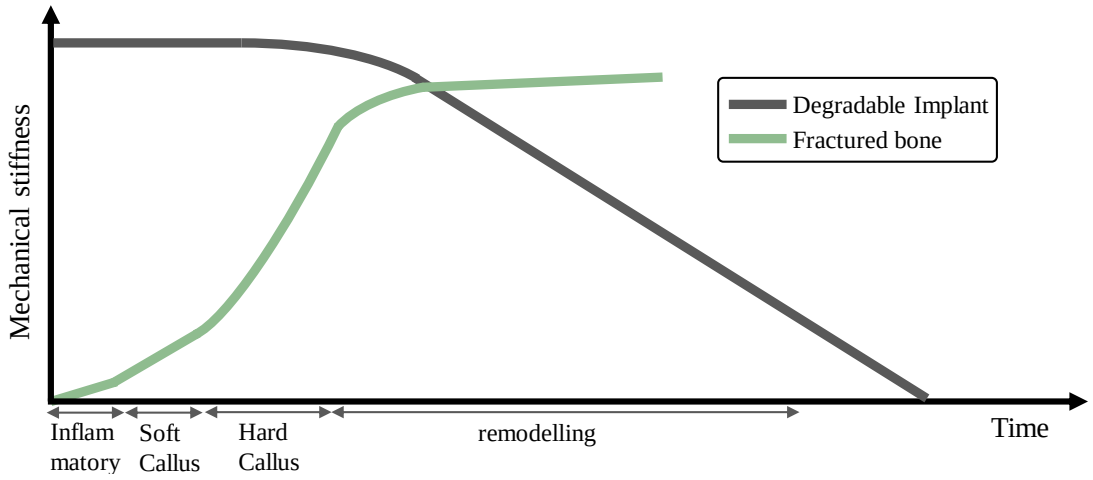

Figure 1.1: Optimal degradation performance for a biodegradable implant in bone fracture scenario, including the theoretical healing procedure of a fractured bone (adapted from Zhao et al. [9])

At this point, implant degradation can take place, with the load-bearing capacity of the implant gradually degrades so that the surrounding tissue can fully undergo long-term remodelling. This represents an idealised scenario and there is substantial variability depending on the degradable material itself and the surrounding environmental conditions, such as anatomical location, loading conditions, levels of inflammation and blood flow [10, 11].

Apart from the load-bearing function of the biodegradable implant, the chosen biomaterial must also be able to fulfil a wide range of other functional properties [12, 13]. Specifically, biodegradable materials should be biocompatible and not cause inflammatory responses once implanted, with their degradation products being non-toxic such that they can be excreted or resorbed by the body. These materials should also exhibit good processability during manufacturing and should be sterilisable. Both polymer- and metal-based biodegradable implant materials have been developed, although several issues relating to low mechanical properties and/or rapid degradation behaviour, respectively, still must be overcome.

1.1.2.1 Polymers

Biodegradable polymers can be categorized as either natural or synthetic, with both groups undergoing degradation processes when exposed to aqueous environments. Synthetic polymers are more widely used, with polylactic acid (PLA), poly-glycolic acid (PGA) and their co-polymers, having been approved for use as implantable materials by the US Food and Drug Administration (FDA) over fifty years ago. Generally, synthetic polymers, approved for medical purposes, show good biocompatibility and controllable degradation rates. Polymer degradation takes place through hydrolysis, which results in water-soluble oligomers or even monomers as final degradation products [8, 14]. This degradation process takes place through either surface- or bulk-erosion processes [15]. The first approved polymer-based implants were biodegradable sutures in the 1960s (Poly-glycolic Acid (PGA)) [15, 16]. Nowadays, a wide variety of applications for polymer-based implants exists, with Figure 1.2 showing an overview of polymer implants currently on the market.

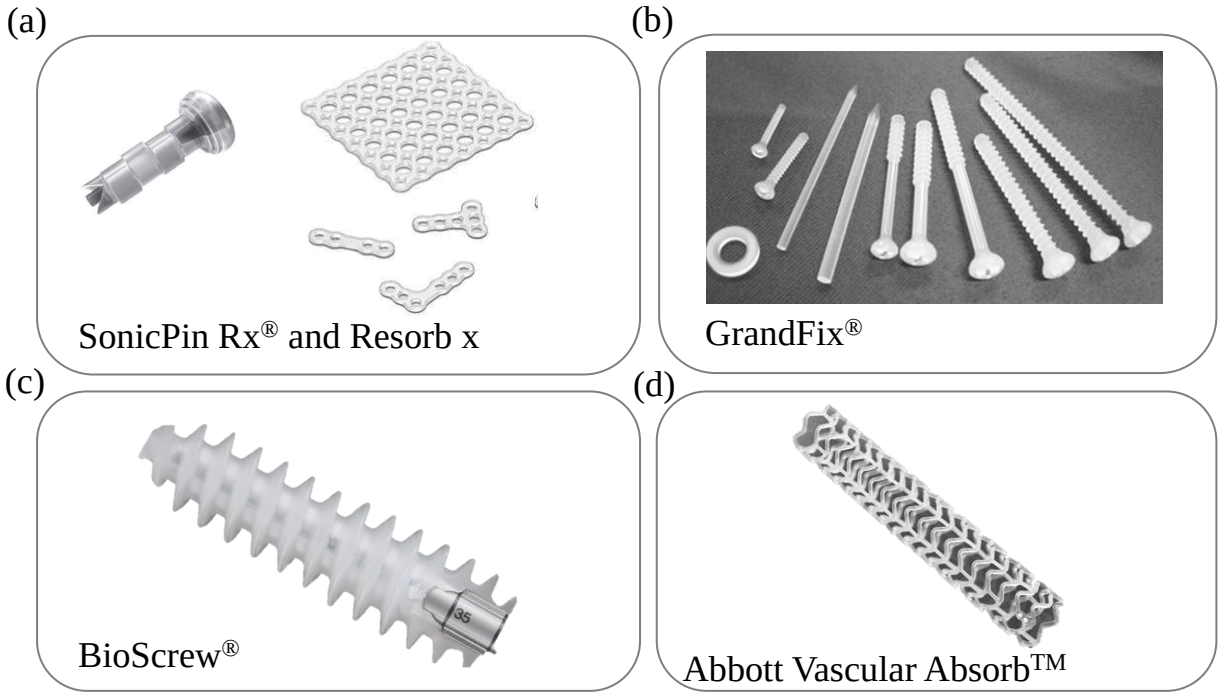

Figure 1.2: Polymer-based biodegradable implants (a) Material: PDLLA, plates and screws for maxillofacial applications (KLS Martin GmbH & Co, Tuttlingen, Germany) (b) Material: PLLA, Gunze, Kyoto, Japan (c) Material: PLLA interference screw (CONMED Largo, FL, USA) (d) Material: PLLA stent (Abbott Vascular Inc., CA, USA).

Several major industry players, including KLS Martin GmbH, have polymer-based bioabsorbable implants on the market that have achieved clinical success in relatively low load-bearing applications, such as soft-tissue reattachment. However, polymer-based implants generally exhibit lower mechanical stiffness and strength compared to metal-based implants [17], which has limited their wider application. More generally, biodegradable polymers are widely used in tissue engineering, drug delivery applications, regenerative medicine, gene therapy, and as coatings on implants [16]. A major disadvantage of implantable polymers is that they can be impacted by enzymes, resulting in heavy inflammatory responses. For example, while Abbott Vascular have pioneered the development of polymer-based bioabsorbable stents for vascular applications, with significant clinical data already generated, late-stage clinical data demonstrate an increased risk of late-stage adverse events compared to permanent metallic drug eluting stents. Consequently, Abbott was forced to withdraw

this device from the market (Figure 1.2 (d)) [18].

1.1.2.2 Metals

Compared to polymer-based implants, degradable metallic implants are more suitable for load bearing applications due to their higher mechanical properties. Several candidates as bioabsorbable metal alloys have been proposed, including magnesium, zinc, iron and their various alloy combinations. Iron-based alloys exhibits high strength and good ductility, but its corrosion process takes place too slowly, which means that it can face similar long-term issues that are encountered by permanent metallic implants [19–21]. While zinc-based alloys have more favourable corrosion properties, they tend to have low tensile strengths and poor creep resistance, which limits their capacity in long-term load-bearing applications [22, 23]. On the other hand, magnesium-based alloys have mechanical properties that are highly suited to orthopaedic applications, and recent strategies to improve their corrosion performance mean they are becoming a viable alternative to permanent metallic biomaterials.

Magnesium is an essential trace element in the human body. The corrosion products of magnesium are absorbed by macrophage cells and then excreted by the kidneys [24]. Magnesium was first used in the medical field by the physician Edward C. Huse, who implanted magnesium wires as a ligature for bleeding vessels [25]. However, this, and many early attempts using magnesium as a biomaterial failed due to the amount of impurities that resulted in a rapid corrosion. Since the turn of the millennium, there has been increasing interest in magnesium as an implantable material [26]. In 2005, Witte et al. [27] conducted an in-vivo study and examined four different alloys, AZ31, AZ91, LAE442, and WE43, which were implanted as small rods into the bone marrow of guinea pig femurs. Compared to a reference with PLA, results showed that LAE442 had the slowest degradation rate and bone formation was significantly increased around all four magnesium alloys. They reported an osteostimulative effect, whereby the release of the corrosion products actually promote bone formation in the implanted region, has also been reported in several other studies [10, 28–32]. Magnesium-

based alloys also have similar mechanical properties to the native bone, which reduces the risk of stress shielding compared to permanent metallic implants made from Titanium or Stainless steel [3, 33]. Table 1.1 provides a summary of the material properties of various implantable materials, although it should be noted that values reported can vary depending on the exact alloy compositions, manufacturing process and applied heat treatments.

Table 1.1 Material properties of Medical device materials and human bone (values vary with exact compositions, manufacturing process, post-processing steps. Further, the values taken from standards are the minimal requirements for the certain alloy

	Tensile strength [MPa]	Compression strength [MPa]	Yield strength [MPa]	E-modulus tensile [GPa]	Max. elongation [%]	Density [g/cm^3]
Cortical Bone [34, 35]	35-283	160-240	115	5-23	6-10	1.8-2.0
Trabecular Bone [34, 35]	1.5-38	1.5-9.3		0.01-3		1.0-1.4
Magnesium pure [34, 36]	90-190	20-115	20	45	10	1.74
Titanium [37]	860	758		100-125	8	4.4
Stainless steel [38–40]	490	1080	190	193	40	8
MgZn [41, 42]	288		227	40	21	1.8
MgZnCa [43]	276		178	40	25	
WE43 [44, 45]	250	500	160	44	4	1.84
AZ31 [44, 46]	240	350	145	44	7	1.78

In the development of magnesium alloys for orthopaedic applications, it is generally desirable that the corrosion takes place at a controlled rate and that it takes place uniformly to ensure appropriate mechanical properties in the later stages of degradation. A wide variety of magnesium alloy compositions have been explored and Figure 1.3 shows the most used alloy elements for magnesium in orthopaedic applications. First magnesium-aluminium alloys (up to 6 wt.% Al) generated interest due to their improved ultimate tensile strength and elongation, as well as to their improved corrosion resistance due to a protective Al_2O_3 film on the surface. Nevertheless, the addition of aluminium is problematic as it results in neurotoxic properties [19]], which has meant that it is not used in any magnesium-based orthopaedic implants. Zinc (up to 4 wt.% Zn) as alloy element also increases ultimate tensile strength and elongation, while adding 0.2 wt.% calcium can further refine the microstruc-

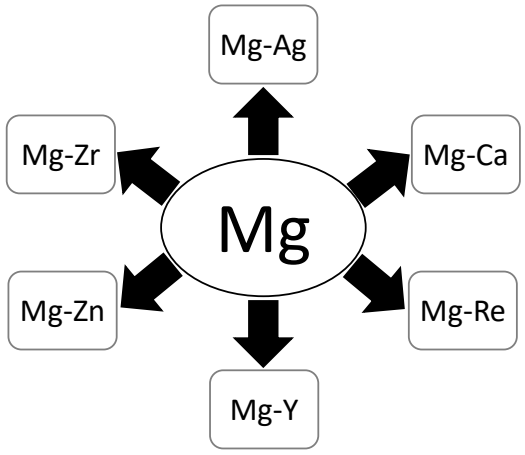

Figure 1.3: The most used Mg-based binary alloys for orthopaedic applications. (adapted from [24])

ture and substantially decrease the degradation rate [19, 47], but has little effect on the mechanical properties. Other alloying elements include rare earth elements, such as yttrium, neodymium, gadolinium. In general, these rare earth elements aim to improve the strength, ductility, and corrosion resistance through solid solution and precipitation hardening [48]. Neodymium is only partially soluble in magnesium, though its addition can greatly improve the corrosion resistance [49]. Yttrium is often induced to enhance the creep and corrosion resistance [50]], although this element can impose adverse effects on DNA transcription factors [51, 52]. Further in-vitro and in-vivo studies of rare earth elements are required to fully evaluate any potentially harmful effects of these alloying elements [50, 53]. Table 1.1 presents the mechanical properties of some magnesium alloy combinations, and how these compare to permanent metallic materials and bone tissue itself.

Furthermore, through specific manufacturing processes or post-manufacturing, such as heat treatments or solid solution strengthening, the mechanical properties can be tailored to improve material strength and creep resistance [47, 48, 54]. Other treatments, such as coatings or surface modifications, are mainly used to enhance the corrosion resistance. Magnesium alloys for medical applications can be produced through a range of techniques like casting followed by extrusion [55, 56], sintering of magnesium powders [57], or even through 3D

printing by laser powder bed fusion [58, 59].

At present, there are several magnesium-based medical products on the market including orthopaedic screws, pins and wires, as well as vascular stents for coronary applications. In 2013, the first CE-approved bioabsorbable WE43-based implant, the MAGNEZIX® hollow compression screw from Syntellix AG (Figure 1.4 (b)) was made available. These screws are mainly used for foot and hand surgeries. In 2016 BIOTRONIK SE & Co. KG received the CE-approval for their Magmaris coronary stent, which is based on a WE43 alloy with a 7 µm PLLA coating (Figure 1.4 (a)). MgCa based orthopaedic implants are also available from U&i Corporation (Figure 1.4 (d)), with the Resomet™ product group receiving CE-approval in 2018. More recently, in 2020, Medical Magnesium GmbH received CE-approval for their mm.X orthopaedic implants (Figure 1.4 (c)), which are also made from a WE43 alloy equipped with a PEO surface treatment. While these devices have demonstrated initial clinical success and have even reached the market, magnesium-based implants are still not widely adopted, and many technologies remain in development phase, with several obstacles still to be overcome. In particular, the degradation mechanism of magnesium results in the release of hydrogen gas, which can lead to severe cell damage and cavitations forming in the surrounding tissue [60]. Furthermore, the corrosion of magnesium-based implants can take place too quickly and through non-uniform processes such as pitting-based mechanisms [61–65]. This localised corrosion mechanism is caused by microstructural inhomogeneities and impurities and can result in early failure of the implant in load-bearing applications. While the spatial and temporal evolution of corrosion is controllable to some degree by varying alloying composition and/or by applying a surface modification [47, 66–69], a better understanding of the corrosion process is required to optimise the performance of magnesium-based medical implants and therefore enable their widespread implementation in the medical field.

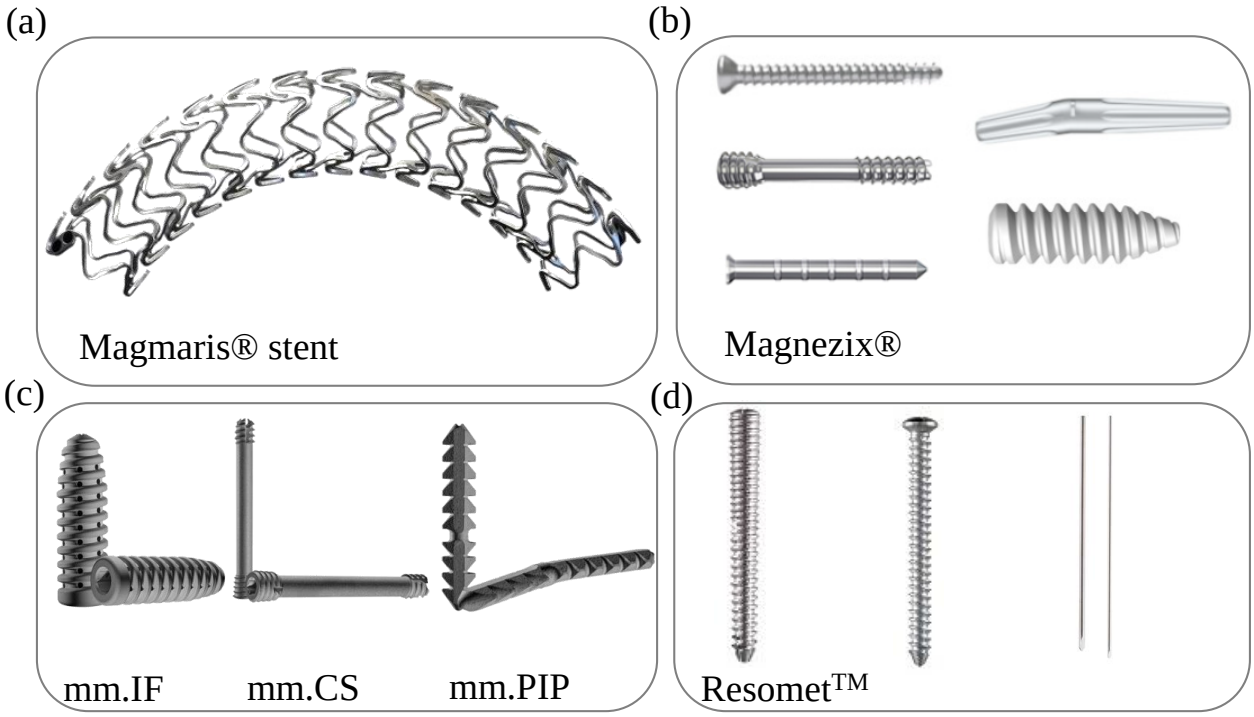

Figure 1.4: Magnesium-based implants (a) Magmaris stent (BIOTRONIK SE & Co. KG, Berlin, Germany) (b) Magnezix product group: bone screw, compression screw, pin, arthrodesis system, interference screw (Syntellix AG, Hannover, Germany) (c) mm.X products: interference screw, compression screw, Proximal phalanges implant (Medical Magnesium GmbH, Aachen Germany) (d) Resomet^{TM} Headless Screw, Cortex Screw, K-wire and Pin (U&i Corp. Seoul, Republic of Korea).

1.2 Corrosion of Magnesium

1.2.1 Background

The term *corrosion* describes a natural process whereby the exposed surface of a metal reacts with its environment, which results in the gradual degradation of the metal through chemical and/or electrochemical reactions. Corrosion is dictated through different ion concentrations in the media, as well as through the alloys' microstructure itself. Research is still ongoing to fully understand the corrosion of magnesium in various aqueous solutions [70–74]. Once magnesium is exposed to air, a thin, more stable oxide layer is formed. However, once this

stable layer becomes damaged through exposure to aqueous solutions, corrosion progresses through the formation of electrochemical cells. This leads to the migration of ions into the solution from the metal surface itself and results in the formation of a hydroxide layer, $Mg(OH)_2$, on the surface [47]. Typical types of corrosion that take place under physiological conditions are galvanic, intergranular and pitting corrosion. These mechanisms tend to promote localised corrosion by the presence of impurities and inhomogeneities that are present throughout the material due to the manufacturing process. Pitting corrosion occurs when magnesium is exposed to an aqueous solution containing chloride ions [75], which break down the passive layer due to the formation of $MgCl_2$. Through impurities or secondary phases in the alloy, local internal galvanic cells form that result in localised corrosion taking place [75]. A quantitative understanding of the onset and evolution of localised corrosion in magnesium alloys is critical to avoid premature implant failure.

1.2.2 Experimental characterisation of Magnesium corrosion

To investigate the corrosion mechanisms of magnesium-based alloys, in-vitro biocorrosion testing is most widely used, whereby samples are immersed in aqueous solutions to enable the corrosion process. Corrosion testing is set out by two ASTM standards, ASTM F3268-18a and ASTM NACE TM0169/G31-21 [76, 77]. Both documents provide guidance on the general test setup, which includes the type of immersion media, testing timeframe, while also providing guidance on evaluation methods, including how the corrosion rate should be measured. While these two standards provide a general framework for corrosion testing, there is still significant room for interpretation, and a wide range of immersion test setups have been used across the literature to experimentally characterise corrosion performance of magnesium-based materials and implants.

Generally, in-vitro testing of magnesium evaluates the corrosion of samples by tracking weight loss measurements at discrete time points, or by capturing measurements of hydrogen evolu-

tion during testing, whereby 1 mol of hydrogen corresponds to 1 mol of released magnesium [78]. Other approaches used micro-CT scanning of the samples and a subsequent 3D reconstruction to determine the change in volume, and mass, during the experiment. However, to date, most studies that perform in-vitro testing consider only bulk measurements of mass loss, with the progression of localised surface-based corrosion generally ignored. If pitting corrosion is considered, it is generally assessed through qualitative approaches such as simple visual inspection [79–81]. However, previous studies have demonstrated that localised corrosion clearly influences the mechanical integrity of specimens, with a disproportional relation between bulk mass loss and mechanical strength observed for different magnesium alloys undergoing corrosion [82–84].

ASTM G46-94 [85] provides a guideline to examine and evaluate pitting corrosion in metals. Here, several metrics are proposed that provide information on the extent and severity of surface corrosion. These include pitting factor, which is the ratio of the deepest pit depth to mean pit depth, mean pit size, and pit density. However, this standard has rarely been used to assess magnesium-based corrosion, with only limited examples from Witte et al. (2010) [79], Kappatos et al. (2010) [86], Kalb et al. (2012) [87] using pitting factor within their studies to assess the severity of localised corrosion. Despite this, there is still no clear link between pitting factor and the mechanical integrity of a specimen undergoing corrosion. This outlines a clear need for a quantitative method to determine the spatial formation of corrosion and how the phenomenological progression of corrosion corresponds to the mechanical integrity.

1.2.3 Enhancing Magnesium corrosion through surface treatments

Most magnesium alloys tend to degrade too fast, especially for late-stage load bearing applications. To overcome this, surface coatings and modifications are commonly used. They

aim to slow down and unify corrosion, while also enhancing properties such as biocompatibility or providing antibiotic or drug-elution mechanisms [88]. Polymers like synthetic aliphatic polyesters (e.g. Polylactic acid, Poly (lactic-co-glycolic) acid), natural polymers (e.g. Collagen, Chitosan) or hydroxyapatites [89, 90] are used as coating material for various magnesium alloys. However, several of these coatings have poor wear resistance [47, 89, 91]. Surface modification is also a promising approach to enhance corrosion properties of magnesium-based samples. Plasma electrolytic oxidation (PEO), where the outer surface is transformed into a hard ceramic layer in an electrolytic bath, under the influence of an electrical potential [55, 68, 91], is a technique that enhances the corrosion performance compared to unmodified magnesium. PEO coatings have already been demonstrated to decelerate corrosion rates across different geometries and different magnesium alloys in in-vitro and in-vivo studies [55, 56, 63, 68, 92, 93]. Further, PEO modified samples provided excellent adhesion to the core material, as well as providing enhanced biocompatibility and improved osseointegration compared to unmodified samples [55, 56, 63]. While PEO surface modification improves corrosion performance, there is limited information available on how surface-corrosion evolves in the presence of this surface-modified layer. Furthermore, there is limited quantitative information on the mechanical performance of PEO modified magnesium undergoing corrosion.

1.2.4 Computational models for Magnesium corrosion

Current modelling approaches to simulate the degradation of magnesium-based alloys are mainly categorised as either phenomenological or physical-based models. Physically-based degradation considers the chemical processes taking place at the interface of the specimen's surface and its environment. However, those modelling approaches are computationally prohibitive and mostly assuming uniform degradation [94–96].

Phenomenological models are more widely used, whereby continuum damage mechanics

(CDM) is utilized in combination with element removal to predict the effects of corrosion on the exposed surface. These models have been used to predict uniform corrosion [97, 98], and localised corrosion, which used weighted probability functions to simulate localised corrosion mechanisms [82, 83, 99–102]. It was demonstrated, that these localised corrosion models result in a significantly better agreement of the relation between specimens' mechanical strength and corresponding mass loss [82–84]. However, little quantitative information has been provided by these studies, in particular how pit development, including severity and spatial distribution, influences overall mechanical performance.

Furthermore, it is challenging to experimentally characterise the whole spectrum of corrosion scenarios. The vast range of conceivable alloy combinations results in different spatial and temporal progression of corrosion. Due to this, a comprehensive mechanistic connection between surface-based corrosion and the metals' mechanical performance is nearly impossible, and necessitates the need for alternative strategies through computational modelling.

1.3 Thesis Objectives

The global objective of this thesis is to investigate the corrosion performance of a magnesium alloy through a combined experimental and numerical approach. In particular, this thesis will focus on establishing relationships between the localised phenomenology of surface corrosion and mechanical performance of a WE43 magnesium alloy. This will be achieved through the following specific objectives:

(i) To develop an automated approach to systematically evaluate the severity and phenomenology of localised surface corrosion in WE43 magnesium alloy and use it to establish relationships between local pitting parameters and mechanical performance.

(ii) To implement an enhanced surface-based corrosion model that predicts both the phenomenology of corrosion and mechanical performance to provide new mechanistic in-

sight into the performance of magnesium-based materials undergoing corrosion.

(iii) To investigate the influence of plasma electrolytic oxidation surface treatment on a WE43 magnesium alloy by characterising both surface-based corrosion formation and the corresponding mechanical integrity through an experimental and computational approach.

(iv) To validate the surface-based corrosion model by investigating the performance of unmodified and plasma electrolytic oxidation surface-modified WE43 bone plate samples, and use this framework to carry out further numerical design optimisation of bone plates.

1.4 Thesis Structure

The outline of this thesis is as follows:

Chapter 2 presents the recent relevant literature for magnesium-based implants. A summary of in-vitro immersion testing for magnesium corrosion is presented, as well key parameters that influence corrosion behaviour and mechanical performance of magnesium. A review of the current state-of-the-art for numerical modelling of surface-based corrosion of magnesium alloys is also provided.

Chapter 3 outlines a summary of the theoretical frameworks used in this thesis, including techniques for automated image processing, fundamental theory of continuum mechanics and its application within the finite element method.

Chapter 4 presents an automated detection framework for tracking the spatial formation of corrosion for circular shaped magnesium samples by calculating several geometrical surface features during corrosion. An in-vitro immersion study was performed, which serves as data basis for geometrical and mechanical characteristics. Furthermore, several correlations are drawn between those surface-based features and the remaining mechanical strength.

In **Chapter 5** a surface-based corrosion model is implemented within the finite element framework to predict geometric features of pitting corrosion and resulting mechanical performance of WE43. Several new relations between severity of localised corrosion and the mechanical performance are established, by simulating different severities of localised corrosion.

Chapter 6 investigates the influence of plasma electrolytic oxidation (PEO) surface treatment on the corrosion behaviour and the corresponding mechanical performance of WE43 specimens, characterised through an extensive in-vitro immersion study. Furthermore, the surface-based corrosion model is calibrated to predict the performance of both unmodified and PEO modified specimens, matching phenomenological features, as well as, mechanical parameters.

In **Chapter 7** the calibrated degradation model from Chapter 6 is applied to a generic bone plate geometry in an effort to validate the degradation model. With this design, an experimental study is performed with in-vitro immersion testing and four-point bending tests. To highlight the potential of the numerical degradation model, not only the experimentally tested bone plate design is simulated, but also two additional design adaptions. All designs underwent degradation and four-point bending simulations to highlight the importance to consider also the degradation performance during the design development of a degradable implant.

Chapter 8 presents the main conclusions of the thesis, as well as an outlook on possible future work in this field.

References

[1] A.-M. Wu *et al.*, "Global, regional, and national burden of bone fractures in 204 countries and territories, 1990–2019: a systematic analysis from the Global Burden of Disease Study 2019," *The Lancet Healthy Longevity*, vol. 2, no. 9, e580–e592, 2021, ISSN: 26667568. DOI: 10.1016/s2666-7568(21)00172-0.

[2] G. Reith, V. Schmitz-Greven, K. O. Hensel, M. M. Schneider, T. Tinschmann, B. Bouillon, and C. Probst, "Metal implant removal: benefits and drawbacks–a patient survey," *BMC Surg*, vol. 15, p. 96, 2015, ISSN: 1471-2482 (Electronic) 1471-2482 (Linking). DOI: 10.1186/s12893-015-0081-6. [Online]. Available: https://www.ncbi.nlm.nih.gov/pubmed/26250649.

[3] D. Sumner, "Long-term implant fixation and stress-shielding in total hip replacement," *Journal of Biomechanics*, vol. 48, no. 5, pp. 797–800, 2015, ISSN: 0021-9290.

[4] O. Bostman and H. Pihlajamaki, "Routine Implant Removal after Fracture Surgery: A Potentially Reducible Consumer of Hospital Resources in Trauma Units," vol. 41, no. 5, pp. 846–849, 1996, ISSN: 2163-0755. [Online]. Available: https://journals.lww.com/jtrauma/Fulltext/1996/11000/Routine_Implant_Removal_after_Fracture_Surgery__A.13.aspx.

[5] I. M. Rutkow, "Surgical operations in the United States: 1979 to 1984," *Surgery*, vol. 101, no. 2, pp. 192–200, 1987, ISSN: 0039-6060. [Online]. Available: https://www.surgjournal.com/article/0039-6060(87)90106-1/abstract.

[6] M. Scharf, B. Krieg, M. Dengler, and B. Füchtmeier, "Die Implantatentfernung – eine Risiko-Nutzen-Abwägung?" *Op-Journal*, vol. 32, no. 02, pp. 80–88, 2016, ISSN: 0178-1715 1439-2496. DOI: 10.1055/s-0042-107036.

[7] J. B. Park and J. D. Bronzino, *Biomaterials : Principles and Applications*. Baton Rouge, UNITED STATES: Taylor & Francis Group, 2002, ISBN: 9781420040036. [Online]. Available: http://ebookcentral.proquest.com/lib/nuig/detail.action?docID=262228.

[8] D. F. Williams, "On the mechanisms of biocompatibility," *Biomaterials*, vol. 29, no. 20, pp. 2941–53, 2008. DOI: 10.1016/j.biomaterials.2008.04.023.

[9] D. Zhao, F. Witte, F. Lu, J. Wang, J. Li, and L. Qin, "Current status on clinical applications of magnesium-based orthopaedic implants: A review from clinical translational perspective," *Biomaterials*, vol. 112, pp. 287–302, 2017, ISSN: 1878-5905 (Electronic) 0142-9612 (Linking). DOI: 10.1016/j.biomaterials.2016.10.017. [Online]. Available: https://www.ncbi.nlm.nih.gov/pubmed/27770632.

[10] T. Kraus, S. F. Fischerauer, A. C. Hanzi, P. J. Uggowitzer, J. F. Loffler, and A. M. Weinberg, "Magnesium alloys for temporary implants in osteosynthesis: in vivo studies of their degradation and interaction with bone," *Acta Biomater*, vol. 8, no. 3,

pp. 1230–8, 2012, ISSN: 1878-7568 (Electronic) 1742-7061 (Linking). DOI: 10.1016/j.actbio.2011.11.008. [Online]. Available: https://www.ncbi.nlm.nih.gov/pubmed/22107870.

[11] E. Willbold, K. Kalla, I. Bartsch, K. Bobe, M. Brauneis, S. Remennik, D. Shechtman, J. Nellesen, W. Tillmann, C. Vogt, and F. Witte, "Biocompatibility of rapidly solidified magnesium alloy RS66 as a temporary biodegradable metal," *Acta Biomaterialia*, vol. 9, no. 10, pp. 8509–8517, 2013, ISSN: 17427061. DOI: 10.1016/j.actbio.2013.02.015.

[12] M. Prakasam, J. Locs, K. Salma-Ancane, D. Loca, A. Largeteau, and L. Berzina-Cimdina, "Biodegradable Materials and Metallic Implants-A Review," *J Funct Biomater*, vol. 8, no. 4, 2017, ISSN: 2079-4983 (Print) 2079-4983 (Linking). DOI: 10.3390/jfb8040044. [Online]. Available: https://www.ncbi.nlm.nih.gov/pubmed/28954399.

[13] A. W. Lloyd, "Interfacial bioengineering to enhance surface biocompatibility," *Medical device technology*, vol. 13, no. 1, pp. 18–21, 2002, ISSN: 1048-6690. [Online]. Available: http://europepmc.org/abstract/MED/11921776.

[14] M. Vert, J. Mauduit, and S. Li, "Biodegradation of PLA/GA polymers: increasing complexity," *Biomaterials*, vol. 15, no. 15, pp. 1209–1213, 1994, ISSN: 0142-9612. DOI: 10.1016/0142-9612(94)90271-2.

[15] S. Markus and H. Marc, "Emerging Trends," in *Emerging Trends in Medical Plastic Engineering and Manufacturing*. William Andrew, 2016, ch. 6, pp. 235–268, ISBN: 978-0-323-37023-3. DOI: https://doi.org/10.1016/B978-0-323-37023-3.00006-3. [Online]. Available: https://www.sciencedirect.com/science/article/pii/B9780323370233000063.

[16] S. Doppalapudi, A. Jain, W. Khan, and A. J. Domb, "Biodegradable polymers-an overview," *Polymers for Advanced Technologies*, vol. 25, no. 5, pp. 427–435, 2014, ISSN: 10427147. DOI: 10.1002/pat.3305.

[17] S. Pina and J. M. Ferreira, "Bioresorbable plates and screws for clinical applications: a review," *Journal of Healthcare Engineering*, vol. 3, no. 2, pp. 243–260, 2012.

[18] M. J. Lipinski, R. O. Escarcega, N. C. Baker, H. A. Benn, J. Gaglia M. A., R. Torguson, and R. Waksman, "Scaffold Thrombosis After Percutaneous Coronary Intervention With ABSORB Bioresorbable Vascular Scaffold: A Systematic Review and Meta-Analysis," *JACC Cardiovasc Interv*, vol. 9, no. 1, pp. 12–24, 2016, ISSN: 1876-7605 (Electronic) 1936-8798 (Linking). DOI: 10.1016/j.jcin.2015.09.024. [Online]. Available: https://www.ncbi.nlm.nih.gov/pubmed/26762906.

[19] Y. F. Zheng, X. N. Gu, and F. Witte, "Biodegradable metals," *Materials Science and Engineering: R: Reports*, vol. 77, pp. 1–34, 2014, ISSN: 0927796X. DOI: 10.1016/j.mser.2014.01.001.

[20] H. Li, Y. Zheng, and L. Qin, "Progress of biodegradable metals," *Progress in Natural Science: Materials International*, vol. 24, no. 5, pp. 414–422, 2014, ISSN: 10020071. DOI: 10.1016/j.pnsc.2014.08.014.

[21] H. Ibrahim, S. N. Esfahani, B. Poorganji, D. Dean, and M. Elahinia, "Resorbable bone fixation alloys, forming, and post-fabrication treatments," *Mater Sci Eng C Mater Biol Appl*, vol. 70, no. Pt 1, pp. 870–888, 2017, ISSN: 1873-0191 (Electronic) 0928-4931 (Linking). DOI: 10.1016/j.msec.2016.09.069. [Online]. Available: https://www.ncbi.nlm.nih.gov/pubmed/27770965.

[22] H.-S. Han, S. Loffredo, I. Jun, J. Edwards, Y.-C. Kim, H.-K. Seok, F. Witte, D. Mantovani, and S. Glyn-Jones, "Current status and outlook on the clinical translation of biodegradable metals," *Materials Today*, vol. 23, pp. 57–71, 2019, ISSN: 13697021. DOI: 10.1016/j.mattod.2018.05.018.

[23] B. Jia, H. Yang, Y. Han, Z. Zhang, X. Qu, Y. Zhuang, Q. Wu, Y. Zheng, and K. Dai, "In vitro and in vivo studies of Zn-Mn biodegradable metals designed for orthopedic applications," *Acta Biomater*, vol. 108, pp. 358–372, 2020, ISSN: 1878-7568 (Electronic) 1742-7061 (Linking). DOI: 10.1016/j.actbio.2020.03.009. [Online]. Available: https://www.ncbi.nlm.nih.gov/pubmed/32165194.

[24] I. Antoniac, M. Miculescu, V. Manescu Paltanea, A. Stere, P. H. Quan, G. Paltanea, A. Robu, and K. Earar, "Magnesium-Based Alloys Used in Orthopedic Surgery," *Materials (Basel)*, vol. 15, no. 3, 2022, ISSN: 1996-1944 (Print) 1996-1944 (Linking). DOI: 10.3390/ma15031148. [Online]. Available: https://www.ncbi.nlm.nih.gov/pubmed/35161092.

[25] E. Huse, "A new ligature," *Chicago Med J Exam*, vol. 172, no. 2, p. 11, 1878.

[26] N. T. Kirkland and N. Birbilis, *Magnesium Biomaterials* (SpringerBriefs in Materials). Springer, 2014, ISBN: 978-3-319-02122-5 978-3-319-02123-2. DOI: 10.1007/978-3-319-02123-2.

[27] F. Witte, V. Kaese, H. Haferkamp, E. Switzer, A. Meyer-Lindenberg, C. J. Wirth, and H. Windhagen, "In vivo corrosion of four magnesium alloys and the associated bone response," *Biomaterials*, vol. 26, no. 17, pp. 3557–63, 2005, ISSN: 0142-9612 (Print) 0142-9612 (Linking). DOI: 10.1016/j.biomaterials.2004.09.049. [Online]. Available: https://www.ncbi.nlm.nih.gov/pubmed/15621246.

[28] H. Nygren, P. Malmberg, and Y. Liu, "MgO Implanted in Rat Tibia Bone Marrow is Osteoinductive through the Formation of a Matrix, Containing Hydroxyapatite," in *Materials Science Forum*, vol. 879, pp. 1404–1407, ISBN: 1662-9752. DOI: 10.4028/www.scientific.net/MSF.879.1404.

[29] A. Burmester, R. Willumeit-Romer, and F. Feyerabend, "Behavior of bone cells in contact with magnesium implant material," *J Biomed Mater Res B Appl Biomater*, vol. 105, no. 1, pp. 165–179, 2017, ISSN: 1552-4981 (Electronic) 1552-4973 (Linking).

DOI: 10.1002/jbm.b.33542. [Online]. Available: https://www.ncbi.nlm.nih.gov/pubmed/26448207.

[30] L. Wu, F. Feyerabend, A. F. Schilling, R. Willumeit-Romer, and B. J. C. Luthringer, "Effects of extracellular magnesium extract on the proliferation and differentiation of human osteoblasts and osteoclasts in coculture," *Acta Biomater*, vol. 27, pp. 294–304, 2015, ISSN: 1878-7568 (Electronic) 1742-7061 (Linking). DOI: 10.1016/j.actbio.2015.08.042. [Online]. Available: https://www.ncbi.nlm.nih.gov/pubmed/26318802.

[31] F. Witte, H. Ulrich, C. Palm, and E. Willbold, "Biodegradable magnesium scaffolds: Part II: peri-implant bone remodeling," *J Biomed Mater Res A*, vol. 81, no. 3, pp. 757–765, 2007, ISSN: 1549-3296 (Print) 1549-3296 (Linking). DOI: 10.1002/jbm.a.31293. [Online]. Available: https://www.ncbi.nlm.nih.gov/pubmed/17390322.

[32] N. Kawamura, Y. Nakao, R. Ishikawa, D. Tsuchida, and M. Iijima, "Degradation and Biocompatibility of AZ31 Magnesium Alloy Implants In Vitro and In Vivo: A Micro-Computed Tomography Study in Rats," *Materials (Basel)*, vol. 13, no. 2, 2020, ISSN: 1996-1944 (Print) 1996-1944 (Linking). DOI: 10.3390/ma13020473. [Online]. Available: https://www.ncbi.nlm.nih.gov/pubmed/31963840.

[33] R. Huiskes, H. Weinans, and B. van Rietbergen, "The relationship between stress shielding and bone resorption around total hip stems and the effects of flexible materials," *Clinical orthopaedics and related researchs*, pp. 124–134, 1992.

[34] G. Eddy Jai Poinern, S. Brundavanam, and D. Fawcett, "Biomedical Magnesium Alloys: A Review of Material Properties, Surface Modifications and Potential as a Biodegradable Orthopaedic Implant," *American Journal of Biomedical Engineering*, vol. 2, no. 6, pp. 218–240, 2013, ISSN: 2163-1050. DOI: 10.5923/j.ajbe.20120206.02.

[35] R. B. Martin, D. B. Burr, N. A. Sharkey, and D. P. Fyhrie, "Mechanical Properties of Bone," in *Skeletal Tissue Mechanics*. New York, NY: Springer New York, 2015, pp. 355–422, ISBN: 978-1-4939-3002-9. DOI: 10.1007/978-1-4939-3002-9_7. [Online]. Available: https://doi.org/10.1007/978-1-4939-3002-9_7.

[36] S. R. Agnew, J. W. Senn, and J. A. Horton, "Mg sheet metal forming: Lessons learned from deep drawing Li and Y solid-solution alloys," *Jom*, vol. 58, no. 5, pp. 62–69, 2006, ISSN: 1047-4838 1543-1851. DOI: 10.1007/s11837-006-0026-8.

[37] ASTM F1108-21, *Standard Specification for Titanium-6Aluminum-4Vanadium Alloy Castings for Surgical Implants (UNS R56406)*. PA: ASTM International West Conshohocken, 2014. DOI: 10.1520/f1108-21.

[38] ASTM F138-19, *Standard Specification for Wrought 18 Chromium- 14 Nickel-2.5 Molybdenum Stainless Steel Bar and Wire for Surgical Implants (UNS S31673)*. PA: ASTM International West Conshohocken, 2020. DOI: 10.1520/f0138-19.

[39] J. Chen, L. Tan, X. Yu, I. P. Etim, M. Ibrahim, and K. Yang, "Mechanical properties of magnesium alloys for medical application: A review," *J Mech Behav Biomed Mater*, vol. 87, pp. 68–79, 2018, ISSN: 1878-0180 (Electronic) 1878-0180 (Linking). DOI: 10.1016/j.jmbbm.2018.07.022. [Online]. Available: https://www.ncbi.nlm.nih.gov/pubmed/30041141.

[40] *Overview of materials for Stainless Steel*, Web Page, Accessed: 10/02/2022. [Online]. Available: https://www.matweb.com/search/DataSheet.aspx?MatGUID=71396e57ff5940b791ece120e4d563e0&ckck=1.

[41] H. Somekawa, Y. Osawa, and T. Mukai, "Effect of solid-solution strengthening on fracture toughness in extruded Mg–Zn alloys," *Scripta Materialia*, vol. 55, no. 7, pp. 593–596, 2006, ISSN: 13596462. DOI: 10.1016/j.scriptamat.2006.06.013.

[42] E. M. Salleh, H. Zuhailawati, S. Ramakrishnan, and M. A.-H. Gepreel, "A statistical prediction of density and hardness of biodegradable mechanically alloyed Mg–Zn alloy using fractional factorial design," *Journal of Alloys and Compounds*, vol. 644, pp. 476–484, 2015, ISSN: 09258388. DOI: 10.1016/j.jallcom.2015.04.090.

[43] L. B. Tong, M. Y. Zheng, X. S. Hu, K. Wu, S. W. Xu, S. Kamado, and Y. Kojima, "Influence of ECAP routes on microstructure and mechanical properties of Mg–Zn–Ca alloy," *Materials Science and Engineering: A*, vol. 527, no. 16-17, pp. 4250–4256, 2010, ISSN: 09215093. DOI: 10.1016/j.msea.2010.03.062.

[44] ASTM B107/B107M13, *Standard Specification for Magnesium-Alloy Extruded Bars, Rods, Profiles, Tubes, and Wire*. PA: ASTM International West Conshohocken, 2021. DOI: 10.1520/b0107_b0107m-13r21.

[45] C. Xiang, N. Gupta, P. Coelho, and K. Cho, "Effect of microstructure on tensile and compressive behavior of WE43 alloy in as cast and heat treated conditions," *Materials Science and Engineering: A*, vol. 710, pp. 74–85, 2018, ISSN: 09215093. DOI: 10.1016/j.msea.2017.10.084.

[46] V. Beura, D. Zhang, N. Overman, J. Darsell, D. R. Herling, K. Solanki, and V. V. Joshi, "Enhanced mechanical behavior and corrosion resistance of AZ31 magnesium alloy through a novel solid-phase processing," *Corrosion Science*, vol. 197, 2022, ISSN: 0010938X. DOI: 10.1016/j.corsci.2021.110074.

[47] S. Agarwal, J. Curtin, B. Duffy, and S. Jaiswal, "Biodegradable magnesium alloys for orthopaedic applications: A review on corrosion, biocompatibility and surface modifications," *Mater Sci Eng C Mater Biol Appl*, vol. 68, pp. 948–963, 2016, ISSN: 1873-0191 (Electronic) 0928-4931 (Linking). DOI: 10.1016/j.msec.2016.06.020. [Online]. Available: https://www.ncbi.nlm.nih.gov/pubmed/27524097.

[48] F. Witte, N. Hort, C. Vogt, S. Cohen, K. U. Kainer, R. Willumeit, and F. Feyerabend, "Degradable biomaterials based on magnesium corrosion," *Current Opinion in Solid*

State and Materials Science, vol. 12, no. 5-6, pp. 63–72, 2008, ISSN: 13590286. DOI: 10.1016/j.cossms.2009.04.001.

[49] J. Weihong, W. Guosong, F. Hongqing, W. Wenhao, Z. Xuming, and K. C. Paul, "Improvement of corrosion resistance and biocompatibility of rare-earth WE43 magnesium alloy by neodymium self-ion implantation," *Corrosion Science*, vol. 94, pp. 142–155, 2015, ISSN: 0010-938X. DOI: https://doi.org/10.1016/j.corsci.2015.01.049. [Online]. Available: https://www.sciencedirect.com/science/article/pii/S0010938X15000608.

[50] Y. Xin, T. Hu, and P. K. Chu, "In vitro studies of biomedical magnesium alloys in a simulated physiological environment: a review," *Acta Biomater*, vol. 7, no. 4, pp. 1452–9, 2011, ISSN: 1878-7568 (Electronic) 1742-7061 (Linking). DOI: 10.1016/j.actbio.2010.12.004. [Online]. Available: https://www.ncbi.nlm.nih.gov/pubmed/21145436.

[51] W. Yang, P. Zhang, J. Liu, and Y. Xue, "Effect of Long-Term Intake of Y3+ in Drinking Water on Gene Expression in Brains of Rats," *Journal of Rare Earths*, vol. 24, no. 3, pp. 369–373, 2006, ISSN: 10020721. DOI: 10.1016/s1002-0721(06)60126-9.

[52] Y. Nakamura, Y. Tsumura, Y. Tonogai, T. Shibata, and Y. Ito, "Differences in Behavior among the Chlorides of Seven Rare Earth Elements Administered Intravenously to Rats," *Toxicological Sciences*, vol. 37, no. 2, pp. 106–116, 1997, ISSN: 1096-6080. DOI: 10.1093/toxsci/37.2.106.

[53] Y. Chen, J. Dou, H. Yu, and C. Chen, "Degradable magnesium-based alloys for biomedical applications: The role of critical alloying elements," *J Biomater Appl*, vol. 33, no. 10, pp. 1348–1372, 2019, ISSN: 1530-8022 (Electronic) 0885-3282 (Linking). DOI: 10.1177/0885328219834656. [Online]. Available: https://www.ncbi.nlm.nih.gov/pubmed/30854910.

[54] L. M. Calado, M. J. Carmezim, and M. F. Montemor, "Rare Earth Based Magnesium Alloys—A Review on WE Series," *Frontiers in Materials*, vol. 8, 2022, ISSN: 2296-8016. DOI: 10.3389/fmats.2021.804906.

[55] O. Jung, D. Porchetta, M. L. Schroeder, M. Klein, N. Wegner, F. Walther, F. Feyerabend, M. Barbeck, and A. Kopp, "In Vivo Simulation of Magnesium Degradability Using a New Fluid Dynamic Bench Testing Approach," *Int J Mol Sci*, vol. 20, no. 19, 2019, ISSN: 1422-0067 (Electronic) 1422-0067 (Linking). DOI: 10.3390/ijms20194859. [Online]. Available: https://www.ncbi.nlm.nih.gov/pubmed/31574947.

[56] C. Rendenbach, H. Fischer, A. Kopp, K. Schmidt-Bleek, H. Kreiker, S. Stumpp, M. Thiele, G. Duda, H. Hanken, B. Beck-Broichsitter, O. Jung, N. Kroger, R. Smeets, and M. Heiland, "Improved in vivo osseointegration and degradation behavior of PEO surface-modified WE43 magnesium plates and screws after 6 and 12 months," *Mater Sci Eng C Mater Biol Appl*, vol. 129, p. 112 380, 2021, ISSN: 1873-0191 (Electronic)

0928-4931 (Linking). DOI: 10.1016/j.msec.2021.112380. [Online]. Available: https://www.ncbi.nlm.nih.gov/pubmed/34579899.

[57] P. Burke, G. Kipouros, D. Fancelli, and V. Laverdiere, "Sintering Fundamentals of Magnesium Powders," *Canadian Metallurgical Quarterly*, vol. 48, pp. 123–132, 2009. DOI: 10.1179/cmq.2009.48.2.123.

[58] F. Benn, N. Kroger, M. Zinser, K. van Gaalen, T. J. Vaughan, M. Yan, R. Smeets, E. Bibiza, S. Malinov, F. Buchanan, and A. Kopp, "Influence of surface condition on the degradation behaviour and biocompatibility of additively manufactured WE43," *Mater Sci Eng C Mater Biol Appl*, vol. 124, p. 112 016, 2021, ISSN: 1873-0191 (Electronic) 0928-4931 (Linking). DOI: 10.1016/j.msec.2021.112016. [Online]. Available: https://www.ncbi.nlm.nih.gov/pubmed/33947530.

[59] F. Benn, F. D'Elia, K. van Gaalen, M. Li, S. Malinov, and A. Kopp, "Printability, mechanical and degradation properties of Mg-(x)Zn elemental powder mixes processed by laser powder bed fusion," *Additive Manufacturing Letters*, vol. 2, 2022, ISSN: 27723690. DOI: 10.1016/j.addlet.2021.100025.

[60] I. Johnson and H. Liu, "A study on factors affecting the degradation of magnesium and a magnesium-yttrium alloy for biomedical applications," *PLoS One*, vol. 8, no. 6, e65603, 2013, ISSN: 1932-6203 (Electronic) 1932-6203 (Linking). DOI: 10.1371/journal.pone.0065603. [Online]. Available: https://www.ncbi.nlm.nih.gov/pubmed/23799028.

[61] M. Abdalla, A. Joplin, M. Elahinia, and H. Ibrahim, "Corrosion Modeling of Magnesium and Its Alloys for Biomedical Applications: Review," *Corrosion and Materials Degradation*, vol. 1, no. 2, pp. 219–248, 2020, ISSN: 2624-5558. DOI: 10.3390/cmd1020011.

[62] M. F. Montemor, "Corrosion issues in joining lightweight materials: A review of the latest achievements," *Physical Sciences Reviews*, vol. 1, no. 2, 2016, ISSN: 2365-659X. DOI: 10.1515/psr-2015-0011.

[63] H. Xu, T. Hu, M. Wang, Y. Zheng, H. Qin, H. Cao, and Z. An, "Degradability and biocompatibility of magnesium-MAO: The consistency and contradiction between in-vitro and in-vivo outcomes," *Arabian Journal of Chemistry*, vol. 13, no. 1, pp. 2795–2805, 2020, ISSN: 18785352. DOI: 10.1016/j.arabjc.2018.07.010.

[64] Y. Koo, H. B. Lee, Z. Dong, R. Kotoka, J. Sankar, N. Huang, and Y. Yun, "The Effects of Static and Dynamic Loading on Biodegradable Magnesium Pins In Vitro and In Vivo," *Sci Rep*, vol. 7, no. 1, p. 14 710, 2017, ISSN: 2045-2322 (Electronic) 2045-2322 (Linking). DOI: 10.1038/s41598-017-14836-5. [Online]. Available: https://www.ncbi.nlm.nih.gov/pubmed/29089642.

[65] Y. Xu, H. Meng, H. Yin, Z. Sun, J. Peng, X. Xu, Q. Guo, W. Xu, X. Yu, Z. Yuan, B. Xiao, C. Wang, Y. Wang, S. Liu, S. Lu, Z. Wang, and A. Wang, "Quantifying

the degradation of degradable implants and bone formation in the femoral condyle using micro-CT 3D reconstruction," *Exp Ther Med*, vol. 15, no. 1, pp. 93–102, 2018, ISSN: 1792-0981 (Print) 1792-0981 (Linking). DOI: 10.3892/etm.2017.5389. [Online]. Available: https://www.ncbi.nlm.nih.gov/pubmed/29375677.

[66] Y. Chen, Z. Xu, C. Smith, and J. Sankar, "Recent advances on the development of magnesium alloys for biodegradable implants," *Acta Biomater*, vol. 10, no. 11, pp. 4561–4573, 2014, ISSN: 1878-7568 (Electronic) 1742-7061 (Linking). DOI: 10.1016/j.actbio.2014.07.005. [Online]. Available: https://www.ncbi.nlm.nih.gov/pubmed/25034646.

[67] G. B. Darband, M Aliofkhazraei, P Hamghalam, and N Valizade, "Plasma electrolytic oxidation of magnesium and its alloys: Mechanism, properties and applications," *Journal of Magnesium and Alloys*, vol. 5, no. 1, pp. 74–132, 2017, ISSN: 2213-9567. DOI: 10.1016/j.jma.2017.02.004.

[68] A. Kopp, T. Derra, M. Muther, L. Jauer, J. H. Schleifenbaum, M. Voshage, O. Jung, R. Smeets, and N. Kroger, "Influence of design and postprocessing parameters on the degradation behavior and mechanical properties of additively manufactured magnesium scaffolds," *Acta Biomater*, vol. 98, pp. 23–35, 2019, ISSN: 1878-7568 (Electronic) 1742-7061 (Linking). DOI: 10.1016/j.actbio.2019.04.012. [Online]. Available: https://www.ncbi.nlm.nih.gov/pubmed/30959185.

[69] H. M. Wong, K. W. Yeung, K. O. Lam, V. Tam, P. K. Chu, K. D. Luk, and K. M. Cheung, "A biodegradable polymer-based coating to control the performance of magnesium alloy orthopaedic implants," *Biomaterials*, vol. 31, no. 8, pp. 2084–96, 2010, ISSN: 1878-5905 (Electronic) 0142-9612 (Linking). DOI: 10.1016/j.biomaterials.2009.11.111. [Online]. Available: https://www.ncbi.nlm.nih.gov/pubmed/20031201.

[70] J. Gonzalez, R. Q. Hou, E. P. S. Nidadavolu, R. Willumeit-Romer, and F. Feyerabend, "Magnesium degradation under physiological conditions - Best practice," *Bioact Mater*, vol. 3, no. 2, pp. 174–185, 2018, ISSN: 2452-199X (Electronic) 2452-199X (Linking). DOI: 10.1016/j.bioactmat.2018.01.003. [Online]. Available: https://www.ncbi.nlm.nih.gov/pubmed/29744455.

[71] G. Song and A. Atrens, "Understanding Magnesium Corrosion - A Framework for Improved Alloy Performance," *Advanced Engineering Materials*, vol. 5, no. 12, pp. 837–858, 2003, ISSN: 1438-1656 1527-2648. DOI: 10.1002/adem.200310405.

[72] A. Atrens, G. Song, Z. Shi, A. Soltan, S. Johnston, and M. Dargusch, "Understanding the Corrosion of Mg and Mg Alloys," *Encyclopedia of Interfacial Chemistry*, pp. 515–534, 2018. DOI: https://doi.org/10.1016/B978-0-12-409547-2.13426-2.

[73] A. D. Atrens, I. Gentle, and A. Atrens, "Possible dissolution pathways participating in the Mg corrosion reaction," *Corrosion Science*, vol. 92, pp. 173–181, 2015, ISSN: 0010938X. DOI: 10.1016/j.corsci.2014.12.004.

[74] Y. Liu, Y. Zheng, X. Chen, J. Yang, H. Pan, D. Chen, L. Wang, J. Zhang, D. Zhu, S. Wu, K. W. K. Yeung, R. Zeng, Y. Han, and S. Guan, "Fundamental Theory of Biodegradable Metals - Definition, Criteria, and Design," *Advanced Functional Materials*, vol. 29, no. 18, 2019, ISSN: 1616-301X 1616-3028. DOI: 10.1002/adfm.201805402.

[75] G. L. Song and A. Atrens, "Corrosion Mechanisms of Magnesium Alloys," *Advanced Engineering Materials*, vol. 1, no. 1, pp. 11–33, 1999, ISSN: 1438-1656 1527-2648. DOI: 10.1002/(sici)1527-2648(199909)1:1<11::Aid-adem11>3.0.Co;2-n.

[76] ASTM F3268-18a, *Standard Guide for in vitro Degradation Testing of Absorbable Metals*. PA: ASTM International West Conshohocken, 2018. DOI: 10.1520/f3268-18a.

[77] ASTM NACE G31-12a, *Standard Guide for Laboratory Immersion Corrosion Testing of Metals*. PA: ASTM International West Conshohocken, 2012. DOI: 10.1520/G0031-21.

[78] G. Song, A. Atrens, and D. StJohn, "An Hydrogen Evolution Method for the Estimation of the Corrosion Rate of Magnesium Alloys," in *Essential Readings in Magnesium Technology*, S. N. Mathaudhu, A. A. Luo, N. R. Neelameggham, E. A. Nyberg, and W. H. Sillekens, Eds. Cham: Springer International Publishing, 2001, pp. 565–572, ISBN: 978-3-319-48099-2. DOI: 10.1007/978-3-319-48099-2_90.

[79] F. Witte, J. Fischer, J. Nellesen, C. Vogt, J. Vogt, T. Donath, and F. Beckmann, "In vivo corrosion and corrosion protection of magnesium alloy LAE442," *Acta Biomater*, vol. 6, no. 5, pp. 1792–9, 2010, ISSN: 1878-7568 (Electronic) 1742-7061 (Linking). DOI: 10.1016/j.actbio.2009.10.012. [Online]. Available: https://www.ncbi.nlm.nih.gov/pubmed/19822226.

[80] A. M. Lafront, W. Zhang, S. Jin, R. Tremblay, D. Dubé, and E. Ghali, "Pitting corrosion of AZ91D and AJ62x magnesium alloys in alkaline chloride medium using electrochemical techniques," *Electrochimica Acta*, vol. 51, no. 3, pp. 489–501, 2005, ISSN: 00134686. DOI: 10.1016/j.electacta.2005.05.013.

[81] J. Mitchell, N. Crow, and A. Nieto, "Effect of Surface Roughness on Pitting Corrosion of AZ31 Mg Alloy," *Metals*, vol. 10, no. 5, 2020, ISSN: 2075-4701. DOI: 10.3390/met10050651.

[82] J. A. Grogan, B. J. O'Brien, S. B. Leen, and P. E. McHugh, "A corrosion model for bioabsorbable metallic stents," *Acta Biomater*, vol. 7, no. 9, pp. 3523–33, 2011, ISSN: 1878-7568 (Electronic) 1742-7061 (Linking). DOI: 10.1016/j.actbio.2011.05.032. [Online]. Available: https://www.ncbi.nlm.nih.gov/pubmed/21664498.

[83] E. L. Boland, R. N. Shirazi, J. A. Grogan, and P. E. McHugh, "Mechanical and Corrosion Testing of Magnesium WE43 Specimens for Pitting Corrosion Model Cali-

bration," *Advanced Engineering Materials*, vol. 20, no. 10, 2018, ISSN: 14381656. DOI: 10.1002/adem.201800656.

[84] I. Adekanmbi, C. Z. Mosher, H. H. Lu, M. Riehle, H. Kubba, and K. E. Tanner, "Mechanical behaviour of biodegradable AZ31 magnesium alloy after long term in vitro degradation," *Mater Sci Eng C Mater Biol Appl*, vol. 77, pp. 1135–1144, 2017, ISSN: 1873-0191 (Electronic). DOI: 10.1016/j.msec.2017.03.216. [Online]. Available: https://www.ncbi.nlm.nih.gov/pubmed/28531989.

[85] ASTM G46-94, *Standard Guide for Examination and Evaluation of Pitting Corrosion*. PA: ASTM International West Conshohocken, 2005. DOI: 10.1520/g0046-94r18.

[86] V. Kappatos, A. N. Chamos, and S. G. Pantelakis, "Assessment of the effect of existing corrosion on the tensile behaviour of magnesium alloy AZ31 using neural networks," *Materials & Design*, vol. 31, no. 1, pp. 336–342, 2010, ISSN: 02613069. DOI: 10.1016/j.matdes.2009.06.009.

[87] H. Kalb, A. Rzany, and B. Hensel, "Impact of microgalvanic corrosion on the degradation morphology of WE43 and pure magnesium under exposure to simulated body fluid," *Corrosion Science*, vol. 57, pp. 122–130, 2012, ISSN: 0010938X. DOI: 10.1016/j.corsci.2011.12.026.

[88] H. Hornberger, S. Virtanen, and A. R. Boccaccini, "Biomedical coatings on magnesium alloys - a review," *Acta Biomater*, vol. 8, no. 7, pp. 2442–55, 2012, ISSN: 1878-7568 (Electronic) 1742-7061 (Linking). DOI: 10.1016/j.actbio.2012.04.012. [Online]. Available: https://www.ncbi.nlm.nih.gov/pubmed/22510401.

[89] L. Y. Li, L. Y. Cui, R. C. Zeng, S. Q. Li, X. B. Chen, Y. Zheng, and M. B. Kannan, "Advances in functionalized polymer coatings on biodegradable magnesium alloys - A review," *Acta Biomater*, vol. 79, pp. 23–36, 2018, ISSN: 1878-7568 (Electronic) 1742-7061 (Linking). DOI: 10.1016/j.actbio.2018.08.030. [Online]. Available: https://www.ncbi.nlm.nih.gov/pubmed/30149212.

[90] X. N. Gu, Y. F. Zheng, Q. X. Lan, Y. Cheng, Z. X. Zhang, T. F. Xi, and D. Y. Zhang, "Surface modification of an Mg-1Ca alloy to slow down its biocorrosion by chitosan," *Biomed Mater*, vol. 4, no. 4, p. 044 109, 2009, ISSN: 1748-605X (Electronic) 1748-6041 (Linking). DOI: 10.1088/1748-6041/4/4/044109. [Online]. Available: https://www.ncbi.nlm.nih.gov/pubmed/19671953.

[91] P. Wan, L. Tan, and K. Yang, "Surface Modification on Biodegradable Magnesium Alloys as Orthopedic Implant Materials to Improve the Bio-adaptability: A Review," *Journal of Materials Science & Technology*, vol. 32, no. 9, pp. 827–834, 2016, ISSN: 10050302. DOI: 10.1016/j.jmst.2016.05.003.

[92] O. Jung, R. Smeets, P. Hartjen, R. Schnettler, F. Feyerabend, M. Klein, N. Wegner, F. Walther, D. Stangier, A. Henningsen, C. Rendenbach, M. Heiland, M. Barbeck, and A. Kopp, "Improved In Vitro Test Procedure for Full Assessment of the Cytocompatibil-

ity of Degradable Magnesium Based on ISO 10993-5/-12," *Int J Mol Sci*, vol. 20, no. 2, 2019, ISSN: 1422-0067 (Electronic) 1422-0067 (Linking). DOI: 10.3390/ijms20020255. [Online]. Available: https://www.ncbi.nlm.nih.gov/pubmed/30634646.

[93] H. R. Bakhsheshi-Rad, E. Hamzah, A. F. Ismail, M. Aziz, A. Najafinezhad, and M. Daroonparvar, "Synthesis and in-vitro performance of nanostructured monticellite coating on magnesium alloy for biomedical applications," *Journal of Alloys and Compounds*, vol. 773, pp. 180–193, 2019, ISSN: 09258388. DOI: 10.1016/j.jallcom.2018.08.310.

[94] J. A. Grogan, S. B. Leen, and P. E. McHugh, "A physical corrosion model for bioabsorbable metal stents," *Acta Biomater*, vol. 10, no. 5, pp. 2313–22, 2014, ISSN: 1878-7568 (Electronic). DOI: 10.1016/j.actbio.2013.12.059. [Online]. Available: https://www.ncbi.nlm.nih.gov/pubmed/24412771.

[95] P. Bajger, J. M. A. Ashbourn, V. Manhas, Y. Guyot, K. Lietaert, and L. Geris, "Mathematical modelling of the degradation behaviour of biodegradable metals," *Biomech Model Mechanobiol*, vol. 16, no. 1, pp. 227–238, 2017, ISSN: 1617-7940 (Electronic) 1617-7940 (Linking). DOI: 10.1007/s10237-016-0812-3. [Online]. Available: https://www.ncbi.nlm.nih.gov/pubmed/27502687.

[96] A. K. Gartzke, S. Julmi, C. Klose, A. C. Waselau, A. Meyer-Lindenberg, H. J. Maier, S. Besdo, and P. Wriggers, "A simulation model for the degradation of magnesium-based bone implants," *J Mech Behav Biomed Mater*, vol. 101, p. 103 411, 2020, ISSN: 1878-0180 (Electronic) 1878-0180 (Linking). DOI: 10.1016/j.jmbbm.2019.103411. [Online]. Available: https://www.ncbi.nlm.nih.gov/pubmed/31546176.

[97] W. Wu, D. Gastaldi, K. Yang, L. Tan, L. Petrini, and F. Migliavacca, "Finite element analyses for design evaluation of biodegradable magnesium alloy stents in arterial vessels," *Materials Science and Engineering: B*, vol. 176, no. 20, pp. 1733–1740, 2011, ISSN: 09215107. DOI: 10.1016/j.mseb.2011.03.013.

[98] D. Gastaldi, V. Sassi, L. Petrini, M. Vedani, S. Trasatti, and F. Migliavacca, "Continuum damage model for bioresorbable magnesium alloy devices - Application to coronary stents," *J Mech Behav Biomed Mater*, vol. 4, no. 3, pp. 352–65, 2011, ISSN: 1878-0180 (Electronic) 1878-0180 (Linking). DOI: 10.1016/j.jmbbm.2010.11.003. [Online]. Available: https://www.ncbi.nlm.nih.gov/pubmed/21316623.

[99] N. Debusschere, P. Segers, P. Dubruel, B. Verhegghe, and M. De Beule, "A Computational Framework to Model Degradation of Biocorrodible Metal Stents Using an Implicit Finite Element Solver," *Ann Biomed Eng*, vol. 44, no. 2, pp. 382–90, 2016, ISSN: 1573-9686 (Electronic). DOI: 10.1007/s10439-015-1530-1. [Online]. Available: https://www.ncbi.nlm.nih.gov/pubmed/26703421.

[100] S. Ma, B. Zhou, and B. Markert, "Numerical simulation of the tissue differentiation and corrosion process of biodegradable magnesium implants during bone fracture healing," *ZAMM - Journal of Applied Mathematics and Mechanics / Zeitschrift für*

Angewandte Mathematik und Mechanik, vol. 98, no. 12, pp. 2223–2238, 2018, ISSN: 0044-2267 1521-4001. DOI: 10.1002/zamm.201700314.

[101] A. Amerinatanzi, R. Mehrabi, H. Ibrahim, A. Dehghan, N. Shayesteh Moghaddam, and M. Elahinia, "Predicting the Biodegradation of Magnesium Alloy Implants: Modeling, Parameter Identification, and Validation," *Bioengineering (Basel)*, vol. 5, no. 4, 2018, ISSN: 2306-5354 (Print). DOI: 10.3390/bioengineering5040105. [Online]. Available: https://www.ncbi.nlm.nih.gov/pubmed/30501102.

[102] C. Quinn, K. van Gaalen, P. E. McHugh, A. Kopp, and T. J. Vaughan, "An enhanced phenomenological model to predict surface-based localised corrosion of magnesium alloys for medical use," *Journal of the Mechanical Behavior of Biomedical Materials*, p. 105 637, 2022, ISSN: 1751-6161. DOI: https://doi.org/10.1016/j.jmbbm.2022.105637. [Online]. Available: https://www.sciencedirect.com/science/article/pii/S1751616122005422.

Chapter 2

Literature Review

This chapter provides an overview of the literature relevant to the subject areas of this thesis. Within the following sections, background details are provided on the general corrosion process of magnesium and its alloys (Section 2.1). An overview of the in-vitro testing approaches that have been used to characterise magnesium corrosion is provided in Section 2.2. Section 2.3 provides an overview on coating technologies. Finally, a summary of the model frameworks used to predict the corrosion behaviour of magnesium and its alloys is summarised in Section 2.4.

2.1 Magnesium corrosion

2.1.1 Corrosion mechanisms

Corrosion describes the reaction of a metal with its surrounding environment, leading to changes of the materials' surface itself. In general, the magnesium corrosion process takes place through an electrochemical reaction that leads to the formation of oxides, hydroxides, and hydrogen [1] on the material surface. As soon as magnesium is exposed to air, mainly a thin oxide layer is formed on the surface that functions as a protective barrier against corrosion. However, this oxide layer can be damaged if it is exposed to an aqueous solution. In the presence of chloride ions and impurities, such as iron, copper, nickel or beryllium, local electrochemical cells are formed between the material and its surrounding environment, leading to what is termed galvanic corrosion [2]. In general, galvanic corrosion occurs

when two dissimilar metals with different electrochemical potentials come into contact in an electrolyte. Whereby the less noble metal serves as the anode which evolves by-products and therefore corrodes at the contact point. In terms of magnesium corrosion, magnesium itself is always the anode due to its high negative standard electrode potential of -2.372 V [3]. Microgalvanic or inter-granular corrosion evolve between impurities or intermetallic elements in the magnesium matrix itself, which then act as cathode [4]. These mechanisms result in a magnesium ions release into the media [1, 5]. However, Song et al. reported that not all magnesium alloys suffer from intergranular corrosion because the secondary phase is more corrosion resistant compared to the magnesium matrix itself [6]. Another corrosion mechanism arises due to the presence of chloride ions, as in saline solutions. Chloride ions tend to break down the passive layer due to the formation of magnesium chloride. Since magnesium chloride is highly soluble in water, local corrosion (e.g. pitting) occurs in these areas [3]. This pitting corrosion gets intensified through impurities due to the galvanic differences in the alloy. Figure 2.1 shows a schematic representation of the different pitting morphologies caused by surface corrosion [7]. Most commonly, pitting occurs in magnesium

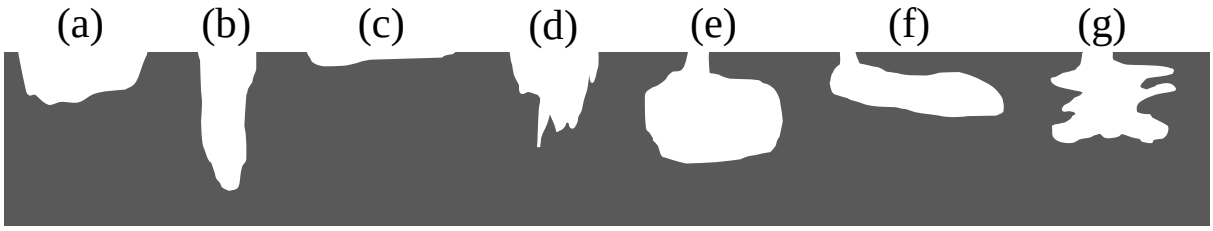

Figure 2.1: Schematics of different pit shapes occurring of corrosion in metals (a) elliptical (d) deep and narrow (c) wide and shallow (d) vertical (e) subsurface (f) undercutting (g) horizontal. (adapted from [7])

alloys in the form of elliptical deep and narrow or wide and shallow pits (Figure 2.1 (a)-(c)) [8, 9]. Hiromoto et al. [9] identified for AZ31 in in-vitro tests filiform pits (Figure 2.2 (a)), corresponding to the schematic vertical pit in Figure 2.1 (d), and elliptical shapes for in-vivo tested specimens (Figure 2.2 (b)), respectively. In-vitro testing was performed in Eagle's minimum essential medium with 10 vol.% FBS, and in-vivo testing was performed in mice

[9]. Cui et al. [8] observed different pit morphologies on AZ31 plate samples, depending on the concentration of added ammonium nitrate to 0.1 M NaCl solution. Whereby, more deep pits were observed on the magnesium surface after 24 hours with an addition of 0.01 M ammonium nitrate solution (Figure 2.2 (c)), and more shallow pits by using 0.1 M ammonium nitrate solution (Figure 2.2 (d)). Through an in-vitro study, Han et al. [10] observed that elliptical pits formed in an AZ31 alloy subject to static uniaxial loading undergoing corrosion in Hank's Balanced Salt Solution. While pitting corrosion is a dominant corrosion mechanism in magnesium alloys, there are only limited studies that quantify the morphology of pit formation during corrosion. Generally, corrosions studies may only indicate whether pitting corrosion is visible or not, but little quantitative information on the morphology of pitting is provided [11–15].

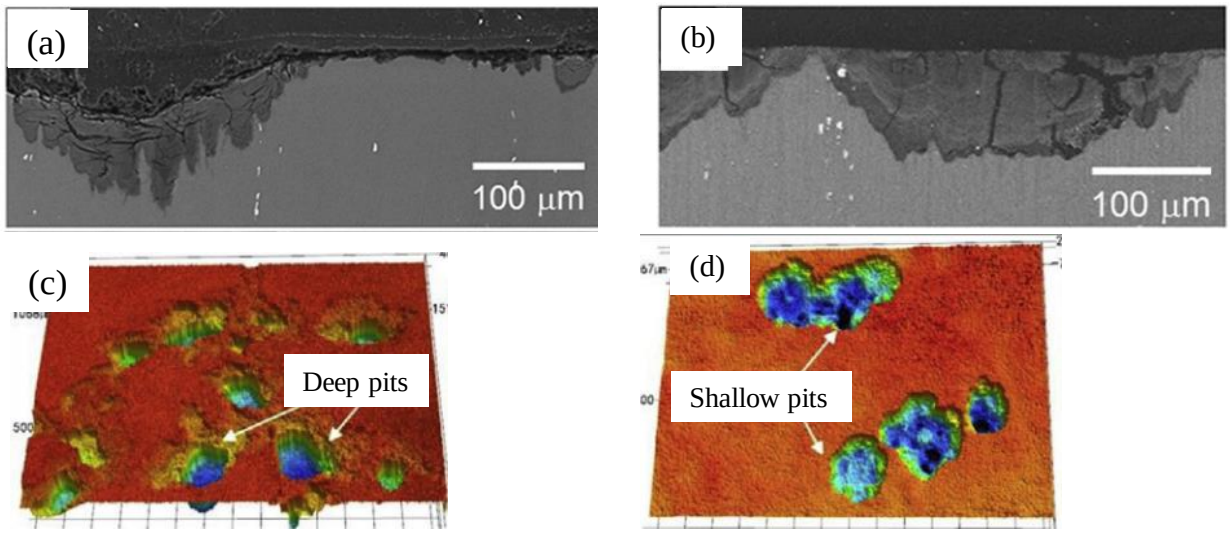

Figure 2.2: (a) SEM cross-sectional images of an AZ31 sample immersed for 14 weeks in-vitro in Eagle's minimum essential medium including FBS [9], (b) SEM cross-sectional images of an AZ31 rod implanted for 16 weeks in-vivo in mice [9], (c) 3D profiles of AZ31 magnesium surface after immersion for 24 hours in 0.1M NaCl solution with 0.01M ammonium nitrate (NH_4NO_3) [8] and (d) immersion for 24 hours in 0.1M NaCl solution and 0.1M NH_4NO_3 [8].

For magnesium alloys in general, the formation of pits depends strongly on both the environmental conditions and material characteristics. Here, the aqueous environment, the flow conditions, the alloy composition, the microstructure configuration and the presence of impurities influenced the formation and evolution of localised corrosion [8, 16, 17]. Several

extensive reviews on fundamental principles of magnesium corrosion in aqueous solutions are available elsewhere [2, 6, 18, 19]. The following section provides a brief overview of magnesium corrosion mechanisms in simulated body fluid, while more details on quantitative phenomenological corrosion tracking are given in Section 2.2.5.

2.1.2 Corrosion in simulated body fluid

Within this section, more details are provided on the corrosion process examined in recent literature for a rare earth magnesium alloy WE43 in simulated body fluid (SBF). This is the examined alloy throughout this thesis, using the TRIS buffered simulated body fluid (c-SBF) for in-vitro testing. In general, SBF aims to replicate the same ion concentration as human blood plasma for in-vitro assessment of biomaterials [20]. SBF is usually prepared in the laboratory itself and not distributed directly by a supplier. Figure 2.3 gives an overview of the corrosion process for a WE43 alloy in c-SBF, which is divided into four stages. Figure 2.3 (a) shows the first stage, where magnesium is exposed to an aqueous solution and directly an electrochemical cell forms. This results in an anode surface, where Mg^{2+}-ions as well as free electrons are built, while a cathodic reduction takes place with H_2O resulting in hydrogen formation. The overall reaction is:

$$Mg + 2H_2O \rightarrow Mg(OH)_2 + H_2 \uparrow \tag{2.1}$$

leading to the formation of magnesium hydroxide $Mg(OH)_2$ on the outer surface. With the anodic reaction:

$$Mg \rightarrow Mg^{2+} + 2e^- \tag{2.2}$$

and the cathodic reaction being

$$2H_2O + 2e^- \rightarrow 2OH^- + H_2 \uparrow \tag{2.3}$$

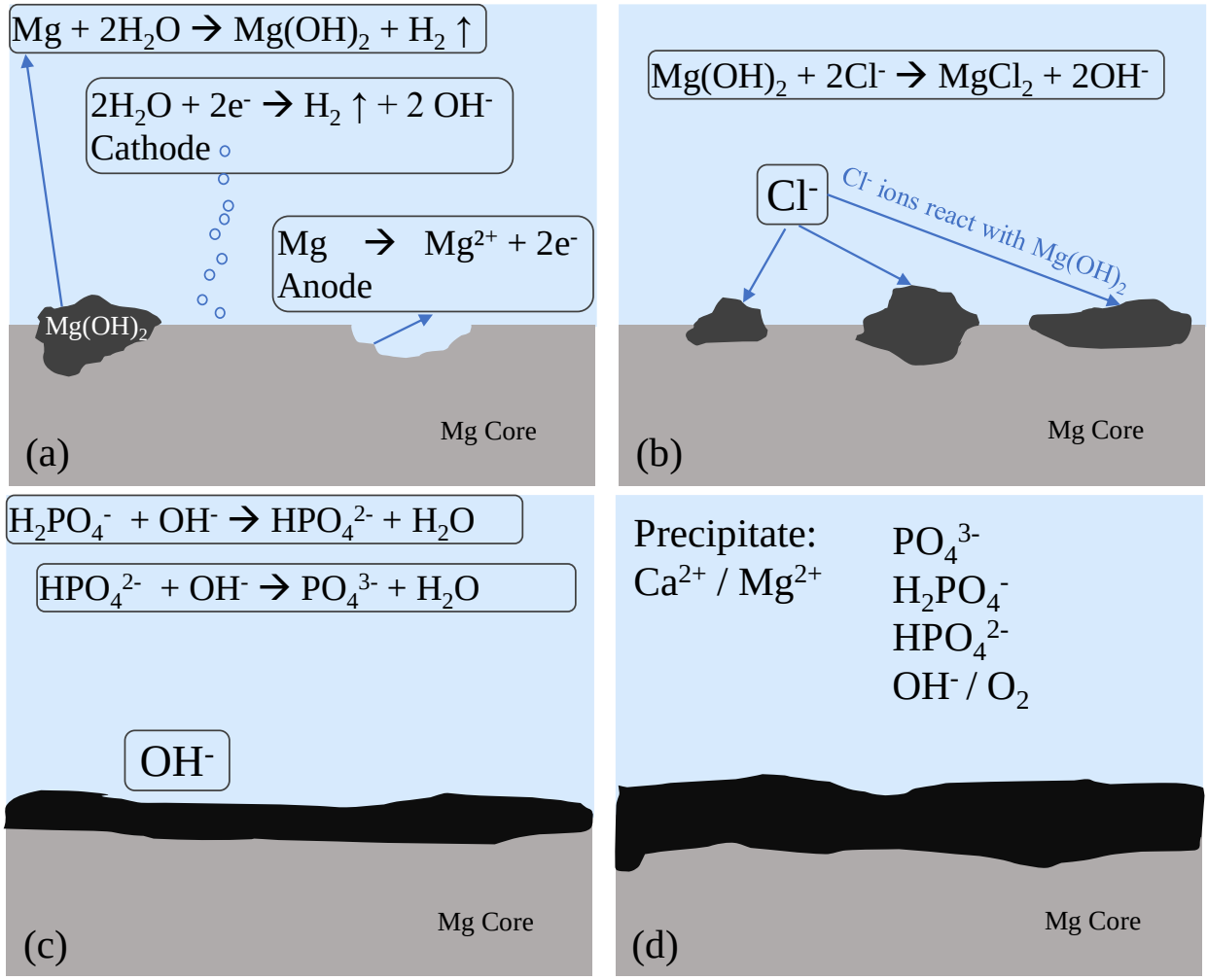

Figure 2.3: Schematic overview of different stages of the corrosion mechanism of WE43 alloy in c-SBF. (adapted from [21])

Stage two is shown in Figure 2.3 (b). Due to the reaction of Cl^--ions with $Mg(OH)_2$ to soluble $MgCl_2$, pH rises and corrosion progresses through the removal of $Mg(OH)_2$ from the material surface. This is described by the following reaction:

$$Mg(OH)_2 + 2Cl^- \rightarrow MgCl_2 + 2OH^- \tag{2.4}$$

In the third stage, phosphate ions increase the density of the passive layer, protecting the core material from the attack of the Cl^--ions [22] (Figure 2.3(c)). Jamesh et al. found that within the fourth stage, shown in Figure 2.3 (d), finally $Ca_{10}(PO_4)_6(OH)_2$, $Ca_3(PO_4)_2{\cdot}3H_2O$

and $Mg(OH)_2$ are formed on the metal surface while immersed in c-SBF solution [21]. $Ca_{10}(PO_4)_6(OH)_2$ is hydroxyapatite, which is a natural component of bone mineral and is essential to bone growth, while $Ca_3(PO_4)_2{\cdot}3H_2O$ is an amorphous calcium phosphate, which is a precursor of bioapatite and plays a key role in biomineralization [21, 23]. The above described mechanism is in alignment with several other studies [24–26].

2.2 Corrosion testing of Magnesium

Within the product development chain, in-vitro characterisation must be carried out to evaluate the corrosion performance of biodegradable implants in a simulated environment through immersion testing. While these corrosion tests aim to replicate physiological conditions as closely as possible, several factors influence the process, including temperature, ion-concentrations of the media, buffer system, pH, sample surface to solution volume ratio, static or dynamic flow conditions in the tests. Other factors related to the specimen itself can also affect corrosion, including the loading history and whether the tests are carried out in static or loaded configurations. Together, these factors influence not only the corrosion rate, but also the formation of the degradation layer and its composition [27]. Consequently, prior to testing, the selection of the testing conditions is an important step. In the following sections, first an overview is given on variables that influence the testing (Section 2.2.1). Then, details are provided on two commonly used setups to determine the corrosion performance (i) immersion testing with gravimetric methods and/or the hydrogen evolution method (Section 2.2.2) (ii) electrochemical testing (Section 2.2.3). Section 2.2.4 summarises studies examining the relation between mass loss measurements and mechanical parameters.

2.2.1 In-vitro testing variables

Two standards are available to describe the appropriate experimental approaches for evaluating the in-vitro degradation of absorbable metal samples, which are (i) *Standard Guide for in vitro Degradation Testing of Absorbable Metals* (ASTM F3268-18a) [28] and (ii) *Standard guide for laboratory immersion corrosion testing of metals* (ASTM G31-21) [29]. These standards aim to provide a framework to control the corrosion test environment through standardisation of conditions and using physiologically relevant electrolyte fluids. Specific guidelines are provided on the samples' surface area to media volume ratio, which must exceed $0.2\,\mathrm{mL/mm^2}$. Standard methods are provided to calculate and report the corrosion rate, which is defined as the speed of corrosion in a specific environment at which the metal deteriorates, defined in terms of mm/year for example. However, while these standards state that an appropriate media and immersion time should be used, there is no strict instruction on the media type to be used for specific absorbable metals, although corrosion performance is highly sensitive to media selection, ion concentrations and buffer system. It is known that the immersion media is the pivotal parameter in dictating the corrosion process, resulting in different corrosion rates and products [20]. Given that there is substantial room for interpretation within these protocols, it can be difficult to compare data from in-vitro corrosion studies from different research groups due to various combinations of test set-ups used. Figure 2.4 provides a summary of several immersion media and illustrates that the complexity progressively increases with the addition of inorganic ions, organic molecules, and proteins to provide a solution more similar to body fluid e.g. blood serum, plasma. Table 2.1 shows the ion concentrations for the most common immersion media that are used for in-vitro corrosion studies for magnesium alloys [31]. Here, isotonic NaCl solution represents the simplest immersion media for in-vitro corrosion testing of magnesium and typically results in the highest corrosion rates among the media. While it has little resemblance to physiological fluids, its high corrosion rate can be advantageous to provide accelerated results

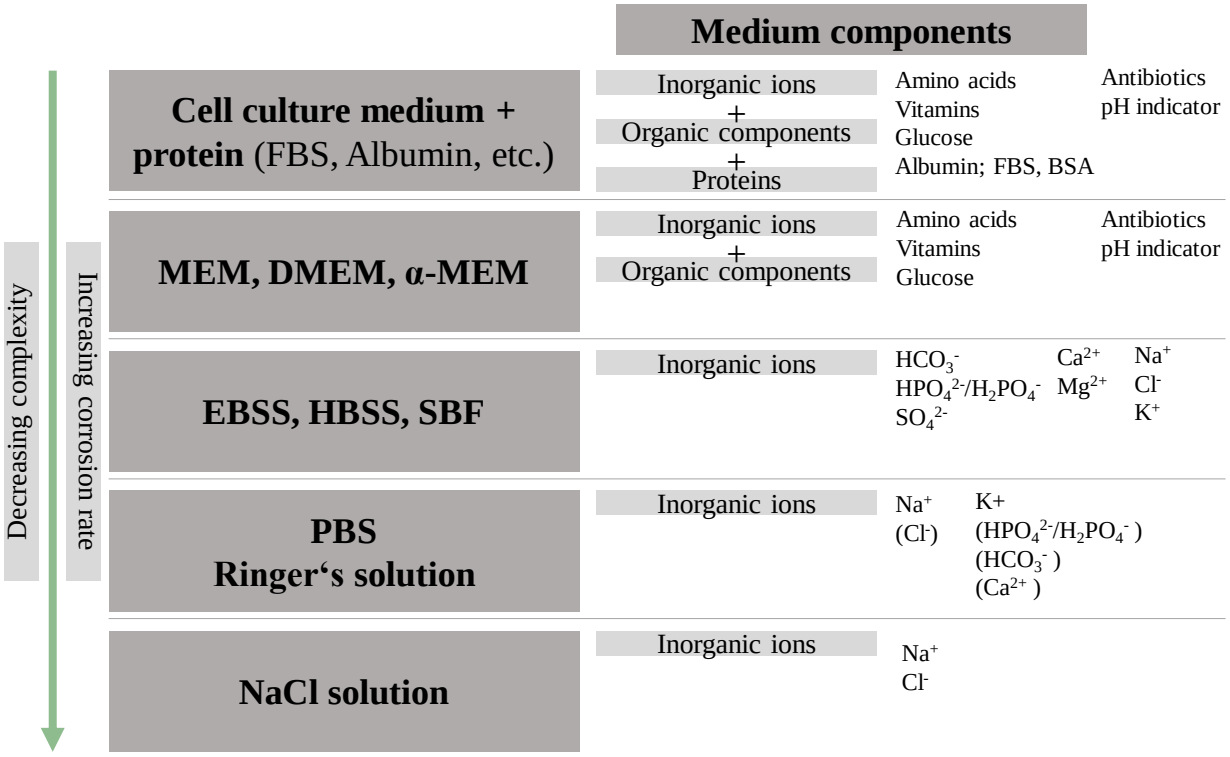

Figure 2.4: Commonly used immersion media for testing absorbable metals. (adapted from [30])

in preliminary testing in biomedical and other engineering applications [32–35], although the corrosion mechanism can be vastly different as in-vivo and more advanced media are required for reliable results. Phosphate buffered saline (PBS) is commonly used to test the biocompatibility of a certain alloy and contains more inorganic ions compared to NaCl solution [36–40]. Media like Hanks balanced salt solution (HBSS), Earle's Balanced Salt Solution (EBSS), or own mixed simulated body fluids are most commonly used in corrosion testing of magnesium alloys. However, it must be noted that there are several formulations of simulated body fluids (SBF) that can result in substantial variation in ion composition [20].

Across the literature, significant variations of the corrosion rate have been reported among studies, even when testing was performed with the same immersion media and alloy. For example, Grogan et al. [41] reported a mean degradation rate of $0.084\,\mathrm{mg/cm^2}$ per hour for an AZ31 alloy tested in HBSS over a testing period of 80 hours. On the other hand, Han et

Table 2.1 Commonly used degradation media and their composition. Concentrations are given in mmol/L (values taken from [31])

Ions	Blood plasma	SBF	HBSS	DMEM
Na^+	142.0	142.0	141.6	155.3
K^+	5.0	5.0	5.4	5.3
Ca^{2+}	2.5	1.6-2.5	1.3-2.5	1.8
Mg^{2+}	1.5	1.0-1.5	0.75-0.87	0.8
Cl^-	103	103.0-148.8	144.0-147.0	115.7
HCO_3^-	22-30	4.2-4.7	4.2	44.1
HPO_4^{2-}	1.0	1.0	0.3	0.9
SO^{2+}	0.5	0.5	0.26-0.8	0.8
Glucose (g/L)	3.6-5.2	–	5.5	25
Amino acids	unknown	–	–	10.6
Vitamines	unknown	–	–	0.15

al. [10] calculated for an AZ31 alloy over a testing period of 120 hours a mean degradation rate of $4\,g/m^2$ per day which is $0.016\,mg/cm^2$ per hour, which is 5 times lower compared to Grogan et al. This difference may arise through different geometries or immersion time.

Several studies have directly compared the effect of immersion media on the corrosion rate of magnesium, comparing different types of media [42] or the addition of specific proteins [43]. Marco et al. [42] compared the corrosion performance of three different alloys (pure magnesium, Mg-10Gd and Mg-2Ag) in PBS, HBSS and Dulbecco's Modified Eagle's Medium (DMEM) under cell culture conditions. While testing was only conducted over four to seven days, it was found that HBSS caused the fastest corrosion rate, followed by PBS, while DMEM resulted in the slowest corrosion rate. They showed that DMEM maintained a physiological pH of ~ 7.4 and achieved a comparable degradation rate to in-vivo studies. They also found that the degradation on DMEM samples had similar characteristics to those observed in-vivo. Liu et al. (2010) investigated the influence of the addition of albumin (10 g/L) in a 0.9 wt.% NaCl solution on a Mg1.5Ca alloy [43]. They measured over a period of 120 h an average degradation rate of $15\,mL/cm^2$ per day, while with the addition of albumin the rate reduced to $4.5\,mL/cm^2$ per day. Other similar studies have proven that the addition of fetal bovine serum (FBS) to cell culture media also inhibited corrosion process in magnesium alloys [44–48]. While the addition of such proteins and sera should better replicate

the physiological environment, there is a major disadvantage with DMEM or the addition of FBS to any media in that it can be difficult to maintain sterile conditions, which can lead to a contamination of the media and inaccurate results [30]. To overcome this issue, antibiotics have been added to inhibit mould formation [30]. However, high concentrations (e.g. 0.001 mol/L and 0.01 mol/L) of penicillin or streptomycin have themselves been found to significantly accelerate the corrosion rate. As a result, lower concentrations (0.0001 mol/L) of antibiotics are recommended, where no differences were found for CP-Mg and Mg-0.8Ca tested in MEM and SBF [49].

In addition to the solution itself, the buffer system plays a decisive role in the degradation process. In general, the buffer system ensures a constant pH during the test, with a desired pH in the range of 7.2-7.6 [28] for in-vitro testing of magnesium. It is known that synthetic buffers like HEPES or TRIS accelerate the degradation [50] significantly. Therefore, a CO_2 buffered atmosphere with the resulting bicarbonate buffer as in the human body is favourable, if testing aims to replicate physiological conditions [31]. The bicarbonate buffer in the human body is dictated through breathing, where a crucial part of the acid load evolves in the form of volatile CO_2. This CO_2 reacts with H_2O to carbonic acid (H_2CO_3), which is in equilibrium with HCO_3^-, according to the following equation:

$$CO_2 + H_2O \leftrightarrows H_2CO_3 \leftrightarrows H^+ + HCO_3^- \tag{2.5}$$

leading to a reduction of the pH value. During the corrosion process of magnesium, the pH rises constantly due to the release of OH^-, H_2 and Mg into the environment [50, 51]. The use of CO_2 incubators provide favourable conditions for in-vitro testing, where the incubator system maintains a constant CO_2 concentration, thereby controlling the pH of the system. On the other hand, few studies have also used an active pH controller by incorporating CO_2 in the solution directly [50, 52]. Although, Schinhammer et al. [50] showed for a WZ21 alloy, tested in SBF buffered with HEPES (100 mmol/L) that the corrosion rate was 60 times

higher compared to testing in SBF buffered with CO_2 only. Furthermore, pH indicators like phenol red are included to observe pH changes over time. Mei et al. showed that the addition of pH indicators have no significant influence on magnesium corrosion [49].
Martinez-Sanchez et al. summarized a range of in-vitro and in-vivo studies in terms of the degradation rate and came up with one to five orders of magnitude lower reported rates for in-vivo tests [53]. Even though with some electrolytes (DMEM, HBSS, and only CO_2 buffered SBF) similar rates can be observed [50].
As mentioned, the immersion media is the decisive part within in-vitro setups. The electrolyte not only influences the rate, but also contributes to the formation of the passivation layer [54]. Further reviews on the role of immersion media on the corrosion of magnesium are available elsewhere [1, 31, 55–57].

2.2.2 In-vitro characterisation of mass loss

The primary purpose of in-vitro immersion testing is to characterise how material degradation is taking place on the corroding surface of the material. To quantify the rate of material removal, immersion testing is combined with several techniques that quantify the mass or volume loss of material. These measurements can be directly quantified through gravimetric and 3D X-ray imaging techniques, or most commonly indirectly by measuring hydrogen evolution from the corroding specimens during the immersion test. Through hydrogen evolution measurements, the specimen mass loss can be determined through Equation (2.1), whereby 1 mol of dissolved magnesium leads to the formation of 1 mol H_2. Thus, the overall volume of hydrogen released, provides an indirect measure of the mass loss from the magnesium specimen undergoing corrosion. Figure 2.5 shows three commonly used immersion setups that quantify mass loss by measuring hydrogen evolution from the corroding magnesium specimens. Inverted burettes with a funnel or eudiometer systems are commonly used to manually read the liquid level [4]. Figure 2.5 (a) shows an example from Song et al. [4],

who used a simple funnel setup placed over the specimen (pure magnesium and AZ91D) and a burette was attached for testing. As media, this study used different concentrations of NaCl and HCl solutions. pH changes were not monitored, and testing was performed at room temperature. Figure 2.5 (b) shows a setup used by Schinhammer et al. [50], whereby

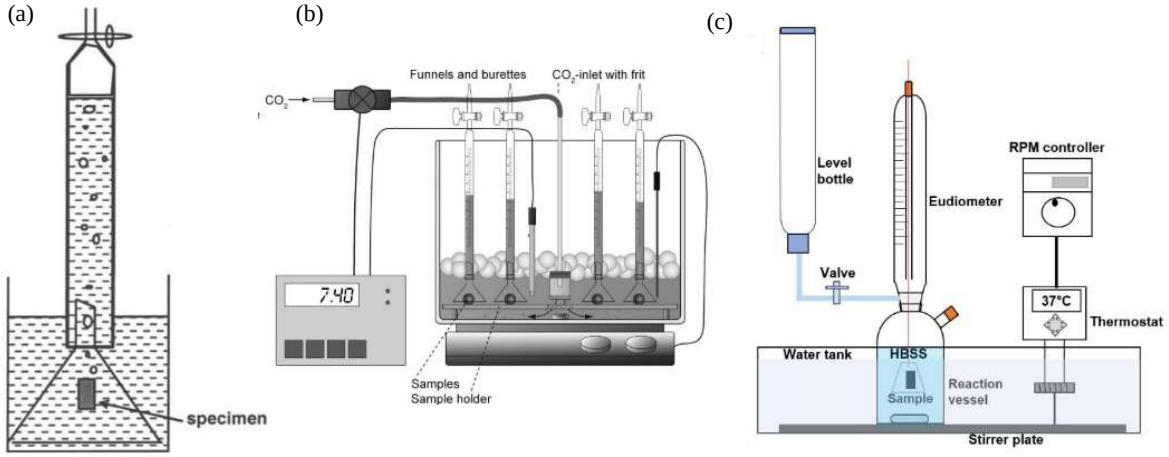

Figure 2.5: Examples for test setups for the hydrogen tracking taken from (a) Song et al. 2001 [4], (b) Schinhammer et al. 2013 [50], (c) Liu et al. 2018 [58].

one reservoir was equipped with several burettes for simultaneous testing of WZ21 samples for different immersion media (e.g. SBF, PBS; α-MEM). Among other things, the setup used an active pH control through CO_2 release, to highlight the difference in degradation rates for different buffer approaches. Figure 2.5 (c) shows the setup published by Liu et al. [58], which was used to examine the corrosion of pure magnesium, Zinc, and different alloy compositions. Testing was performed in HBSS at a target temperature of 37 °C. These three setups demonstrate the variety within the test setups themselves. A major advantage of the hydrogen evolution method is the possibility of real-time data recording, which ensures that time-dependent corrosion phenomena are captured, in particular the initial high rates of corrosion that are observed in the early phase of corrosion. However, the capture of hydrogen also results in inaccuracies and the method is sensitive to errors due to both atmospheric pressure changes and leakages through the equipment. Additionally, the redox reaction described in Equation (2.1) is not yet fully explored, and it is not clear whether

hydrogen is used in other reactions within the different immersion media [2].

Several studies identified challenges in a correct determination of the mass loss through hydrogen tracking, leading to an underestimation of the corrosion rate [55, 59–61]. These studies have typically compared the measure from hydrogen evolution to mass loss measured through gravimetric methods. A major challenge with gravimetric methods is the requirement to remove the passive layer from the corroding surface. This is typically carried out using a chromic acid solution, although this is hazardous and can dissolve applied coatings [31] and requires a special recycling process to dispose of the solution. Furthermore, the gravimetric method can only capture the final mass loss of the specimen as once the sample is cleaned, it cannot be returned to the corrosion set up. Despite these disadvantages, gravimetric methods do provide accurate final mass loss values. In terms of testing WE43 magnesium alloys, Galvin et al. [62] determined a degradation rate of 0.52 mm/year for wires and a rate of 0.99 mm/year for dog bone specimens by sample weighing after cleaning in chromic acid. Testing was performed in HBSS at 37 °C with 5 % CO_2. Cao et al. [63] measured a corrosion rate of 38.41 mm/year for a reference WE43 material and 15.12 mm/year for WE43 samples which underwent an extra friction stir process. Testing was performed here in TRIS buffered SBF at 37 °C. Corrosion rate was measured through sample weighing after chromic acid cleaning.

Several studies have compared the corrosion rates from gravimetric methods and hydrogen evolution. In particular, Marco et al. [59], Liu et al. [60] and Denkena et al. [64] have measured up to three times higher mass loss through gravimetric methods in comparison to values derived from the hydrogen evolution. Within these studies, they have also used micro-computed tomography (µCT) scanning to provide a detailed measure of material loss from the corroding surface. In general, it was found that gravimetric measurement compared well to micro-CT measurements, and it is favourable to use a combination of hydrogen tracking and gravimetric measurements, or micro-CT scanning [60]. However, if the objective of immersion testing is to demonstrate differences between different materials (e.g. surface

treatments or alloy composition), it is suitable to use only one method and to compare the relative mass losses. From all this information, it is advisable to identify a clear target of the in-vitro testing prior to testing, and then to define the testing boundary conditions and suitable characterisation procedures.

2.2.3 Electrochemical testing of corrosion

Electrochemical tests have also been used to quantify the extent of corrosion. They take advantage of the effect that electrochemical reactions produce measurable electric energy or, vice versa, applied electric energy leads to chemical reactions. As mentioned in Section 2.1, the corrosion of a metal in an electrolytic solution is an electrochemical reaction whereby an electric potential is formed and current flows through the sample [65]. Most electrochemical tests in the literature are the potentiodynamic polarisation (PDP) and the electrochemical impedance spectroscopy (EIS) method, which require an additional electrode to provide a constant potential.

The PDP method initially records the open circuit potential (OCP) in a defined time window. OCP is the potential between the reference electrode and working electrode without applying current [66]. It contains information on the corrosion tendency of the examined material, whereby the more negative this potential, the higher is the tendency for spontaneous corrosion [67]. After a stabilising phase of the material surface in the media, a potential is induced between the counter electrode (anode) and working electrode (cathode) and this potential is continuously increased (e.g. 1 mV/s), and the required current is measured [27]. Another non-destructive electrochemical test method is EIS, that provides results on the formation and growth of the passive layer during corrosion. It is an accelerated measurement for the corrosion performance with quantitative results [18, 30]. Here, a low AC polarisation magnitude is used over a range of frequencies, which oscillate from anodic to a cathodic peak, whereby for every tested frequency the resistant and capacitance value is measured

[27]. However, EIS is susceptible to errors evolving from corrosion that occurs over time by the change of the surface area and proceeding degradation itself during testing. Furthermore, choosing an appropriate equivalent circuit can be difficult, which is indispensable for a correct evaluation [55].

Electrochemical testing of magnesium alloys has proven to be a valuable tool in assessing corrosion behaviour. With the use of PDP and EIS methods, results can be obtained quickly, with a single PDP measurement taking only 5 minutes. However, it should be noted that these methods measure the corrosion rate at a specific time point, which may not accurately represent the overall corrosion rate in cases where non-uniform and localissed corrosion effects are present. Despite this limitation, electrochemical testing remains a highly useful and efficient means of evaluating the corrosion behaviour of magnesium alloys [27].

2.2.4 Immersion testing and mechanical performance

While many in-vitro studies have characterised corrosion of magnesium alloys, these studies focused on corrosion rate or on formation of the degradation layer. In numerous instances, the corrosion of different alloys and/or different manufacturing processes are directly compared to one other. Detailed studies that evaluate the mechanical performance of magnesium alloys undergoing corrosion are more limited. Although localised corrosion has been qualitatively associated with accelerated loss of mechanical integrity of specimens exposed to corrosion [41, 68], the mechanistic relationships between corrosion and mechanical performance have not been adequately investigated. Tables 2.2 - 2.4 provide a summary of the relevant studies that have focussed on the mechanical integrity over the degradation process. Comparing results across these studies can be difficult as there has been substantial variation in the experimental test conditions used, with a range of media, immersion times, specimen geometries and different magnesium alloys, in particular AZ31 and WE43. Furthermore, the mechanical performance of specimens has been characterised through a range

of different loading conditions such as uniaxial tensile tests, three-point bending, four-point bending and compression testing. Despite the variability in test setups and conditions, generally a disproportional behaviour between the tracked mass loss and reduction in mechanical strength, is reported. No study reported a linear behaviour, which supports the statement that uniform corrosion is non-existent for magnesium alloys.

While the primary focus of this thesis is the corrosion performance of magnesium WE43, Table 2.2 shows that several authors have quantified the mechanical performance of other alloys undergoing corrosion. In particular, earlier studies (∼2010) have tended to be performed with AZ31 [41, 69, 70], although the suitability of Aluminium containing alloys is controversial, due to its neurotoxic ability [3]. Of these studies, the specimen geometries that have been examined include foil specimens [41], rectangular plates [69–72], dog bone tensile specimens [69, 71–73] and coins [73]. Across these studies, testing times varied between 30 minutes and 9 months, while the immersion media used included SBFs, NaCl-Solution, PBS, HBSS and DMEM.

Grogan et al. [41] provided a detailed study on AZ31 foil specimens measuring 0.23 mm thickness that were immersed in HBSS for a period of 72 hours, tracking hydrogen evolution and mass loss from gravimetric measurements. Here, it was found that at only 20 % mass loss, foil specimens showed a five-fold reduction in specimen strength. This disproportionate reduction in specimen strength with mass loss is shown in Figure 2.6 (a). The study also examined the behaviour of foil specimens under constant applied stress, showing that the time to fracture was considerably reduced with increasing levels of applied load (see Figure 2.6 (b)). Adekanmbi et al. [71] used rectangular plates for 4-point bending tests and dog bone specimens for uniaxial tensile tests measuring 2 mm thickness. Testing was performed in PBS, renewed every 2-5 days, over a test period of 9 months. It was found that at only 18 % mass loss, the tensile specimens only had 2 % left of the initial observed tensile strength. However, within this study, the mass loss measurements were derived through sample weighing without removing the degradation layer.

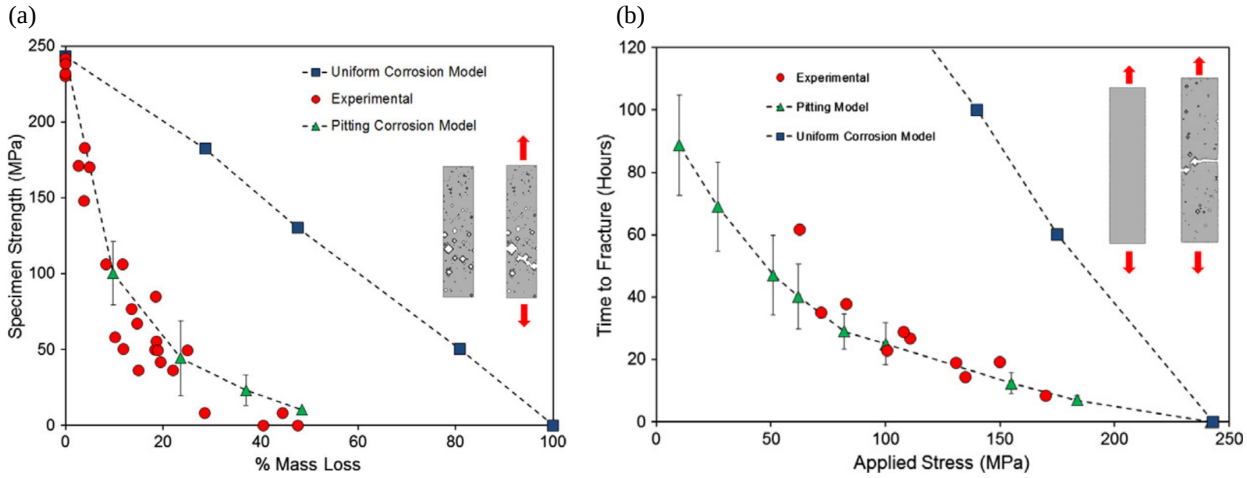

Figure 2.6: (a) Reduction of specimen strength with corrosion mass loss; (b) The effect of mechanical loading on specimen fracture time. (taken from [41])

Boland et al. examined ungrounded WE43 rectangular shaped bar specimens (2 mm x 2 mm x 50 mm) over an immersion time of 4 weeks in HBSS [68]. After 20 % mass loss, the samples had only one third of their initial strength and after 50 % mass loss, the samples had almost completly lost their initial strength. Galvin et al. measured for WE43 dog bone samples (0.14 mm thick, width 0.12 mm, length 10 mm) at 40 % mass loss after immersion for 11 days in HBSS, a 54 % reduced maximum strength [62]. Although characterisation techniques and test conditions have varied somewhat, across these studies, there is generally a disproportionate reduction in load-bearing capacity compared to corresponding mass loss. While the underlying relationship is not clearly defined, the reason for the drastic reductions in mechanical performance has been hypothesised to be attributed to pitting corrosion observed across specimens [41, 68, 71]. However, there remains little quantitative understanding on how pit formation (e.g. severity and spatial distribution) affects overall mechanical performance, with other studies generally examining pitting corrosion in magnesium through largely qualitative approaches [41, 68].

Variations within the studies from Tables 2.2 - 2.4 arise through different objectives of the studies, and a lack of standardisation (see Section 2.2.1). Interestingly, several studies did not actually track mass loss at all [69, 74], or instead different samples were used for mass

loss observations and mechanical testing [63, 75]. Also, within one study no statement was given whether corroded samples were cleaned or not, prior to weighing [72]. Mostly uniaxial tensile tests [15, 41, 62, 63, 68, 69, 71, 73, 76, 77] or compression tests [16, 74, 75, 78] were performed for mechanical tracking. Few studies performed 3-point bending [15, 70] or 4-point bending tests [71, 72].

No trend can be identified in terms of identifying an evolution of immersion testing over the last 10 years. Variations in boundary/testing conditions still arise. It is also striking that no studies within the tables used DMEM as immersion media, though it is favourable due to similar reported corrosion rates and corrosion layers, but has a high ability to contaminate (Section 2.2.1). Consequently, studies stick to simpler media like different SBFs, HBSS, PBS.

Table 2.2 In-vitro degradation study including mechanical testing

Sample Type	Alloy	Media	Time	Loading Conditions	Characterization	Referred Standard	Mass loss vs. strength	Ref.
Foil specimens (50 x 0.21 x 4.65 mm)	AZ31	HBSS 37°C	3 days	· unloaded (static) · compression	· Mass loss (H_2) · Uniaxial tensile test		Non-proportional behaviour	[41]
· Tensile specimens (l=25 mm, d=3 mm) · coins (d=18 mm, t=10 mm)	· AZ31Ti · AZ31	SBF 37°C pH control (initial 7.4) by HCL	1,3,14 days	dynamic environment (flow: 0.336 cm/s)	· Mass loss (chromic acid) · Uniaxial tensile test	ASTM E8M-99	Non-proportional behaviour	[73]
· Rectangle (100x50x2 mm) · tensile specimens l=50 mm w=12.5 mm	AZ31	Salt spray fog 35°C	0.5, 3, 6, 12, 24, 48, 72 h	unloaded	· corrosion damage (max. + av. Pit depth + std, av. Pit density + STD, aspect ratio pits, pitting factor) · Uniaxial tensile test	· ASTM B117 (Salt spray test) · ASTM G1: Cleaning · ASTM G46: pit characterisation	Missing mass loss tracking	[69]
· Rectangle (50x8x2 mm) · Dumbbell samples t=2 mm, gauge section 60x25 mm	AZ31	PBS 37°C (renewed 2-3 days)	· 1,3,6,9 months (tensile test) · 3 months (4-pt. bending)	unloaded	· Tensile test · 4-pt. bending · Mass loss (gravimetric w/o cleaning) · pH monitoring	ASTM G31–72	Non-proportional behaviour	[71]
· Rectangle (30×4×3 mm)	· AZ31B · AZ31B Ca-P coated	HBSS 37°C (refreshed every day)	0, 5, 10, 20, 30, 45, 60, 90, 120 days	unloaded	· 3-pt. bending · pH monitoring			[70]
Rectangle plate l=89 mm	· AZ31B · ZE41A	HBSS 37°C, 5 days media change	30, 90 days	· 4-point bending · unloaded	· Degradation rate · Pitting · pH control weight loss (no cleaning)	ASTM G39	Wrong tracking mass loss (no cleaning)	[72]

Table 2.3 In-vitro degradation study including mechanical testing (continued)

Sample Type	Alloy	Media	Time	Loading Conditions	Characterization	Referred Standard	Mass loss vs. strength	Ref.
Tensile samples d=3 mm l=25 mm	·AZ91D ·Mg3Zn1Ca	m-SBF (HEPES) 37°C	SCC	Slow strain-rate testing (SSRT), continuously circulating (flow conditions), 1.2×10^{-7} and 5×10^{-7}	Stress-corrosion cracking in air vs. corrosive enivornment			[79]
· Coins · Dog bones t=1.8 mm, l=27 mm	ZX-11 (rolled and annealed)	α- MEM + 10 % FBS, 37°C 5 % CO_2, 20% O_2, 95 % RH	3, 7, 14, 21, 28, 35 and 42 days	unloaded	· Degradation rate (gravimetric) · Uniaxial tensile test · pH Control		Non-proportional behaviour	[76]
· Coins d= 3mm, t= 3mm · cylinders d=11.3 mm t=5 mm · Tensile samples l=25 mm	Pure Mg (99.99%)	different SBFs 37°C	6h, 1, 3, 7, 10, 14 and 28 days	unloaded	· Degradation rate (gravimetric) · Mass loss (H_2) · Uniaxial tensile test · pH Control · EIS	ASTM-G31-72, ASTM-E8-04	Non-proportional behaviour	[77]
Cylinders d=10 mm l=11 mm	· Mg-3ZN · Mg-3Zn-5HA	SBF 37°C	3,7,14 days	unloaded	uniaxial compression testing	ASTM E9-09	No tracking of mass loss	[74]
· Tensile specimens l=11 mm A=8.5 mm^2 · Coins d=3 mm h=5 mm · Bars l,w,t= (30, 4.5, 3)mm	· ZE41 + RE · EZ33 + RE	HBSS 37°C, pH control by HEPES	1,4,7 days	unloaded	· Compression test · weight loss (cromic acid) · Corrosion rate (H_2) Electrochemical · Drop test	ASTM G119-09		[16]
· Tensile samples d=5 mm l=25 mm · Plates (25.0×4.5×1.3 mm)	Mg4Zn 0.2Mn0.2Ca	HBSS (renewed 2nd day, initial pH=7.4)	· 0, 15, 30, 60, 90, 180 days (Tensile test) · 0,15,30,60 (bending)	unloaded	· mass loss (chromic acid) · Tensile test · 3-pt. bending	ASTM-G31-72	Disproportional behaviour weight loss bending strength	[15]

Table 2.4 In-vitro degradation study including mechanical testing (continued)

Sample Type	Alloy	Media	Time	Loading Conditions	Characterization	Referred Standard	Mass loss vs. strength	Ref.
· Rectangle (10x10x5 mm)´ · Cylinders d=10 mm l=15 mm	· Mg-1.4wt. %Ca-6.1wt. %Zn · Mg-1.4wt. %Ca-6.1wt. %Zn PEO · Mg-1.4wt. %Ca-6.1wt. %Zn PEO monticellite	SBF 37°C inital pH 7.44	· 3, 7, 14 days (corrosion rate) · 10 days (compression test)	unloaded	· uniaxial compression testing · Corrosion rate (chromic acid) · EIS · pH monitoring	· ASTM G1-03 · ASTM E9 · ASTM F1044	no mass loss of compressed samples	[75]
Cylinders (d=8 mm l=12 mm)	· Mg-3wt. %Zn · Mg-3wt. % Zn-5wt. % 5HA · Mg-3wt. % Zn-5wt. % 15HA	SBF and m-SBF 37°C	3, 7, 14 days	unloaded	· Mass loss (chromic acid) · compression test	ASTM E9-09	Disproportional behaviour	[78]
· Dog bones (t=6 mm) · EDM bars (l=50 mm, l=20 mm)	WE43	HBSS 37°C	· 3 days (unground) · 4 weeks (ground)	unloaded	· Mass loss (H_2) · Uniaxial tensile test	ASTME8/ E8M-15a (dog bones)	Non-proportional behaviour	[68]
· Tensile samples (t,w=0.14, 0.12 mm l=10 mm) · wires (d=2 mm)	WE43	HBSS 37°C 5 % CO_2	3, 7, 14 days	unloaded	· Mass loss (chromic acid) · Tensile test · pH monitroing	ASTM E111-04	slightly disproportinal behaviour (dogbones) high disproportinal bahaviour (wires)	[62]
· Tensile samples (t,w=1.3, 3.5 mm l=5 mm) · Cuboids 6x4x2 mm immersion	· WE43 · FSP WE43	SBF 37°C renewed 2nd day	· 5 days (tensile test) · 12 days (weight loss)	unloaded	· Mass loss (chromic acid) · Tensile test · EIS	ASTM-G31-72	different samples weight loss and tensile testing	[63]

2.2.5 Phenomenological corrosion tracking

ASTM G46-94 [7] is the *Standard Guide for Examination and Evaluation of Pitting Corrosion*, providing guidance on techniques that can be applied to the inspection and assessment of pitted metals in general. This standard provides an overview of both destructive (e.g. cross-sections through metallography) and non-destructive techniques (e.g. X-ray, ultrasound, profilometry) to assess the severity of pitting corrosion. Figure 2.1 highlights the variations of the appearance of pit shape in corroding metals, while Figure 2.7 provides a standardised scheme from ASTM G46-94 that estimates the severity of pitting corrosion in terms of either average pitting depth, average pit size, and/or the pit density, which is the number of pits per unit area. The degree of metal penetration may also be expressed in terms of a pitting factor, which is the ratio defined as the largest depth divided by the average depth. However, this scheme is not applicable to some magnesium alloys as they do

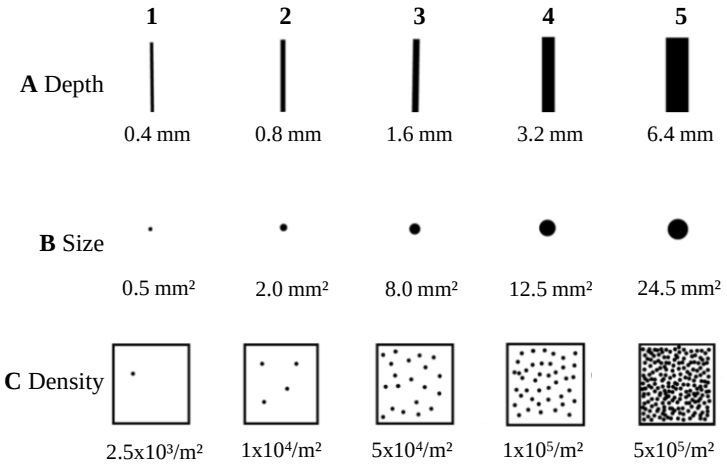

Figure 2.7: Evaluation scheme of pitting corrosion from ASTM G46-94 which rates the pits in terms of density, size and depth. (adapted from [7])

not corrode exclusively by pitting corrosion and the pitting is not always clearly visible in a simple visual inspection. Until now, few studies have been published that describe corrosion of magnesium under in-vitro test conditions using this schema. Kappatos et al. [69] examined corroding AZ31 for up to three days in a fog environment through salt spray according

to ASTM G46-94. They reported a linear increase in the pitting density over exposure time and an exponential relation of the average depth until the pits went completely through the sample's thickness. Whereby, only a small amount of cross-sections was used for the metallography analyses, and testing was performed in a simple environment. Most studies only describe corrosion in terms of bulk measurements of mass loss e.g. [68, 73, 80, 81], while a limited number of studies providing information on pitting corrosion, obtained their results through visual inspection only. Primarily, these studies have only stated whether pitting corrosion has occurred or not [11–15, 82], while no study to date has provided quantitative information on the extent of localised corrosion in magnesium alloys. However, Tables 2.2 - 2.4 clearly outline a disproportional reduction of mechanical strength with mass loss, with studies attributing this to the existence of pitting corrosion [41, 68, 76]. This phenomenon is independent of the examined alloys (e.g. AZ31, WE43, ZX).

A key challenge in this area is that there is no established methodology to systematically evaluate localised pitting parameters. Only a limited number of studies have proposed methods to automatically track pitting corrosion in other metals, through techniques such as 3D surface examination through profilometry [58, 83–85]. However, these have never been applied to magnesium. To gain a better quantitative understanding of how the severity of corrosion affects the mechanical integrity of the corroding samples, standardised detection methods are required.

2.2.6 In-vivo testing

To enable safe medical devices, in-vivo testing is mandatory in the development process chain. Many studies already performed in-vivo testing for several magnesium alloys in different animal models. For biocompatibility and initial assessment of corrosion, sub-cutaneous models of mice and rodents are commonly used. For functional performance testing of orthopaedic implant designs, the femur of guinea pigs or rabbits are commonly used models.

So far, mostly lower degradation rates compared to in-vitro testing are observed. Though, establishing a reliable relation between in-vitro and in-vivo experiments is still part of current research [42, 51, 53, 86, 87]. Different studies already came up with first correlation [42, 51, 61, 88–92], though results among each other are not in agreement and reporting a one to four times higher rate in-vitro than in-vivo. For example, Marco et al. [42] examined pure-Mg, Mg-10Gd and Mg-2Ag in-vitro in PBS, HBSS and DMEM solution and performed an in-vivo study with Prague-Dawley rats where cylindrical pins were implanted in the femur. In-vivo the mean degradation rate was 0.15 mm/year for pure magnesium, while the in-vitro rates were in PBS 1.8, HBSS 4.8 and DMEM 7.1 times higher. For the other two alloys, the ratio of the in-vitro to in-vivo corrosion rate was between 0.37 and 53, depending on the immersion media. Differences in the ratios of in-vivo and in-vitro corrosion rates arise mainly due to differences in alloy composition and the testing media, whereby difficulties in replicating the complex physiological conditions are always unavoidable [93].

In-vivo studies demonstrated the osteoconductive effect and anti-inflammatory properties of magnesium-based devices [51, 94–98], but also demonstrated the major drawback with the formation of by-products like hydrogen [98]. This gas was mostly resorbed by the surrounding tissue, it had no negative impact on bone healing. In 2010, Witte et al. [11] and Xu et al. (2009) [92] reported in their in-vivo studies no appearance of subcutaneous gas cavities. Chaya et al. [99] showed a good clinical outcome of a pure Mg plate and screw for treating bone fractures of the ulna in New Zealand White rabbits. Fracture healing with bone overgrowth was visible in the 8 weeks control X-rays. The evolving hydrogen gas did not affect the fracture healing, new bone formation nor another negative effect on the surround tissue was found.

As mentioned in Section 1.1.2.2, only few magnesium-based devices are on the market and human clinical studies are available on those products. For example, one study regarding ZX (Mg-Zn-Ca) screws for the treatment of isolated, bimalleolar or trimalleolar ankle fractures showed good outcome and after 12 months the majority of the screws were degraded

[100]. Other studies examining the performance of WE43 based devices also showed their safe usage for treating wrist bone fractures, tibial tubercle osteotomy, osteosynthesis of the mandibular condyle, treatment of hallux valgus etc. [101–105].

2.3 Surface treatments

A major challenge of magnesium as biodegradable material is its rapid corrosion behaviour and the occurrence of localised, non-uniform corrosion [106]. In an effort to reduce corrosion rates, and make corrosion more uniform, several surface coatings and modifications have been examined. In general, the material properties of magnesium dictate the mechanical integrity, while the surface properties are essential for several physiochemical processes that take place through the interaction of body fluids, adhesion of biomolecules and cells with the final implant, which initiate the corrosion process [3]. The surface of magnesium alloys can be adapted by either (i) coating deposition, typically using polymer/composite materials or (ii) by surface modification through conversion treatment(s) [107]. Conversion coatings, are formed on the surface of the material at the interface between the environment (e.g. electrolyte) and the core material through an electrochemical reaction process. Typically, an oxide layer is formed on the material surface that results in an outer inorganic, ceramic-like layer [106]. On the other hand, deposited coatings consist mostly of organic-based materials, but also metals or inorganic materials have been used [106]. Generally, surface treatments should not hinder the biodegradation process completely, which means that they should only provide a certain amount of protection and still allow the degradation process at a controlled rate. In addition to corrosion protection, surface treatments for biomedical applications can also be used to improve biocompatibility, osseointegration for orthopaedic applications, antibiotic property, or enable local drug delivery [106, 107].

2.3.1 Deposited coatings

Deposited surface coatings include organic and inorganic polymers, and even in some cases metallic compounds, with a range of approaches used to improve the corrosion performance of several magnesium alloys. Deposited surface coatings are applied through a range of different techniques like spraying, dip coating, sputtering, etc. [106], which results in a thin micron-scale coating over the surface of the component. Polymer surface coatings consist of inorganic, synthetic aliphatic-polyesters, while natural polymers such as collagen, chitosan and silk fibroin have also been extensively used [1]. PLA is one of the most widely used degradable inorganic polymers in medical devices, having applications such as surgical sutures, drug carriers, stents, tissue engineering, etc. It exhibits good biocompatibility, biodegradability, and it is FDA approved [108]. Using dip coating, Alabbasi et al. [109] created a PLA coating that improved the corrosion resistance of AZ91, immersion testing in TRIS buffered SBF showing the coated AZ91 alloy had a significant higher corrosion resistance, which was in the range of an order of magnitude, compared to uncoated AZ91 even among an immersion time of 48 h. Testing was performed though Electro Impedance Spectroscopy (EIS). While synthetic polymer-based coatings can prevent corrosion, they can also increase the acidity in the local environment and, when implanted in the human body, this can lead to foreign body reactions, such as inflammation and thrombosis [110, 111]. In comparison to inorganic polymers, organic polymers generally show better biocompatibility, due to the absence of strongly acidic corrosion products [112]. They even show antithrombotic [113] properties and an improved corrosion performance. For example, Gu et al. [114] used a Chitosan coating on a MgCa alloy, showing improved corrosion properties within in-vitro testing in SBF over a test period of 10 days. They also demonstrated that the later corrosion performance depend on both the chitosan molecular weight and the coating thickness, which corresponded to the number of applied layers.

However, one of the disadvantages of deposited surface coatings is their lack of adhesion to

the magnesium substrate. While quantitative studies characterising the adhesion of polymer coatings to the bulk material are limited [1, 112, 115], several studies have observed coating delamination from metallic substrates. This can be particularly problematic when load-bearing applications area considered, particularly where high-contact stresses might be experienced, such as orthopaedic devices, or when devices may be required to undergo large deformations, such as minimally-invasive vascular devices. To date, there are no polymer-coated magnesium-based orthopaedic implants available on the market. Though, for vascular application, the Magmaris stent by BIOTRONIK SE & Co. KG, Germany is equipped with a 7 µm thick bioabsorbable Poly-L-Lactide (PLLA) coating.

2.3.2 Conversion coatings and plasma electrolytic oxidation (PEO)

As an alternative to deposited coatings, conversion coatings transform the outer surface structure through an electrochemical reaction process to modify the surface through the formation of an oxide layer that provides a protective barrier on the material. Typically, the treatment is performed in an electrolytic solution, which results in a reaction of the precipitation from the electrolyte and metals' dissolution that results in an outer inorganic, ceramic-like layer [106]. It must be noted that this treatment will slightly influence the samples' geometry. Many studies have already shown that such conversion coatings are an effective treatment to increase the corrosion performance of various magnesium alloys. As well as reducing the corrosion rate, these surface modifications can also improve osseointegration [106].

One of the primary techniques for surface modification of magnesium alloys is plasma electrolytic oxidation (PEO), also referred as micro-arc oxidation (MAO). PEO is an electrochemical process that uses a high voltage anodising procedure, whereby plasma discharges on the metallic surface leading to the formation of an outer porous oxide film.

The PEO process is carried out in an electrolytic bath, which contains a working electrode

composed of the connected Mg alloy component and a counter-electrode, which often is the wall material (e.g. Stainless steel), contained within the electrolytic solution [106]. In general, PEO coating on magnesium alloys takes place through four stages: (i) passivation, (ii) spark anodising, (iii) plasma electrolytic oxidation, and (iv) arc discharge [116–118] (see Figure 2.8 (a)). In the passivation phase, as soon as the metal gets in contact with the electrolyte, dissolution degradation starts and the formation of a passive layer occurs. Here, the thin insulting oxide layer causes a rapid linear increasing voltage, and gas bubbles are formed. Blawert et al. [118] described the chemical reaction taking place during the first stage, as follows:

$$Mg \rightarrow Mg^{2+} + 2e^{-} \tag{2.6}$$

$$Mg^{2+} + 2OH^{-} \rightarrow Mg(OH)_2 \tag{2.7}$$

$$Mg(OH)_2 \rightarrow MgO + H_2O \tag{2.8}$$

Following this, spark anodizing takes place, whereby the breakdown current depends on the electrolyte and once reached this voltage, sparks appear over the surface, and the initial passivation layer starts to break down. In Figure 2.8 (a) this breakdown current is labelled as dielectric breakdown, and the second phase starts. The current continues to increase linearly, although with a lower rate and once critical voltage is reached plasma electrolytic oxidation is initiated, where nearly a constant voltage is reached. In this third and main phase, magnesium oxide (MgO) is formed by the reaction of the melted substrate with the ionised oxygen of the electrolyte, upon the breakdown current:

$$2H_2O \rightarrow 2H_2 + O_2 \tag{2.9}$$

$$2Mg + O_2 \rightarrow 2MgO \tag{2.10}$$

Following this, depending on the electrolyte, different phases are formed. For example, with phosphate-ions containing electrolytes, trimagnesium phosphate ($Mg_3(PO_4)_2$) is formed

[118]. If the voltage is further increased, the process enters a stage of increasingly stationary and high-energy spark discharge. However, this effect is unwanted because the occurrence of these burns lead to a destruction of the previously formed layer. Consequently, in most applications, the voltage is limited to avoid these burnings [119, 120].

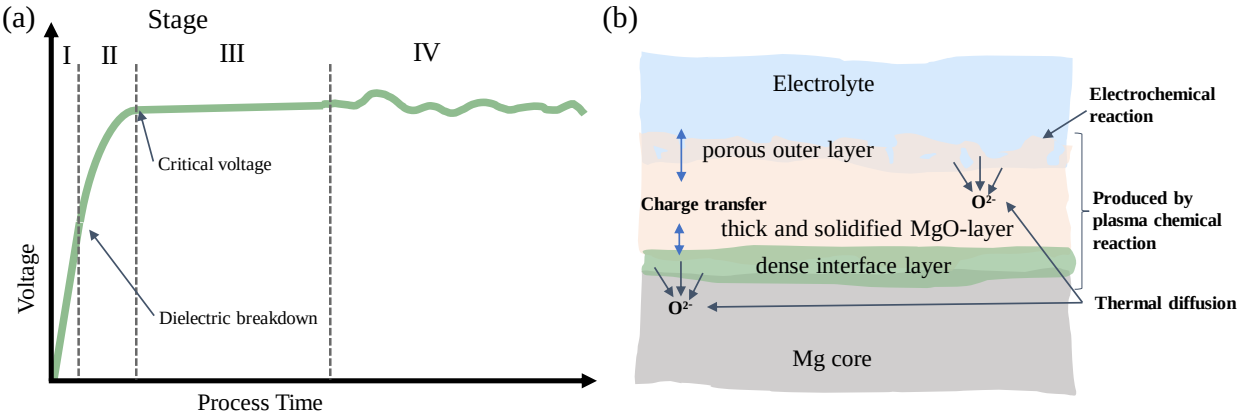

Figure 2.8: (a) Schematic PEO process plot: applied voltage over processing time with the four stages (adapted from [116, 117]), (b) surface layers of a PEO modified Mg sample, consisting out of porous outer MgO-layer, intermediate dense layer, a dense interface layer and the Mg substrate. (adapted from [121])

Figure 2.8 (b) shows the evolving layers after coating. First there is a porous outer layer with poor mechanical properties, followed by a thick and solidified MgO-layer, providing good corrosion resistance. Below is a very thin but dense interface layer before the initial magnesium alloy core arises [121]. Three different reactions take place simultaneously during the coating process: electrochemical reaction, oxygen thermal diffusion, and plasma chemical reaction [122].

Figure 2.9 shows sample SEM images from [81] that shows the (a) a surface of an unmodified WE43 sample and (b) a PEO surface treated sample, whereby the evolving porous structure of the modified surface is clearly visible.

The properties of the surface layer are controlled by the different process variables: (i) composition and concentration of the used electrolyte [123, 124], (ii) temperature [125], (iii) applied voltage, (iv) type of the used substrate, (v) exposure time [119]. Though, it is known that the electrolyte has the most impact on the later surface layer [119, 123–125].

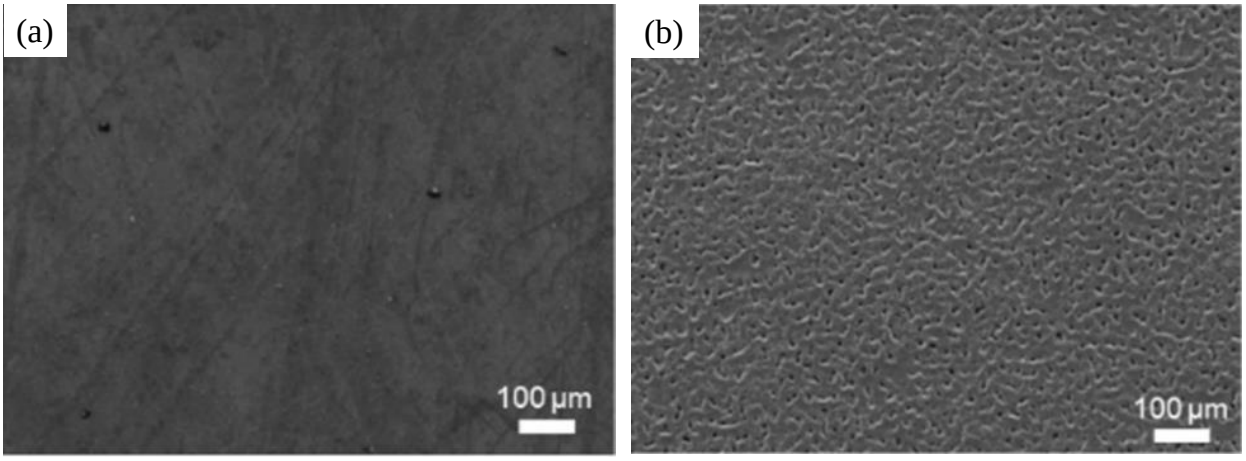

Figure 2.9: Scanning electron microscopy of the surface of (a) a WE43 unmodified sample and (b) a PEO modified sample. (adapted from [81])

Zhang et al. [126] were the first to apply a PEO surface treatment to a magnesium alloy for a biomedical application. Here, magnesium AZ91 plates measuring 25 mm x 25 mm x 2 mm underwent the PEO process and were then immersed in Hank's solution over a test period of 21 days. The PEO process was found to reduce the corrosion rate substantially, with 15 times more mass loss observed in the untreated control group compared to the PEO modified group. Xu et al. [127] applied a PEO treatment to WE42 alloy and showed a 30 times higher corrosion resistance for modified samples trough electrochemical testing of machined plate samples (10 mm x 10 mm x 2 mm) in Hank's solution, compared to unmodified WE42. Jo et al. [128] examined PEO modification on pure magnesium plates (30 mm x 20 mm x 3 mm), also demonstrating significant improved corrosion rates by electrochemical testing and immersion testing for 7 days in SBF. PEO modified magnesium has also shown good biocompatibility properties though in-vitro testing, typically examining cell attachment, alkaline phosphatase (ALP) tests and DNA measurements. Results showed about a 6 to 10 times higher DNA levels of the PEO modified group than the pure magnesium [128]. In terms of the ALP activity, two times higher levels were observed for the modified samples [128]. Fischerauer et al. [129] performed in-vivo testing in rats over 24 weeks of ZX50 pins which were unmodified and PEO treated samples. Interestingly, they observed within

the PEO modified group that almost no corrosion took place in the first week, although an accelerated corrosion rate was observed in week three, compared to unmodified ZX50 implants. Histological images revealed a positive effect on bone and tissue response in the initial stage due to the decelerated corrosion rate in the PEO modified group. Rendenbach et al. [130] performed in-vitro and in-vivo testing in Göttingen Miniature Pigs of unmodified WE43 and WE43 PEO-modified samples. Through cell viability testing, a favourable response for the PEO modified group was found, although the unmodified group was also found to be biocompatibility. In-vitro immersion testing for 14 days in c-SBF showed again a significant lower corrosion rate for PEO modified samples, whereby up to 25 times more hydrogen was released through the unmodified group. Additionally, it was highlighted that WE43 PEO-modified plate systems had improved osseointegration and resulted also in a significant reduced corrosion rate in-vivo. Through µCT analysis, it was concluded that up to 2 times more screw material was left for the WE43-PEO modified group after 6 month implantation.

While PEO modification clearly reduces the corrosion rate of magnesium-based specimens, surprisingly few studies have quantified its effect on the mechanical integrity of specimens undergoing corrosion. Kopp et al. [82] examined additive manufactured WE43 magnesium scaffold structures using laser powder-bed fusion, which underwent PEO modification and it was shown that these scaffolds also had significantly decelerated corrosion rates compared to unmodified samples. Furthermore, they also showed that the remaining compression strength of PEO modified scaffolds is up to 5 times higher after an immersion time of 7 days in DMEM. While this study demonstrated that the PEO modification is effective in improving the mechanical performance of magnesium undergoing corrosion, the specimens used were scaffolds with complex geometries fabricated through additive manufacturing. While this indicated that bulk mechanical stiffness and strength of the scaffolds were improved, it was not possible to quantify material-level properties of the corroding samples due to the complex shape. Therefore, even though bulk corrosion rates are decreased on PEO modified specimens, it is

not yet clear how this surface treatment influence the progression of localised corrosion on the samples' surface. To enhance the corrosion performance of magnesium-based implants through surface treatments, a more detailed understanding is required due to the potential to alter localised corrosion mechanisms, and ultimately its mechanical performance.

Additionally, conversion coatings are used within a composite coating strategy to improve the adhesion of outer deposited polymer coatings, whereby the intermediate porous layer is used to enhance the generally weak mechanical adhesion. For example, Liu et al. [131] sealed a poly-L-lactic acid (PLLA) coating on a previous Plasma electrolytic oxidation (PEO) modified layer, whereby micropores evolve on the surface, of an AZ31 wire. This combined treatment resulted in significant enhanced degradation properties compared to unmodified AZ31. However, data is missing on the wear resistance again and only PEO modified wires resulted in a similar remaining strength after immersion for six days as the composite treatment of PLLA and PEO. Details on the PEO treatment are given in the next Section.

2.4 Numerical modelling of Magnesium degradation

2.4.1 Background

Currently, the medical device industry relies almost completely on experimental testing during the development phase of new medical implants, whereby "trial-and-error" design practices generally require large amounts of physical prototyping of devices, which leads to high costs and unsustainable practices [132]. Numerical modelling of the corrosion behaviour of magnesium-based implants has so far played a minor role in their development. However, there is increasing interest in the development of predictive tools that provide insights into performance of implants during the design process to reduce the large amounts of design iterations required during physical prototyping and testing. In the pre-clinical phase, each design iteration requires an extensive suite of bench tests that contributes to high develop-

ment costs. Computational models offer the possibility to optimise designs at an early stage of the design process and thus save time and costs during the development process.
Several approaches are available to predict corrosion formation of magnesium, with models most commonly using either physically-based or phenomenological frameworks. While physical models consider the electrochemical interactions that are taking place between the corroding surface and its environment, phenomenological models use continuum-based damage mechanics (CDM), often in combination with element removal, to predict material loss from the corroding surface. The following sections cover both approaches, with Tables 2.5 and 2.6 provide a summary of recent publications in these areas.

2.4.2 Physical models

Physical-based models consider the electrochemical- and physical interactions of the material itself and with its environment [133]. Abdalla et al. [133] further divided these model types into either (i) activation-controlled and (ii) transport-controlled corrosion models [80, 133]. Activation-controlled models consider the potential difference of the surrounding solution and the anodic material, which results in a faster release of Mg^{2+}-ions than the rate at which $Mg(OH)_2$ is formed on the surface (see Equation (2.1)). It was shown that this activation effect only plays a minor role in long-term degradation [134]. Alternatively, transport-controlled models include the formation of the protective outer degradation layer, whereby the diffusion of Mg^{2+}-ions from the corroding surface into the solution is controlled [133]. These physically-based models are still outnumbered today. Most studies that use physically-based models aim to replicate the corrosion rate (mass loss over time) [80, 135–137] and predict the formation and dissolution of the corrosion layer [135]. Nevertheless, these models present substantial challenges due to high computational cost, which means that the majority have examined uniform corrosion [138], or instead simulated corrosion at the scale of an individual pits. Larger models that examine non-uniform and localised

corrosion over a material surface have not been possible. Furthermore, the physical nature of these models means that it is very difficult to accurately describe model parameters, as experiments on this scale are challenging. As a consequence, only a limited number of studies have used physically-based models to predict the mechanical performance of materials undergoing corrosion [80, 137, 139]. Bajger et al. (2017) used a transport-driven model to predict corrosion rate across a pure magnesium solid and scaffold specimen [135]. Here, the geometrical formation of the corroding surface was compared to experimental data through a quantitative approach by visual inspection. However, they were only able to simulate two-dimensional models of the samples due to computational limits. Grogan et al. [80] developed a three-dimensional physically-based model to predict the corroding surface of a bioabsorbable metallic stent through a diffusion-controlled corrosion process that was implemented through the finite element method. This model predicted uniform corrosion through a moving mesh algorithm and enabled comparisons to other phenomenological corrosion models for these devices. In this study, correlations were established between the solubility of the alloy and the diffusion rate of the dissolved alloy constituents in the corrosion environment, but no prediction of localised or non-uniform corrosion was made.

More recently, Marvi-Mashhadi et al. [136] simulated pitting corrosion in a diffusion-based model to predict the response of a 3D printed WE43 scaffold. This study predicted the overall mass loss of the scaffold over time and achieved a reasonable agreement between the predicted mechanical properties of the degraded scaffolds at different stages of corrosion in subsequent compression tests.

Further examples of physically-based models are summarized in Table 2.6, with more detailed reviews available elsewhere [140].

Table 2.5 Numerical modelling of Magnesium degradation

Model Type	Alloy	Application	Description	Key equation	Code	Output	Ref.
Phenomenological uniform corrosion	ZM21	· Tensile samples · Coronary stent	Continuum damage mechanics (CDM) by element deletion introducing damage parameter and the effective Cauchy stress tensor σ_{ij} including SCC	$\sigma_{ij} = \frac{\widetilde{\sigma}_{ij}}{1-D}$ $D = D_u + D_{sc}$ $\frac{dD_u}{dt} = \frac{\delta_u}{L_e} k_u$	Abaqus/ Explicit	Mass loss over time	[138]
Phenomenological uniform and pitting corrosion	AZ31	· Foil specimens	Continuum damage model by element deletion introducing damage parameter (D_u uniform, and D_p for pitting by applying random numbers to the outer active surface representing a Weibull curve) and the effective Cauchy stress tensor σ_{ij}	$\sigma_{ij} = \frac{\widetilde{\sigma}_{ij}}{1-D}$ $\frac{dD_u}{dt} = \frac{\delta_u}{L_e} \lambda_e k_u$	Abaqus/ Explicit	· Mass loss vs. time · Mass loss vs. strength	[41]
Phenomenological uniform and pitting corrosion	· WE43 (ground) · WE43 ungrounded	Rectangles	Used same degradation model as Grogan et al. [41]	$\sigma_{ij} = \frac{\widetilde{\sigma}_{ij}}{1-D}$ $\frac{dD_u}{dt} = \frac{\delta_u}{L_e} \lambda_e k_u$	Abaqus/ Explicit	· Mass loss vs. time · Mass loss vs. strength	[68]
Phenomenological pitting corrosion	WE43	Bone Plate	Used the phenomenological pitting corrosion model by Grogan et al. [41]	$\sigma_{ij} = \frac{\widetilde{\sigma}_{ij}}{1-D}$ $\frac{dD_u}{dt} = \frac{\delta_u}{L_e} \lambda_e k_u$	Abaqus/ Standard	· Mass loss vs. time · Youngs modulus vs. time	[141]
Phenomenological pitting corrosion	Mg–1.2Zn–0.5Ca	Coins	Used the phenomenological pitting corrosion model by Grogan et al. [41] but using ψ as second shape parameter for the Weibull curve	$\sigma_{ij} = \frac{\widetilde{\sigma}_{ij}}{1-D}$ $\frac{dD_u}{dt} = \frac{\delta_u}{L_e} \lambda_e k_u$	Abaqus/ Explicit	Mass loss vs. dimensionless time	[142]
Phenomenological pitting /stress corrosion		Stents	Same as Grogan et al. [41] with a translation to Abaqus/Standard with appropriate time steps	$\sigma_{ij} = \frac{\widetilde{\sigma}_{ij}}{1-D}$ $\frac{dD_u}{dt} = \frac{\delta_u}{L_e} \lambda_e k_u$	Abaqus/ Standard	Mass loss vs. strength loss	[143]

Table 2.6 Numerical modelling of Magnesium degradation (continued)

Model Type	Alloy	Application	Description	Key equation	Code	Output	Ref.
Phenomenological uniform model including exposed surfaces	AZ31B	Stents	Used the phenomenological pitting corrosion model by Grogan et al. [41] and extended it by implementing a factor of the exposed surface λ_d	$\sigma_{ij} = \frac{\widetilde{\sigma}_{ij}}{1-D}$ $\frac{dD_u}{dt} = \frac{\delta_u}{L_e}\lambda_d k_u$	Abaqus/ Explicit	· Mass loss vs. time · Stress vs. time	[144]
Phenomenological uniform corrosion	AZ31	Stents	Continuum damage mechanics (CDM), similar to Gestaldi et al. [138]	$\sigma_{ij} = \frac{\widetilde{\sigma}_{ij}}{1-D}$ $D = D_u + D_{sc}$ $\frac{dD_u}{dt} = \frac{\delta_u}{L_e}k_u$	Abaqus/ Explicit	Mass loss vs. normalized time	[145]
Phenomenological uniform corrosion	· HP-Mg · WE43	Stents	Continuum damage mechanics (CDM) and Fatigue damage	$\frac{dD_f}{dN} = \frac{\sigma_e^{2q}}{B(1-D_f)^{2q}}$	Abaqus/· Standard	Mass loss vs. normalized time · Corrosion rate vs. cyclic load	[146]
Diffusion model Transport-driven corrosion	Pure magnesium	Scaffold	Formation/dissolution of the protective film	$D^e_{Mg}\nabla_n[Mg] - (Mg_{sol} - Mg_{sat})\upsilon = 0$	FreeFem++	Mass loss vs. time	[135]
Physical diffusion model (uniform)	LAE442	Scaffolds		$\frac{dc}{dt} = \nabla(D\nabla c)$ $-D\frac{dc}{dx} = \beta(c - c_{env})$	Abaqus/ Standard	Effective E-modulus vs. time	[139]
Physical diffusion model (uniform+pitting)	WE43MEO	Scaffolds	Diffusion based model and outer nodes get a random magnitude (Weibull-curve) to simulate pitting corrosion	$\frac{dc}{dt} = \nabla(D\nabla c)$	Abaqus/ Explicit	· Mass loss vs. time · Stress strain response	[136]
Physical uniform corrosion	AZ31	Stents	Assumption: Corrosion rate is governed by the diffusion of magnesium ions in solution. Velocity of the moving stent surface depends on metallic ion concentration gradient.	$\vartheta = \frac{D_{ion}(\nabla cn)}{c_{sol}-c_{sat}}$	Abaqus/ Standard	· concentration Mg · Mass loss vs. time · Mechanical integrity vs. time	[137][80]

2.4.3 Phenomenological models

Phenomenological models of magnesium corrosion are more commonly used because they are relatively easy to implement compared to physical approaches. Generally, phenomenological models are based on continuum damage mechanics (CDM) and have been implemented through a finite element framework. Gastaldi et al. were the first to develop and apply such an approach to a magnesium alloy [138]. Within this model framework, a damage variable (D) was allocated to every element in the structure, with the fundamental equation describes the effective stress tensor $\boldsymbol{\sigma}$, as

$$\boldsymbol{\sigma} = (1 - D)\tilde{\boldsymbol{\sigma}} \tag{2.11}$$

where $\tilde{\boldsymbol{\sigma}}$ is the undamaged stress tensor and the damage variable has a value in their initial work of $D = 0$ for undamaged elements, whereas $D = 1$ indicates fully degraded elements. Gastaldi et al. used their modelling approach to predict a uniform corrosion process, assuming that localised corrosion in-vivo plays only a minor role in the later implant performance [147]. Here, the evolution of uniform corrosion D_U was described by the following equation:

$$\dot{D_U} = \frac{\delta_U}{L_e} k_u \tag{2.12}$$

Where δ_U represents the critical thickness of the evolving corrosion film, k_U a time dependent kinetic parameter and L_e the characteristic element length. This model framework [138] was also extended to consider the role of stress during the corrosion process through the addition of several stress-based terms as follows:

$$\dot{D}_{SC} = \frac{L_e}{\delta_{SC}} \left(\frac{S\sigma^*_{eq}}{1 - D} \right)^R \tag{2.13}$$

Where σ^*_{eq} is the equivalent stress corrosion, dictating the threshold for stress corrosion mechanism, while S and R are kinetic constants, which can be linked to the environment.

δ_{SC} is a characteristic dimension for stress corrosion, which is linked to the thickness of the degradation layer. Once an element reaches $D > 1$, it is removed from the simulation, and adjacent elements become activated as they become part of the exposed surface to the outer environment [138]. While this model captures some features of non-uniform corrosion, these are purely a result of the stress distribution across the specimen and are not represented any of the mechanisms of localised corrosion that occur in magnesium-based devices due to pitting and/or micro-galvanic processes. Furthermore, this framework was developed in Abaqus/Explicit (Dassault Systemes Simulia Corp., RI, USA) by means of a user subroutine (VUSDFLD).

To capture non-uniform corrosion, the model framework of Gastaldi et al. was extended by Grogan et al. [41], introducing localised/pitting corrosion mechanisms by assigning a set of pseudo-random numbers (λ_e) to all elements on the exposed surface. This random number distribution was implemented using a Weibull-shaped probability density function, which is described as follows:

$$f(x) = \gamma(x)^{\gamma-1} e^{-(x)^{\gamma}} \tag{2.14}$$

with γ as a dimensionless shape parameter of the probability density function, with $x \geq 0$ and $\gamma \geq 0$, ensuring a non-uniform distribution (as shown in Figure 2.10 (a)) to capture aspects of localised corrosion (e.g. inter-granular corrosion, pitting, etc. [1]). The extent of localised corrosion is controlled by the distribution generated, with high values of γ being associated with more uniform corrosion (e.g. $\gamma > 5$), while smaller values of γ providing progressively more pitted profiles. The parameter x of Equation (2.14) is a scale factor and initially attributed to the corrosion rate. The implementation of pseudo-random numbers λ_e in Equation (2.12) leads to Equation (2.15):

$$\dot{D_U} = \frac{\delta_U}{L_e} \lambda_e k_u \tag{2.15}$$

Figure 2.10 (b) shows a sample 2D finite element mesh that demonstrates the basic principle

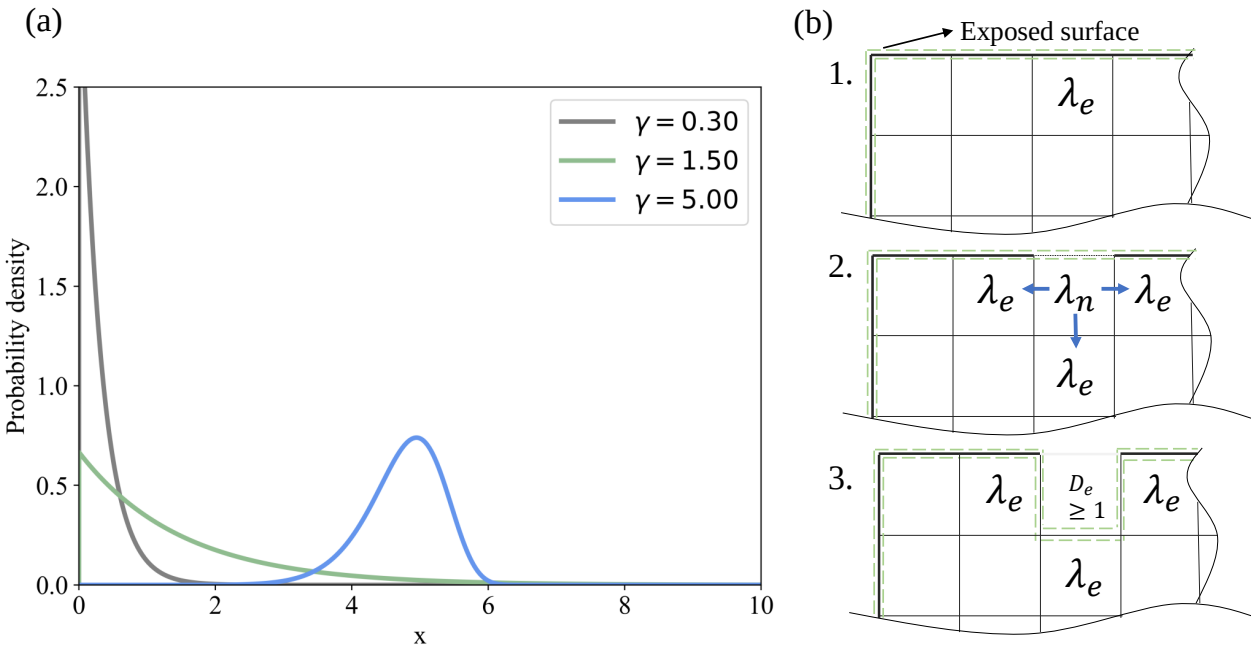

Figure 2.10: (a) Probability density function of Weibull curve for random numbers for different γ values; (b) Sample 2D FE mesh showing the exposed surface area with the basic principle of element removal including the heritage of the random numbers. (adapted from Grogan et al. [41])

of element removal, including the heritage of the random number. Here, once the element reaches $D \geq 1$, its adjacent element gets activated and they inherit the random number of the removed element according to the following equation:

$$\lambda_e = \beta \lambda_n \tag{2.16}$$

where λ_n is the random number of the deleted element, λ_e the random number of the adjacent newly activated elements, and β a constant factor that dictates the acceleration of the pit evolution [41]. Model calibration was performed through in-vitro immersion testing (see Section 2.2) of foil samples undergoing tensile testing. This enabled model calibration by capturing mass loss over time, in addition to mass loss vs. overall specimen strength, which is shown in Figure 2.6 [41, 68]. Figure 2.6 (a) clearly shows the non-linear relationship between

mass loss and specimen strength for a metallic sample undergoing non-uniform corrosion. This phenomenological model from Grogan et al. (2011) [41] has been widely used by others to predict the performance of magnesium specimens and devices undergoing corrosion [68, 141, 143, 144, 146]. Grogan and co-workers used this corrosion model themselves to predict the performance of bioabsorbable metallic stents made from AZ31 [41]. This study highlighted the need for including the simulation of pitting corrosion to fully capture the device performance over time. Both models were able to follow the experimental data of the mass loss over time, while the uniform model fails to predict the mechanical strength with regard to the corresponding mass loss (see Figure 2.6).

Boland et al. [68] also used this model to calibrate a set of parameters for WE43 samples that underwent immersion and mechanical testing. This study used rectangular WE43 rods and similar to Grogan et al. [41], showed that uniform corrosion was unable to replicate the disproportional relation between mass loss and failure strength. Boland et al. [68] applied their calibrated corrosion model to investigate the performance of a bioabsorbable metallic stent implanted within an artery that was undergoing remodelling. Gao et al. [144] also implemented the Grogan model to simulate the performance of a bioabsorbable metallic stent. Through immersion testing, it was demonstrated that the amount of corrosion depended on the exposed surface area of the specimen/device. Therefore, this study extended the model framework by including a factor that accounted for the exposed surface area of each element to better predict the corrosion of the bioabsorbable metallic stent. This corrosion model provided more insight into morphology and mechanics of corrosion of magnesium-based stents. Similarly, Debusschere et al. [143] also translated the Grogan model to the implicit finite element solver, to reduce the simulation time and expand the general applicability of this model. Their implicit implementation meant that the model no longer required the explicit finite-element integration scheme, which could be computationally expensive due to the small element size required to model corrosion mechanisms in vascular stent applications in particular.

2.4.4 Magnesium corrosion of orthopaedic devices

To date, the vast majority of computational studies that have predicted corrosion of magnesium-based materials have been for cardiovascular stent applications, with models that predict corrosion of orthopaedic implants much more limited. Of these, Ma et al. [141] implemented a pitting corrosion model to predict the corrosion process of a WE43 magnesium bone plate and screw configuration during fracture repair. This study developed a fracture repair model for a fractured tibia, by considering tissue differentiation and healing through a mechano-regulatory model. Figure 2.11 (a) shows the developed simplified 3D model including the fractured tibia, the evolving callus and the fixation screw-plate system. In Figure 2.11 (b) the results from the pitting model with the damaged elements in red, are shown. The degradation of this tibia-fixation device assembly was simulated in 3D, including physiological loadings, during a 16-week period in conjunction with the healing of a fractured tibia. The simulated data are in agreement with experimental findings they have taken from other studies.

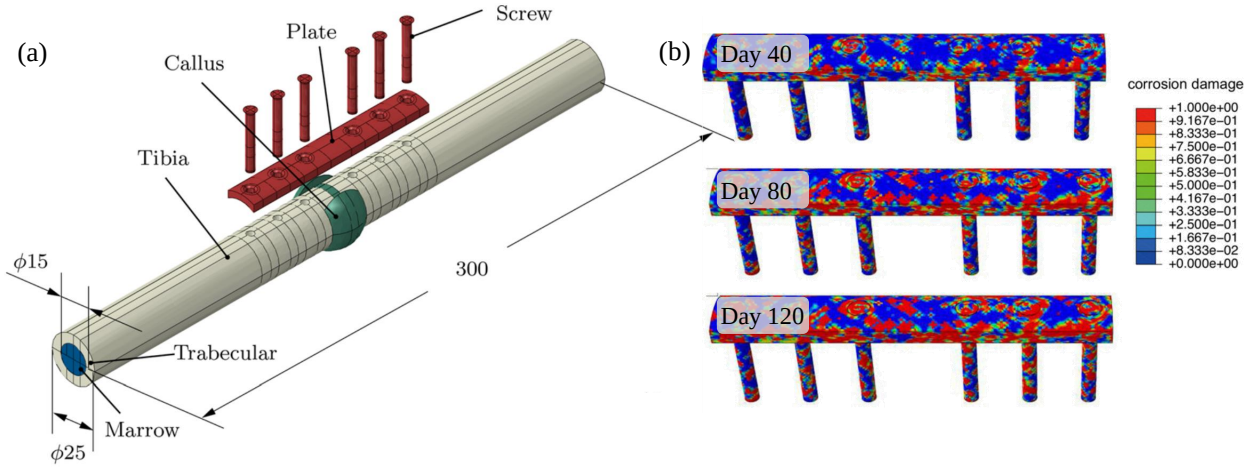

Figure 2.11: Overview of the pitting corrosion model in combination with fracture repair of a tibia by Ma et al. [141] (a) Geometry of the 3D model with the fractured tibia and the magnesium WE43 plate-screw fixation system (b) Results of the degradation model of the internal fixation WE43 magnesium implant, whereby a corrosion damage value of 0 indicates a fully undegraded element and a value of 1 is attributed to fully degraded elements. (adapted from Ma et al. [141])

While few studies have implemented a physical-based model, Gartzke et al. [139] simulated

the corrosion progression of a scaffold geometry of a LAE442 magnesium alloy through a diffusion based uniform model. This study showed the reduction of the magnesium concentration within the interface of the sample and environment. The model also predicted a reduction of the effective Young's modulus as corrosion progressed. However, a robust comparison with experimental data was not possible, with only qualitative visual comparisons of experimental cross-sections.

Barzegaria et al. [148] also relied on a diffusion-based model to simulate the diffusion of Mg^{2+}-ions into the environment of pure magnesium. As calibration, they performed immersion tests in 0.85 wt. % NaCl-solution and SBF of 0.5 g metallic chips under hydrogen gas measurement, as well as pH measurements were taken directly at the sample's surface. This calibrated framework was finally translated to a generic bone screw. However, they focused only on the prediction of mass loss and neglecting any mechanical features.

Although Marvi-Mashhadi et al. [136] simulated pitting corrosion in a diffusion-based model to predict the response of a 3D printed WE43 scaffold. This study predicted the overall mass loss of the scaffold over time and achieved a reasonable agreement between the predicted mechanical properties of the degraded scaffolds at different stages of corrosion in subsequent compression tests. For the model calibration, the same cubic scaffold geometry was additive manufactured by LPBF and immersion testing was carried out with hydrogen gas measurements over a period of 7 days.

2.5 Conclusion

Magnesium and its alloys have emerged as an alternative material for orthopaedic implant applications over the last decade. Bioabsorbable magnesium implants have the potential to support the fractured tissue during the healing period, while gradually degrading once their functional role is completed, which eliminates the need for a later removal surgery. However, the surface-based degradation of magnesium tends to take place through localised corrosion

mechanisms, which can lead to early failure of the implant systems. This literature review has revealed several crucial areas of interest, which require further understanding.

While there are many experimental studies available that characterize the corrosion process of various magnesium-based alloys, it is difficult to compare findings among them due to the lack of standardisation of testing approaches despite formal guidance being available [28, 29]. Furthermore, the vast majority of studies neglect the local morphological evolution of surface corrosion, which actually aligns with two available ASTM standards on degradation testing for biodegradable metals, ASTM F3268-18a [28] and ASTM G31-21 [29], which only provide guidelines for bulk measurements like mass loss and the corrosion rate. There is a distinct need to develop a quantitative, reproducible and robust methodology to quantify the severity and distribution of localised surface corrosion for magnesium-based alloys. This is increasingly important as it is known that localised corrosion is highly detrimental to the mechanical properties of specimens undergoing corrosion. Already, several studies have identified the disproportional relationship between the bulk mass loss and specimen strength through in-vitro testing. However, there remains little understanding on the relation between the extent and distribution of localised surface corrosion and mechanical performance. Therefore, there is a need to design in-vitro studies that provide a mechanistic link to geometrical corrosion features that dictate the mechanical performance.

This literature review highlighted that a range of approaches is available to model the degradation progress of magnesium and its alloys. While these models were able to predict the non-linear relationship between bulk mass loss and mechanical strength, these approaches tended to calibrate models directly to capture these features. To date, there has been no study that has sought to capture the specific geometrical features of localised surface corrosion of magnesium samples, which would enable a better phenomenological model description of specimens undergoing corrosion. This again highlights the need for more quantitative investigation on geometrical surface corrosion, and the implementation of a suitable numerical model to capture key features that describe the extent and distribution of corrosion, which

could be described by parameters such as average pit depth, pitting factor, pit density etc. Addressing these critical elements will facilitate a better understanding of the influence of localised corrosion mechanisms on the mechanical integrity of magnesium-based alloys, which could streamline the industrial development process and reduce the overall need for cost-intensive design optimisations.

References

[1] S. Agarwal, J. Curtin, B. Duffy, and S. Jaiswal, "Biodegradable magnesium alloys for orthopaedic applications: A review on corrosion, biocompatibility and surface modifications," *Mater Sci Eng C Mater Biol Appl*, vol. 68, pp. 948–963, 2016, ISSN: 1873-0191 (Electronic) 0928-4931 (Linking). DOI: 10.1016/j.msec.2016.06.020. [Online]. Available: https://www.ncbi.nlm.nih.gov/pubmed/27524097.

[2] F. Witte, N. Hort, C. Vogt, S. Cohen, K. U. Kainer, R. Willumeit, and F. Feyerabend, "Degradable biomaterials based on magnesium corrosion," *Current Opinion in Solid State and Materials Science*, vol. 12, no. 5-6, pp. 63–72, 2008, ISSN: 13590286. DOI: 10.1016/j.cossms.2009.04.001.

[3] Y. F. Zheng, X. N. Gu, and F. Witte, "Biodegradable metals," *Materials Science and Engineering: R: Reports*, vol. 77, pp. 1–34, 2014, ISSN: 0927796X. DOI: 10.1016/j.mser.2014.01.001.

[4] G. Song, A. Atrens, and D. StJohn, "An Hydrogen Evolution Method for the Estimation of the Corrosion Rate of Magnesium Alloys," in *Essential Readings in Magnesium Technology*, S. N. Mathaudhu, A. A. Luo, N. R. Neelameggham, E. A. Nyberg, and W. H. Sillekens, Eds. Cham: Springer International Publishing, 2001, pp. 565–572, ISBN: 978-3-319-48099-2. DOI: 10.1007/978-3-319-48099-2_90.

[5] R.-c. Zeng, J. Zhang, W.-j. Huang, W. Dietzel, K. U. Kainer, C. Blawert, and W. Ke, "Review of studies on corrosion of magnesium alloys," *Transactions of Nonferrous Metals Society of China*, vol. 16, s763–s771, 2006, ISSN: 10036326. DOI: 10.1016/s1003-6326(06)60297-5.

[6] G. Song and A. Atrens, "Understanding Magnesium Corrosion - A Framework for Improved Alloy Performance," *Advanced Engineering Materials*, vol. 5, no. 12, pp. 837–858, 2003, ISSN: 1438-1656 1527-2648. DOI: 10.1002/adem.200310405.

[7] ASTM G46-94, *Standard Guide for Examination and Evaluation of Pitting Corrosion*. PA: ASTM International West Conshohocken, 2005. DOI: 10.1520/g0046-94r18.

[8] Z. Cui, F. Ge, Y. Lin, L. Wang, L. Lei, H. Tian, M. Yu, and X. Wang, "Corrosion behavior of AZ31 magnesium alloy in the chloride solution containing ammonium nitrate," *Electrochimica Acta*, vol. 278, pp. 421–437, 2018, ISSN: 00134686. DOI: 10.1016/j.electacta.2018.05.059.

[9] S. Hiromoto, M. Inoue, T. Taguchi, M. Yamane, and N. Ohtsu, "In vitro and in vivo biocompatibility and corrosion behaviour of a bioabsorbable magnesium alloy coated with octacalcium phosphate and hydroxyapatite," *Acta Biomater*, vol. 11, pp. 520–30, 2015, ISSN: 1878-7568 (Electronic) 1742-7061 (Linking). DOI: 10.1016/j.actbio.2014.09.026. [Online]. Available: https://www.ncbi.nlm.nih.gov/pubmed/25257316.

[10] L. Han, Z. Zhang, J. Dai, X. Li, J. Bai, Z. Huang, C. Guo, F. Xue, and C. Chu, "In vitro bio-corrosion behaviors of biodegradable AZ31B magnesium alloy under static stresses of different forms and magnitudes," *Journal of Magnesium and Alloys*, 2021, ISSN: 22139567. DOI: 10.1016/j.jma.2021.09.018.

[11] F. Witte, J. Fischer, J. Nellesen, C. Vogt, J. Vogt, T. Donath, and F. Beckmann, "In vivo corrosion and corrosion protection of magnesium alloy LAE442," *Acta Biomater*, vol. 6, no. 5, pp. 1792–9, 2010, ISSN: 1878-7568 (Electronic) 1742-7061 (Linking). DOI: 10.1016/j.actbio.2009.10.012. [Online]. Available: https://www.ncbi.nlm.nih.gov/pubmed/19822226.

[12] A. M. Lafront, W. Zhang, S. Jin, R. Tremblay, D. Dubé, and E. Ghali, "Pitting corrosion of AZ91D and AJ62x magnesium alloys in alkaline chloride medium using electrochemical techniques," *Electrochimica Acta*, vol. 51, no. 3, pp. 489–501, 2005, ISSN: 00134686. DOI: 10.1016/j.electacta.2005.05.013.

[13] J. Mitchell, N. Crow, and A. Nieto, "Effect of Surface Roughness on Pitting Corrosion of AZ31 Mg Alloy," *Metals*, vol. 10, no. 5, 2020, ISSN: 2075-4701. DOI: 10.3390/met10050651.

[14] Z.-Y. Ding, L.-Y. Cui, X.-B. Chen, R.-C. Zeng, S.-K. Guan, S.-Q. Li, F. Zhang, Y.-H. Zou, and Q.-Y. Liu, "In vitro corrosion of micro-arc oxidation coating on Mg-1Li-1Ca alloy – The influence of intermetallic compound Mg2Ca," *Journal of Alloys and Compounds*, vol. 764, pp. 250–260, 2018, ISSN: 09258388. DOI: 10.1016/j.jallcom.2018.06.073.

[15] Y.-f. Cheng, W.-b. Du, K. Liu, J.-j. Fu, Z.-h. Wang, S.-b. Li, and J.-l. Fu, "Mechanical properties and corrosion behaviors of Mg-4Zn-0.2Mn-0.2Ca alloy after long term in vitro degradation," *Transactions of Nonferrous Metals Society of China*, vol. 30, no. 2, pp. 363–372, 2020, ISSN: 10036326. DOI: 10.1016/s1003-6326(20)65218-9.

[16] M. AbdelGawad, C. A. Usman, V. C. Shunmugasamy, I. Karaman, and B. Mansoor, "Corrosion behavior of Mg-Zn-Zr-RE alloys under physiological environment – Impact on mechanical integrity and biocompatibility," *Journal of Magnesium and Alloys*, 2021, ISSN: 22139567. DOI: 10.1016/j.jma.2021.11.025.

[17] X. N. Gu, Y. Lu, F. Wang, W. Lin, P. Li, and Y. Fan, "The effect of tensile and fluid shear stress on the in vitro degradation of magnesium alloy for stent applications," *Bioactive Materials*, vol. 3, no. 4, pp. 448–454, 2018, ISSN: 2452-199X (Electronic) 2452-199X (Linking). DOI: 10.1016/j.bioactmat.2018.08.002. [Online]. Available: https://www.ncbi.nlm.nih.gov/pubmed/30182072.

[18] A. Atrens, G. Song, Z. Shi, A. Soltan, S. Johnston, and M. Dargusch, "Understanding the Corrosion of Mg and Mg Alloys," *Encyclopedia of Interfacial Chemistry*, pp. 515–534, 2018. DOI: https://doi.org/10.1016/B978-0-12-409547-2.13426-2.

[19] A. D. Atrens, I. Gentle, and A. Atrens, "Possible dissolution pathways participating in the Mg corrosion reaction," *Corrosion Science*, vol. 92, pp. 173–181, 2015, ISSN: 0010938X. DOI: 10.1016/j.corsci.2014.12.004.

[20] A. Oyane, H. Kim, T. Furuya, T. Kokubo, T. Miyazaki, and T. Nakamura, "Preparation and assessment of revised simulated body fluids," *J. Biomed. Mater. Res.*, vol. 65A, no. 2, pp. 188–195, 2003, ISSN: 1549-3296. DOI: 10.1002/jbm.a.10482.

[21] M. I. Jamesh, G. Wu, Y. Zhao, D. R. McKenzie, M. M. M. Bilek, and P. K. Chu, "Electrochemical corrosion behavior of biodegradable Mg–Y–RE and Mg–Zn–Zr alloys in Ringer's solution and simulated body fluid," *Corrosion Science*, vol. 91, pp. 160–184, 2015, ISSN: 0010938X. DOI: 10.1016/j.corsci.2014.11.015.

[22] R. Rettig and S. Virtanen, "Composition of corrosion layers on a magnesium rare-earth alloy in simulated body fluids," *J Biomed Mater Res A*, vol. 88, no. 2, pp. 359–69, 2009, ISSN: 1552-4965 (Electronic) 1549-3296 (Linking). DOI: 10.1002/jbm.a.31887. [Online]. Available: https://www.ncbi.nlm.nih.gov/pubmed/18286623.

[23] K. J. Burg, S. Porter, and J. F. Kellam, "Biomaterial developments for bone tissue engineering," *Biomaterials*, vol. 21, no. 23, pp. 2347–2359, 2000.

[24] L. Müller and F. A. Müller, "Preparation of SBF with different HCO3- content and its influence on the composition of biomimetic apatites," *Acta Biomater*, vol. 2, no. 2, pp. 181–9, 2006, ISSN: 1742-7061 (Print) 1742-7061 (Linking). DOI: 10.1016/j.actbio.2005.11.001. [Online]. Available: https://www.ncbi.nlm.nih.gov/pubmed/16701876.

[25] H. Kalb, A. Rzany, and B. Hensel, "Impact of microgalvanic corrosion on the degradation morphology of WE43 and pure magnesium under exposure to simulated body fluid," *Corrosion Science*, vol. 57, pp. 122–130, 2012, ISSN: 0010938X. DOI: 10.1016/j.corsci.2011.12.026.

[26] Y. Song, D. Shan, R. Chen, F. Zhang, and E.-H. Han, "Biodegradable behaviors of AZ31 magnesium alloy in simulated body fluid," *Materials Science and Engineering: C*, vol. 29, no. 3, pp. 1039–1045, 2009, ISSN: 09284931. DOI: 10.1016/j.msec.2008.08.026.

[27] N. T. Kirkland and N. Birbilis, *Magnesium Biomaterials* (SpringerBriefs in Materials). Springer, 2014, ISBN: 978-3-319-02122-5 978-3-319-02123-2. DOI: 10.1007/978-3-319-02123-2.

[28] ASTM F3268-18a, *Standard Guide for in vitro Degradation Testing of Absorbable Metals*. PA: ASTM International West Conshohocken, 2018. DOI: 10.1520/f3268-18a.

[29] ASTM NACE G31-12a, *Standard Guide for Laboratory Immersion Corrosion Testing of Metals*. PA: ASTM International West Conshohocken, 2012. DOI: 10.1520/G0031-21.

[30] D. Mei, S. V. Lamaka, X. Lu, and M. L. Zheludkevich, "Selecting medium for corrosion testing of bioabsorbable magnesium and other metals – A critical review," *Corrosion Science*, vol. 171, 2020, ISSN: 0010938X. DOI: 10.1016/j.corsci.2020.108722.

[31] J. Gonzalez, R. Q. Hou, E. P. S. Nidadavolu, R. Willumeit-Romer, and F. Feyerabend, "Magnesium degradation under physiological conditions - Best practice," *Bioact Mater*, vol. 3, no. 2, pp. 174–185, 2018, ISSN: 2452-199X (Electronic) 2452-199X (Linking). DOI: 10.1016/j.bioactmat.2018.01.003. [Online]. Available: https://www.ncbi.nlm.nih.gov/pubmed/29744455.

[32] B. Hadzima, M. Mhaede, and F. Pastorek, "Electrochemical characteristics of calcium-phosphatized AZ31 magnesium alloy in 0.9 % NaCl solution," *J Mater Sci Mater Med*, vol. 25, no. 5, pp. 1227–37, 2014, ISSN: 1573-4838 (Electronic) 0957-4530 (Linking). DOI: 10.1007/s10856-014-5161-0. [Online]. Available: https://www.ncbi.nlm.nih.gov/pubmed/24477876.

[33] X. Lu, Y. Li, P. Ju, Y. Chen, J. Yang, K. Qian, T. Zhang, and F. Wang, "Unveiling the inhibition mechanism of an effective inhibitor for AZ91 Mg alloy," *Corrosion Science*, vol. 148, pp. 264–271, 2019, ISSN: 0010938X. DOI: 10.1016/j.corsci.2018.12.025.

[34] A. Pardo, M. C. Merino, A. E. Coy, R. Arrabal, F. Viejo, and E. Matykina, "Corrosion behaviour of magnesium/aluminium alloys in 3.5wt. % NaCl," *Corrosion Science*, vol. 50, no. 3, pp. 823–834, 2008, ISSN: 0010938X. DOI: 10.1016/j.corsci.2007.11.005.

[35] K. Yan, H. Liu, N. Feng, J. Bai, H. Cheng, J. Liu, and F. Huang, "Preparation of a single-phase Mg–6Zn alloy via ECAP-stimulated solution treatment," *Journal of Magnesium and Alloys*, vol. 7, no. 2, pp. 305–314, 2019, ISSN: 22139567. DOI: 10.1016/j.jma.2019.02.006.

[36] Y. Xin, T. Hu, and P. K. Chu, "Influence of Test Solutions on In Vitro Studies of Biomedical Magnesium Alloys," *Journal of The Electrochemical Society*, vol. 157, no. 7, p. C238, 2010. DOI: 10.1149/1.3421651. [Online]. Available: https://doi.org/10.1149/1.3421651.

[37] M. Alvarez-Lopez, M. D. Pereda, J. A. del Valle, M. Fernandez-Lorenzo, M. C. Garcia-Alonso, O. A. Ruano, and M. L. Escudero, "Corrosion behaviour of AZ31 magnesium alloy with different grain sizes in simulated biological fluids," *Acta Biomater*, vol. 6, no. 5, pp. 1763–71, 2010, ISSN: 1878-7568 (Electronic) 1742-7061 (Linking). DOI: 10.1016/j.actbio.2009.04.041. [Online]. Available: https://www.ncbi.nlm.nih.gov/pubmed/19446048.

[38] W. D. Mueller, M. F. de Mele, M. L. Nascimento, and M. Zeddies, "Degradation of magnesium and its alloys: dependence on the composition of the synthetic biological media," *J Biomed Mater Res A*, vol. 90, no. 2, pp. 487–95, 2009, ISSN: 1552-4965 (Electronic) 1549-3296 (Linking). DOI: 10.1002/jbm.a.32106. [Online]. Available: https://www.ncbi.nlm.nih.gov/pubmed/18563809.

[39] C. Schille, M. Braun, H. P. Wendel, L. Scheideler, N. Hort, H. P. Reichel, E. Schweizer, and J. Geis-Gerstorfer, "Corrosion of experimental magnesium alloys in blood and PBS: A gravimetric and microscopic evaluation," *Materials Science and Engineering: B*, vol. 176, no. 20, pp. 1797–1801, 2011, ISSN: 09215107. DOI: 10.1016/j.mseb.2011.04.007.

[40] D. Xue, Y. Yun, Z. Tan, Z. Dong, and M. J. Schulz, "In Vivo and In Vitro Degradation Behavior of Magnesium Alloys as Biomaterials," *Journal of Materials Science & Technology*, vol. 28, no. 3, pp. 261–267, 2012, ISSN: 10050302. DOI: 10.1016/s1005-0302(12)60051-6.

[41] J. A. Grogan, B. J. O'Brien, S. B. Leen, and P. E. McHugh, "A corrosion model for bioabsorbable metallic stents," *Acta Biomater*, vol. 7, no. 9, pp. 3523–33, 2011, ISSN: 1878-7568 (Electronic) 1742-7061 (Linking). DOI: 10.1016/j.actbio.2011.05.032. [Online]. Available: https://www.ncbi.nlm.nih.gov/pubmed/21664498.

[42] I. Marco, A. Myrissa, E. Martinelli, F. Feyerabend, R. Willumeit-Romer, A. M. Weinberg, and O. Van der Biest, "In vivo and in vitro degradation comparison of pure Mg, Mg-10Gd and Mg-2Ag: a short term study," *Eur Cell Mater*, vol. 33, pp. 90–104, 2017, ISSN: 1473-2262 (Electronic) 1473-2262 (Linking). DOI: 10.22203/eCM.v033a07. [Online]. Available: https://www.ncbi.nlm.nih.gov/pubmed/28197988.

[43] C. L. Liu, Y. J. Wang, R. C. Zeng, X. M. Zhang, W. J. Huang, and P. K. Chu, "In vitro corrosion degradation behaviour of Mg–Ca alloy in the presence of albumin," *Corrosion Science*, vol. 52, no. 10, pp. 3341–3347, 2010, ISSN: 0010938X. DOI: 10.1016/j.corsci.2010.06.003.

[44] A. Yamamoto and S. Hiromoto, "Effect of inorganic salts, amino acids and proteins on the degradation of pure magnesium in vitro," *Materials Science and Engineering: C*, vol. 29, no. 5, pp. 1559–1568, 2009, ISSN: 09284931. DOI: 10.1016/j.msec.2008.12.015.

[45] X. N. Gu, Y. F. Zheng, and L. J. Chen, "Influence of artificial biological fluid composition on the biocorrosion of potential orthopedic Mg-Ca, AZ31, AZ91 alloys," *Biomed Mater*, vol. 4, no. 6, p. 065 011, 2009, ISSN: 1748-605X (Electronic) 1748-6041 (Linking). DOI: 10.1088/1748-6041/4/6/065011. [Online]. Available: https://www.ncbi.nlm.nih.gov/pubmed/19966381.

[46] N. T. Kirkland, N. Birbilis, J. Walker, T. Woodfield, G. J. Dias, and M. P. Staiger, "In-vitro dissolution of magnesium-calcium binary alloys: clarifying the unique role of calcium additions in bioresorbable magnesium implant alloys," *J Biomed Mater Res B Appl Biomater*, vol. 95, no. 1, pp. 91–100, 2010, ISSN: 1552-4981 (Electronic) 1552-4973 (Linking). DOI: 10.1002/jbm.b.31687. [Online]. Available: https://www.ncbi.nlm.nih.gov/pubmed/20725953.

[47] V. Wagener and S. Virtanen, "Protective layer formation on magnesium in cell culture medium," *Mater Sci Eng C Mater Biol Appl*, vol. 63, pp. 341–51, 2016, ISSN: 1873-

0191 (Electronic) 0928-4931 (Linking). DOI: 10.1016/j.msec.2016.03.003. [Online]. Available: https://www.ncbi.nlm.nih.gov/pubmed/27040228.

[48] J. Zhang, N. Kong, Y. Shi, J. Niu, L. Mao, H. Li, M. Xiong, and G. Yuan, "Influence of proteins and cells on in vitro corrosion of Mg–Nd–Zn–Zr alloy," *Corrosion Science*, vol. 85, pp. 477–481, 2014, ISSN: 0010938X. DOI: 10.1016/j.corsci.2014.04.020.

[49] D. Mei, S. V. Lamaka, C. Feiler, and M. L. Zheludkevich, "The effect of small-molecule bio-relevant organic components at low concentration on the corrosion of commercially pure Mg and Mg-0.8Ca alloy: An overall perspective," *Corrosion Science*, vol. 153, pp. 258–271, 2019, ISSN: 0010938X. DOI: 10.1016/j.corsci.2019.03.039.

[50] M. Schinhammer, J. Hofstetter, C. Wegmann, F. Moszner, J. F. Löffler, and P. J. Uggowitzer, "On the Immersion Testing of Degradable Implant Materials in Simulated Body Fluid: Active pH Regulation Using CO2," *Advanced Engineering Materials*, vol. 15, no. 6, pp. 434–441, 2013, ISSN: 14381656. DOI: 10.1002/adem.201200218.

[51] N. Kawamura, Y. Nakao, R. Ishikawa, D. Tsuchida, and M. Iijima, "Degradation and Biocompatibility of AZ31 Magnesium Alloy Implants In Vitro and In Vivo: A Micro-Computed Tomography Study in Rats," *Materials (Basel)*, vol. 13, no. 2, 2020, ISSN: 1996-1944 (Print) 1996-1944 (Linking). DOI: 10.3390/ma13020473. [Online]. Available: https://www.ncbi.nlm.nih.gov/pubmed/31963840.

[52] J. Hofstetter, E. Martinelli, A. M. Weinberg, M. Becker, B. Mingler, P. J. Uggowitzer, and J. F. Löffler, "Assessing the degradation performance of ultrahigh-purity magnesium in vitro and in vivo," *Corrosion Science*, vol. 91, pp. 29–36, 2015, ISSN: 0010938X. DOI: 10.1016/j.corsci.2014.09.008.

[53] A. H. Martinez Sanchez, B. J. Luthringer, F. Feyerabend, and R. Willumeit, "Mg and Mg alloys: how comparable are in vitro and in vivo corrosion rates? A review," *Acta Biomater*, vol. 13, pp. 16–31, 2015, ISSN: 1878-7568 (Electronic) 1742-7061 (Linking). DOI: 10.1016/j.actbio.2014.11.048. [Online]. Available: https://www.ncbi.nlm.nih.gov/pubmed/25484334.

[54] D. Mei, S. V. Lamaka, J. Gonzalez, F. Feyerabend, R. Willumeit-Römer, and M. L. Zheludkevich, "The role of individual components of simulated body fluid on the corrosion behavior of commercially pure Mg," *Corrosion Science*, vol. 147, pp. 81–93, 2019, ISSN: 0010938X. DOI: 10.1016/j.corsci.2018.11.011.

[55] N. T. Kirkland, N. Birbilis, and M. P. Staiger, "Assessing the corrosion of biodegradable magnesium implants: a critical review of current methodologies and their limitations," *Acta Biomater*, vol. 8, no. 3, pp. 925–36, 2012, ISSN: 1878-7568 (Electronic) 1742-7061 (Linking). DOI: 10.1016/j.actbio.2011.11.014. [Online]. Available: https://www.ncbi.nlm.nih.gov/pubmed/22134164.

[56] A. Dhanapal, S. Rajendra Boopathy, and V. Balasubramanian, "Influence of pH value, chloride ion concentration and immersion time on corrosion rate of friction

stir welded AZ61A magnesium alloy weldments," *Journal of Alloys and Compounds*, vol. 523, pp. 49–60, 2012, ISSN: 09258388. DOI: 10.1016/j.jallcom.2012.01.070.

[57] L. Han, X. Li, J. Bai, F. Xue, Y. Zheng, and C. Chu, "Effects of flow velocity and different corrosion media on the in vitro bio-corrosion behaviors of AZ31 magnesium alloy," *Materials Chemistry and Physics*, vol. 217, pp. 300–307, 2018, ISSN: 02540584. DOI: 10.1016/j.matchemphys.2018.06.047.

[58] H. Li, M. R. Garvan, J. Li, J. Echauz, D. Brown, and G. J. Vachtsevanos, "Imaging and Information Processing of Pitting-Corroded Aluminum Alloy Panels with Surface Metrology Methods," Georgia Institute of Technology Atlanta United States, Report, 2014.

[59] I. Marco, F. Feyerabend, R. Willumeit-Romer, and O. Van der Biest, "Degradation testing of Mg alloys in Dulbecco's modified eagle medium: Influence of medium sterilization," *Mater Sci Eng C Mater Biol Appl*, vol. 62, pp. 68–78, 2016, ISSN: 1873-0191 (Electronic) 0928-4931 (Linking). DOI: 10.1016/j.msec.2016.01.039. [Online]. Available: https://www.ncbi.nlm.nih.gov/pubmed/26952399.

[60] L. Liu, K. Gebresellasie, B. Collins, H. Zhang, Z. Xu, J. Sankar, Y.-C. Lee, and Y. Yun, "Degradation Rates of Pure Zinc, Magnesium, and Magnesium Alloys Measured by Volume Loss, Mass Loss, and Hydrogen Evolution," *Applied Sciences*, vol. 8, no. 9, 2018, ISSN: 2076-3417. DOI: 10.3390/app8091459.

[61] Y. B. Ren, H. Wang, J. J. Huang, B. C. Zhang, and K. Yang, "Study of Biodegradation of Pure Magnesium," *Key Engineering Materials*, vol. 342, pp. 601–604, 2007. DOI: 10.4028/www.scientific.net/KEM.342-343.601.

[62] E. Galvin, S. Jaiswal, C. Lally, B. MacDonald, and B. Duffy, "In Vitro Corrosion and Biological Assessment of Bioabsorbable WE43 Mg Alloy Specimens," *Journal of Manufacturing and Materials Processing*, vol. 1, no. 1, 2017, ISSN: 2504-4494. DOI: 10.3390/jmmp1010008.

[63] G. Cao, D. Zhang, W. Zhang, and W. Zhang, "In Vitro Corrosion Study of Friction Stir Processed WE43 Magnesium Alloy in a Simulated Body Fluid," *Materials (Basel)*, vol. 9, no. 7, 2016, ISSN: 1996-1944 (Print) 1996-1944 (Linking). DOI: 10.3390/ma9070542. [Online]. Available: https://www.ncbi.nlm.nih.gov/pubmed/28773664.

[64] B. Denkena and A. Lucas, "Biocompatible Magnesium Alloys as Absorbable Implant Materials – Adjusted Surface and Subsurface Properties by Machining Processes," *CIRP Annals*, vol. 56, no. 1, pp. 113–116, 2007, ISSN: 00078506. DOI: 10.1016/j.cirp.2007.05.029.

[65] A. J. Bard, L. R. Faulkner, and H. S. White, *Electrochemical methods : fundamentals and applications.* Third. John Wiley & Sons Inc., 2002, ISBN: 9781119334064.

[66] S. Hiromoto, "Corrosion of metallic biomaterials," in *Metals for Biomedical Devices* (Woodhead Publishing Series in Biomaterials), M. Niinomi, Ed., Woodhead Publishing Series in Biomaterials. 2010, ch. 4, pp. 99–121, ISBN: 978-1-84569-434-0. DOI: 10.1533/9781845699246.2.99. [Online]. Available: https://www.sciencedirect.com/science/article/pii/B9781845694340500048.

[67] S. Papavinasam, "Electrochemical polarization techniques for corrosion monitoring," in *Techniques for Corrosion Monitoring* (Woodhead Publishing Series in Metals and Surface Engineering), Second Edition, Woodhead Publishing Series in Metals and Surface Engineering. 2021, ch. 3, pp. 45–77, ISBN: 9780081030035. DOI: 10.1016/b978-0-08-103003-5.00003-5.

[68] E. L. Boland, R. N. Shirazi, J. A. Grogan, and P. E. McHugh, "Mechanical and Corrosion Testing of Magnesium WE43 Specimens for Pitting Corrosion Model Calibration," *Advanced Engineering Materials*, vol. 20, no. 10, 2018, ISSN: 14381656. DOI: 10.1002/adem.201800656.

[69] V. Kappatos, A. N. Chamos, and S. G. Pantelakis, "Assessment of the effect of existing corrosion on the tensile behaviour of magnesium alloy AZ31 using neural networks," *Materials & Design*, vol. 31, no. 1, pp. 336–342, 2010, ISSN: 02613069. DOI: 10.1016/j.matdes.2009.06.009.

[70] Q. Wang, L. Tan, W. Xu, B. Zhang, and K. Yang, "Dynamic behaviors of a Ca–P coated AZ31B magnesium alloy during in vitro and in vivo degradations," *Materials Science and Engineering: B*, vol. 176, no. 20, pp. 1718–1726, 2011, ISSN: 09215107. DOI: 10.1016/j.mseb.2011.06.005.

[71] I. Adekanmbi, C. Z. Mosher, H. H. Lu, M. Riehle, H. Kubba, and K. E. Tanner, "Mechanical behaviour of biodegradable AZ31 magnesium alloy after long term in vitro degradation," *Mater Sci Eng C Mater Biol Appl*, vol. 77, pp. 1135–1144, 2017, ISSN: 1873-0191 (Electronic). DOI: 10.1016/j.msec.2017.03.216. [Online]. Available: https://www.ncbi.nlm.nih.gov/pubmed/28531989.

[72] Y. Koo, Y. Jang, and Y. Yun, "A study of long-term static load on degradation and mechanical integrity of Mg alloys-based biodegradable metals," *Mater Sci Eng B Solid State Mater Adv Technol*, vol. 219, pp. 45–54, 2017, ISSN: 0921-5107 (Print). DOI: 10.1016/j.mseb.2017.02.009. [Online]. Available: https://www.ncbi.nlm.nih.gov/pubmed/29520128.

[73] S. Candan, S. Emir, and E. Candan, "In Vitro Degradation Behavior of Ti-Microalloyed AZ31 Magnesium Alloy in Simulated Body Fluid," *Journal of Materials Engineering and Performance*, vol. 31, no. 1, pp. 1–10, 2021, ISSN: 1059-9495. DOI: 10.1007/s11665-021-06142-z.

[74] A. Dubey, S. Jaiswal, and D. Lahiri, "Mechanical Integrity of Biodegradable Mg–HA Composite During In Vitro Exposure," *Journal of Materials Engineering and Per-*

formance, vol. 28, no. 2, pp. 800–809, 2019, ISSN: 1059-9495. DOI: 10.1007/s11665-018-3778-8.

[75] H. R. Bakhsheshi-Rad, E. Hamzah, A. F. Ismail, M. Aziz, A. Najafinezhad, and M. Daroonparvar, "Synthesis and in-vitro performance of nanostructured monticellite coating on magnesium alloy for biomedical applications," *Journal of Alloys and Compounds*, vol. 773, pp. 180–193, 2019, ISSN: 09258388. DOI: 10.1016/j.jallcom.2018.08.310.

[76] R. Hou, J. Victoria-Hernandez, P. Jiang, R. Willumeit-Romer, B. Luthringer-Feyerabend, S. Yi, D. Letzig, and F. Feyerabend, "In vitro evaluation of the ZX11 magnesium alloy as potential bone plate: Degradability and mechanical integrity," *Acta Biomater*, vol. 97, pp. 608–622, 2019, ISSN: 1878-7568 (Electronic). DOI: 10.1016/j.actbio.2019.07.053. [Online]. Available: https://www.ncbi.nlm.nih.gov/pubmed/31365881.

[77] W. Ma, Y. Liu, W. Wang, and Y. Zhang, "Effects of electrolyte component in simulated body fluid on the corrosion behavior and mechanical integrity of magnesium," *Corrosion Science*, vol. 98, pp. 201–210, 2015, ISSN: 0010938X. DOI: 10.1016/j.corsci.2015.05.012.

[78] A. Dubey, S. Jaiswal, and D. Lahiri, "Assessment of biomechanical stability and formulation of a statistical model on magnesium based composite in two different milieus," *Journal of the Mechanical Behavior of Biomedical Materials*, vol. 111, p. 103 980, 2020, ISSN: 1878-0180 (Electronic). DOI: 10.1016/j.jmbbm.2020.103980. [Online]. Available: https://www.ncbi.nlm.nih.gov/pubmed/32830104.

[79] L. Choudhary and R. K. Singh Raman, "Mechanical integrity of magnesium alloys in a physiological environment: Slow strain rate testing based study," *Engineering Fracture Mechanics*, vol. 103, pp. 94–102, 2013, ISSN: 00137944. DOI: 10.1016/j.engfracmech.2012.09.016.

[80] J. A. Grogan, S. B. Leen, and P. E. McHugh, "A physical corrosion model for bioabsorbable metal stents," *Acta Biomater*, vol. 10, no. 5, pp. 2313–22, 2014, ISSN: 1878-7568 (Electronic). DOI: 10.1016/j.actbio.2013.12.059. [Online]. Available: https://www.ncbi.nlm.nih.gov/pubmed/24412771.

[81] O. Jung, D. Porchetta, M. L. Schroeder, M. Klein, N. Wegner, F. Walther, F. Feyerabend, M. Barbeck, and A. Kopp, "In Vivo Simulation of Magnesium Degradability Using a New Fluid Dynamic Bench Testing Approach," *Int J Mol Sci*, vol. 20, no. 19, 2019, ISSN: 1422-0067 (Electronic) 1422-0067 (Linking). DOI: 10.3390/ijms20194859. [Online]. Available: https://www.ncbi.nlm.nih.gov/pubmed/31574947.

[82] A. Kopp, T. Derra, M. Muther, L. Jauer, J. H. Schleifenbaum, M. Voshage, O. Jung, R. Smeets, and N. Kroger, "Influence of design and postprocessing parameters on the degradation behavior and mechanical properties of additively manufactured magnesium scaffolds," *Acta Biomater*, vol. 98, pp. 23–35, 2019, ISSN: 1878-7568 (Electronic)

1742-7061 (Linking). DOI: 10.1016/j.actbio.2019.04.012. [Online]. Available: https://www.ncbi.nlm.nih.gov/pubmed/30959185.

[83] P. Guo, E. C. La Plante, B. Wang, X. Chen, M. Balonis, M. Bauchy, and G. Sant, "Direct observation of pitting corrosion evolutions on carbon steel surfaces at the nano-to-micro- scales," *Scientific Reports*, vol. 8, no. 1, p. 7990, 2018, ISSN: 2045-2322 (Electronic) 2045-2322 (Linking). DOI: 10.1038/s41598-018-26340-5. [Online]. Available: https://www.ncbi.nlm.nih.gov/pubmed/29789654.

[84] C. Leising, "Pitting corrosion measurement using 3D profilometry," *NANOVEA*, 2014. DOI: 10.13140/RG.2.1.5098.3840.

[85] A. Turnbull, "Corrosion pitting and environmentally assisted small crack growth," *Proc Math Phys Eng Sci*, vol. 470, no. 2169, p. 20 140 254, 2014, ISSN: 1364-5021 (Print) 1364-5021 (Linking). DOI: 10.1098/rspa.2014.0254.

[86] J. Walker, S. Shadanbaz, N. T. Kirkland, E. Stace, T. Woodfield, M. P. Staiger, and G. J. Dias, "Magnesium alloys: predicting in vivo corrosion with in vitro immersion testing," *J Biomed Mater Res B Appl Biomater*, vol. 100, no. 4, pp. 1134–41, 2012, ISSN: 1552-4981 (Electronic) 1552-4973 (Linking). DOI: 10.1002/jbm.b.32680.

[87] H. Xu, T. Hu, M. Wang, Y. Zheng, H. Qin, H. Cao, and Z. An, "Degradability and biocompatibility of magnesium-MAO: The consistency and contradiction between in-vitro and in-vivo outcomes," *Arabian Journal of Chemistry*, vol. 13, no. 1, pp. 2795–2805, 2020, ISSN: 18785352. DOI: 10.1016/j.arabjc.2018.07.010.

[88] F. Witte, J. Fischer, J. Nellesen, H. A. Crostack, V. Kaese, A. Pisch, F. Beckmann, and H. Windhagen, "In vitro and in vivo corrosion measurements of magnesium alloys," *Biomaterials*, vol. 27, no. 7, pp. 1013–8, 2006, ISSN: 0142-9612 (Print) 0142-9612 (Linking). DOI: 10.1016/j.biomaterials.2005.07.037. [Online]. Available: https://www.ncbi.nlm.nih.gov/pubmed/16122786.

[89] H. M. Wong, K. W. Yeung, K. O. Lam, V. Tam, P. K. Chu, K. D. Luk, and K. M. Cheung, "A biodegradable polymer-based coating to control the performance of magnesium alloy orthopaedic implants," *Biomaterials*, vol. 31, no. 8, pp. 2084–96, 2010, ISSN: 1878-5905 (Electronic) 0142-9612 (Linking). DOI: 10.1016/j.biomaterials.2009.11.111. [Online]. Available: https://www.ncbi.nlm.nih.gov/pubmed/20031201.

[90] Z. Li, X. Gu, S. Lou, and Y. Zheng, "The development of binary Mg-Ca alloys for use as biodegradable materials within bone," *Biomaterials*, vol. 29, no. 10, pp. 1329–44, 2008, ISSN: 0142-9612 (Print) 0142-9612 (Linking). DOI: 10.1016/j.biomaterials.2007.12.021. [Online]. Available: https://www.ncbi.nlm.nih.gov/pubmed/18191191.

[91] Y. Ren, J. Huang, B. Zhang, and K. Yang, "Preliminary study of biodegradation of AZ31B magnesium alloy, journal = Frontiers of Materials Science in China," vol. 1,

no. 4, pp. 401–404, 2007, ISSN: 1673-7377 1673-7482. DOI: 10.1007/s11706-007-0073-2.

[92] L. Xu, F. Pan, G. Yu, L. Yang, E. Zhang, and K. Yang, "In vitro and in vivo evaluation of the surface bioactivity of a calcium phosphate coated magnesium alloy," *Biomaterials*, vol. 30, no. 8, pp. 1512–23, 2009, ISSN: 1878-5905 (Electronic) 0142-9612 (Linking). DOI: 10.1016/j.biomaterials.2008.12.001. [Online]. Available: https://www.ncbi.nlm.nih.gov/pubmed/19111896.

[93] A. H. Martinez Sanchez, B. J. Luthringer, F. Feyerabend, and R. Willumeit, "Mg and mg alloys: How comparable are in vitro and in vivo corrosion rates? a review," *Acta Biomater*, vol. 13, pp. 16–31, 2015, ISSN: 1878-7568 (Electronic) 1742-7061 (Linking). DOI: 10.1016/j.actbio.2014.11.048. [Online]. Available: https://www.ncbi.nlm.nih.gov/pubmed/25484334.

[94] H. Nygren, P. Malmberg, and Y. Liu, "MgO Implanted in Rat Tibia Bone Marrow is Osteoinductive through the Formation of a Matrix, Containing Hydroxyapatite," in *Materials Science Forum*, vol. 879, pp. 1404–1407, ISBN: 1662-9752. DOI: 10.4028/www.scientific.net/MSF.879.1404.

[95] A. Burmester, R. Willumeit-Romer, and F. Feyerabend, "Behavior of bone cells in contact with magnesium implant material," *J Biomed Mater Res B Appl Biomater*, vol. 105, no. 1, pp. 165–179, 2017, ISSN: 1552-4981 (Electronic) 1552-4973 (Linking). DOI: 10.1002/jbm.b.33542. [Online]. Available: https://www.ncbi.nlm.nih.gov/pubmed/26448207.

[96] L. Wu, F. Feyerabend, A. F. Schilling, R. Willumeit-Romer, and B. J. C. Luthringer, "Effects of extracellular magnesium extract on the proliferation and differentiation of human osteoblasts and osteoclasts in coculture," *Acta Biomater*, vol. 27, pp. 294–304, 2015, ISSN: 1878-7568 (Electronic) 1742-7061 (Linking). DOI: 10.1016/j.actbio.2015.08.042. [Online]. Available: https://www.ncbi.nlm.nih.gov/pubmed/26318802.

[97] F. Witte, H. Ulrich, C. Palm, and E. Willbold, "Biodegradable magnesium scaffolds: Part II: peri-implant bone remodeling," *J Biomed Mater Res A*, vol. 81, no. 3, pp. 757–765, 2007, ISSN: 1549-3296 (Print) 1549-3296 (Linking). DOI: 10.1002/jbm.a.31293. [Online]. Available: https://www.ncbi.nlm.nih.gov/pubmed/17390322.

[98] T. Kraus, S. F. Fischerauer, A. C. Hanzi, P. J. Uggowitzer, J. F. Loffler, and A. M. Weinberg, "Magnesium alloys for temporary implants in osteosynthesis: in vivo studies of their degradation and interaction with bone," *Acta Biomater*, vol. 8, no. 3, pp. 1230–8, 2012, ISSN: 1878-7568 (Electronic) 1742-7061 (Linking). DOI: 10.1016/j.actbio.2011.11.008. [Online]. Available: https://www.ncbi.nlm.nih.gov/pubmed/22107870.

[99] A. Chaya, S. Yoshizawa, K. Verdelis, N. Myers, B. J. Costello, D. T. Chou, S. Pal, S. Maiti, P. N. Kumta, and C. Sfeir, "In vivo study of magnesium plate and screw

degradation and bone fracture healing," *Acta Biomater*, vol. 18, pp. 262–9, 2015, ISSN: 1878-7568 (Electronic) 1742-7061 (Linking). DOI: 10.1016/j.actbio.2015.02.010. [Online]. Available: https://www.ncbi.nlm.nih.gov/pubmed/25712384.

[100] V. Herber, V. Labmayr, N. G. Sommer, R. Marek, U. Wittig, A. Leithner, F. Seibert, and P. Holweg, "Can Hardware Removal be Avoided Using Bioresorbable Mg-Zn-Ca Screws After Medial Malleolar Fracture Fixation? Mid-Term Results of a First-In-Human Study," *Injury*, vol. 53, no. 3, pp. 1283–1288, 2022, ISSN: 1879-0267 (Electronic) 0020-1383 (Linking). DOI: 10.1016/j.injury.2021.10.025. [Online]. Available: https://www.ncbi.nlm.nih.gov/pubmed/34758916.

[101] O. Polat, S. Toy, and B. Kibar, "surgical outcomes of scaphoid fracture osteosynthesis with magnesium screws,"

[102] M. Unal, E. Demirayak, M. B. Ertan, O. F. Kilicaslan, and O. Kose, "Bioabsorbable magnesium screw fixation for tibial tubercle osteotomy; a preliminary study," *Acta Biomed*, vol. 92, no. 6, e2021263, 2022, ISSN: 2531-6745 (Electronic) 0392-4203 (Linking). DOI: 10.23750/abm.v92i6.11716. [Online]. Available: https://www.ncbi.nlm.nih.gov/pubmed/35075077.

[103] J. Sturznickel, M. M. Delsmann, O. D. Jungesblut, R. Stucker, C. Knorr, T. Rolvien, M. Kertai, and M. Rupprecht, "Safety and performance of biodegradable magnesium-based implants in children and adolescents," *Injury*, vol. 52, no. 8, pp. 2265–2271, 2021, ISSN: 1879-0267 (Electronic) 0020-1383 (Linking). DOI: 10.1016/j.injury.2021.03.037. [Online]. Available: https://www.ncbi.nlm.nih.gov/pubmed/33775413.

[104] H. Leonhardt, A. Ziegler, G. Lauer, and A. Franke, "Osteosynthesis of the Mandibular Condyle With Magnesium-Based Biodegradable Headless Compression Screws Show Good Clinical Results During a 1-Year Follow-Up Period," *J Oral Maxillofac Surg*, vol. 79, no. 3, pp. 637–643, 2021, ISSN: 1531-5053 (Electronic) 0278-2391 (Linking). DOI: 10.1016/j.joms.2020.02.025. [Online]. Available: https://www.ncbi.nlm.nih.gov/pubmed/32224081.

[105] C. Plaass, C. von Falck, S. Ettinger, L. Sonnow, F. Calderone, A. Weizbauer, J. Reifenrath, L. Claassen, H. Waizy, K. Daniilidis, C. Stukenborg-Colsman, and H. Windhagen, "Bioabsorbable magnesium versus standard titanium compression screws for fixation of distal metatarsal osteotomies - 3 year results of a randomized clinical trial," *J Orthop Sci*, vol. 23, no. 2, pp. 321–327, 2018, ISSN: 1436-2023 (Electronic) 0949-2658 (Linking). DOI: 10.1016/j.jos.2017.11.005. [Online]. Available: https://www.ncbi.nlm.nih.gov/pubmed/29174422.

[106] H. Hornberger, S. Virtanen, and A. R. Boccaccini, "Biomedical coatings on magnesium alloys - a review," *Acta Biomater*, vol. 8, no. 7, pp. 2442–55, 2012, ISSN: 1878-7568 (Electronic) 1742-7061 (Linking). DOI: 10.1016/j.actbio.2012.04.012. [Online]. Available: https://www.ncbi.nlm.nih.gov/pubmed/22510401.

[107] J. Gray and B. Luan, "Protective coatings on magnesium and its alloys - a critical review," *Journal of Alloys and Compounds*, vol. 336, pp. 88–113, 2002.

[108] R. P. Pawar, S. U. Tekale, S. U. Shisodia, J. T. Totre, and A. J. Domb, "Biomedical Applications of Poly(Lactic Acid)," *Recent Patents on Regenerative Medicine*, vol. 4, no. 1, pp. 40–51, 2014, ISSN: 22102965. DOI: 10.2174/22102965046661404022350 24.

[109] A. Alabbasi, S. Liyanaarachchi, and M. B. Kannan, "Polylactic acid coating on a biodegradable magnesium alloy: An in vitro degradation study by electrochemical impedance spectroscopy," *Thin Solid Films*, vol. 520, no. 23, pp. 6841–6844, 2012, ISSN: 00406090. DOI: 10.1016/j.tsf.2012.07.090.

[110] W. J. Long, S. Nayyar, K. K. Chen, D. Novikov, R. I. Davidovitch, and J. M. Vigdorchik, "Early aseptic loosening of the Tritanium primary acetabular component with screw fixation," *Arthroplasty today*, vol. 4, no. 2, pp. 169–174, 2018.

[111] M. Tatullo, M. Marrelli, F. Mastrangelo, and E. Gherlone, "Bone inflammation, bone infection and dental implants failure: histological and cytological aspects related to cement excess," *Journal of Bone and Joint Infection*, vol. 2, no. 2, pp. 84–89, 2017.

[112] L. Y. Li, L. Y. Cui, R. C. Zeng, S. Q. Li, X. B. Chen, Y. Zheng, and M. B. Kannan, "Advances in functionalized polymer coatings on biodegradable magnesium alloys - A review," *Acta Biomater*, vol. 79, pp. 23–36, 2018, ISSN: 1878-7568 (Electronic) 1742-7061 (Linking). DOI: 10.1016/j.actbio.2018.08.030. [Online]. Available: https://www.ncbi.nlm.nih.gov/pubmed/30149212.

[113] N. Kröger, A. Kopp, M. Staudt, M. Rusu, A. Schuh, and E. A. Liehn, "Hemocompatibility of plasma electrolytic oxidation (PEO) coated Mg-RE and Mg-Zn-Ca alloys for vascular scaffold applications," *Materials Science and Engineering: C*, vol. 92, pp. 819–826, 2018.

[114] X. N. Gu, Y. F. Zheng, Q. X. Lan, Y. Cheng, Z. X. Zhang, T. F. Xi, and D. Y. Zhang, "Surface modification of an Mg-1Ca alloy to slow down its biocorrosion by chitosan," *Biomed Mater*, vol. 4, no. 4, p. 044 109, 2009, ISSN: 1748-605X (Electronic) 1748-6041 (Linking). DOI: 10.1088/1748-6041/4/4/044109. [Online]. Available: https://www.ncbi.nlm.nih.gov/pubmed/19671953.

[115] P. Wan, L. Tan, and K. Yang, "Surface Modification on Biodegradable Magnesium Alloys as Orthopedic Implant Materials to Improve the Bio-adaptability: A Review," *Journal of Materials Science & Technology*, vol. 32, no. 9, pp. 827–834, 2016, ISSN: 10050302. DOI: 10.1016/j.jmst.2016.05.003.

[116] A. G. Rakoch, E. P. Monakhova, Z. V. Khabibullina, M. Serdechnova, C. Blawert, M. L. Zheludkevich, and A. A. Gladkova, "Plasma electrolytic oxidation of AZ31 and AZ91 magnesium alloys: Comparison of coatings formation mechanism," *Journal of Magnesium and Alloys*, vol. 8, no. 3, pp. 587–600, 2020, ISSN: 22139567. DOI: 10.1016/j.jma.2020.06.002.

[117] P. H. Sobrinho, Y. Savguira, Q. Ni, and S. J. Thorpe, "Statistical analysis of the voltage-time response produced during PEO coating of AZ31B magnesium alloy," *Surface and Coatings Technology*, vol. 315, pp. 530–545, 2017, ISSN: 02578972. DOI: 10.1016/j.surfcoat.2017.02.029.

[118] C. Blawert and P. Bala Srinivasan, "Plasma electrolytic oxidation treatment of magnesium alloys," in *Surface Engineering of Light Alloys*. Elsevier, 2010, pp. 155–183, ISBN: 9781845695378. DOI: 10.1533/9781845699451.2.155.

[119] A. Jangde, S. Kumar, and C. Blawert, "Evolution of PEO coatings on AM50 magnesium alloy using phosphate-based electrolyte with and without glycerol and its electrochemical characterization," *Journal of Magnesium and Alloys*, vol. 8, no. 3, pp. 692–715, 2020, ISSN: 22139567. DOI: 10.1016/j.jma.2020.05.002.

[120] J. Martin, A. V. Nominé, J. Stef, A. Nominé, J. X. Zou, G. Henrion, and T. Grosdidier, "The influence of metallurgical state of substrate on the efficiency of plasma electrolytic oxidation (PEO) process on magnesium alloy," *Materials & Design*, vol. 178, 2019, ISSN: 02641275. DOI: 10.1016/j.matdes.2019.107859.

[121] R. O. Hussein, X. Nie, and D. O. Northwood, *Production of high quality coatings on light alloys using Plasma Electrolytic Oxidation (PEO)*, Conference Paper, 2016. DOI: 10.2495/hpsm160411.

[122] S. Sikdar, P. V. Menezes, R. Maccione, T. Jacob, and P. L. Menezes, "Plasma Electrolytic Oxidation (PEO) Process-Processing, Properties, and Applications," *Nanomaterials (Basel)*, vol. 11, no. 6, 2021, ISSN: 2079-4991 (Print) 2079-4991 (Linking). DOI: 10.3390/nano11061375. [Online]. Available: https://www.ncbi.nlm.nih.gov/pubmed/34067483.

[123] A. Ghasemi, V. S. Raja, C. Blawert, W. Dietzel, and K. U. Kainer, "The role of anions in the formation and corrosion resistance of the plasma electrolytic oxidation coatings," *Surface and Coatings Technology*, vol. 204, no. 9-10, pp. 1469–1478, 2010, ISSN: 02578972. DOI: 10.1016/j.surfcoat.2009.09.069.

[124] S. Ono, S. Moronuki, Y. Mori, A. Koshi, J. Liao, and H. Asoh, "Effect of Electrolyte Concentration on the Structure and Corrosion Resistance of Anodic Films Formed on Magnesium through Plasma Electrolytic Oxidation," *Electrochimica Acta*, vol. 240, pp. 415–423, 2017, ISSN: 00134686. DOI: 10.1016/j.electacta.2017.04.110.

[125] M. Fazel, H. R. Salimijazi, and M. Shamanian, "Improvement of Corrosion and Tribocorrosion Behavior of Pure Titanium by Subzero Anodic Spark Oxidation," *ACS Appl Mater Interfaces*, vol. 10, no. 17, pp. 15 281–15 287, 2018, ISSN: 1944-8252 (Electronic) 1944-8244 (Linking). DOI: 10.1021/acsami.8b02331. [Online]. Available: https://www.ncbi.nlm.nih.gov/pubmed/29624363.

[126] X. P. Zhang, Z. P. Zhao, F. M. Wu, Y. L. Wang, and J. Wu, "Corrosion and wear resistance of AZ91D magnesium alloy with and without microarc oxidation coating in

Hank's solution," *Journal of Materials Science*, vol. 42, no. 20, pp. 8523–8528, 2007, ISSN: 0022-2461 1573-4803. DOI: 10.1007/s10853-007-1738-z.

[127] X. Xu, P. Lu, M. Guo, and M. Fang, "Cross-linked gelatin/nanoparticles composite coating on micro-arc oxidation film for corrosion and drug release," *Applied Surface Science*, vol. 256, no. 8, pp. 2367–2371, 2010, ISSN: 01694332. DOI: 10.1016/j.apsusc.2009.10.069.

[128] J. H. Jo, J. Y. Hong, K. S. Shin, H. E. Kim, and Y. H. Koh, "Enhancing biocompatibility and corrosion resistance of Mg implants via surface treatments," *J Biomater Appl*, vol. 27, no. 4, pp. 469–76, 2012, ISSN: 1530-8022 (Electronic) 0885-3282 (Linking). DOI: 10.1177/0885328211412633. [Online]. Available: https://www.ncbi.nlm.nih.gov/pubmed/21862515.

[129] S. F. Fischerauer, T. Kraus, X. Wu, S. Tangl, E. Sorantin, A. C. Hanzi, J. F. Loffler, P. J. Uggowitzer, and A. M. Weinberg, "In vivo degradation performance of micro-arc-oxidized magnesium implants: a micro-CT study in rats," *Acta Biomater*, vol. 9, no. 2, pp. 5411–20, 2013, ISSN: 1878-7568 (Electronic) 1742-7061 (Linking). DOI: 10.1016/j.actbio.2012.09.017. [Online]. Available: https://www.ncbi.nlm.nih.gov/pubmed/23022544.

[130] C. Rendenbach, H. Fischer, A. Kopp, K. Schmidt-Bleek, H. Kreiker, S. Stumpp, M. Thiele, G. Duda, H. Hanken, B. Beck-Broichsitter, O. Jung, N. Kroger, R. Smeets, and M. Heiland, "Improved in vivo osseointegration and degradation behavior of PEO surface-modified WE43 magnesium plates and screws after 6 and 12 months," *Mater Sci Eng C Mater Biol Appl*, vol. 129, p. 112 380, 2021, ISSN: 1873-0191 (Electronic) 0928-4931 (Linking). DOI: 10.1016/j.msec.2021.112380. [Online]. Available: https://www.ncbi.nlm.nih.gov/pubmed/34579899.

[131] X. Li, C. Shi, J. Bai, C. Guo, F. Xue, P.-H. Lin, and C.-L. Chu, "Degradation behaviors of surface modified magnesium alloy wires in different simulated physiological environments," *Frontiers of Materials Science*, vol. 8, no. 3, pp. 281–294, 2014, ISSN: 2095-025X 2095-0268. DOI: 10.1007/s11706-014-0257-5.

[132] M. Viceconti, A. Henney, and E. Morley-Fletcher, "In silico clinical trials: how computer simulation will transform the biomedical industry," *International Journal of Clinical Trials*, vol. 3, no. 2, pp. 37–46, 2016.

[133] M. Abdalla, A. Joplin, M. Elahinia, and H. Ibrahim, "Corrosion Modeling of Magnesium and Its Alloys for Biomedical Applications: Review," *Corrosion and Materials Degradation*, vol. 1, no. 2, pp. 219–248, 2020, ISSN: 2624-5558. DOI: 10.3390/cmd1020011.

[134] S. Scheiner and C. Hellmich, "Stable pitting corrosion of stainless steel as diffusion-controlled dissolution process with a sharp moving electrode boundary," *Corrosion Science*, vol. 49, no. 2, pp. 319–346, 2007, ISSN: 0010938X. DOI: 10.1016/j.corsci.2006.03.019.

[135] P. Bajger, J. M. A. Ashbourn, V. Manhas, Y. Guyot, K. Lietaert, and L. Geris, "Mathematical modelling of the degradation behaviour of biodegradable metals," *Biomech Model Mechanobiol*, vol. 16, no. 1, pp. 227–238, 2017, ISSN: 1617-7940 (Electronic) 1617-7940 (Linking). DOI: 10.1007/s10237-016-0812-3. [Online]. Available: https://www.ncbi.nlm.nih.gov/pubmed/27502687.

[136] M. Marvi-Mashhadi, W. Ali, M. Li, C. Gonzalez, and L. L. J, "Simulation of corrosion and mechanical degradation of additively manufactured Mg scaffolds in simulated body fluid," *J Mech Behav Biomed Mater*, vol. 126, p. 104 881, 2022, ISSN: 1878-0180 (Electronic). DOI: 10.1016/j.jmbbm.2021.104881. [Online]. Available: https://www.ncbi.nlm.nih.gov/pubmed/34702672.

[137] J. A. Grogan, S. B. Leen, and P. E. McHugh, "Computational micromechanics of bioabsorbable magnesium stents," *Journal of the Mechanical Behavior of Biomedical Materials*, vol. 34, pp. 93–105, 2014, ISSN: 1878-0180 (Electronic). DOI: 10.1016/j.jmbbm.2014.01.007. [Online]. Available: https://www.ncbi.nlm.nih.gov/pubmed/24566380.

[138] D. Gastaldi, V. Sassi, L. Petrini, M. Vedani, S. Trasatti, and F. Migliavacca, "Continuum damage model for bioresorbable magnesium alloy devices - Application to coronary stents," *J Mech Behav Biomed Mater*, vol. 4, no. 3, pp. 352–65, 2011, ISSN: 1878-0180 (Electronic) 1878-0180 (Linking). DOI: 10.1016/j.jmbbm.2010.11.003. [Online]. Available: https://www.ncbi.nlm.nih.gov/pubmed/21316623.

[139] A. K. Gartzke, S. Julmi, C. Klose, A. C. Waselau, A. Meyer-Lindenberg, H. J. Maier, S. Besdo, and P. Wriggers, "A simulation model for the degradation of magnesium-based bone implants," *J Mech Behav Biomed Mater*, vol. 101, p. 103 411, 2020, ISSN: 1878-0180 (Electronic) 1878-0180 (Linking). DOI: 10.1016/j.jmbbm.2019.103411. [Online]. Available: https://www.ncbi.nlm.nih.gov/pubmed/31546176.

[140] E. L. Boland, R. Shine, N. Kelly, C. A. Sweeney, and P. E. McHugh, "A Review of Material Degradation Modelling for the Analysis and Design of Bioabsorbable Stents," *Ann Biomed Eng*, vol. 44, no. 2, pp. 341–56, 2016, ISSN: 1573-9686 (Electronic) 0090-6964 (Linking). DOI: 10.1007/s10439-015-1413-5. [Online]. Available: https://www.ncbi.nlm.nih.gov/pubmed/26271520.

[141] S. Ma, B. Zhou, and B. Markert, "Numerical simulation of the tissue differentiation and corrosion process of biodegradable magnesium implants during bone fracture healing," *ZAMM - Journal of Applied Mathematics and Mechanics / Zeitschrift für Angewandte Mathematik und Mechanik*, vol. 98, no. 12, pp. 2223–2238, 2018, ISSN: 0044-2267 1521-4001. DOI: 10.1002/zamm.201700314.

[142] A. Amerinatanzi, R. Mehrabi, H. Ibrahim, A. Dehghan, N. Shayesteh Moghaddam, and M. Elahinia, "Predicting the Biodegradation of Magnesium Alloy Implants: Modeling, Parameter Identification, and Validation," *Bioengineering (Basel)*, vol. 5, no. 4, 2018, ISSN: 2306-5354 (Print). DOI: 10.3390/bioengineering5040105. [Online]. Available: https://www.ncbi.nlm.nih.gov/pubmed/30501102.

[143] N. Debusschere, P. Segers, P. Dubruel, B. Verhegghe, and M. De Beule, "A Computational Framework to Model Degradation of Biocorrodible Metal Stents Using an Implicit Finite Element Solver," *Ann Biomed Eng*, vol. 44, no. 2, pp. 382–90, 2016, ISSN: 1573-9686 (Electronic). DOI: 10.1007/s10439-015-1530-1. [Online]. Available: https://www.ncbi.nlm.nih.gov/pubmed/26703421.

[144] Y. Gao, L. Wang, X. Gu, Z. Chu, M. Guo, and Y. Fan, "A quantitative study on magnesium alloy stent biodegradation," *Journal of Biomechanics*, vol. 74, pp. 98–105, 2018, ISSN: 1873-2380 (Electronic) 0021-9290 (Linking). DOI: 10.1016/j.jbiomech.2018.04.027. [Online]. Available: https://www.ncbi.nlm.nih.gov/pubmed/29735265.

[145] W. Wu, D. Gastaldi, K. Yang, L. Tan, L. Petrini, and F. Migliavacca, "Finite element analyses for design evaluation of biodegradable magnesium alloy stents in arterial vessels," *Materials Science and Engineering: B*, vol. 176, no. 20, pp. 1733–1740, 2011, ISSN: 09215107. DOI: 10.1016/j.mseb.2011.03.013.

[146] Z. Shen, M. Zhao, X. Zhou, H. Yang, J. Liu, H. Guo, Y. Zheng, and J.-A. Yang, "A numerical corrosion-fatigue model for biodegradable Mg alloy stents," *Acta Biomaterialia*, vol. 97, pp. 671–680, 2019, ISSN: 17427061. DOI: 10.1016/j.actbio.2019.08.004.

[147] R. Zeng, W. Dietzel, F. Witte, N. Hort, and C. Blawert, "Progress and Challenge for Magnesium Alloys as Biomaterials," *Advanced Engineering Materials*, vol. 10, no. 8, B3–B14, 2008, ISSN: 14381656 15272648. DOI: 10.1002/adem.200800035.

[148] M. Barzegaria, D. Meib, L. S. V., and G. L., "Computational modeling of degradation process of biodegradable magnesium biomaterials," *CoRR*, vol. 2102.10064, no. 10064, 2021. [Online]. Available: https://arxiv.org/abs/2102.10064.

Chapter 3

Theory

Within the current chapter, a fundamental theoretical background is provided on topics related to this thesis, including image processing (Section 3.1), continuum mechanics (Section 3.2), elasto-plastic constitutive laws (Section 3.3) and the Finite Element Method (Section 3.4).

3.1 Digital image processing

Digital image processing is an automated way of processing of image-based data through some kind of algorithm by a digital computer. Over the last number of decades, digital image processing has become significantly less expensive due to powerful digital computers becoming widely available. Combining advanced image detectors with powerful computers, results in powerful systems that can create, manipulate and analyse image-based data. Common applications in the medical field include the reconstruction of X-ray or magnetic resonance images, with wider applications including the analysis of aerial and satellite images, autonomous driving and motion capture [1, 2]. In general, an image is described by a function $f(x, y)$ of two spatial variables (for two-dimensional images), where f represents the brightness and x, y are the Cartesian coordinates of a single pixel. Prior to image processing, the information within the image must be converted into an array of integers, which is easily processed or manipulated through computational means. Typical processes include image transformation, enhancement, restoration, segmentation, recognition or coding [1, 3]. Image enhancements can increase the perceptibility for the observer, or could be necessary for

pre-processing for subsequent automatic image analysis. The following steps are commonly performed [4, 5]:

- Original image is acquired as input.
- Converting to gray scale image. Prior to testing, mostly images are converted to gray scale image where a value from 0-255 (white to black) is assigned to every single images, which is then the input array for following processes.
- Optional resizing in cases where a faster enhancement is needed.
- Image filtering algorithms to eliminate noise.
- Enhancement of image contrast and edge sharpening.
- Enhanced output image for further processing.

An almost infinite number of applications are conceivable where image processing is used. Thus, in the following subsections, more details are provided on filtering and noise reduction algorithms and edge detection.

3.1.1 Image noise

In general, image noise is an undesired effect during the image acquisition that results in random small variations in either colour or brightness, which can occur due to damaged camera sensors, incorrect memory locations in hardware, or the transmission was processed through a noisy channel [5, 6]. For computer tomography images, the main reason for the presence of noise is a result from statistical errors caused by the detection of a limited number of transmitted x-ray quanta. In addition, structural noise and artefacts can appear in CT scans, as well [7]. Medical images, in general, tend to have always a certain amount of noise that results in a mottled, grainy, textured, and/or snowy appearance [5]. Different types of noise include:

- **Salt-and-Pepper Noise:** Described randomly occurring black and white pixels, also called spike or impulsive noise, which is most frequently seen in images. It occurs under rapid transients, like defective swapping.

- **Gaussian Noise:** Usually while Gaussian noise occurs, each value of a pixel varies a small amount from its true value, which leads to a blurry looking image. These variations are represented by a probability density function of a normal distribution.

- **Speckle Noise:** It is mostly seen in ultrasound images as a granular noise. This type of noise is caused by interference of a bunch of waves with the same frequency, with different amplitudes and phases.

- **Shot or Poisson Noise:** Dominant in lighter parts of an image due to statistical quantum fluctuation. This means a variation of the amount of photons detected at the current exposure level. It can be modelled through a Poisson process (which describes randomly located points on a mathematical space [8]).

3.1.2 Filtering

An image filter is a predefined array that is applied by a kernel to each pixel and its neighbouring pixels within the image. It is a beneficial technique to smooth, sharpen, remove noise and detect edges. Many types of filters are available for image de-noising, with the most common being median, Gaussian and mean filters [4] which commonly available in image processing software. The median filter is commonly used due to its ability to remove noise while preserving edges. Figure 3.1 (a) shows an example of a 3x3 median filter with its basic principle. Here, for every pixel, its neighbouring pixel is also included (e.g. a 3x3 matrix) to detect whether it is a true representation of the surroundings, by replacing the value of the pixel with the median of the adjacent pixel values [9]. The output value of the current pixel is the median value that replaces the existing pixel at position (x, y). The mean filter

is similar to the median filter, while taking the average of the pixel values in the predefined kernel (Figure 3.1 (b)). Again, commonly a kernel of a 3x3 matrix is taken. Increasing the kernel size leads to a higher smoothing effect [10]. The Gaussian filter is a low-pass filter

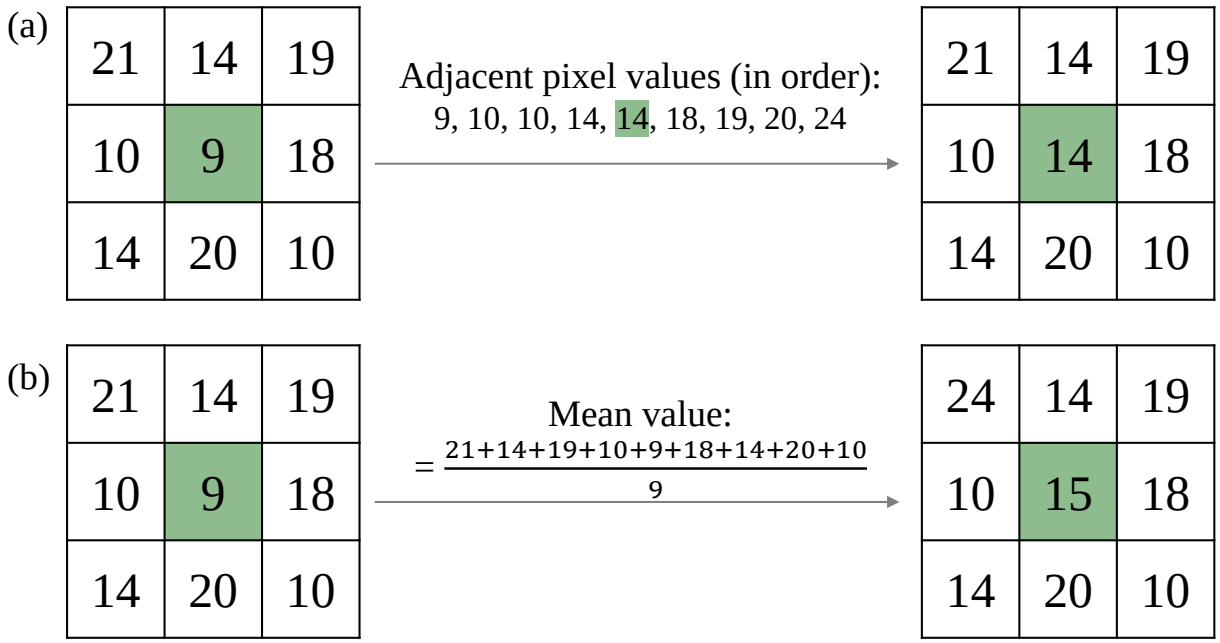

Figure 3.1: Basic principle of a (a) Median filter and (b) Mean filter with a 3x3 kernel.

that is commonly used to overcome noise by suppressing high-frequency details like noise and edges, while conserving the low-frequency details [5]. However, this filter results in an unavoidable decrease in the quality of the edges. The values inside the kernel are computed by following Gaussian function [4]:

$$G(x,y) = \frac{1}{2\pi\sigma^2} e^{-\frac{x^2+y^2}{s\sigma^2}} \tag{3.1}$$

with x, y again representing the Cartesian coordinates, and σ the standard deviation of the Gaussian distribution. σ is the most important value, since it controls the extent of the kernel and consequently the degree of smoothing. Furthermore, for most applications the kernel size (e.g. 3x3 matrix) must be defined [4, 11].

3.1.3 Edge detection

Edge detection is the localisation and identification of sharp discontinuities, which are sudden changes in pixel values in an image. It is assumed that these discontinuities are related to boundary structures of the examined image. The basic principle is that filters applied to images are sensitive to large gradient differences and return zero values for uniform areas. A variety of different edge detection algorithms exist, although these are typically classified into two groups: (i) Gradient based Edge Detection and (ii) Laplacian based Edge Detection. While the gradient-based method detects the minimum and maximum of the image through the first derivative (see Figure 3.2 (b)), the Laplacian method uses zero crossing of the second derivative to identify edges (see Figure 3.2 (c)). The gradient method implies a predefined threshold. Once the gradient of a certain pixel of the image exceeds this threshold, it is defined as edge [12]. Within this thesis the Python package OpenCV is used where two edge

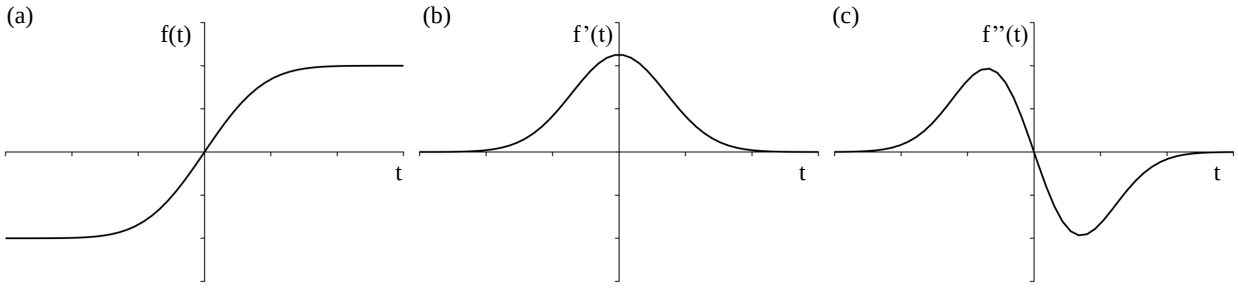

Figure 3.2: (a) Image signal with a jump in the intensity (b) Gradient of the signal (First derivative with respect to t) (c) Second derivative of the signal. (adapted from [12])

detection algorithms are mainly used (i) Sobel detection and (ii) Canny detection.

3.1.3.1 Sobel Edge Detection

The Sobel Edge Detection is a widely used detection algorithm and is based on the gradient method, where the minimum and maximum values of the first derivative of the intensity function of an image is detected (see Figure 3.2 (b)). Here, two kernels can be used to detect edges in the x or y direction, or even combined in both directions. For the x directions, the

following gradient gets calculated by convoluting (with convolution operator $*$) the original image intensity I with the kernel ([12, 13]):

$$G_x = \begin{bmatrix} -1 & 0 & +1 \\ -2 & 0 & +2 \\ -1 & 0 & +1 \end{bmatrix} * I \tag{3.2}$$

and the respect Gradient in y direction:

$$G_y = \begin{bmatrix} +1 & +2 & +1 \\ 0 & 0 & 0 \\ -1 & -2 & -1 \end{bmatrix} * I \tag{3.3}$$

The gradient magnitude is then given by:

$$G = \sqrt{G_x^2 * G_y^2} \tag{3.4}$$

and the angle of the edge orientation is:

$$\theta = \arctan\left(\frac{G_y}{G_x}\right) \tag{3.5}$$

3.1.3.2 Canny Edge Detection

The Canny filter algorithm is also classified as a gradient filter [14] and it is considered one of the most accurate edge detectors available. The Canny filter algorithm is based on three main criteria: (i) low error rate, (ii) optimal localization of the edge pixels and (iii) a single response to one edge [12, 14]. The algorithm first removes noise by smoothing using a Gaussian filter (see Section 3.1.2) and this is followed by the gradient calculation to detect areas with high spatial derivatives. Whereby, first filtering is conducted with the Sobel kernel in horizontal and vertical direction to compute the first derivative in horizontal direction, G_x

(Equation (3.2)) and vertical direction, G_y (Equation (3.3)). Again, from these two tensors, the edge gradient is achieved:

$$G = \sqrt{G_x^2 * G_y^2} \tag{3.6}$$

and the angle of the edge orientation is:

$$\theta = \arctan\left(\frac{G_y}{G_x}\right) \tag{3.7}$$

These pixel regions are further processed by suppressing pixels that are not at the maximum. Then, a hysteresis is applied within an upper and lower threshold. If the magnitude is below or above these set thresholds, the pixel is set to zero and declined as an edge. In cases where the magnitude is within the range of the two thresholds, the pixel is defined as an edge, only in cases where the pixel has a direct path to another one, which has a magnitude above the high threshold [12].

3.2 Continuum Mechanics

Within this Section, the theoretical background is given on the fundamentals of Continuum Mechanics, with its application in Finite Element Analysis. Here, continuum-based formulations are used to describe the response of materials under specific loading conditions. Finite Element Simulations conducted in this thesis are implemented in the commercially available software Abaqus (Dassault Systèmes Simulia Corp., RI, USA) with more details on the Finite Element Method (FEM) provided in Section 3.4.

Throughout the following sections, regular italic typeface (e.g t, σ) represent scalar quantities, while bold typeface describes vectors, tensors and matrices ($\boldsymbol{\sigma}, \boldsymbol{D}$). Further, these

vectors can be shown in their component form. so in the case of a 3D-vector:

$$\boldsymbol{u} = u_i = \begin{pmatrix} u_1 \\ u_2 \\ u_3 \end{pmatrix} \tag{3.8}$$

Analogously, a 3x3 tensor has two indices (e.g: $\boldsymbol{u}_{i,j}$) with $i, j = 1, 2, 3$. Information in this section is mostly taken from [15–18].

3.2.1 Deformation and Stress

The fundamental theory of a body undergoing a deformation is represented in Figure 3.3. Here, a body undergoes a deformation/motion $\boldsymbol{\chi}$ from the reference configuration (Ω_R) at time $t = 0$ to the current configuration (Ω_c) at time $t = t$. The position of point P at $t = 0$ is defined by the vector $\boldsymbol{X}$, and its position at $t = t$ changed to $\boldsymbol{x}$, which is calculated through: $\boldsymbol{x} = \boldsymbol{\chi}(\boldsymbol{X}, t)$, whereby the components of $\boldsymbol{X}$ define the material coordinates of P and the single components of $\boldsymbol{x}$ define the corresponding spatial coordinates. The displacement of P is mapped by the deformation vector $\boldsymbol{u}$ [16, 19].

$$\boldsymbol{u} = \boldsymbol{x} - \boldsymbol{X} \tag{3.9}$$

Moreover, the relation between two points (here point P and Q) in the body under the deformation is defined as $d\boldsymbol{X}$ in the reference configuration and $d\boldsymbol{x}$ in the current configuration. Whereby, a deformation gradient $\boldsymbol{F}$ defines the conversion from $d\boldsymbol{X}$ to $d\boldsymbol{x}$, while the body moves between the two configurations. This deformation gradient tensor $\boldsymbol{F}$ is defined as follows:

$$\boldsymbol{F} = \frac{\partial \boldsymbol{x}}{\partial \boldsymbol{X}} \tag{3.10}$$

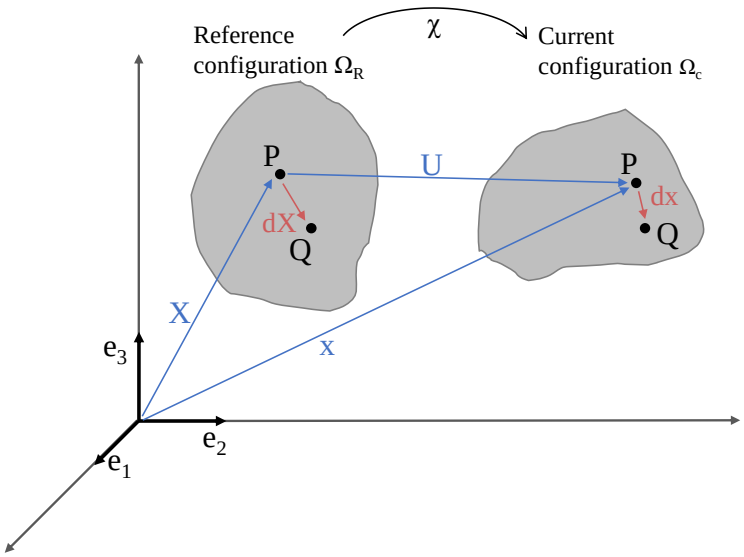

Figure 3.3: Fundamental schematic overview of a body undergoing between a reference and the current configuration. (adapted from [16])

and can be used to determine corresponding strain values. One commonly used value is the so called Green-Lagrange strain $\boldsymbol{E}$ which is given by:

$$\boldsymbol{E} = \frac{1}{2}(\boldsymbol{F}^T \cdot \boldsymbol{F} - \boldsymbol{I}) \tag{3.11}$$

with $\boldsymbol{F}^T$ as the transpose of $\boldsymbol{F}$ and $\boldsymbol{I}$ the identity tensor which results in $\boldsymbol{F} = \boldsymbol{F} \cdot \boldsymbol{I}$. The corresponding index notation is given as

$$E_{ij} = \frac{1}{2}\left(\frac{\partial u_i}{\partial X_j} + \frac{\partial u_j}{\partial X_i} + \frac{\partial u_k}{\partial X_i}\frac{\partial u_k}{\partial X_j}\right) \tag{3.12}$$

With the assumption that the product of infinitesimals is zero $\left(\frac{\partial u_k}{\partial X_i}\frac{\partial u_k}{\partial X_j} \approx 0\right)$, the final infinitesimal strain is described as:

$$\varepsilon_{ij} = \frac{1}{2}\left(\frac{\partial u_i}{\partial X_j} + \frac{\partial u_j}{\partial X_i}\right) \tag{3.13}$$

Measurements to determine the stretch are $\boldsymbol{B}$ and $\boldsymbol{C}$ indicating the left and right Chauchy-Green tensor, respectively, as follows:

$$\boldsymbol{B} = \boldsymbol{F} \cdot \boldsymbol{F}^T \qquad \boldsymbol{C} = \boldsymbol{F}^T \cdot \boldsymbol{F} \tag{3.14}$$

With the left and right stretch tensors $\boldsymbol{V}$, $\boldsymbol{U}$ and an orthogonal rotation tensor $\boldsymbol{R}$ the deformation gradient $\boldsymbol{F}$ is decomposed, according to the polar decomposition theorem to:

$$\boldsymbol{F} = \boldsymbol{R}\boldsymbol{U} = \boldsymbol{V}\boldsymbol{U} \tag{3.15}$$

These two stretch tensors are directly linked to the left and right Cauchy-Green tensors with $\boldsymbol{V}^2 = \boldsymbol{B}$ and $\boldsymbol{U}^2 = \boldsymbol{C}$. Eigenvalues of $\boldsymbol{U}$ are the principal stretch ($\boldsymbol{\lambda}_{i=123}$) and the eigenvectors are the respective principle referential axes. With $\boldsymbol{V}$ the logarithmic strain is written as:

$$\boldsymbol{\varepsilon} = ln\boldsymbol{V} \tag{3.16}$$

As mentioned above, λ_i represents the stretches and by combing λ_i, three principal invariants are derived as follows:

$$I_1 = tr(\boldsymbol{C}) = {\lambda_1}^2 + {\lambda_2}^2 + {\lambda_3}^2 \tag{3.17}$$

$$I_2 = \frac{1}{2}[{I_1}^2 tr(\boldsymbol{C}^2)] = {\lambda_1}^2{\lambda_2}^2 + {\lambda_1}^2{\lambda_3}^2 + {\lambda_2}^2{\lambda_3}^2 \tag{3.18}$$

$$I_3 = det(\boldsymbol{C}) = J^2 \qquad \text{with} \qquad J = det(\boldsymbol{F}) \tag{3.19}$$

The velocity of point P (see Figure 3.3) is expressed as:

$$\boldsymbol{v} = \frac{\partial \boldsymbol{x}}{\partial t} \tag{3.20}$$

being the rate (partial derivative with respect to time) of changes of $\boldsymbol{x}$ for fixed $\boldsymbol{X}$. The spatial velocity gradient tensor $\boldsymbol{L}$ is used to describe the difference in velocity of two neigh-

bouring elements:

$$\boldsymbol{v} = \frac{\partial \boldsymbol{x}}{\partial \boldsymbol{t}} dx = \boldsymbol{L} dx \tag{3.21}$$

$\boldsymbol{L}$ is also directly related to the deformation gradient $\boldsymbol{F}$:

$$\boldsymbol{L} = \frac{\partial \boldsymbol{v}}{\partial \boldsymbol{x}} dx = \frac{\partial \boldsymbol{v}}{\partial \boldsymbol{X}} \cdot \frac{\partial \boldsymbol{X}}{\partial \boldsymbol{x}} = \frac{\partial \boldsymbol{F}}{\partial t} \cdot \boldsymbol{F}^{-1} = \dot{\boldsymbol{F}} \cdot \boldsymbol{F}^{-1} \tag{3.22}$$

and $\boldsymbol{L}$ can be further decomposed into (i) a symmetric rate of deformation tensor $\boldsymbol{D}$ and (ii) an asymmetric spin tensor $\boldsymbol{\omega}$:

$$\boldsymbol{D} = \frac{1}{2}\left(\boldsymbol{L} + \boldsymbol{L}^T\right) = sym(\boldsymbol{L}) \text{ and} \tag{3.23}$$

$$\boldsymbol{\omega} = \frac{1}{2}\left(\boldsymbol{L} - \boldsymbol{L}^T\right) = asym(\boldsymbol{L}) \tag{3.24}$$

The true strain rate $\dot{\boldsymbol{\varepsilon}}$ is based on the definition of the symmetric rate tensor $\boldsymbol{D}$ and is identified as:

$$\dot{\boldsymbol{\varepsilon}} = \boldsymbol{D} \tag{3.25}$$

The FE solver used within this thesis is Abaqus (Dassault Systèmes Simulia Corp., RI, USA) and within this software the logarithmic strain $\boldsymbol{\varepsilon}$ is defined in the theory manual [15] as:

$$\boldsymbol{\varepsilon}(t) = \int_0^t \boldsymbol{D} dt \tag{3.26}$$

under the assumption that the principal reference axes are fixed with regard to the material coordinates. Figure 3.4 depicts a scheme of the traction vector $\boldsymbol{t}$, which is the force per unit area on an infinitesimal surface body cut dS by a plane with the normal vector $\boldsymbol{n}$, in the vicinity of a material Point P. The corresponding Cauchy true stress ($\boldsymbol{\sigma}$) is expressed as:

$$\boldsymbol{t} = \boldsymbol{\sigma} \cdot \boldsymbol{n} \tag{3.27}$$

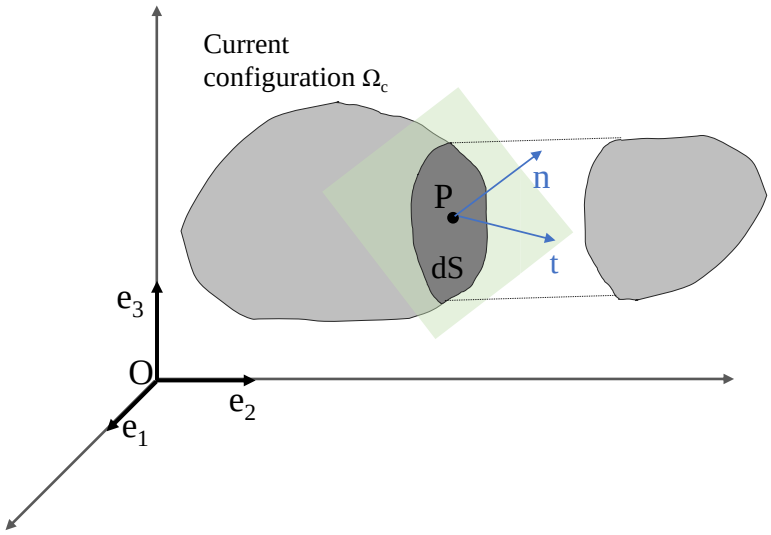

Figure 3.4: Scheme representing a traction vector $\boldsymbol{t}$ acting on an infinitesimal surface cut dS by a plane with the normal vector $\boldsymbol{n}$ in the current configuration. (adapted from [16])

which can be further decomposed into two parts: (i) the deviatoric stress $\boldsymbol{S}$, which determines the shape changes of the body and (ii) the hydrostatic pressure stress part p. This results in,

$$\boldsymbol{\sigma} = \boldsymbol{S} - p\boldsymbol{I} \qquad \text{with} \qquad p = \frac{-Tr(\boldsymbol{\sigma})}{3} \tag{3.28}$$

Within this thesis, elasto-plastic material models are used to describe the constitutive behaviour of magnesium. In this context, the von Mises equivalent stress is useful, which is expressed as:

$$\sigma_e = \sqrt{\frac{3}{2} S_{ij} S_{ij}} \tag{3.29}$$

Another measure of stress is the Kirchhoff stress $\boldsymbol{\tau}$, which is a symmetric tensor:

$$\boldsymbol{\tau} = J\boldsymbol{\sigma} \tag{3.30}$$

with J as the ratio of infinitesimal volumes in the vicinity of Point P in the current configuration ($d\Omega$) and the reference configuration (Ω_0). A third expression for stress is the Piola

stress, which is a non-symmetric tensor:

$$\boldsymbol{P} = J\boldsymbol{\sigma}\boldsymbol{F}^{-T} \tag{3.31}$$

The transposed tensor of $\boldsymbol{P}$ is equivalent to the nominal:

$$\widetilde{\boldsymbol{\sigma}} = J\boldsymbol{F}^{-1}\boldsymbol{\sigma} = \boldsymbol{P}^{T} \tag{3.32}$$

3.3 Material Constitutive Behaviour: Elasto-Plasticity

The investigated magnesium alloy in Chapters 4 - 7 is assumed throughout as homogenous, isotropic, rate-independent and thus perfectly elastic-plastic, which results in a reversible elastic deformation followed by an irreversible plastic deformation. The constitutive formulation is described as:

$$\boldsymbol{F} = \boldsymbol{F}^{e} \cdot \boldsymbol{F}^{p} \tag{3.33}$$

with $\boldsymbol{F}^{e}$ as the elastic component and $\boldsymbol{F}^{p}$ the plastic component. Under the assumption that the elastic strain component is small (suitable for metal simulations) the total strain rate ($\dot{\boldsymbol{\varepsilon}}$) is decomposed again into an elastic ($\dot{\boldsymbol{\varepsilon}}^{e}$) and plastic ($\dot{\boldsymbol{\varepsilon}}^{p}$) strain rate, following classical additive decomposition:

$$\dot{\boldsymbol{\varepsilon}} = \dot{\boldsymbol{\varepsilon}}^{e} + \dot{\boldsymbol{\varepsilon}}^{p} \tag{3.34}$$

This can be expressed in integrated form using the common notion of corotational measures as follows:

$$\boldsymbol{\varepsilon} = \boldsymbol{\varepsilon}^{e} + \boldsymbol{\varepsilon}^{p} \tag{3.35}$$

Since isotropy is assumed, the elastic strain component is determined through the bulk modulus K and the corresponding shear modulus G. Both moduli are defined through the material constants E (Young's modulus) and ϑ (Poisson's ratio) according to:

$$K = \frac{E}{3(1-2\vartheta)} \qquad (3.36) \qquad\qquad G = \frac{E}{2(1+\vartheta)} \qquad (3.37)$$

Volumetric and deviatoric components of the elastic strain are attributed to (i) the hydrostatic pressure $\boldsymbol{p}$ and (ii) the deviatoric stress $\boldsymbol{S}$, respectively, as follows:

$$\boldsymbol{\varepsilon}^e_{vol} = tr(\boldsymbol{\varepsilon}^e) = -\frac{\boldsymbol{p}}{K} \qquad (3.38)$$

and the corresponding deviatoric elastic strain $\boldsymbol{e}^e$ and deviatoric stress $\boldsymbol{S}$ is:

$$\boldsymbol{e}^e = \boldsymbol{\varepsilon}^e - \frac{1}{3}\boldsymbol{\varepsilon}^e_{vol}\boldsymbol{I} \qquad (3.39)$$

and

$$\boldsymbol{S} = 2G\boldsymbol{\varepsilon}^e \qquad (3.40)$$

Throughout this thesis isotropic yielding is assumed, whereby the uniaxial yield stress is a function of uniaxial equivalent plastic strain that forms the input values for yield behaviour. This von Mises plasticity formulation, also known as J_2 plasticity, results in equal yield strengths in tension and compression. Plastic yielding is assumed to be independent of the equivalent pressure stress (p) in the von Mises plasticity formulation, implying that the plastic component of deformation is incompressible. The corresponding yield criterion is defined as:

$$F = J_2 + \kappa^2 = 0 \qquad (3.41)$$

Where J_2 is the second invariant of the deviatoric stress tensor, which is already given in another form in Equation (3.18), and κ is a hardening parameter. The uniaxial yield stress of a material can be defined as $\sigma_y = \sqrt{3}\kappa$, if the material is under uniaxial stress. This leads, under substituting in Equation (3.41) the definitions of κ and J_2, to the final von Mises yield

criterion:

$$F = \frac{3}{2} S_{ij} S_{ij} - \sigma_y^2 = 0 \tag{3.42}$$

3.4 Finite Element Method

The finite element method (FEM) is a computer aided simulation method whereby the examined part is divided into a finite amount of single elements connected through nodes into a so-called finite element mesh. Under the application of physical properties (e.g. material properties, loading condition, flow conditions, temperature etc.), the behaviour of a certain body can be predicted, whereby the governing equations are calculated for each element. The first publication of the FEM arise from the early 1940s [20, 21] and the method is currently widely used in the automotive, marine and aircraft industries to conduct structural analysis under predefined boundary conditions [22].

The FEM forms a global system that describes the behaviour of the body as a whole, which determines the governing equations for each element in a mesh. The fundamental equation for the finite element approach is given by the principle of virtual work, and the principle that all work performed through all forces in the system in static equilibrium is zero, which is expressed as:

$$\int_V \delta \boldsymbol{\varepsilon}^T \boldsymbol{\sigma} dV = \int_S \delta \boldsymbol{u}^T \boldsymbol{t} dS \tag{3.43}$$

With V as the reference volume on which the equilibrium is performed and S is the surface area limiting the reference volume. $\boldsymbol{\sigma}$ is the corresponding stress vector, $\boldsymbol{t}$ the traction vector, and $\delta\boldsymbol{\varepsilon}$, $\delta\boldsymbol{u}$ are the virtual- strain and displacement vectors, respectively. Equation (3.43) is calculated for every element e of the finite element mesh, which results in following formulation for displacement and strain:

$$\delta \boldsymbol{u} = \boldsymbol{N}_e \delta \boldsymbol{u}_e \tag{3.44}$$

and

$$\delta\boldsymbol{\varepsilon} = \boldsymbol{B}_e \delta\boldsymbol{u}_e \tag{3.45}$$

where $\boldsymbol{N}_e$ is a matrix of shape function in the element e, and $\boldsymbol{u}_e$ is the nodal displacement vector of the element, and $\boldsymbol{B}_e$ is the element's gradient matrix of the shape function. By substituting Equation (3.44) and Equation (3.45) back into the principle of virtual work (Equation (3.43)) results in:

$$\sum_e \int_{V_e} \delta\boldsymbol{u}_e^T \boldsymbol{B}_e^T \boldsymbol{\sigma}(\boldsymbol{u}_e) dV = \sum_e \int_{S_e} \delta\boldsymbol{u}_e^T \boldsymbol{N}_e^T \boldsymbol{t} dS \tag{3.46}$$

where the summations are conducted over all elements in the mesh. The element values can be combined into global values, and the arbitrary virtual displacement $\delta\boldsymbol{u}_e^T$ can be eliminated. The overall expression appears as follows:

$$\int_V \widehat{\boldsymbol{B}}^T \boldsymbol{\sigma}(\boldsymbol{u}) dV - \int_S \widehat{\boldsymbol{N}}^T \boldsymbol{t} dS = 0 \tag{3.47}$$

with $\widehat{\boldsymbol{B}}^T$ as the gradient matrix of the global shape function, $\widehat{\boldsymbol{B}}^T$ the matrix of the global shape function and $\boldsymbol{u}$ represents the global nodal displacements. Since this expression indicates the equilibrium of forces in a simulation, the difference of these forces is equal to the residual force G, which is not in equilibrium:

$$\boldsymbol{G}(\boldsymbol{u}) = \int_v \widehat{\boldsymbol{B}}^T \boldsymbol{\sigma}(\boldsymbol{u}) dV - \int_S \widehat{\boldsymbol{N}}^T \boldsymbol{t} dS \tag{3.48}$$

In general, to generate a solution to a predefined continuum mechanical problem, an equilibrium stress state must be achieved so that $\boldsymbol{G}(\boldsymbol{u}) = 0$.

The finite element analysis in this thesis was all performed in the commercially available FE code Abaqus/Explicit (Dassault Systèmes Simulia Corp., RI, USA), to solve the continuum mechanics problems. An extended description is available in the Abaqus Theory Manual [15]. Within the two following sections, the fundamental background is provided on the

implicit and explicit solver. In general, while the explicit approach solves for $t + \Delta t$ based on information at time t, a fully implicit procedure indicates that the state at time $t + \Delta t$ is determined based on knowledge at time $t + \Delta t$ [18].

3.4.1 Implicit Method

The implicit solver applies displacements in increments over time steps Δt. A linked system of equations must be solved in order to calculate the new state using an implicit algorithm. Analyses, using an implicit solver, update the state of the body from time t to $t + \Delta t$. Non-linear solution algorithms, such as the Newton-Raphson method (used in the Abaqus/-Standard implicit solver), are necessary for this. Figure 3.5 depicts the basic principle of an implicit solver, which calculates consecutive approximations of a tangent function $f(x_i)$ until the solution converges to an accurate solution within a predefined tolerance. This tolerance is defined as:

$$x_{i+1} = x_i - \frac{f(x_i)}{f'(x_i)} \tag{3.49}$$

Point A in Figure 3.5 is the solution of the first iteration, which results in point A in the

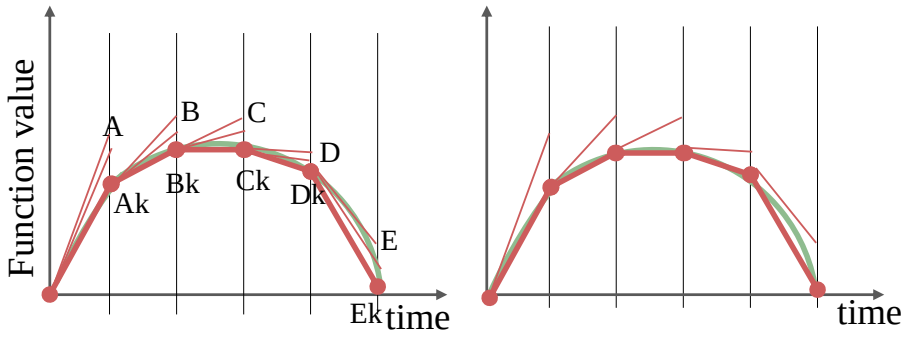

Figure 3.5: Time incrementation of the implicit (standard) solver. Green underlying curve is the analytical solution and the red curve represents the numerical solution. (adapted from [23])

graph. Then, a back calculation is performed by checking for equilibrium. From this, adapted assumptions for the matrices are used and a new iteration is performed. This corresponds

in Figure 3.5 to a solution (2nd thin red line) that is closer to the theoretical target point Ak than the first result A. This iterative process is performed again and then yields a result close to the target point Ak. If the deviation in the control is smaller than a limit value, then convergence is reached. Subsequently, the next solution step is initiated with the new load, which leads to point B (1st iteration). Again, controls and further iterations are performed until convergence is reached close to Bk.

Abaqus/Standard implicit uses the Newton-Raphson formulation for each iteration, which calculates a tangent stiffness matrix $\boldsymbol{K}$ for every i$^{\text{th}}$ iteration, which is expressed as:

$$\boldsymbol{K}\left(\boldsymbol{u}_{i+1}^{t+\Delta t}\right) = \frac{\partial \boldsymbol{G}(\boldsymbol{u}_i^{t+\Delta t})}{\partial \boldsymbol{u}} \tag{3.50}$$

These equations are solved until the magnitude of $\boldsymbol{G}(\boldsymbol{u}_i^{t+\Delta t})$ is smaller than the defined convergence tolerance. Furthermore, the tangent stiffness matrix $\boldsymbol{K}$ can be expressed through the displacements taken from Equation (3.48) (derived in Section 3.4), as follows:

$$\boldsymbol{K}(u) = \frac{\partial \boldsymbol{G}(\boldsymbol{u}}{\partial \boldsymbol{u}} = \frac{\partial}{\partial \boldsymbol{u}}\left(\int_v \widehat{\boldsymbol{B}}^T \boldsymbol{\sigma}(\boldsymbol{u}) dV - \boldsymbol{F}_{ext}\right) \tag{3.51}$$

with

$$\frac{\partial}{\partial \boldsymbol{u}}\left(\int_v \widehat{\boldsymbol{B}}^T \boldsymbol{\sigma}(\boldsymbol{u}) dV\right) = \int_V \widehat{\boldsymbol{B}}^T \frac{\partial \boldsymbol{\sigma}(\boldsymbol{u})}{\partial \boldsymbol{u}} dV \tag{3.52}$$

Multiplying Equation (3.52) with $\frac{\partial \boldsymbol{\varepsilon}}{\partial \boldsymbol{\varepsilon}}$ results in:

$$\int_V \widehat{\boldsymbol{B}}^T \frac{\partial \boldsymbol{\sigma}(\boldsymbol{u})}{\partial \boldsymbol{\varepsilon}} \frac{\partial \boldsymbol{\varepsilon}}{\partial \boldsymbol{u}} dV = \int_V \widehat{\boldsymbol{B}}^T \frac{\partial \boldsymbol{\sigma}(\boldsymbol{\varepsilon})}{\partial \boldsymbol{\varepsilon}} \widehat{\boldsymbol{B}} dV \tag{3.53}$$

under substitution the consistent tangent matrix $\boldsymbol{D}^{tan} = \frac{\partial \boldsymbol{\sigma}(\boldsymbol{\varepsilon})}{\partial \boldsymbol{\varepsilon}}$ (Jacobian of the constitutive law) the stiffness matrix $\boldsymbol{K}$ is defined as:

$$\boldsymbol{K}(\boldsymbol{u}) = \int_V \widehat{\boldsymbol{B}}^T \boldsymbol{D}^{tan} \widehat{\boldsymbol{B}} dV \tag{3.54}$$

This tangent stiffness matrix K must be solved for every iteration. Analyses with a highly nonlinear stress–strain response, or large amounts of contact between two surfaces may become extremely complicated, leading to high computational cost and, in some cases, may not achieve a converged solution. For highly non-linear problems, where convergence might be difficult to achieve, the use of explicit solver approaches may be preferred.

3.4.2 Explicit Method

The explicit method calculates the state (displacement) at the time step $t + \delta t$ and it is recommended to use this solver for dynamic analysis, or where large deformations or large amount of contact lead to highly non-linear solutions. While the main disadvantage of implicit solvers can be long execution time, for explicit solvers the equations using the tangent stiffness at the time t, and therefore require extremely small increments to avoid error propagation and ensure a robust solution. Figure 3.6 demonstrates the problem which may arise under a too large time increment. Therefore, sufficient small time increments must

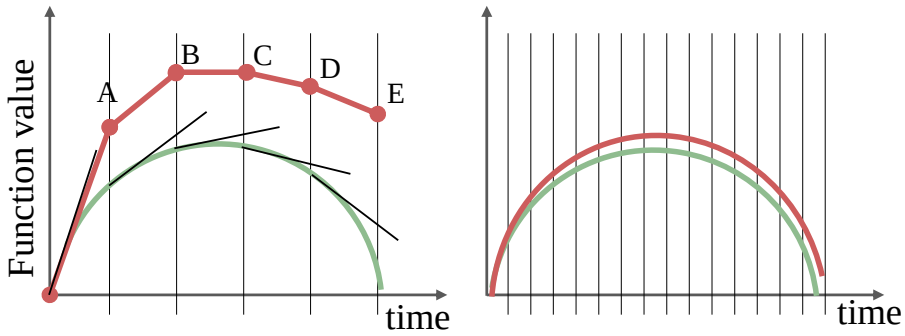

Figure 3.6: Left graph: Result for a larger time increments; right graph: Result for smaller time increments. Larger time increments result in to large errors on the solution (left). Green underlying curve is the analytical solution and the red curve represents the numerical solution. (adapted from [23])

be chosen, which follow the stability limit:

$$\Delta t \leq \frac{2}{\omega_{max}} \tag{3.55}$$

with ω_{max} as the maximum eigenvalue of the elements. This criterion practically correlates with the fact that equations can only be solved when Δt is smaller than the time which is needed for an elastic strain wave to get through the smallest element. This can be expressed as:

$$\Delta t = min \frac{L^e}{c^d} \tag{3.56}$$

with L^e as the characteristic element length and c^d the wave speed. c^d is described through

$$c^d = \sqrt{\frac{\lambda + 2\mu}{\rho}} \tag{3.57}$$

where ρ is the material density, and λ, μ are the Lamé constants.

In general, Abaqus/Explicit always calculates a dynamic equilibrium, which is simply: force = mass x acceleration. In order to solve this equilibrium for time point $t + \Delta t$, the explicit finite element solution runs under the assumption that acceleration and velocity are constant at a given time point t. It employs the central difference integration scheme, so the displacement vector $\boldsymbol{u}$ is defined as:

$$\boldsymbol{u}^{i+1} = \boldsymbol{u}^i + \Delta t^{i+1} \dot{\boldsymbol{u}}^{i+\frac{1}{2}} \tag{3.58}$$

Note that i here, is the increment number, while in Section 3.4.1 (Implicit solver) i was referred to the number of iterations, which are necessary to solve the equilibrium for one increment. The belonging velocity vector $\dot{\boldsymbol{u}}$, is expressed as:

$$\dot{\boldsymbol{u}}^{i+\frac{1}{2}} = \dot{\boldsymbol{u}}^{i-\frac{1}{2}} + \frac{\Delta t^{i+1} + \Delta t^i}{2} \ddot{\boldsymbol{u}}^i \tag{3.59}$$

with the corresponding acceleration vector $\ddot{\boldsymbol{u}}$:

$$\ddot{\boldsymbol{u}}^i = \boldsymbol{M}^{-1} \left(\boldsymbol{F}^i - \boldsymbol{I}^i \right) \tag{3.60}$$

These accelerations are first calculated for every increment, where $\boldsymbol{M}$ is the lumped mass matrix, defined as:

$$\boldsymbol{M} = \int_V \rho \boldsymbol{N} dV \tag{3.61}$$

where ρ is the material density (must be always given for explicit analysis) and $\boldsymbol{N}$ is the element shape function matrix (see Equation (3.44)).

$\boldsymbol{F}^i$ in Equation (3.60) is the vector of the externally applied forces, which are decomposed as:

$$\boldsymbol{F}^i = \int_S \boldsymbol{N}^T \boldsymbol{t}^i dS + \int_V \boldsymbol{N}^T \boldsymbol{P}^i dV \tag{3.62}$$

with $\boldsymbol{P}^i$ as the nodal force vector. The vector $\boldsymbol{I}^i$ (Equation (3.60)) is related to the internal element forces and given by:

$$\boldsymbol{I}^i = \int_V \boldsymbol{B}^T \boldsymbol{\sigma}^i dV \tag{3.63}$$

with $\boldsymbol{B}$, as the element shape function gradient matrix (see Equation (3.45)). In contrast to the global stiffness matrix in the implicit solution approach (Equation (3.54)), the lumped mass matrix (Equation (3.61)) can be easily inverted because it can be diagonalized. Consequently, the solution is more computationally inexpensive to solve for one time increment. Moreover, mass scaling is an often applied method, especially for rate independent analysis, to further reduce the solving time for explicit problems.

References

[1] R. L. Easton, *Digital Image Processing I*. September, 2010.

[2] I. Pitas and A. N. Venetsanopoulos, "Order Statistics in Digital Image Processing," *Proceedings of the IEEE*, vol. 80, no. 12, pp. 1893–1921, 1992.

[3] R. Ravikumar and A. V., "Digital Image Processing-A Quick Review," *International Journal of Intelligent Computing and Technology (IJICT)*, vol. 2, no. 2, pp. 11–19, 2019.

[4] K. D. Toennies, *Guide to Medical Image Analysis*. Springer London, 2017.

[5] R. Seetha and S. Santhosh Baboo, "Analysis of enhancement techniques for medical images," *International Journal of Control Theory and Applications*, vol. 9, no. 40, 141–147, 2016.

[6] R. H. Chan, C. W. Ho, and M. Nikolova, "Salt-and-Pepper noise removal by median-type noise detectors and detail-preserving regularization," *IEEE Trans Image Process*, vol. 14, no. 10, pp. 1479–85, 2005, ISSN: 1057-7149 (Print) 1057-7149 (Linking). DOI: 10.1109/tip.2005.852196. [Online]. Available: https://www.ncbi.nlm.nih.gov/pubmed/16238054.

[7] B. Goyal, S. Agrawal, and B. Sohi, "Noise issues prevailing in various types of medical images," *Biomedical & Pharmacology Journal*, vol. 11, no. 3, p. 1227, 2018.

[8] D. Stoyan, W. S. Kendall, S. N. Chiu, and J. Mecke, *Stochastic geometry and its applications*. John Wiley & Sons, 2013, ISBN: 1118658256.

[9] H. S. Ahmed and M. J. Nordin, "Improving diagnostic viewing of medical images using enhancement algorithms," *Journal of Computer Science*, vol. 7, no. 12, pp. 1831–1838, 2011, ISSN: 1549-3636. DOI: 10.3844/jcssp.2011.1831.1838.

[10] G. Gupta, "Algorithm for image processing using improved median filter and comparison of mean, median and improved median filter," *International Journal of Soft Computing and Engineering*, vol. 1, no. 5, pp. 304–311, 2011.

[11] D. Charalampidis, "Recursive Implementation of the Gaussian Filter Using Truncated Cosine Functions," *IEEE Transactions on Signal Processing*, vol. 64, no. 14, pp. 3554–3565, 2016, ISSN: 1053-587X 1941-0476. DOI: 10.1109/tsp.2016.2549985.

[12] R. Maini and H. Aggarwal, "Study and comparison of various image edge detection techniques," *International journal of image processing*, vol. 3, no. 1, pp. 1–11, 2009.

[13] S. Mallick, *Edge Detection Using OpenCV*, Web Page, Accessed: 24/05/2022. [Online]. Available: https://learnopencv.com/edge-detection-using-opencv/.

[14] J. Canny, "A computational approach to edge detection," *IEEE Transactions on pattern analysis and machine intelligence*, vol. PAMI-8, no. 6, pp. 679–698, 1986. DOI: 10.1109/TPAMI.1986.4767851.

[15] M. Smith, *ABAQUS/Standard User's Manual, Version 6.9*. Dassault Systèmes Simulia Corp., 2009.

[16] D. Gross, W. Hauger, W. Schnell, J. Schröder, and W. A. Wall, *Technische Mechanik 3 - Kinetik*. Springer, 2009, vol. 4.

[17] J. Lions, G. Papanicolaou, H. Fujita, and H. Keller, "Chapter 3 Elastic Materials and their Constitutive Equations," in *Mathematical Elasticity Volume I: Three-Dimensional Elasticity* (Studies in Mathematics and Its Applications), P. G. Ciarlet, Ed., Studies in Mathematics and Its Applications. Elsevier, 1988, vol. 20, pp. 89–136. DOI: /10.1016/S0168-2024(08)70060-2. [Online]. Available: www.sciencedirect.com/science/article/pii/S0168202408700602.

[18] F. J. Harewood and P. E. McHugh, "Comparison of the implicit and explicit finite element methods using crystal plasticity," *Computational Materials Science*, vol. 39, no. 2, pp. 481–494, 2007, ISSN: 09270256. DOI: 10.1016/j.commatsci.2006.08.002.

[19] J. A. Grogan, "The Mechanical Performance of Permanent and Bioabsorbable Metal Stents," Thesis, 2012.

[20] A. Hrennikoff, "Solution of problems of elasticity by the framework method," *Journal of Applied Mechanics*, vol. 8, no. 4, A169–A175, 1941, ISSN: 0021-8936. DOI: 10.1115/1.4009129. [Online]. Available: https://doi.org/10.1115/1.4009129.

[21] R. Courant, "Variational methods for the solution of problems of equilibrium and vibrations," *Lecture notes in pure and applied mathematics*, no. 49, pp. 1–23, 1943, ISSN: 0075-8469. DOI: 10.1090/S0002-9904-1943-07818-4.

[22] M. Jung and U. Langer, *Methode der finiten Elemente für Ingenieure*. Springer, 2001, ISBN: 366310785X.

[23] C. Obbink-Huizer, *Implicit vs explicit finite element analysis: when to use which?* Web Page, Accessed: 22/06/2022, 2021. [Online]. Available: https://info.simuleon.com/blog/implicit-vs-explicit-finite-element-analysis.

Chapter 4

Automated ex-situ detection of pitting corrosion and its effect on the mechanical integrity of rare earth Magnesium alloy – WE43

4.1 Introduction

Magnesium alloys show great potential as biodegradable alternatives to permanent metallic orthopaedic implants as they show an osteostimulative effect [1–6] and their mechanical properties are comparable to native bone, thereby avoiding stress-shielding, complications raised by traditional metallic implants [7]. Magnesium-based implants could eliminate the need for implant removal surgeries, thus reducing additional trauma and recovery time to the patient. However, rapid degradation behaviour has meant that magnesium-based implants have been unable to fulfil load-bearing requirements for the duration of the tissue healing process [8, 9].

Magnesium alloys undergo degradation through a range of surface-based corrosion mechanism, including galvanic, pitting and intergranular corrosion in physiological conditions [10]. Galvanic corrosion results in a protective oxide layer formation on the implant surface. The surrounding presence of chloride ions is able to break down this partly protective oxide layer, leading to an ongoing transformation of bulk material to oxide layer. A theoretical uniform corrosion is practically non-existent for light weight metal alloys, as microstructural inhomogeneities and impurities are induced during the manufacturing process. Consequently,

non-uniform corrosion phenomena such as pitting corrosion subsequently take place on the material surface [11–16]. Pitting corrosion, which describes the locally varying corrosion rate, induces high variation of mechanical integrity of medical implants, which has limited their implementation in load-bearing applications [17, 18]. Recent efforts to improve performance have sought to control the corrosion rate of magnesium by varying the alloy composition or through the application of protective surface coatings [10, 19–22]. With these, and the vast majority of other in-vitro studies of magnesium, bulk measurements of corrosion are generally considered, whereby corrosion rates are determined through techniques such as electrochemical tests [23–26], hydrogen evolution [17, 18, 21, 25, 27–31] or mass/volume loss measurements [32–34]. However, these studies provide limited information on how localised corrosion affects mechanical performance. Recent studies have quantified the non-uniform relationship between bulk mass loss and mechanical strength of both AZ31 and WE43 magnesium alloys undergoing corrosion [17, 18]. While the disproportionate reduction in load-bearing capacity of magnesium alloys, compared to corresponding mass loss, is attributed to the evolution of pitting corrosion observed across specimens, there remains little quantitative understanding on how pit formation (e.g. extent and spatial distribution) affects overall mechanical performance with other studies generally examining pitting corrosion in magnesium through largely qualitative approaches [15, 26, 35].

Pitting corrosion affects a wide range of metals and is a critical aspect of environmental degradation of components in other structural applications, including marine and aerospace. ASTM G46-94 provides the standard guide for the examination and evaluation of metals undergoing pitting corrosion [36], whereby the severity of pitting is established through metallography and visual analysis. Here, material surfaces are examined two-dimensionally and standard ratings for pitting may be expressed in terms of the pit density, pit size or pit depth. The degree of metal penetration may also be expressed in terms of a pitting factor, which is the ratio defined as the deepest surface penetration depth divided by the average depth. However, only a few studies have examined magnesium alloys using the parameters outlined

in this standard guide [15, 37] and there are still several limitations with the approaches. Firstly, there is no established methodology available that can systematically evaluate these parameters, with current techniques using cross-sectional microscopy or surface examination through profilometry to determine pitting metrics. The main disadvantage with these approaches is that they are two-dimensional and do not consider the entirety of the specimen. Furthermore, they require destructive processing, and a major difficulty is that material will be actually removed by polishing and cannot be analysed [38]. Secondly, there is little or no quantitative understanding as to how pit density, pit size, pit depth and/or pitting factor relate to the mechanical integrity of the specimen. To advance the current understanding of pitting corrosion, it is critical that standardised detection methods are established to measure key pitting parameters and their effect on the load-bearing integrity of structure, determined through concurrent mechanical testing. To date, only a limited number of studies have proposed methods to automatically track pitting corrosion in metals, but these have never been applied to magnesium [39–42].

The objective of this study is to develop a three-dimensional automated detection framework that systematically evaluates the severity and phenomenology of corrosion and relationships between key pitting parameters and mechanical performance are established. This detection framework (from now on called *PitScan*) uses a Python-based algorithm to analyse microcomputer-tomography scans (µCT) of cylindrical specimens undergoing corrosion. The approach systematically identifies several pitting features on the corroding surface, enabling full geometric characterisation of pitting parameters, including pit density, pit size, pit depth and pitting factor. Within this study, *pitting corrosion* as a term unifies all localised surfaced-based corrosion effects like pitting and intergranular corrosion [10].

4.2 Materials and Methods

Cylindrical dog-bone test specimens were produced from a chill-casted and extruded magnesium WE43MEO alloy that had a nominal composition of 1.4 - 4.2 % Y, 2.5 - 3.5 % Nd, < 1 % (Al, Fe, Cu, Ni, Mn, Zn, Zr) and balance Mg (in wt %) (Meotec GmbH, Germany). The cast material underwent an extrusion process to form 6.5 mm rods, which was followed by a turning process that produced cylindrical dog-bone samples whose dimensions are shown in Figure 4.1 (a). Inductively coupled plasma atomic emission spectroscopy (ISC-OES) measurements confirmed the chemical composition according to the manufacture's specification. Immersion testing was performed for 28 days to induce pitting-based corrosion in the sample, as shown in Figure 4.1 (b). At weekly time-points, micro-computed tomography (µCT) scanning and mechanical testing of corroded samples were carried out. Correlations were established between mechanical performance and the geometrical pit formation using a novel pit detection algorithm that describes the pit formation of the corroding magnesium rods.

4.2.1 Immersion testing

Immersion testing followed a similar protocol to that described by Kopp et al. [21] and is represented schematically in Figure 4.1 (c). Samples were placed in the bottle by mounting them under a silicone funnel that was fixed to the glass burette. Bottles were placed on a magnetic stirrer to ensure a homogenous pH level in the solution. Here, a conventional simulated body fluid (c-SBF) was used [43], whose composition is provided in Table 4.1. Each bottle was filled with 600 ml, which leads to a volume to sample surface ratio (V/S) of 3.36 mL/mm^2, which is more than 10 times greater than the ratio suggested in the standard (minimum of 0.20 mL/mm^2) [44]. Clamping areas were protected with chemically inert polyolefin shrinking hose to ensure that these areas are not degrading.

Table 4.1 Chemical compositions of c-SBF in one litre pure water [43]

Reagents	in 1 litre
NaCl	8.035 g
$NaHCO_3$	0.355 g
KCl	0.225 g
K_2HPO_4	0.176 g
$MgCl_2$	0.145 g
$CaCl_2$	0.292 g
Na_2SO_4	0.072 g
Tris buffer pH 7.5 (1 mol/L)	50 ml

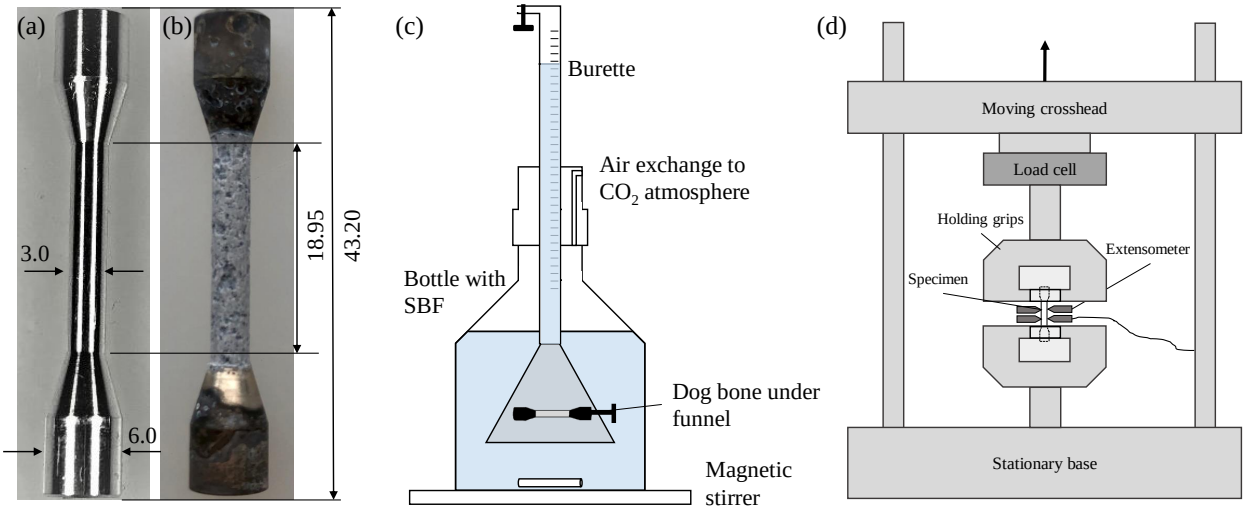

Figure 4.1: Dimensions of the magnesium WE43 test specimens that were turned from a 6.5 mm cylindrical rod a) undegraded sample and b) following 14 days immersion; c) Schematic overview of immersion test setup [21]; d) Schematic overview of tensile test.

Separate sample groups were immersed for periods of 7, 14, 21 and 28 days, with n = 3 per group. Tests were carried out in a humidified incubator (HERAcell 150i, Thermo Fischer Scientific Inc., Waltham, USA) at 37 ± 1 °C, under an atmosphere with 5 % CO_2. Hydrogen gas measurement is a widely used method for tracking mass loss for magnesium and its alloys in in-vitro immersion test setups [45]. The evolved hydrogen gas (H_2) was captured in the burette and tracked by an eudiometer. Mass loss (ML) was derived from hydrogen gas evolution based on the cathodic reaction equation describing the corrosion process [45], given by:

$$2H_2O + 2e^- \rightarrow 2OH^- + H_2 \tag{4.1}$$

The corresponding anodic reaction of magnesium corrosion is

$$\mathrm{Mg} \rightarrow \mathrm{Mg}^{2}+ + 2\mathrm{e}^{-} \tag{4.2}$$

So the overall reaction is described by

$$\mathrm{Mg} + 2\mathrm{H_2O} \rightarrow \mathrm{Mg(OH)_2} + \mathrm{H_2} \tag{4.3}$$

The degradation layer (passive layer) mostly consists of magnesium hydroxide ($\mathrm{Mg(OH)_2}$). In the presence of chloride ions, like in body fluids, this layer can be destroyed by the formation of magnesium chloride

$$\mathrm{Mg(OH)_2} + 2\mathrm{Cl}^{-} \rightarrow \mathrm{Mg(Cl)_2} + 2\mathrm{OH}^{-} \tag{4.4}$$

Because magnesium chloride has a greater solubility in water, local corrosion (pitting) occurs in these areas [46]. Additionally, the corrosion rate can be calculated as described in ASTM G31-12a [44], according to the following equation that represents corrosion rate in mm/year:

$$CR = \frac{8.76 \cdot 10^{4} W}{At\rho} = \frac{8.76 \cdot 10^{4} V_{H_2} \rho_{H_2}}{At\rho_{Mg}} \tag{4.5}$$

where V_{H_2} is the hydrogen gas volume in mL and ρ is the density in g/cm^3. M is the molecular weight in g/mol, A is the exposed surface area in cm^2, and t is the overall immersion time in hours. After removal from the c-SBF immersion media, samples were immediately dried to ensure the corrosion process had stopped. Then pH of each solution media was measured with a pH meter (Sartorius PB-11, Satorius AG, Göttingen, Germany).

4.2.2 Micro computed tomography

Following sample immersion, µCT scans of all dog bone specimens were performed (Skyscan 1272, Bruker, Belgium). Samples were scanned with X-ray emission parameters of 100 kV and 100 µA, which provided a pixel size of 15 µm and enabled segmentation of both the inner magnesium core and the degradation layer of each cylindrical sample. This resolution also means that localised corrosion under 15 µm remains undetected. The work here focuses on the magnesium core, as it is assumed that the degradation layer does not contribute to the load-bearing capacity of the specimen. Imalytics Preclinical Software (Gremse-IT GmbH, Germany) [47] in combination with ImageJ (version 1.52, Wayne Rasband, National Institutes of Health, Bethesda, MD, USA) was used to generate binary images of the inner magnesium core, with the process shown schematically in Figure 4.2 (a). Firstly, a Gaussian filter was applied to the raw input stack and the inner magnesium core was identified by manually adjusting the threshold for the brighter part of the specimen. With Imalytics software, the total volume of the remaining core was calculated and the corresponding volume loss (VL) of the gauge length of each dog-bone specimen was determined. With Equation (4.5) the corrosion rate was determined, and the weight loss was calculated with $W = \Delta V L_{Mg} \rho_{Mg}$. Subsequently, the segmentation file was imported into ImageJ to receive the single cross-section images from the stack, with the inner core existing only of white pixels and the remaining part of black ones (binarization).

4.2.3 Mechanical testing

Following micro-CT scanning, uniaxial tensile testing of the cylindrical dog bone specimens was carried out at a constant velocity of 1.0 mm/min until failure (10 kN load cell, ZwickRoell GmbH & Co. KG, Germany). Displacement of the gauge length was tracked through extensometers (makroXtens, ZwickRoell GmbH & Co. KG, Germany) attached at the sur-

face (see Figure 4.1 (d)). In all cases, the initial cross-section area of the gauge section ($A = \pi r^2 = \pi 1.5^2\,\mathrm{mm}^2 = 7.07\,\mathrm{mm}^2$) was used to determine the nominal stress.

4.2.4 Pit detection

The algorithms developed within this study for *PitScan*, enable a standardised detection of the three-dimensional degradation formation in the cylindrical magnesium specimens through automated image recognition of micro-CT scans. *PitScan* analyses a stack of two-dimensional images of the material cross-section, derived from the micro-CT scan, within an automated process chain of image recognition implemented in Python with OpenCV. *PitScan* uses the binary images of the solid inner magnesium core and starts with radial contouring of this core, with a subsequent pit detection. All this is individually implemented for each layer, and then a three-dimensional reconstruction of the pitting formation is performed. Firstly, radial contouring of each binary image is carried out. The complete tracking is fundamentally based on the correct definition of the initial (before degradation) centre point of the sample. To exclude the influence of slightly oblique positioned samples in the scanner, the first and the last image are taken to generate a linear correction equation (see Figure 4.2 (b)). These two images are processed by the following steps: First, the outer contour is detected (see Figure 4.2 (c)ii). Then a circle is fitted around this contour, which gives the coordinates of the centre points. Consequently, two points are identified $P_1 = (x_1|y_1)$ and $P_2 = (x_2|y_2)$. From these two points, a linear equation is computed. To get the centre points of every single image, the step size s for calculating the x-coordinates is defined by:

$$s = \frac{x_2 - x_1}{amountofimages} \tag{4.6}$$

So x_i can be calculated by

$$x_i = x_1 + (i \cdot s) \tag{4.7}$$

The corresponding y-coordinates are calculated by

$$y_i = (x_i \cdot m) + n. \tag{4.8}$$

After the centre point generation, every image runs through the same process chain, depicted in Figure 4.2 (c). First, a pit tracking in 2D of the images takes place. The process starts with the contour detection of the raw black and white image. Second, a circle is fitted with the radius as the greatest distance from the previous calculated centre point to the contour. In a subsequent step, the fitted radius is reduced to avoid tiny sharp edges having any influence on the fitted radius. Hence, a smoothing takes place and the radius is decreased until a material ratio of 20 % is reached (Figure 4.2 (c)iv) [48]. It indicates the ratio of the circumference of the decreased radius around the contour to the intersections with the contour. This radius r_1 will be considered for the calculation of the radius loss (r_1/r_0) in every cross-section, respectively. It is assumed that r_1 is related to the uniform degradation, which needs to be subtracted to identify pits. In this study r_0 is always 1500 µm which is the initial gauge length radius of the tensile test specimen. With this radius, the radial distances to the contour are tracked for every two degrees circumferentially (Figure 4.2 (c)v). All these values are stored in a one-dimensional array: $\boldsymbol{d_i}$ (with $i \in \{j \leftarrow \mathbb{N} \big| j \leq 180\}$) that allows the start and end points of an individual pit to be tracked. Full details of this process are described in Algorithm 1. The output array is $\boldsymbol{P}$, where 1 corresponds to a pit, 0 to no pit. As mentioned, this process automatically runs through all cross-section images (or layers), while the output is stored in one combined array: $\boldsymbol{A}$ (with the number of rows corresponding to the total number of cross-section images). Every row has the following information: (i) Array $\boldsymbol{d}$ distance from fitted radius to contour every 2 degrees; (ii) Array $\boldsymbol{P}$: Pit on ($P_i = 1$) Pit off ($P_i = 0$) value for every 2$^{\text{nd}}$ degree and (iii) Fitted radius r_1. The tracking in three-dimensions is based on checking whether there are pits at the same range of degrees layer-by-layer. If there is a pit at the same location in two images next to each other, the algorithm will "bond"

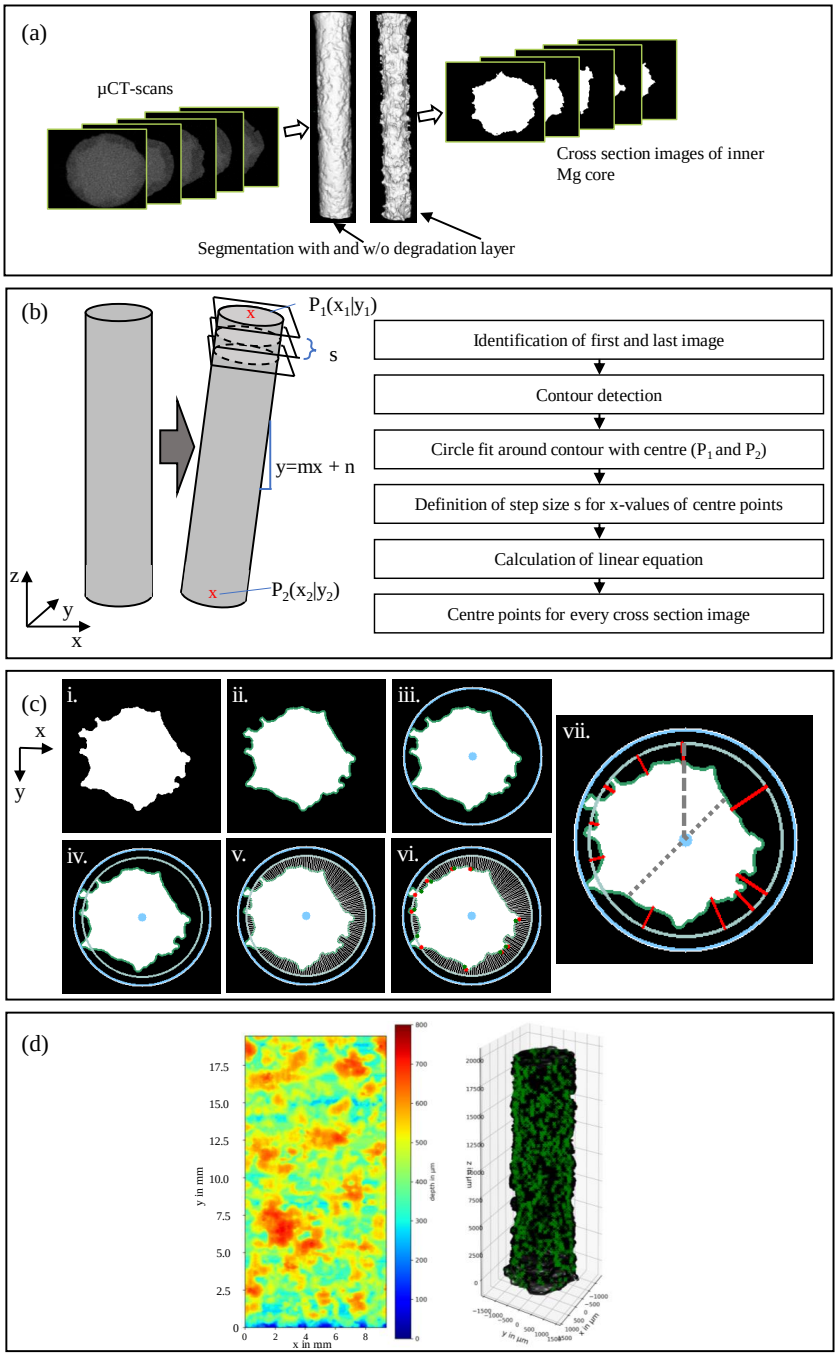

Figure 4.2: Basic principle of *PitScan* (a) from µCT cross-section images to the segmentation of inner Mg core to black and white cross-section images of Mg core; (b) Basic principle of the correction function to correct oblique positions during the scanning procedure. Left: perfect straight sample; middle: Oblique positioned sample; Right: description of basic algorithm of the centre point detection chain (c) Automated image recognition process chain i. Raw input, ii. Contour detection, iii. Circle plotting, iv. Material portion, v. Depth tracking, vi. Pit on-off tracking, vii. Determination of deepest point of each pit. Grey dashed line fitted radius, grey dotted line minimum Mg core width; (d) Output images: left: Heatplot of the surface of the cylinder, right: total 3D reconstruction of the gauge length, every green cross marks the deepest point of one pit.

Require: r_1: perfect radius, **d**: distance contour to r_1
Ensure: Pit on/off values in 2D **P**
  $i \leftarrow range(0, 180)$
  for $k \leftarrow 1$ to y **do**
    if $r_1 - d_i < 0.98 * r_1$ **then**
      $Pit_{on} \leftarrow true$
      $P_i = 1$
    else
      if $Pit_{on} = true$ and $((r_1 - d_i) > 0.98 r_1$ or $(1.1d_i < d_{i-1}$ and $1.1d_i < d_{i-2}$ and $d_i < d_{i+1}$ and $d_i < d_{i+2})$ or $(d_i < d_{i-1}$ and $d_i < d_{i-2}$ and $1.1d_i < d_{i+1}$ and $1.1d_i < d_{i+2}))$ **then**
        $Pit_{on} \leftarrow false$
      end if
      if $Pit_{on} = true$ **then**
        $P_i \leftarrow 1$
      end if
    end if
    return P
  end for

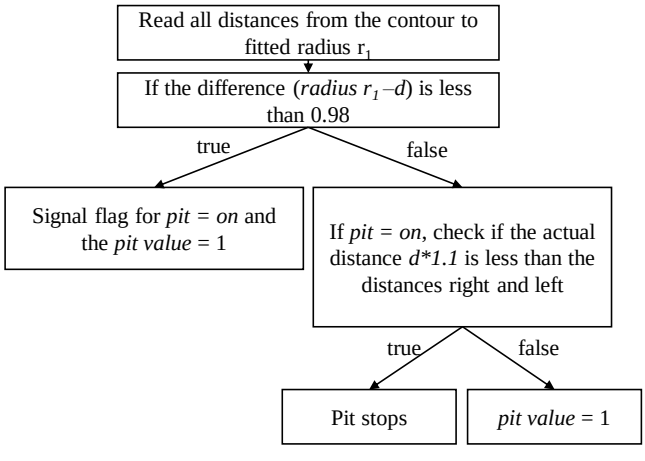

Algorithm 1: Pit on off definition.

those two as one pit and checks in the next layer to determine if there is also a pit at the same range of degrees, and so on. One main achievement of this process is that the deepest point of a pit can be identified for each 3D pit, with its exact position. This principle is further described in Algorithm 2. As input, the array $\boldsymbol{B}$ is taken. $\boldsymbol{B}$ is generated from $\boldsymbol{A}$, where every row belongs to one pit ($P_i = 1$, with no interruption) with the following information: (i) The layer of the pit; (ii) Range of degrees; and (iii) Distance contour to r_1. Only pits with a maximum depth greater than 50 µm are considered as a pit. The algorithm provides the following outputs. Firstly, two images are generated: A surface contour plot of pit depth around the cylindrical gauge length (Figure 4.2 (d) left); and a total three-dimensional reconstruction of the specimen where every green cross marks the deepest point of one tracked pit (Figure 4.2 (d) right). Second, several characteristic parameters are calculated to get a fully quantified description of the pit formation. All tested dog bone specimens were analysed by this method (described in detail in Section 4.2.5). Verification of the detection process was conducted by considering manual measurements across one specimen from each time point. For each one, radial measurements were taken using ImageJ in 2.5 mm distance increments along the longitudinal and radial axis (initial radius to the interface – degradation layer – Mg core) and were compared with the corresponding generated 3D contour plots. This analysis did not show any discrepancies between manual and automated measurements. These results

Require: **B**, x
Ensure: Bonding 2D pits to 3D pits by assignment of numbers (Pit_{no})

```
Pit_no = 0
y = length(B)
for k ← 1 to y do
    Pit_inital ← B_k5
    stopdegree ← False
    if Pit_inital = 0 then
        Pit_no ← Pit_no + 1
        layer ← B_k0
        degrees ← B_k1
        layer_above ← layer + 1
        B_k5 = Pit_no
    end if
    while stopdegree = False do
        for i ← 1 to y do
            if B_i0 = layer_above then
                potential_degrees ← B_i1
                overlay_nb ← B_i5
                stop ← False
                for deg in degrees do
                    if deg in potential_degrees and stop = False then
                        stop ← True
                        layer_above ← layer_above + 1
                        degrees ← potential_degrees
                        if B_i5 = 0 then
                            B_i5 = Pit_no
                        else
                            B_i5 = (Pit_no, Overlay_nb)
                        end if
                    else
                        stopdegree = True
                    end if
                end for
            end if
        end for
    end while
end for
return B
```

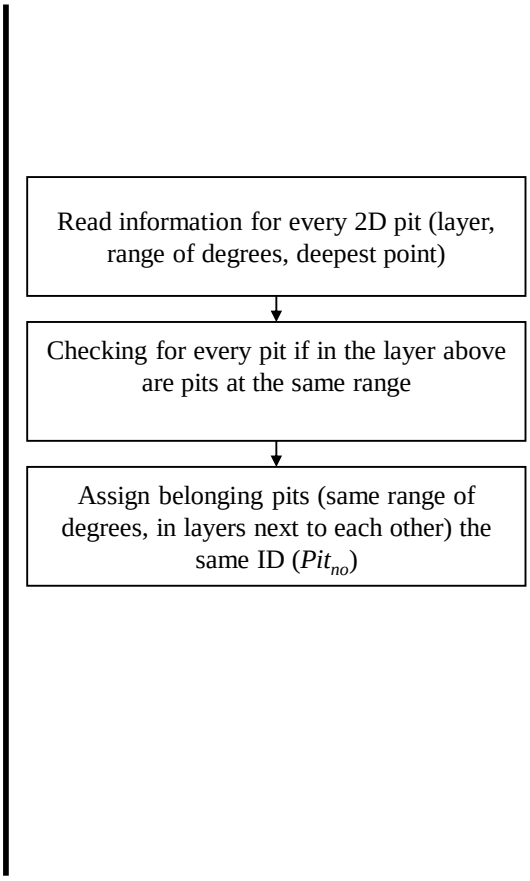

Algorithm 2: Pit tracking in 3D running through the entities of $\boldsymbol{P}$.

may be found in the Appendix A.

4.2.5 Regression fitting

Subsequent to the three-dimensional analysis, several geometric parameters describing pit formation are directly calculated by the pit detection tool. Table 4.2 outlines all parameters that are calculated, along with a detailed description. For samples undergoing corrosion, correlation between each of these geometric parameters and the residual maximum tensile strength of the specimen were determined by fitting both linear ($y = mx+n$) and exponential

Table 4.2 Detailed description of generated geometrical parameters within the pit detection tool (d: single pit depth, i: number of cross-section images, r: fitted radius, r_0 initial radius).

Parameter	Symbol	Description
Mass loss H_2 (%)	ML	Mass loss generated by hydrogen evolution during immersion testing
Volume loss from μCT (%)	VL	Volume loss calculated in Imalytics software from μCT scans
No pits	n	Total number of pits
Pits per cm^2	$\bar{n}$	Tracked pits per cm^2 (with the average fitted radius)
Volume loss through pits (%)	VL_{pits}	Sums up only the volumes of the real pits ($d > 50\mu m$)
Av. Radius loss	$\overline{RL}$	Average of all fitted radii for every layer: $\overline{RL} = \frac{\sum_0^{x=i} 1-(r_x/r_0)}{i}$
Radius loss Standard Deviation (std)	s_{RL}	$s_{RL} = \frac{\sum_0^{x=i}(1-r_x/r_0-\overline{RL})}{i-1}$
Pitting Factor [36]	PF	$PF = \frac{\text{deepest metal penetration}}{\text{average metal penetration}}$
Max. pit depth μm	d_{max}	Maximum depth of all detected pits: $max(d_x)$
Av. of ten deepest pits (μm)	$\bar{d}_10$	$\bar{d}_10 = \frac{\sum_0^{x=10} d_x}{10}$
Av. pit depth (μm)	$\bar{d}$	$\bar{d} = \frac{\sum_0^{x=n} d_x}{n}$
Pit depth Standard Deviation (std) (μm)	$s_{\bar{d}}$	$s_{\bar{d}} = \frac{\sum_0^{x=n}(d_x-\bar{d})^2}{n-1}$
Av. pit opening (μm^2)	$\bar{o}$	This is the average pit opening area of all detected pits: $\bar{o} = \frac{\sum_0^{x=n} o_x}{n}$
Pit opening Standard Deviation (std) (μm^2)	$s_{\bar{o}}$	$s_{\bar{o}} = \frac{\sum_0^{x=n}(o_x-\bar{o})^2}{n-1}$
Av. volume pit (μm^3)	$\bar{v}$	Average volume of all detected pits: $\bar{v} = \frac{\sum_0^{x=n} v_x}{n}$
Volume pit Standard Deviation (std) (μm^3)	$s_{\bar{v}}$	$s_{\bar{v}} = \frac{\sum_0^{x=n}(v_x-\bar{v})^2}{n-1}$
Minimum fitted radius	r_{min}	The minimum of all fitted radii in every cross section (Figure 4.2 (c,vii), exemplarily for one layer dashed line): $min(r_x)$
Minimum Mg core width	d_{min}	Minimum of all detected magnesium core widths (Figure 4.2 (c,vii), exemplarily for one layer dotted line): $min(d_{Mg})$

functions ($y = a \cdot e^{bx}$), with the coefficient of determination calculated for each fit.

4.3 Results

4.3.1 Immersion testing

Figure 4.3 (a) shows hydrogen evolution (left axis) of the magnesium specimens over the 28-day immersion period. The corresponding mass loss of the specimens is also shown in

Figure 4.3 (a) (secondary y-axis). In general, the hydrogen evolution (or mass loss) rate was greatest in the first day following immersion, with the rate flattening up to day five, after which there was a secondary increase. This phenomenon can be attributed to the breakage of the protective magnesium oxide layer. The measured pH value showed only slight pH increases during the study, increasing from 7.4 ± 0.15 at day zero over 7.43 ± 0.005 after seven days, to 7.6 ± 0.04 at day 21. Within the next week, no further increase was observed, and the standard deviation even decreased. Ng et al. showed that even a pH of 8 leads to a similar hydrogen evolution response during in-vitro testing, so the measurements are valid [49].

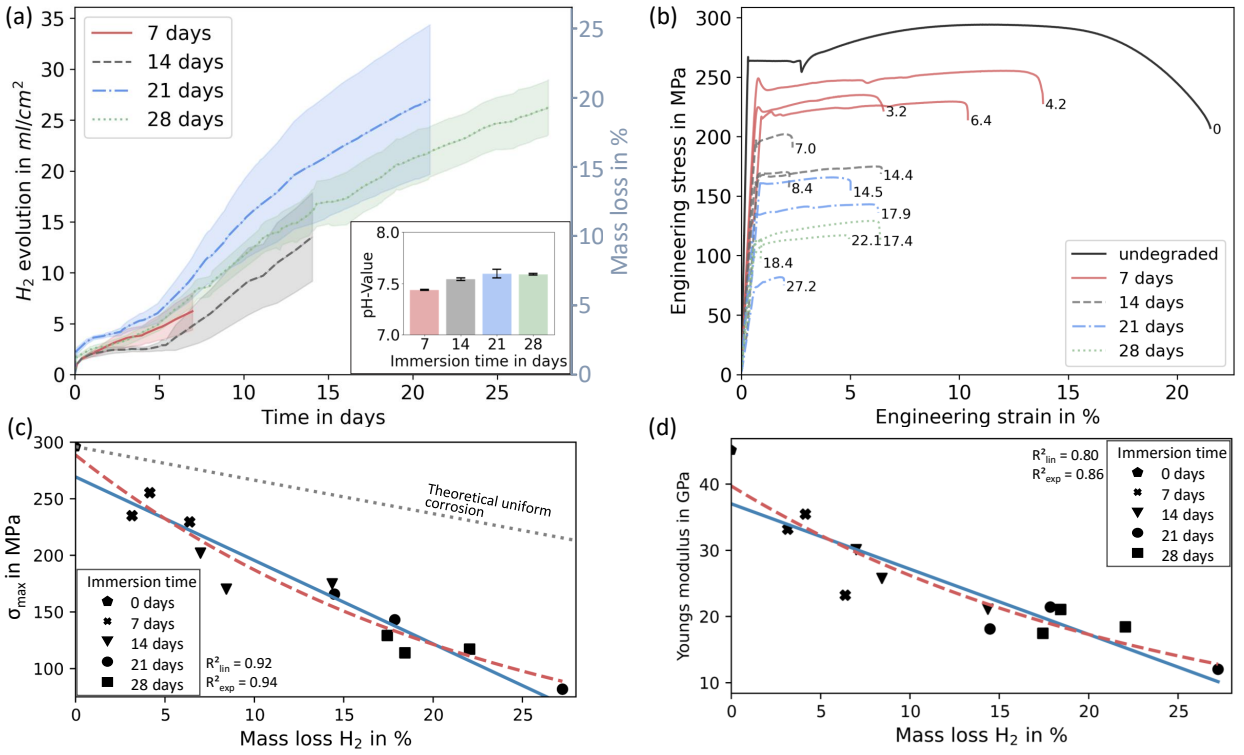

Figure 4.3: (a) Mean measured hydrogen gas evolution during immersion testing in c-SBF over time. pH values of the solution with standard deviation after immersion; (b) Tensile test data of every test specimen after specified immersion time. Number after curves is the measured mass loss calculated from hydrogen evolution. (c) Specimen strength ($\sigma_{\max}$) plotted against mass loss (blue solid line: linear fit, red dashed line: exponential fit, grey dotted line: theoretical uniform corrosion; p-values ¡ 0.05) (d) Young's modulus plotted against mass loss (blue solid line: linear fit, red dashed line: exponential fit, p-values ¡ 0.05).

4.3.2 Tensile testing

Figure 4.3 (b) shows the uniaxial stress strain response from each WE43 dog bone specimen (corresponding mass loss plotted at the end of every curve). These results show decreasing mechanical performance as maximum stress, yield strength and strain-to-failure of the samples are reduced as corrosion progresses. Interestingly, this magnesium alloy displays a distinct upper and lower yield point, with substantial yield elongation, likely a result of a Lüders front forming in the alloy under tension [50]. Here, engineering stress was used to emphasize the impact of corrosion. True stress would not exhibit such a significant difference, as it considers the current minimal cross-sectional area, thereby neglecting the effects of corrosion on the stress measurements. Additionally, the stress-strain response depicted in Figure 4.3 (b) shows that as corrosion progresses, there is a transition from a ductile failure mode to a slightly more brittle behaviour. Plotting maximum specimen strength ($\sigma_{\max}$) as a function of mass loss in Figure 4.3 (c), an exponential and linear fit is possible, but the mechanical integrity of the specimens is substantially reduced. For example, at approximately 15 % mass loss, the strength has reduced by approximately 50 %. To underline the disproportionate relationship, the theoretical uniform corrosion behaviour is included in the figure (dotted grey line). Theoretical uniform corrosion is derived from the assumption that with a material loss of 50 % the remaining specimen strength is 50 % from the initial strength. Figure 4.3 (d) shows the reduction of the stiffness with increasing mass loss, including the linear and exponential fits.

4.3.3 Micro computed tomography

Figure 4.4 shows the processing of one dog bone sample, after 14 days immersion time. Segmentation of the inner magnesium core and outer degradation layer was determined using Imalytics. Figure 4.5 (a) shows the correlation between the mass loss from hydrogen

evolution and volume loss determined through µCT. Figure 4.5 (b) shows the yearly corrosion rate calculated through ASTM G31-12a [44], using both methods, with the rate determined through volume loss being three-fold higher than the rate calculated from the hydrogen measurement method.

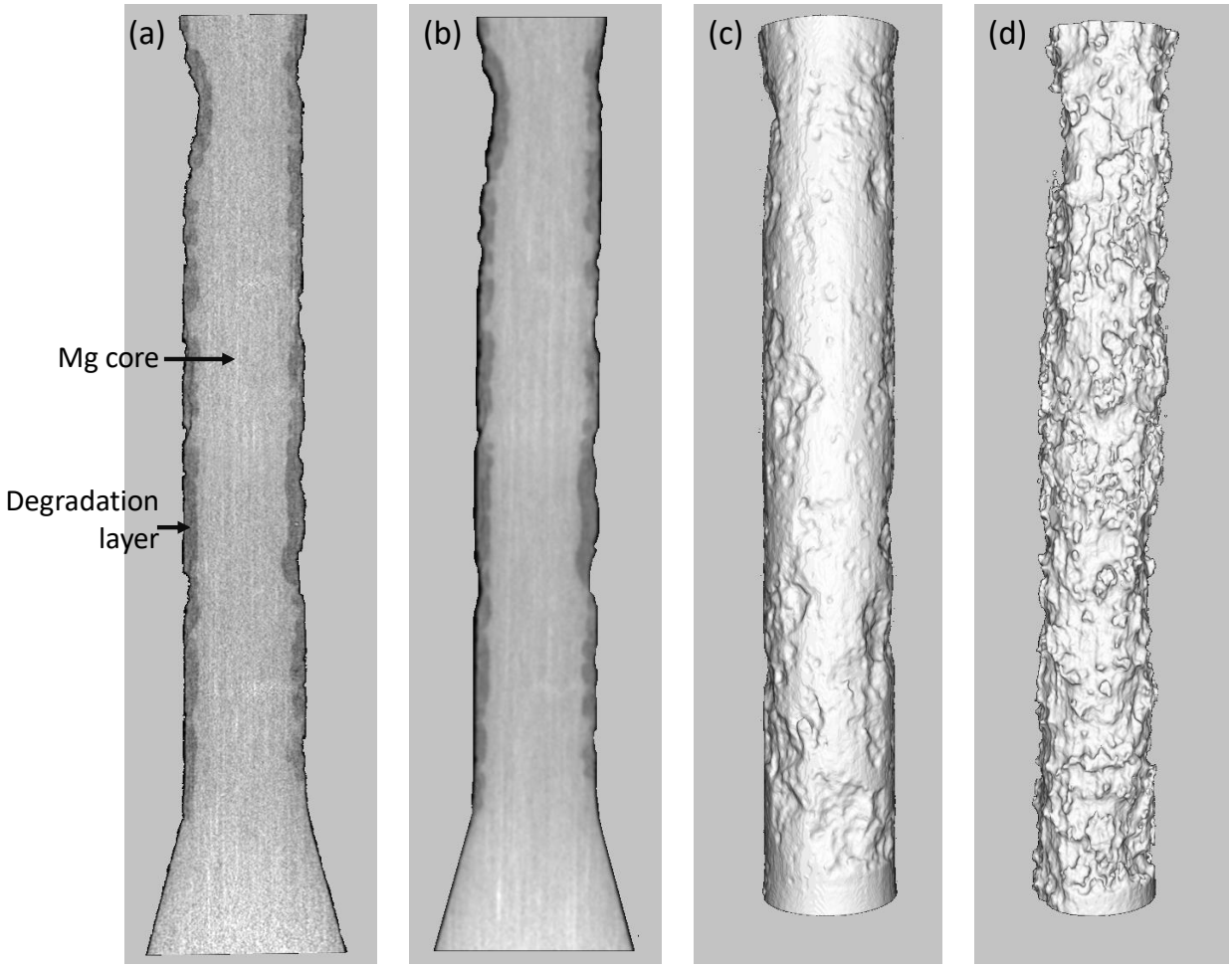

Figure 4.4: µCT scan process chain of a 14 days immersed dog bone in SBF (a) raw input cross-section, darker area degradation layer, lighter area inner magnesium core (b) Gaussian filter stddev = 2.0 pixel (standard deviation of the Gaussian distribution) (c) Segmentation of the complete gauge length of dog bone (d) segmentation of inner magnesium core only.

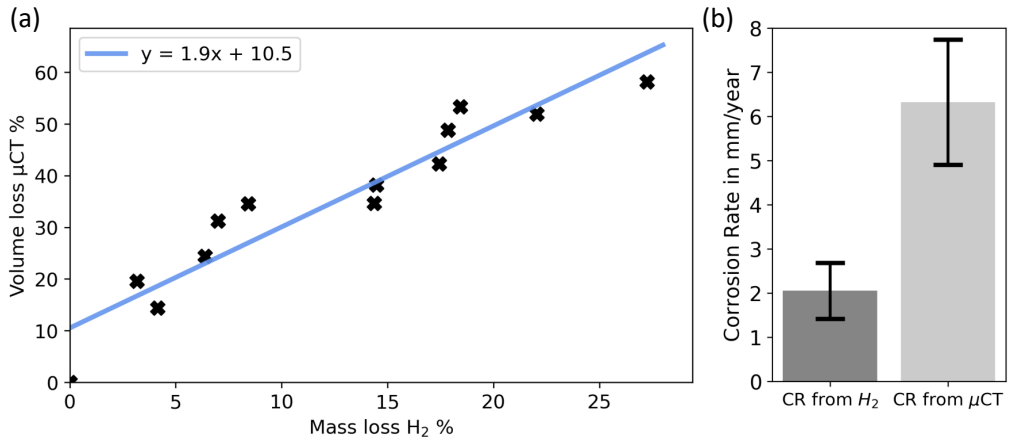

Figure 4.5: (a) Correlation: measured volume loss of µCT scans to the calculated mass loss from hydrogen evolution; (b) Mean corrosion rate (CR) calculated from hydrogen evolution and evaluation of µCT-scans.

4.3.4 Pit detection

PitScan provides a three-dimensional reconstruction of the processed µCT scans, along the entire gauge length of the dog bone specimens. Figure 4.6 shows contour plots which describe the spatial distribution of pit depth on the (flattened) surface of the gauge section of each cylindrical specimen. Here, the contour represents the radial distance from the surface of the Mg core to the initial radius of the gauge section. Figure 4.7 shows the probability distribution of pit depths (calculated by Algorithm 2) for each specimen. While Figure 4.6 shows the total depth, which is the loss of material from the original surface, Figure 4.7 shows the quantity of the actual pit depth compared to the current corroding surface (e.g. uniform corrosion was subtracted). At day 7, pit depths up to 400 µm are measured and there is a general increase in pit depth over time. At day 21, there is substantial localised material loss visible in certain specimens. By day 28, pit depths of over 800 µm are visible in each examined specimen and there is a general flattening of the pitting distribution visible (Figure 4.7 (d)), which suggest that many smaller pits develop first and these coalesce in deeper and wider pits over time.

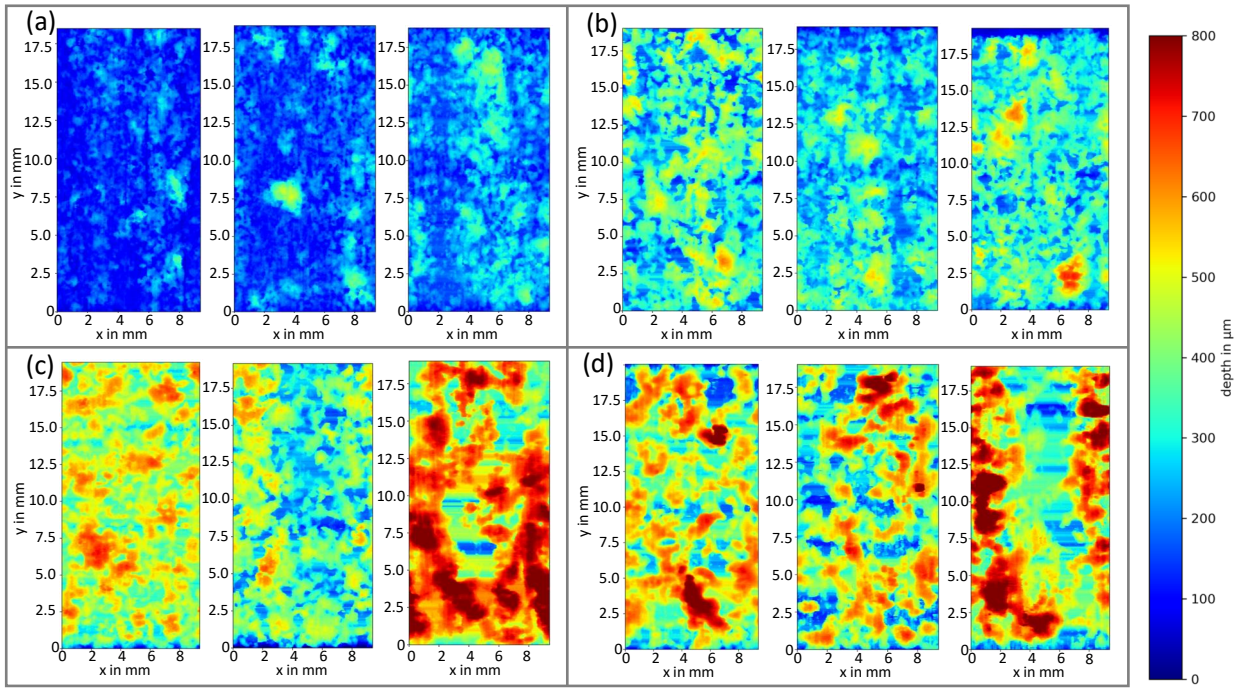

Figure 4.6: Heat plot of the measured distance from the initial radius to the surface of the magnesium core of every tested dog bone; a) 7 days; b) 14 days; c) 21 days; d) 28 days.

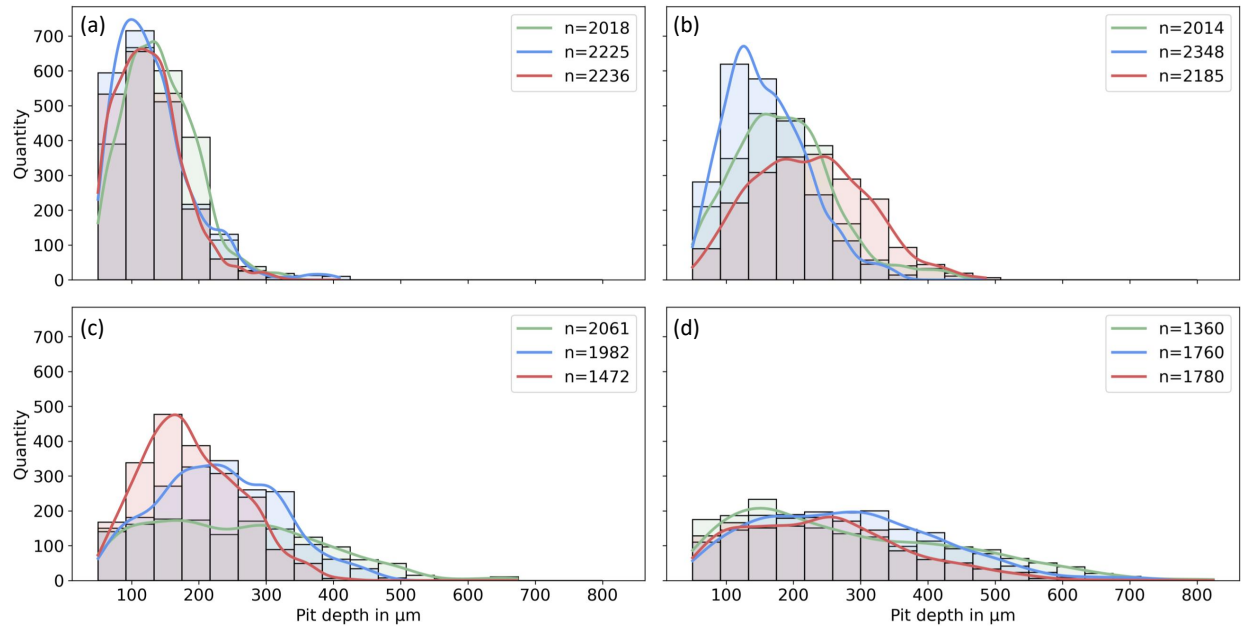

Figure 4.7: Pit depth distribution for every tested sample with n the total number of detected pits (a) 7 days; (b) 14 day; (c) 21 days; (d) 28 days.

4.3.5 Regression fitting

The main advantage of the developed method is the automatic and systematic generation of different geometrical parameters, which describe the phenomenology of pitting formation. Figure 4.8 presents correlations of a range of geometric parameters that describe pitting corrosion to the residual specimen strength of the samples. Here, Figure 4.8 (a) shows again a disproportionality between the detected volume loss through micro-CT scanning and $\sigma_{\max}$. This relation is also tracked with the detected mass loss through the hydrogen gas measurement (Figure 4.3 (c)). But since the volume loss measurements are higher than mass loss, the disproportionality is not that severe. Further, a linear and exponential correlation is visible ($R^2_{lin} = 0.96$ and $R^2_{exp} = 0.95$). The parameters described in ASTM G46-94 [36] are included in the examination matrix (Figure 4.8 (b-h)). The lowest correlation to the sample strength was found for pitting factor (Figure 4.8 (b)). Here, the coefficient of determination for the linear and exponential fits are lower than 0.04. The generated pitting values vary from 2.1 to 3.2, but no systematic correlation was evident. Surprisingly, it was found that the strength was higher with increasing number of pits and pit density (Figure 4.8 (e, f)). This relationship underlines the tracked behaviour of the pit formation in Figure 4.7, showing initial high values of single pits, which merge over time to form bigger and deeper pits. Looking at the two pit features regarding pit depth, suggested in the standard (max. pit depth and the average of the ten deepest pits), trends of a linear or exponential correlation can be found (Figure 4.8 (c, d)). Though, the average pit depth and the average opening area of a pit with the associated standard deviations show slightly better results (R^2 between 0.72 and 0.83) (Figure 4.8 (g-j)). The highest correlating pit features (both linear and exponential) are the parameters that are directly linked to the reduction of the cross-sectional area (Figure 4.8 (l, m, p-r))

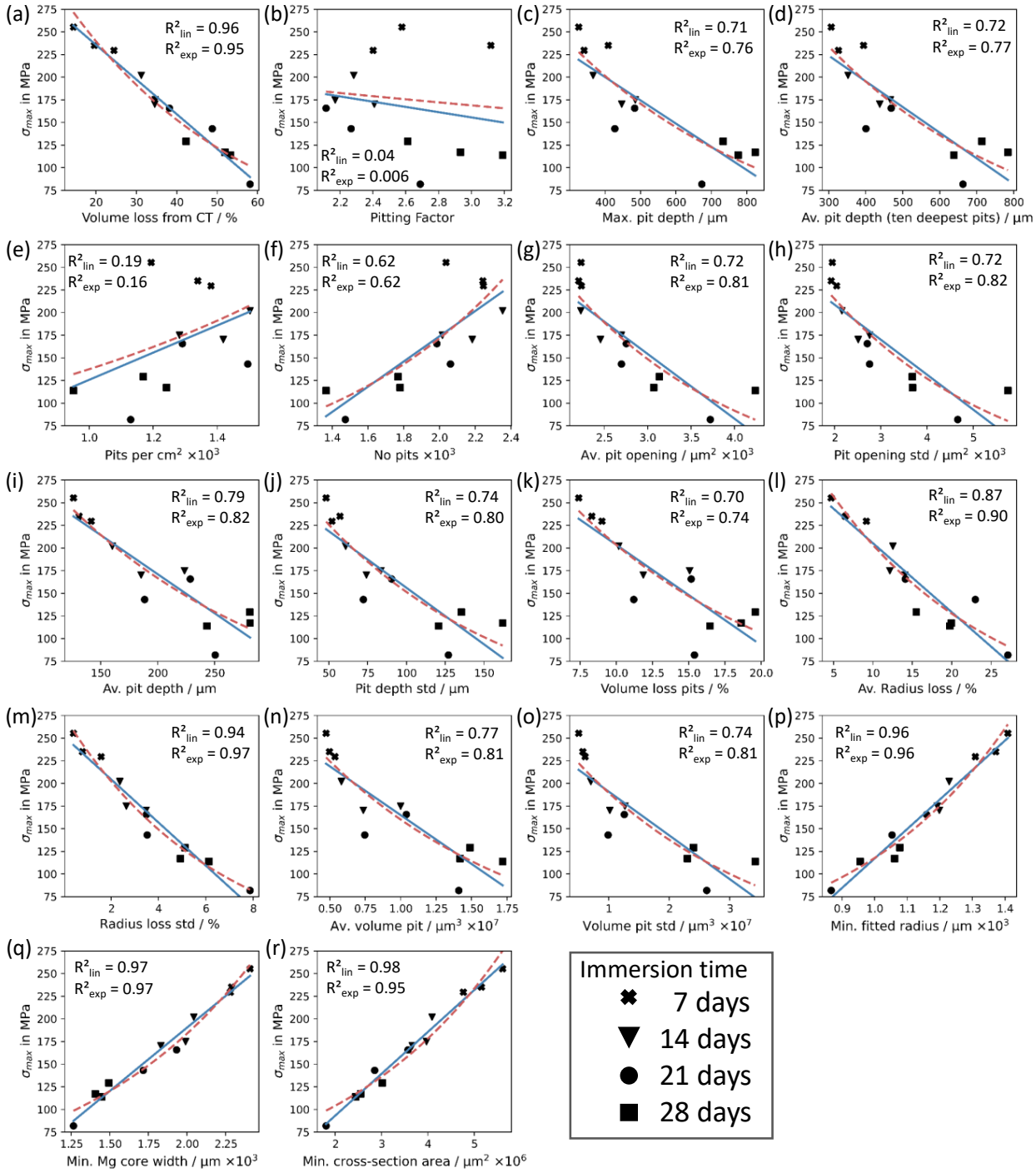

Figure 4.8: Correlation of 18 pitting features vs. max. specimen strength ($\sigma_{\max}$) (a-r); blue solid line: linear correlation, red dashed line: exponential correlation; p-values ¡ 0.05 except for (b) pitting factor, (e) Pits per cm^2.

4.4 Discussion

In this study, a three-dimensional automated detection framework that systematically evaluates the extent and phenomenology of pitting corrosion was developed. This approach used a Python-based algorithm that automatically computed geometric features of pitting from micro-CT scans of cylindrical shape specimens undergoing corrosion. Furthermore, this framework automatically outputs standardised parameters of pitting corrosion on the specimen surface, including pit density, pit size, pit depth, and pitting factor (ASTM G46-94 [36]). *PitScan* was used to evaluate pitting formation in cylindrical tensile specimens of a magnesium WE43 alloy, and several relationships between pitting parameters and mechanical performance were determined. Interestingly, it was found that several of the parameters described in ASTM G46-94 showed little correlation to mechanical performance. However, several other parameters were found to show strong correlations with $\sigma_{\max}$ and these tended to be directly linked to the reduction of the cross-sectional area of the specimen. Specifically, the results indicate that the minimum magnesium core width and the average fitted radius over all layers (including standard deviation) are parameters that are most suited to provide an indication of the specimen's mechanical performance. *PitScan*, which was developed in this study, has the potential to provide a basis to standardise measurements of pitting corrosion across a range of metals. Testing conditions, like considering depths only greater than 50 µm as pits and the reduction of uniform corrosion by implementing a material ratio of 20 %, were equally good applicable for samples with little and much material loss. However, it must be noted that changing those parameters would have a significant influence on the calculated features. Moreover, a reliable mechanical strength prediction is possible in the future, by investigating a wider sample set.

Rapid mechanical deterioration of magnesium-based medical implants has limited their implementation in load-bearing applications [8, 9]. While the accelerated loss of mechanical integrity has previously been linked to pitting corrosion [17, 18], the current study is the first

to establish quantitative relationships between key phenomenological parameters of the pit formation and the mechanical performance of medical-grade magnesium. Here, it was clearly demonstrated, that the reduction in maximum specimen strength for a WE43 magnesium alloy undergoing corrosion is directly linked to pitting formation and is always the predominant corrosion mechanism in all magnesium alloys. However, the results demonstrate that several parameters described in ASTM G46-94 provide little insight into the mechanical integrity of specimens undergoing corrosion. In particular, pitting factor showed poor correlations with maximum tensile strength. Pitting factor describes the non-uniformity of pitting on the surface, with values of 1 corresponding to uniform corrosion. However, in scenarios with lots of similar deep pits, pitting factor does not sufficiently describe pitting formation because it would be approximately 1 which would be an indicator for uniform corrosion, even though similar deep pits could exist. The current results also demonstrate that pit number and pit density are actually negatively correlated with reductions in maximum tensile strength of specimens. While this may appear counter-intuitive, the detailed information provided by *PitScan* shows that many small pits are formed early on in the corrosion process, which eventually coalesce into one another over time to form larger pits (e.g. histograms in Figure 4.7) that are more detrimental to load-bearing capacity. As such, it was found that parameters that are linked to maximum pit dimensions or specimen's minimum cross-sectional area better represented mechanical integrity. Therefore, pit features such as average radius loss, the minimum fitted radius and the minimum core width are potentially the best candidates for predictors of the mechanical strength (see Figure 4.8). It was also observed that variabilities of factors, represented by the associated standard deviations, should be considered as candidates. The results of this study demonstrate the novel functionality of the automated detection framework that has been developed, which enables three-dimensional systematic evaluation of surface-based pitting formation in cylindrical specimens undergoing corrosion. To date, the vast majority of studies of magnesium alloy corrosion only consider bulk measurements of material loss by monitoring hydrogen gas evolution or mass/volume loss [17,

18, 21, 25, 27–31]. When studies consider local pitting formation, they generally rely on techniques where visual inspection of surfaces and/or cross-sections are conducted [6, 14, 22, 51, 52]. This has meant that standardised measurements of pitting have been largely qualitative, two-dimensional and may require destructive processes. While certain studies have used micro-CT based approaches to analyse pitting corrosion [6, 14, 22, 51, 52], *PitScan* has the distinct advantage of providing quantitative measures through non-destructive means, with the capacity to provide complete spatial reconstruction of test specimens, which enables a complete, reproducible investigation of the corrosion progress. This framework could easily be applied to other metallic alloys undergoing corrosion and could be adapted to evaluate corrosion in more complex geometries.

Certain limitations of the study must be noted. In-vitro testing was performed according to ASTM G31-12a [44], to determine the corrosion process of the magnesium alloy for different time steps with its mechanical integrity. While this does not fully represent the conditions of medical implants undergoing corrosion in-vivo, it does provide insight into the correlation between certain pit formations and the remaining mechanical strength. Additionally, the more aggressive in-vitro environment is helpful to observe earlier specific characteristics like pitting corrosion. Further testing could be carried out to provide a broader dataset to establish accurate trends for magnesium corrosion over wider timescales (e.g. mass loss percentages). Gastaldi et al. [53] demonstrated that stress corrosion cracking plays a significant role in the corrosion performance of magnesium alloys. However, this phenomenon was not taken into account here, as the specimens were immersed in the corrosion setup without any applied stress. Further testing would be necessary to fully investigate the influence of stress corrosion on the corrosion behaviour of magnesium. It is also worth noting that, in this study, there was a three-fold difference between the tracked mass loss calculated from hydrogen evolution and the actual detected volume loss from micro-CT analysis. Liu et al. demonstrated similar differences between the corrosion rates calculated from hydrogen evolution and from micro-CT scans for different magnesium alloys [51]. They reported the

corrosion rates (from volume loss and mass loss) for pure magnesium immersed in Hank's Balanced Salt Solution (HBSS) for 14 days. They measured 0.64 mm/year for the hydrogen gas measurement (H_2) and 1.14 mm/year for the volume loss (micro-CT), which leads to a ratio of 1.8. In general, pure magnesium degrades more slowly than its alloys [31, 51, 54]. In this study, a mean degradation rate of 2.0 mm/year (H_2) and 6.5 mm/years (micro-CT) was measured, leading to a ratio of 3.2. The ratio difference could be caused by the different material itself, immersion time and immersion solution. The lower detected mass loss values can be explained by the fact that to date, the amount of the reduction of dissolved oxygen during the corrosion process is not fully understood, and hydrogen is also built into the degradation layer itself [55]. Further, the collection of hydrogen is susceptible to errors, like the formation of bubbles on the funnel, diffusion into solution, or diffusion through the equipment [45]. All this must be considered while comparing the two different approaches for measuring the material loss. Micro-CT scanning seem to be more reliable in terms of identifying the overall volume loss. However, this is associated with high costs and greater effort. Furthermore, the resolution of the micro-CT scanning (15 µm) and the thresholding for the segmentation serves as pivotal limit in terms of mass loss detection, as well as subsequent pit detection. Thus, careful consideration and selection of appropriate resolution and threshold values are essential for reliable and reproducible detection of mass loss and localised corrosion during micro-CT scanning of corroded magnesium samples.

4.5 Conclusion

This study presented for the first time a three-dimensional automated detection framework that systematically evaluates the spatial progression of pitting corrosion from micro-CT scans of metallic specimens (*PitScan*). This framework is non-destructive and automatically determines a wide range of geometric measures of pitting corrosion on the specimen surface according to ASTM G46-94 [36]. By conducting mechanical tests of magnesium alloy

specimens undergoing corrosion, it was found that several of the parameters (e.g. pitting factor, no. of pits) described in ASTM G46-94 showed little correlation to mechanical performance. However, several other parameters (e.g. radius loss, minimum core width) were found to show strong correlations with the residual specimen strength and these tended to be directly linked to the reduction of the cross-sectional area of the specimen. This framework could easily be applied to other metallic alloys undergoing corrosion and further be adapted to evaluate corrosion in more complex geometries. Furthermore, coated specimens can be investigated in terms of their corrosion formation in conjunction with the mechanical integrity.

References

[1] H. Nygren, P. Malmberg, and Y. Liu, "MgO Implanted in Rat Tibia Bone Marrow is Osteoinductive through the Formation of a Matrix, Containing Hydroxyapatite," in *Materials Science Forum*, vol. 879, pp. 1404–1407, ISBN: 1662-9752. DOI: 10.4028/www.scientific.net/MSF.879.1404.

[2] A. Burmester, R. Willumeit-Romer, and F. Feyerabend, "Behavior of bone cells in contact with magnesium implant material," *J Biomed Mater Res B Appl Biomater*, vol. 105, no. 1, pp. 165–179, 2017, ISSN: 1552-4981 (Electronic) 1552-4973 (Linking). DOI: 10.1002/jbm.b.33542. [Online]. Available: https://www.ncbi.nlm.nih.gov/pubmed/26448207.

[3] L. Wu, F. Feyerabend, A. F. Schilling, R. Willumeit-Romer, and B. J. C. Luthringer, "Effects of extracellular magnesium extract on the proliferation and differentiation of human osteoblasts and osteoclasts in coculture," *Acta Biomater*, vol. 27, pp. 294–304, 2015, ISSN: 1878-7568 (Electronic) 1742-7061 (Linking). DOI: 10.1016/j.actbio.2015.08.042. [Online]. Available: https://www.ncbi.nlm.nih.gov/pubmed/26318802.

[4] F. Witte, H. Ulrich, C. Palm, and E. Willbold, "Biodegradable magnesium scaffolds: Part II: peri-implant bone remodeling," *J Biomed Mater Res A*, vol. 81, no. 3, pp. 757–765, 2007, ISSN: 1549-3296 (Print) 1549-3296 (Linking). DOI: 10.1002/jbm.a.31293. [Online]. Available: https://www.ncbi.nlm.nih.gov/pubmed/17390322.

[5] N. Kawamura, Y. Nakao, R. Ishikawa, D. Tsuchida, and M. Iijima, "Degradation and Biocompatibility of AZ31 Magnesium Alloy Implants In Vitro and In Vivo: A Micro-Computed Tomography Study in Rats," *Materials (Basel)*, vol. 13, no. 2, 2020, ISSN: 1996-1944 (Print) 1996-1944 (Linking). DOI: 10.3390/ma13020473. [Online]. Available: https://www.ncbi.nlm.nih.gov/pubmed/31963840.

[6] T. Kraus, S. F. Fischerauer, A. C. Hanzi, P. J. Uggowitzer, J. F. Loffler, and A. M. Weinberg, "Magnesium alloys for temporary implants in osteosynthesis: in vivo studies of their degradation and interaction with bone," *Acta Biomater*, vol. 8, no. 3, pp. 1230–8, 2012, ISSN: 1878-7568 (Electronic) 1742-7061 (Linking). DOI: 10.1016/j.actbio.2011.11.008. [Online]. Available: https://www.ncbi.nlm.nih.gov/pubmed/22107870.

[7] D. Sumner, "Long-term implant fixation and stress-shielding in total hip replacement," *Journal of Biomechanics*, vol. 48, no. 5, pp. 797–800, 2015, ISSN: 0021-9290.

[8] X. Gu, F. Wang, X. Xie, M. Zheng, P. Li, Y. Zheng, L. Qin, and Y. Fan, "In vitro and in vivo studies on as-extruded Mg- 5.2 wt.%Zn- 0.6 wt.%Ca alloy as biodegradable metal," *Science China Materials*, vol. 61, no. 4, pp. 619–628, 2018, ISSN: 2095-8226 2199-4501. DOI: 10.1007/s40843-017-9205-x.

[9] Y. Liu, Y. Zheng, X. Chen, J. Yang, H. Pan, D. Chen, L. Wang, J. Zhang, D. Zhu, S. Wu, K. W. K. Yeung, R. Zeng, Y. Han, and S. Guan, "Fundamental Theory of Biodegradable Metals - Definition, Criteria, and Design," *Advanced Functional Materials*, vol. 29, no. 18, 2019, ISSN: 1616-301X 1616-3028. DOI: 10.1002/adfm.201805402.

[10] S. Agarwal, J. Curtin, B. Duffy, and S. Jaiswal, "Biodegradable magnesium alloys for orthopaedic applications: A review on corrosion, biocompatibility and surface modifications," *Mater Sci Eng C Mater Biol Appl*, vol. 68, pp. 948–963, 2016, ISSN: 1873-0191 (Electronic) 0928-4931 (Linking). DOI: 10.1016/j.msec.2016.06.020. [Online]. Available: https://www.ncbi.nlm.nih.gov/pubmed/27524097.

[11] M. Abdalla, A. Joplin, M. Elahinia, and H. Ibrahim, "Corrosion Modeling of Magnesium and Its Alloys for Biomedical Applications: Review," *Corrosion and Materials Degradation*, vol. 1, no. 2, pp. 219–248, 2020, ISSN: 2624-5558. DOI: 10.3390/cmd1020011.

[12] M. F. Montemor, "Corrosion issues in joining lightweight materials: A review of the latest achievements," *Physical Sciences Reviews*, vol. 1, no. 2, 2016, ISSN: 2365-659X. DOI: 10.1515/psr-2015-0011.

[13] H. Xu, T. Hu, M. Wang, Y. Zheng, H. Qin, H. Cao, and Z. An, "Degradability and biocompatibility of magnesium-MAO: The consistency and contradiction between in-vitro and in-vivo outcomes," *Arabian Journal of Chemistry*, vol. 13, no. 1, pp. 2795–2805, 2020, ISSN: 18785352. DOI: 10.1016/j.arabjc.2018.07.010.

[14] Y. Koo, H. B. Lee, Z. Dong, R. Kotoka, J. Sankar, N. Huang, and Y. Yun, "The Effects of Static and Dynamic Loading on Biodegradable Magnesium Pins In Vitro and In Vivo," *Sci Rep*, vol. 7, no. 1, p. 14 710, 2017, ISSN: 2045-2322 (Electronic) 2045-2322 (Linking). DOI: 10.1038/s41598-017-14836-5. [Online]. Available: https://www.ncbi.nlm.nih.gov/pubmed/29089642.

[15] F. Witte, J. Fischer, J. Nellesen, C. Vogt, J. Vogt, T. Donath, and F. Beckmann, "In vivo corrosion and corrosion protection of magnesium alloy LAE442," *Acta Biomater*, vol. 6, no. 5, pp. 1792–9, 2010, ISSN: 1878-7568 (Electronic) 1742-7061 (Linking). DOI: 10.1016/j.actbio.2009.10.012. [Online]. Available: https://www.ncbi.nlm.nih.gov/pubmed/19822226.

[16] Y. Xu, H. Meng, H. Yin, Z. Sun, J. Peng, X. Xu, Q. Guo, W. Xu, X. Yu, Z. Yuan, B. Xiao, C. Wang, Y. Wang, S. Liu, S. Lu, Z. Wang, and A. Wang, "Quantifying the degradation of degradable implants and bone formation in the femoral condyle using micro-CT 3D reconstruction," *Exp Ther Med*, vol. 15, no. 1, pp. 93–102, 2018, ISSN: 1792-0981 (Print) 1792-0981 (Linking). DOI: 10.3892/etm.2017.5389. [Online]. Available: https://www.ncbi.nlm.nih.gov/pubmed/29375677.

[17] E. L. Boland, R. N. Shirazi, J. A. Grogan, and P. E. McHugh, "Mechanical and Corrosion Testing of Magnesium WE43 Specimens for Pitting Corrosion Model Cali-

bration," *Advanced Engineering Materials*, vol. 20, no. 10, 2018, ISSN: 14381656. DOI: 10.1002/adem.201800656.

[18] J. A. Grogan, B. J. O'Brien, S. B. Leen, and P. E. McHugh, "A corrosion model for bioabsorbable metallic stents," *Acta Biomater*, vol. 7, no. 9, pp. 3523–33, 2011, ISSN: 1878-7568 (Electronic) 1742-7061 (Linking). DOI: 10.1016/j.actbio.2011.05.032. [Online]. Available: https://www.ncbi.nlm.nih.gov/pubmed/21664498.

[19] Y. Chen, Z. Xu, C. Smith, and J. Sankar, "Recent advances on the development of magnesium alloys for biodegradable implants," *Acta Biomater*, vol. 10, no. 11, pp. 4561–4573, 2014, ISSN: 1878-7568 (Electronic) 1742-7061 (Linking). DOI: 10.1016/j.actbio.2014.07.005. [Online]. Available: https://www.ncbi.nlm.nih.gov/pubmed/25034646.

[20] G. B. Darband, M Aliofkhazraei, P Hamghalam, and N Valizade, "Plasma electrolytic oxidation of magnesium and its alloys: Mechanism, properties and applications," *Journal of Magnesium and Alloys*, vol. 5, no. 1, pp. 74–132, 2017, ISSN: 2213-9567. DOI: 10.1016/j.jma.2017.02.004.

[21] A. Kopp, T. Derra, M. Muther, L. Jauer, J. H. Schleifenbaum, M. Voshage, O. Jung, R. Smeets, and N. Kroger, "Influence of design and postprocessing parameters on the degradation behavior and mechanical properties of additively manufactured magnesium scaffolds," *Acta Biomater*, vol. 98, pp. 23–35, 2019, ISSN: 1878-7568 (Electronic) 1742-7061 (Linking). DOI: 10.1016/j.actbio.2019.04.012. [Online]. Available: https://www.ncbi.nlm.nih.gov/pubmed/30959185.

[22] H. M. Wong, K. W. Yeung, K. O. Lam, V. Tam, P. K. Chu, K. D. Luk, and K. M. Cheung, "A biodegradable polymer-based coating to control the performance of magnesium alloy orthopaedic implants," *Biomaterials*, vol. 31, no. 8, pp. 2084–96, 2010, ISSN: 1878-5905 (Electronic) 0142-9612 (Linking). DOI: 10.1016/j.biomaterials.2009.11.111. [Online]. Available: https://www.ncbi.nlm.nih.gov/pubmed/20031201.

[23] E Angelini, S Grassini, F Rosalbino, F Fracassi, and R d'Agostino, "Electrochemical impedance spectroscopy evaluation of the corrosion behaviour of Mg alloy coated with PECVD organosilicon thin film," *Progress in Organic Coatings*, vol. 46, no. 2, pp. 107–111, 2003, ISSN: 0300-9440. DOI: 10.1016/S0300-9440(02)00217-5.

[24] B. Zhang, Y. Hou, X. Wang, Y. Wang, and L. Geng, "Mechanical properties, degradation performance and cytotoxicity of Mg–Zn–Ca biomedical alloys with different compositions," *Materials Science and Engineering: C*, vol. 31, no. 8, pp. 1667–1673, 2011, ISSN: 09284931. DOI: 10.1016/j.msec.2011.07.015.

[25] X. Gu, Y. Zheng, Y. Cheng, S. Zhong, and T. Xi, "In vitro corrosion and biocompatibility of binary magnesium alloys," *Biomaterials*, vol. 30, no. 4, pp. 484–498, 2009, ISSN: 0142-9612. DOI: 10.1016/j.biomaterials.2008.10.021.

[26] A. M. Lafront, W. Zhang, S. Jin, R. Tremblay, D. Dubé, and E. Ghali, "Pitting corrosion of AZ91D and AJ62x magnesium alloys in alkaline chloride medium using electrochemical techniques," *Electrochimica Acta*, vol. 51, no. 3, pp. 489–501, 2005, ISSN: 00134686. DOI: 10.1016/j.electacta.2005.05.013.

[27] O. Jung, R. Smeets, P. Hartjen, R. Schnettler, F. Feyerabend, M. Klein, N. Wegner, F. Walther, D. Stangier, A. Henningsen, C. Rendenbach, M. Heiland, M. Barbeck, and A. Kopp, "Improved In Vitro Test Procedure for Full Assessment of the Cytocompatibility of Degradable Magnesium Based on ISO 10993-5/-12," *Int J Mol Sci*, vol. 20, no. 2, 2019, ISSN: 1422-0067 (Electronic) 1422-0067 (Linking). DOI: 10.3390/ijms20020255. [Online]. Available: https://www.ncbi.nlm.nih.gov/pubmed/30634646.

[28] G. Song, A. Atrens, and D. StJohn, "An Hydrogen Evolution Method for the Estimation of the Corrosion Rate of Magnesium Alloys," in *Essential Readings in Magnesium Technology*, S. N. Mathaudhu, A. A. Luo, N. R. Neelameggham, E. A. Nyberg, and W. H. Sillekens, Eds. Cham: Springer International Publishing, 2001, pp. 565–572, ISBN: 978-3-319-48099-2. DOI: 10.1007/978-3-319-48099-2_90.

[29] M. Li, Y. Cheng, Y. F. Zheng, X. Zhang, T. F. Xi, and S. C. Wei, "Surface characteristics and corrosion behaviour of WE43 magnesium alloy coated by SiC film," *Applied Surface Science*, vol. 258, no. 7, pp. 3074–3081, 2012, ISSN: 01694332. DOI: 10.1016/j.apsusc.2011.11.040.

[30] D. Mei, S. V. Lamaka, J. Gonzalez, F. Feyerabend, R. Willumeit-Römer, and M. L. Zheludkevich, "The role of individual components of simulated body fluid on the corrosion behavior of commercially pure Mg," *Corrosion Science*, vol. 147, pp. 81–93, 2019, ISSN: 0010938X. DOI: 10.1016/j.corsci.2018.11.011.

[31] I. Marco, F. Feyerabend, R. Willumeit-Romer, and O. Van der Biest, "Degradation testing of Mg alloys in Dulbecco's modified eagle medium: Influence of medium sterilization," *Mater Sci Eng C Mater Biol Appl*, vol. 62, pp. 68–78, 2016, ISSN: 1873-0191 (Electronic) 0928-4931 (Linking). DOI: 10.1016/j.msec.2016.01.039. [Online]. Available: https://www.ncbi.nlm.nih.gov/pubmed/26952399.

[32] J. Harmuth, B. Wiese, J. Bohlen, T. Ebel, and R. Willumeit-Römer, "Wide Range Mechanical Customization of Mg-Gd Alloys With Low Degradation Rates by Extrusion," *Frontiers in Materials*, vol. 6, 2019, ISSN: 2296-8016. DOI: 10.3389/fmats.2019.00201.

[33] N. A. Agha, F. Feyerabend, B. Mihailova, S. Heidrich, U. Bismayer, and R. Willumeit-Romer, "Magnesium degradation influenced by buffering salts in concentrations typical of in vitro and in vivo models," *Mater Sci Eng C Mater Biol Appl*, vol. 58, pp. 817–25, 2016, ISSN: 1873-0191 (Electronic) 0928-4931 (Linking). DOI: 10.1016/j.msec.2015.09.067. [Online]. Available: https://www.ncbi.nlm.nih.gov/pubmed/26478376.

[34] J. Walker, S. Shadanbaz, N. T. Kirkland, E. Stace, T. Woodfield, M. P. Staiger, and G. J. Dias, "Magnesium alloys: predicting in vivo corrosion with in vitro immersion testing," *J Biomed Mater Res B Appl Biomater*, vol. 100, no. 4, pp. 1134–41, 2012, ISSN: 1552-4981 (Electronic) 1552-4973 (Linking). DOI: 10.1002/jbm.b.32680.

[35] J. Mitchell, N. Crow, and A. Nieto, "Effect of Surface Roughness on Pitting Corrosion of AZ31 Mg Alloy," *Metals*, vol. 10, no. 5, 2020, ISSN: 2075-4701. DOI: 10.3390/met10050651.

[36] ASTM G46-94, *Standard Guide for Examination and Evaluation of Pitting Corrosion*. PA: ASTM International West Conshohocken, 2005. DOI: 10.1520/g0046-94r18.

[37] J. Wang, V. Giridharan, V. Shanov, Z. Xu, B. Collins, L. White, Y. Jang, J. Sankar, N. Huang, and Y. Yun, "Flow-induced corrosion behavior of absorbable magnesium-based stents," *Acta Biomaterialia*, vol. 10, no. 12, pp. 5213–5223, 2014, ISSN: 1742-7061. DOI: https://doi.org/10.1016/j.actbio.2014.08.034. [Online]. Available: https://www.sciencedirect.com/science/article/pii/S174270611400381X.

[38] D. Coelho, O. A. Cuadros Linares, A. L. S. Oliveira, M. A. S. Andrade Jr, L. H. Mascaro, J. E. S. Batista Neto, O. M. Bruno, and E. C. Pereira, "Introducing a low-cost tool for 3D characterization of pitting corrosion in stainless steel," *Journal of Solid State Electrochemistry*, 2020, ISSN: 1432-8488 1433-0768. DOI: 10.1007/s10008-020-04586-2.

[39] P. Guo, E. C. La Plante, B. Wang, X. Chen, M. Balonis, M. Bauchy, and G. Sant, "Direct observation of pitting corrosion evolutions on carbon steel surfaces at the nano-to-micro- scales," *Scientific Reports*, vol. 8, no. 1, p. 7990, 2018, ISSN: 2045-2322 (Electronic) 2045-2322 (Linking). DOI: 10.1038/s41598-018-26340-5. [Online]. Available: https://www.ncbi.nlm.nih.gov/pubmed/29789654.

[40] C. Leising, "Pitting corrosion measurement using 3D profilometry," *NANOVEA*, 2014. DOI: 10.13140/RG.2.1.5098.3840.

[41] H. Li, M. R. Garvan, J. Li, J. Echauz, D. Brown, and G. J. Vachtsevanos, "Imaging and Information Processing of Pitting-Corroded Aluminum Alloy Panels with Surface Metrology Methods," Georgia Institute of Technology Atlanta United States, Report, 2014.

[42] A. Turnbull, "Corrosion pitting and environmentally assisted small crack growth," *Proc Math Phys Eng Sci*, vol. 470, no. 2169, p. 20 140 254, 2014, ISSN: 1364-5021 (Print) 1364-5021 (Linking). DOI: 10.1098/rspa.2014.0254.

[43] A. Oyane, H. Kim, T. Furuya, T. Kokubo, T. Miyazaki, and T. Nakamura, "Preparation and assessment of revised simulated body fluids," *J. Biomed. Mater. Res.*, vol. 65A, no. 2, pp. 188–195, 2003, ISSN: 1549-3296. DOI: 10.1002/jbm.a.10482.

[44] ASTM NACE TM0169/G31-21, *Standard guide for laboratory immersion corrosion testing of metals*, Standard, 2021.

[45] N. T. Kirkland and N. Birbilis, *Magnesium Biomaterials* (SpringerBriefs in Materials). Springer, 2014, ISBN: 978-3-319-02122-5 978-3-319-02123-2. DOI: 10.1007/978-3-319-02123-2.

[46] Y. F. Zheng, X. N. Gu, and F. Witte, "Biodegradable metals," *Materials Science and Engineering: R: Reports*, vol. 77, pp. 1–34, 2014, ISSN: 0927796X. DOI: 10.1016/j.mser.2014.01.001.

[47] F. Gremse, M. Stärk, J. Ehling, J. R. Menzel, T. Lammers, and F. Kiessling, "Imalytics preclinical: interactive analysis of biomedical volume data," *Theranostics*, vol. 6, no. 3, pp. 328–341, 2016. DOI: 10.7150/thno.13624.

[48] ISO 4287:1997, *Geometrical Product Specifications (GPS) – Surface texture: Profile method – Terms, definitions and surface texture parameters*, Standard, 1997.

[49] W. F. Ng, K. Y. Chiu, and F. T. Cheng, "Effect of pH on the in vitro corrosion rate of magnesium degradable implant material," *Materials Science and Engineering: C*, vol. 30, no. 6, pp. 898–903, 2010, ISSN: 09284931. DOI: 10.1016/j.msec.2010.04.003.

[50] M. R. Barnett, M. D. Nave, and A. Ghaderi, "Yield point elongation due to twinning in a magnesium alloy," *Acta Materialia*, vol. 60, no. 4, pp. 1433–1443, 2012, ISSN: 13596454. DOI: 10.1016/j.actamat.2011.11.022.

[51] L. Liu, K. Gebresellasie, B. Collins, H. Zhang, Z. Xu, J. Sankar, Y.-C. Lee, and Y. Yun, "Degradation Rates of Pure Zinc, Magnesium, and Magnesium Alloys Measured by Volume Loss, Mass Loss, and Hydrogen Evolution," *Applied Sciences*, vol. 8, no. 9, 2018, ISSN: 2076-3417. DOI: 10.3390/app8091459.

[52] T. A. Huehnerschulte, N. Angrisani, D. Rittershaus, D. Bormann, H. Windhagen, and A. Meyer-Lindenberg, "In Vivo Corrosion of Two Novel Magnesium Alloys ZEK100 and AX30 and Their Mechanical Suitability as Biodegradable Implants," *Materials (Basel)*, vol. 4, no. 6, pp. 1144–1167, 2011, ISSN: 1996-1944 (Print) 1996-1944 (Linking). DOI: 10.3390/ma4061144. [Online]. Available: https://www.ncbi.nlm.nih.gov/pubmed/28879972.

[53] D. Gastaldi, V. Sassi, L. Petrini, M. Vedani, S. Trasatti, and F. Migliavacca, "Continuum damage model for bioresorbable magnesium alloy devices - Application to coronary stents," *J Mech Behav Biomed Mater*, vol. 4, no. 3, pp. 352–65, 2011, ISSN: 1878-0180 (Electronic) 1878-0180 (Linking). DOI: 10.1016/j.jmbbm.2010.11.003. [Online]. Available: https://www.ncbi.nlm.nih.gov/pubmed/21316623.

[54] A. H. Martinez Sanchez, B. J. Luthringer, F. Feyerabend, and R. Willumeit, "Mg and Mg alloys: how comparable are in vitro and in vivo corrosion rates? A review," *Acta Biomater*, vol. 13, pp. 16–31, 2015, ISSN: 1878-7568 (Electronic) 1742-7061 (Linking). DOI: 10.1016/j.actbio.2014.11.048. [Online]. Available: https://www.ncbi.nlm.nih.gov/pubmed/25484334.

[55] E. L. Silva, S. V. Lamaka, D. Mei, and M. L. Zheludkevich, "The Reduction of Dissolved Oxygen During Magnesium Corrosion," *ChemistryOpen*, vol. 7, no. 8, pp. 664–668, 2018, ISSN: 2191-1363 (Print) 2191-1363 (Linking). DOI: 10.1002/open.201800076. [Online]. Available: https://www.ncbi.nlm.nih.gov/pubmed/30181945.

Chapter 5

Linking the effect of localised pitting corrosion with mechanical integrity of rare earth Magnesium alloy for implant use

5.1 Introduction

Magnesium and its alloys have significant potential in orthopaedic applications, as they have osteostimulative properties [1–6] and they have similar mechanical properties to native bone [7]. Magnesium-based alloys are also biodegradable, whereby the implant is gradually resorbed from the body once its load bearing function is completed. This reduces the need for revision surgeries, thereby reducing patient risk and costs to health systems. However, magnesium-based alloys can undergo increased and localised corrosion, which may lead to an unwanted early failure of the implant. In unloaded physiological scenarios, magnesium-based alloys degrade through several surface-based corrosion mechanisms including galvanic, intergranular and pitting corrosion [8]. The localised corrosion mechanisms are generally caused by impurities and inhomogeneities in the material, which are largely unavoidable due to the manufacturing process of such alloys. While the spatial and temporal evolution of corrosion can be controlled to some degree by varying alloying composition and/or by applying a surface coating [8–12], it is generally not possible to achieve uniform, or non-localised, corrosion in magnesium-based biomaterials [13–17]. Despite this, many studies investigating the degradation performance of magnesium alloys only consider bulk measurements of corro-

sion, evaluated by gravimetric methods, hydrogen evolution, μCT images, or electrochemical tests, and ignore aspects of localised surface corrosion, which can greatly impact overall performance and cause early failures of devices. While some studies provide limited qualitative assessments of surface corrosion through visual examination, there is a lack of quantitative data on the spatial progression of surface corrosion [11, 18–31]. Furthermore, only a limited number of studies give results on the extent of localised corrosion for Mg alloys [32–34] following ASTM G46-94 [35], which provides specific guidelines to evaluate pitting corrosion and describes several local parameters that quantify the severity and spatial distribution of corrosion features, including pit size, pit depth, pit density and pitting factor.

To date, few in-vivo and in-vitro studies [19, 20, 36, 37] have quantified the non-uniform relationship between specimen corrosion and mechanical strength of magnesium alloys. While the disproportionate reduction in load-bearing capacity, compared to corresponding mass loss, has clearly attributed to pitting corrosion observed across specimens [19, 20, 37], these studies have provided little quantitative understanding on how pit formation (e.g. extent and spatial distribution) affects overall mechanical performance. In Chapter 4 an automated detection framework that enables a fully systematic evaluation of surface corrosion through a micro-CT based detection algorithms (*PitScan*), was established [33]. This study identified a clearly non-linear relationship between overall mass loss and specimen strength for a magnesium-based alloy and systematically characterised the extent and spatial distribution of pitting features on the corroding surface. While this study provided important information on the relationship between spatial features of corrosion and mechanical performance, it was limited by the fact that it only considered one magnesium alloy undergoing corrosion. Of course, there is a wide range of possible alloy combinations, and the spatial and temporal progression of corrosion will likely vary extensively across these different material systems. However, it is difficult to experimentally characterise the full range of corrosion scenarios. This limits the capacity to fully understand the mechanistic relationships between surface-based corrosion and mechanical performance of these metals and alternative

approaches through computational modelling are required.

Modelling approaches to predict corrosion of magnesium-based alloys are generally categorised as either physical or phenomenological approaches. While physically-based corrosion models use theoretical frameworks that capture the chemical processes taking place on the corroding surface, they are computationally prohibitive and their implementation in the finite element method generally employ moving-mesh approaches, which tend to only allow uniform corrosion, thereby limiting their ability to predict localised, non-uniform corrosion [38–40]. On the other hand, a wide range of phenomenological corrosion models have been proposed for magnesium-based alloys that use combinations of a continuum-based damage mechanics and/or element removal on the corroding surface to simulate mass loss. While several of these approaches have also been limited to uniform corrosion [41, 42], many other models have used random distribution functions to prescribe weighted probabilities across the corroding surface that enable localised pits to form and evolve [19, 20, 43–45]. These have been shown to be superior to uniform-based models in capturing the non-linear reductions in specimen strength during corrosion [19, 20, 42, 44]. However, while these models have captured non-linear reductions in strength, very few models have been directly compared to experimental samples undergoing corrosion. Therefore, it is not clear whether these models actually capture (i) the overall stress-strain behaviour of samples undergoing corrosion and (ii) whether they actually capture the severity and spatial distribution of pitting features on the corroding surface. To maximise the utility of these models in corrosion-based investigations, it is critical that robust validation of these models is carried out to fully understand how the spatial and temporal progression of corrosion impacts the mechanics of magnesium-based implants.

The objective of the current study is to establish the mechanistic relationship between the severity of localised corrosion and mechanical performance of magnesium-based specimens. To achieve this, a computational modelling approach was used, whereby a range of different corrosion profiles were generated through a surface-based corrosion model. Geometric

features of these corrosion profiles were quantified using the *PitScan* framework from Chapter 4 [33] and tensile failure of corroding samples was simulated through finite element modelling. In the first instance, the suitability of the surface-based corrosion modelling approach in capturing both the (i) geometric phenomenology of pitting corrosion and (ii) resulting mechanical response of corroded specimens, by comparing to in-vitro degraded samples (Chapter 4) was evaluated [33]. Following this, systematically the relationships between key phenomenological features that describe pitting corrosion and the mechanical performance (ultimate strength, elastic modulus and strain at maximum strength) were investigated, to establish new mechanistic insight into the performance of magnesium-based materials undergoing corrosion.

5.2 Material and Methods

5.2.1 Study design

To generate corroding profiles, three-dimensional cylindrical geometries were considered that had identical dimensions as the gauge sections of the tensile dog bone specimens used in Chapter 4, with a length of 18.95 mm and a 3 mm diameter [33]. Whereby immersion testing in c-SBF [46] was carried out over 28 days with weekly time points (37 °C, 5 % CO_2). Following immersion, samples were cleaned in ethanol and fully dried with the degradation layer still attached on the sample's surfaces. Then all samples underwent microcomputer tomography scanning with subsequent uniaxial tensile tests (see Chapter 4) [33]. In this study, a range of corrosion profiles were generated using an enhanced surface-based corrosion model that was initially developed by Grogan et al. and further developed by Quinn et al. [20, 47] (described in more detail in Section 5.2.2). The surface geometric features of these corrosion profiles were fully quantified using the automated detection framework *PitScan*, which is an in-house developed Python tool based on automated image processing with OpenCV fully

described in Chapter 4 [33, 48]. By creating binary cross-sectional images of corroding finite element geometries, *PitScan* enables quantification of key corrosion parameters (e.g. average pit depth, pit density, average radius loss, minimal cross-section, etc.) that describe the spatial phenomenology of the surface profile (described in more detail in Section 5.2.3). An elastic-plastic constitutive material model was calibrated from the undegraded experimental response, and the corroded samples were simulated under uniaxial tension to predict the mechanical response of samples as corrosion progressed (described in Section 5.2.4). Finally, correlations were established between mechanical properties and the geometrical features that describe the phenomenology of surface-based corrosion (Section 5.2.5).

5.2.2 Corrosion model

The corrosion model is based on the model originally developed by Grogan et al. (2011) [20], which is implemented in a finite element framework through a continuum damage mechanics (CDM) based approach [49]. This surface-based corrosion model has been widely implemented [19, 20, 44, 45, 50]. The corrosion model assumes a scalar damage factor (D) to initialise damage on corroding elements so that the effective stress tensor ($\tilde{\boldsymbol{\sigma}}$) is:

$$\tilde{\boldsymbol{\sigma}} = \frac{\sigma_{ij}}{1 - D}. \tag{5.1}$$

First, a finite element mesh is created on the geometry with exposed elements to the environment defined as active. Including the recent adaptation of the model, described by Quinn et al. [47], considering an enhanced surface-based approach to corrosion, whereby impurities within the specimen volume also direct corrosion processes resulting in more realistic pit shapes compared to the original model by Grogan et al. (2011). Firstly, random numbers (λ_e) are assigned to all elements which potentially can degrade, using a Weibull curve, with

the probability density function described in Equation (5.2):

$$f(x) = \gamma(x)^{\gamma-1} e^{-(x)^{\gamma}}. \tag{5.2}$$

Where γ is the dimensionless shape parameter of the probability density function with the condition $x \geq 0$ and $\gamma \geq 0$ (see Figure 5.1 (d)), which enables modelling of localised corrosion (pitting, intergranular corrosion, etc. [8]). These pre-generated random numbers throughout the complete mesh mainly depend on the shape parameter γ. The first adaptation

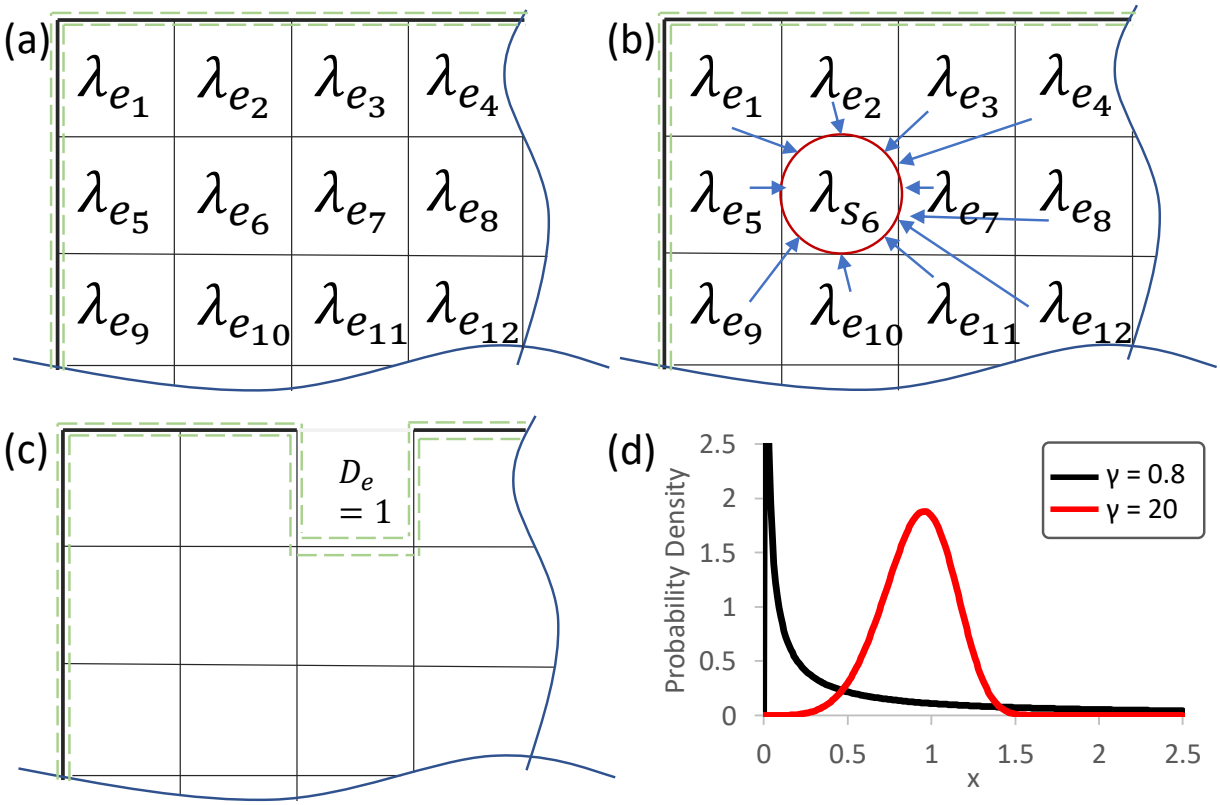

Figure 5.1: Sectional view of a finite element mesh: Basic principle of pre-processing step for the adaptation of the initial random numbers (green dashed line symbolizes the active surface) (a) initial random numbers (b) Redistribution of the random numbers, here: influence of all other elements on element 6 for the adapted random number (c) removed element where $D_e = 1$ (d) Probability density function for a standard Weibull-Curve for pitting ($\gamma = 0.8$) and uniform corrosion ($\gamma = 20$).

implemented by Quinn et al. [47] uses a smoothing process to adjust the distribution, as depicted in Figure 5.1 (a and b). Here, the influence of each element on each other is shown

schematically for element number 6, to show the influence of impurities/alloying elements on each other. This smoothing process considers the random number values of all other degradable elements, including the distance from elements among themselves (d_{ei}) and the initial random numbers (λ_e):

$$\lambda_{e_{max}} = max(\lambda_{si}) = max(\lambda_{ei} - (B * d_{ei}) * \lambda_{ei}), \quad i = 1, Max.ElementNo. \tag{5.3}$$

Where B describes the loss in pitting per unit distance, which dictates the extent of the influence of the other random numbers on each other. This step is performed once throughout the complete mesh. Then, the random numbers are normalised according to Equation (5.4):

$$\lambda_{e_{norm}} = \frac{\lambda_{e_{max}}}{\sum_{i=0}^{i} \lambda_{e_{max}}}, \quad \sum_{i=0}^{i} \lambda_{e_{norm}} = 1. \tag{5.4}$$

During the final degradation step, elements that will be removed for the specified mass loss are determined by looping through all active elements. The current damage increment dD_e is calculated within each active element according to Equation (5.5):

$$\frac{dD_e}{dt} = k_u \lambda_{e_{norm}} L_{active}. \tag{5.5}$$

Where k_u is a time dependant parameter, and L_{active} is the ratio of the exposed active surface area to the respective element volume. Equation (5.6) represents the addition of the increment step to the previous calculated total damage for an element:

$$D_e = D_{e-1} + dD_e. \tag{5.6}$$

The current total damage (D_e) of each active element is calculated by adding the current damage increment (dD_e) to the old total damage (D_{e-1}). Once $D_e \geq 1$ the element is removed (Figure 5.1 (c)) and its adjacent elements, which were inactive so far, will get active

and get included in the loop. To avoid too high single damage increments to ensure that each element needs at least two steps to degrade, an adaption is implemented following Equation (5.7):

$$\text{if} \quad D_e > D_{e_{max}}, dt_{new} = \frac{D_{e_{max}}}{D_e} dt_{old}. \tag{5.7}$$

With $D_{e_{max}} = 0.5$, dt_{new} and dt_{old} the new and old time step, respectively. Full details on the localised degradation model are given in the original studies by Grogan et al. and Quinn et al. [20, 47].

Within this chapter, constant values were assigned to time dependent parameters: $k_u = 2.7 \cdot 10^8$ to enable appropriate number of loops. In this, and previous implementations of the original corrosion model [19, 20, 47], executing the code directly in a VUMAT/UMAT in Abaqus (Dassault Systèmes Simulia Corp., RI, USA) requires substantial computational power, especially with the implemented adaptation from Quinn et al. [47]. To improve the efficiency of this code and enable high mesh resolution ($>$300,000 elements), the corrosion model was carried out as a pre-processing step through a Python code, which offers the additional advantage of being readily implemented in a range of finite element software codes. It should be noted that the initial continuum damage mechanics (CDM) [42, 49] was not considered in this study. This is because the Python code used, only translates the geometrical values of an element, and does not consider the influence of the loading condition. Since the experimental data used here, were obtained from unstressed specimens, the lack of CDM is acceptable. However, it would be necessary to consider CDM and stress corrosion in future studies to obtain a more comprehensive understanding of the material behaviour under loading.

By varying the shape parameter of the Weibull curve (γ) and the pitting parameter (B) of the degradation code, eight different corrosion profiles were generated from uniform corrosion to severe pitting corrosion. First, four profiles with a constant pitting parameter ($B = 0.8$) and a varying γ (20.0, 1.5, 0.3) were simulated, and then γ was set constant to 0.8 and B was changed ($B =$1.2, 0.8, 0.5, 0.3). Additionally, $\gamma = 0.5$ and $B = 0.5$ was chosen as

Table 5.1 Tested input parameter combinations of the degradation code for the model with different localised corrosion extent.

γ	B
0.3	0.8
0.3	0.5
0.8	0.3
0.8	0.5
0.8	0.8
0.8	1.2
1.5	0.8
20.0	0.8

input parameter combination. Each model was degraded to 5, 10, 20, 30, 40, 50 % mass loss. The input parameter combinations are summarised in Table 5.1. All models considered, had an element size of 80 µm, whereby the uncorroded geometry consisted of a total of 329,128 elements. To corrode the surface to 50 % mass lass for one input set, the computational algorithm took approximately 1 h to execute on a computer workstation that had an Intel® Xeon® Gold 5118 CPU @ 2.30 GHz.

5.2.3 Automated spatial tracking of corrosion (*PitScan*)

For full spatial reconstruction of the surface profile, the active finite element mesh was binaries and cross-sectional images taken every 80 µm along the y-axis (equivalent to mesh size). The approach was the same as the geometrical evaluation conducted with the µCT images from the in-vitro testing in the previous Chapter 4 [33]. The basic principle for the image processing for one layer is shown in Figure 5.2, whereby a contour of the magnesium core and a circle fit provides the depths in 2-degree radial increments. In the second step, the profile is reconstructed to a 3D geometry to enable all geometrical features to be quantified. A pit is defined if the detected depth exceeds 50 µm.

The *PitScan* algorithm provided quantitative information on the geometrical corrosion formation on the outer surface. Surface contour plots were generated with the tracked

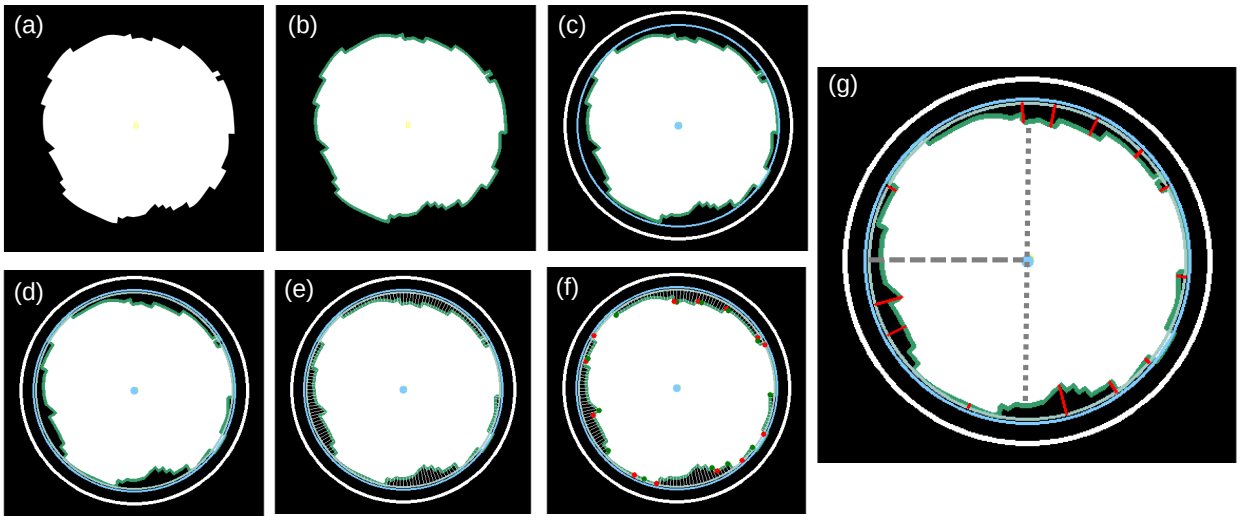

Figure 5.2: Automated image recognition process chain for FE cross-sectional images (a) Raw input (b) Contour detection (c) Circle plotting (d) Material portion (e) Depth tracking (f) Pit on-off tracking (g) Determination of deepest point of each pit. Grey dashed line fitted radius, grey dotted line minimum Mg core width, similar to van Gaalen et al. [33].

depth from the initial surface. Further, probability distributions were obtained and plotted that describe the frequency of pit depth ranges at the predefined mass losses. *PitScan* also evaluated key parameters that describe the spatial distribution and extent of localised corrosion. Table 5.2 provides a summary of these parameters and information about how they are calculated.

Table 5.2 Detailed description of generated geometrical parameters within the pit detection tool (d: single pit depth, i: number of cross-section images, r: fitted radius, r_0 initial radius [33]).

Parameter	Symbol	Description
Pitting Factor [35]	PF	$PF = \frac{\text{deepest metal penetration}}{\text{average metal penetration}}$
Average of the deepest pits (μm)	$\bar{d}_{10}$	$\bar{d}_{10} = \frac{\sum_0^{x=10} d_x}{10}$
Pits per cm^2	$\bar{n}$	Tracked pits per cm^2
Volume loss through pits (%)	VL_{pits}	Sums up only the volumes of the real pits ($d > 50\mu m$)
Av. Radius loss	$\overline{RL}$	Average of all fitted radii for every layer: $\overline{RL} = \frac{\sum_0^{x=i} 1-(r_x/r_0)}{i}$
Minimum fitted radius	r_{min}	The minimum of all fitted radii in every cross section: $min(r_x)$
Minimum Mg core width	d_{min}	Minimum of all detected magnesium core widths: $min(d_{Mg})$
Max. area loss in one layer	ΔA_{max}	$\Delta A_{max} = max(y - \frac{A_0}{A_x})$

5.2.4 Mechanical model

Computational modelling was carried out in the Abaqus/Explicit finite element code (Dassault Systèmes Simulia Corp., RI, USA), with all cylindrical geometries meshed using three-dimensional reduced integration brick elements (C3D8R). Material input data for the computational model was derived based on uniaxial tensile test data measured for the WE43MEO alloy in the previous chapter (Figure 5.3 (b)). Here, the Young's modulus was $E = 44.70MPa$, while a Von Mises plasticity formulation was set to define isotropic yielding [51]. The plasticity input curve was calibrated on an axisymmetric model with two different element sizes with the exact geometry of the dog bones used within the experimental study in Chapter 4 (Figure 5.3 (a)) [33]. The Poisson's ratio was assumed as $\nu = 0.3$ [52] and the density of magnesium as $\rho_{WE43} = 1.84g/cm^3$. Only the gauge section was used as model geometry for the final finite element analysis, to save computational time. To enable uniaxial test conditions, a layer of non-degradable elements was included at the ends of the model (see Figure 5.3 (c)). Here, equational constraints were used to implement displacement-based uniaxial tension on each model. Simulations were carried out on an Intel® Xeon® Gold 5118 CPU @ 2.30 GHz with 30 CPUs and took between 1.5 h and 7 h to complete, depending on the number of remaining elements following corrosion. The effective stress-strain behaviour of corroding samples was determined based on the initial cross-sectional area of the cylindrical specimens ($A_{t_i} = A_{t_0} = \pi r^2 = \pi(1.5mm)^2$). From this, the overall specimen strength was determined as the ratio of the maximum tracked Force to A_{t_0}: $\sigma_{max} = F_{max}/A_{t_0}$, the effective modulus was the respective elastic modulus of the linear-elastic region, while the specimen strain-to-failure was determined as the strain at σ_{max}.

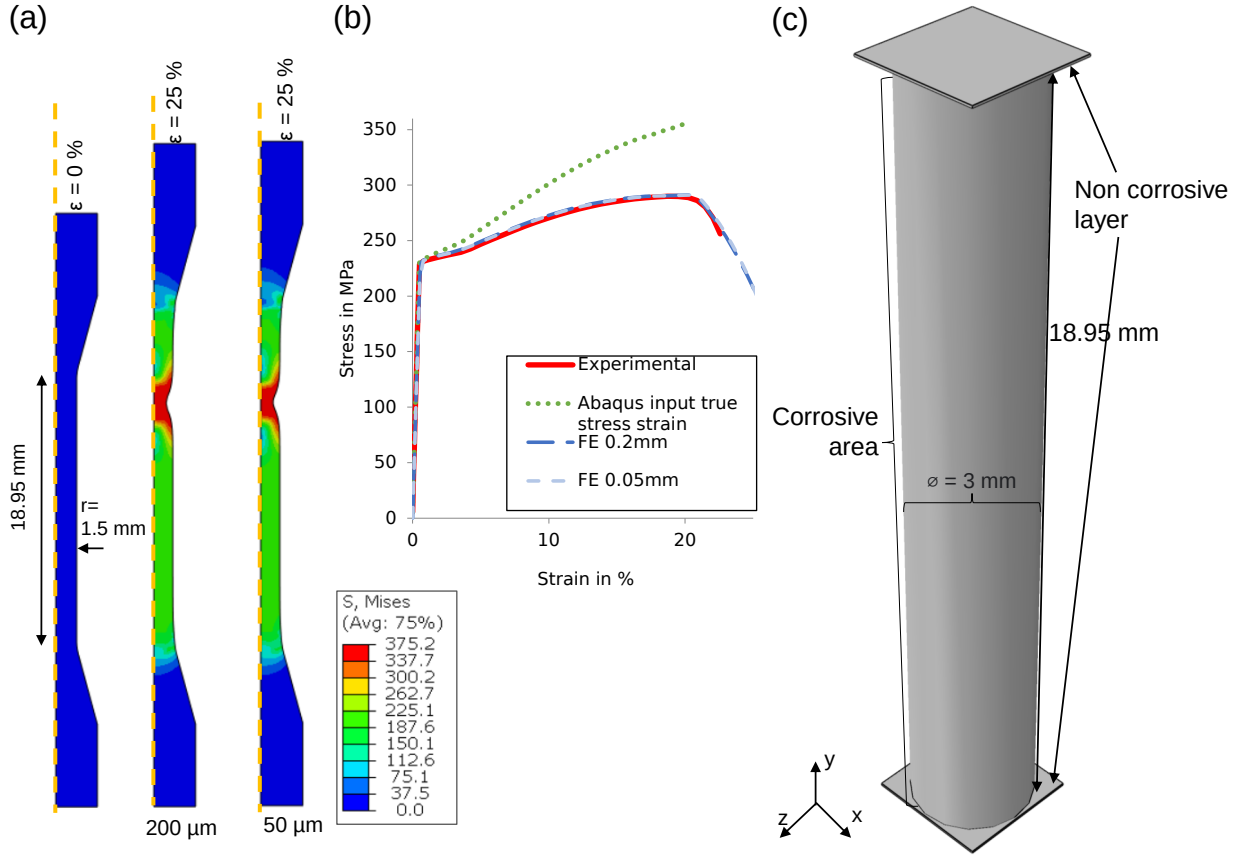

Figure 5.3: (a) axisymmetric finite element model for $\epsilon = 0\%$ and $\epsilon = 25\%$ for two different mesh sizes (200 and 50 µm) (b) Results calibration with axisymmetric model (c) simplified dimensions of the 3D model undergoing corrosion.

5.2.5 Data analysis

To analyse results, the key geometrical features (described in Section 5.2.3) were plotted against three main material properties, namely the (i) maximum specimen strength (σ_{max}), (ii) effective elastic modulus (Young's modulus) and (iii) strain at maximum specimen strength (ϵ at σ_{max}). The coefficient of determination (R^2) for a linear fitting was calculated for all data points (experimental and simulated data) to identify relationships between mechanical performance and spatial features of corrosion. In this data, results from the previous experimental study provided in Chapter 4 [33] characterising corrosion of magnesium WE43MEO alloy (Meotec GmbH, Aachen, Germany) were included. This data was

derived from an immersion study of cylindrical dog bone samples manufactured from a chill casted WE43MEO alloy for 28 days with weekly time steps in an incubator at 37 °C and 5 % CO_2 in simulated body fluid (c-SBF) [33, 46].

5.3 Results

5.3.1 Corrosion model

Several different corrosion profiles were generated that ranged from uniform corrosion to severe pitting/localised corrosion. Figure 5.4 (a) shows resulting 3D images of the corroding cylindrical specimens for the predefined mass losses for one of the corrosion scenarios ($B = 0.8$, $\gamma = 0.8$).

Figure 5.4 (b) shows 2D representations of the resulting corrosion profiles generated by *PitScan*, whereby the depth from the original cylindrical surfaces of each specimen is plotted at 50 % mass loss for each scenario. The influence of the Weibull-shape parameter (γ) on the severity of localised corrosion is clearly evident in the top row. Here, the spatial distribution of corrosion is almost uniform for the highest Weibull-shape parameter ($\gamma = 20$), while severe pitting and highly localised non-uniform corrosion becomes evident as the Weibull-shape parameter is decreased. Meanwhile, variation of the pit parameter B dictates the pit depth, pit area and pit density (see second row Figure 5.4 (b)). Higher values of B result in increasing pit density and pit depth, while the opening area of individual pits reduces. Consequently, lower values of B are attributed with wider but less deep pits and a lower density. Pseudo-random numbers were used, evolving from a predefined random seed. This results in the same pit locations being generated each time, with the only variation being the value of parameter B. As a result, the extent of individual pits varies, while their locations remain the same, only the Weibull-shape parameter γ influences the pit location. Though, γ is still the decisive parameter which controls the extent and location of localised corrosion

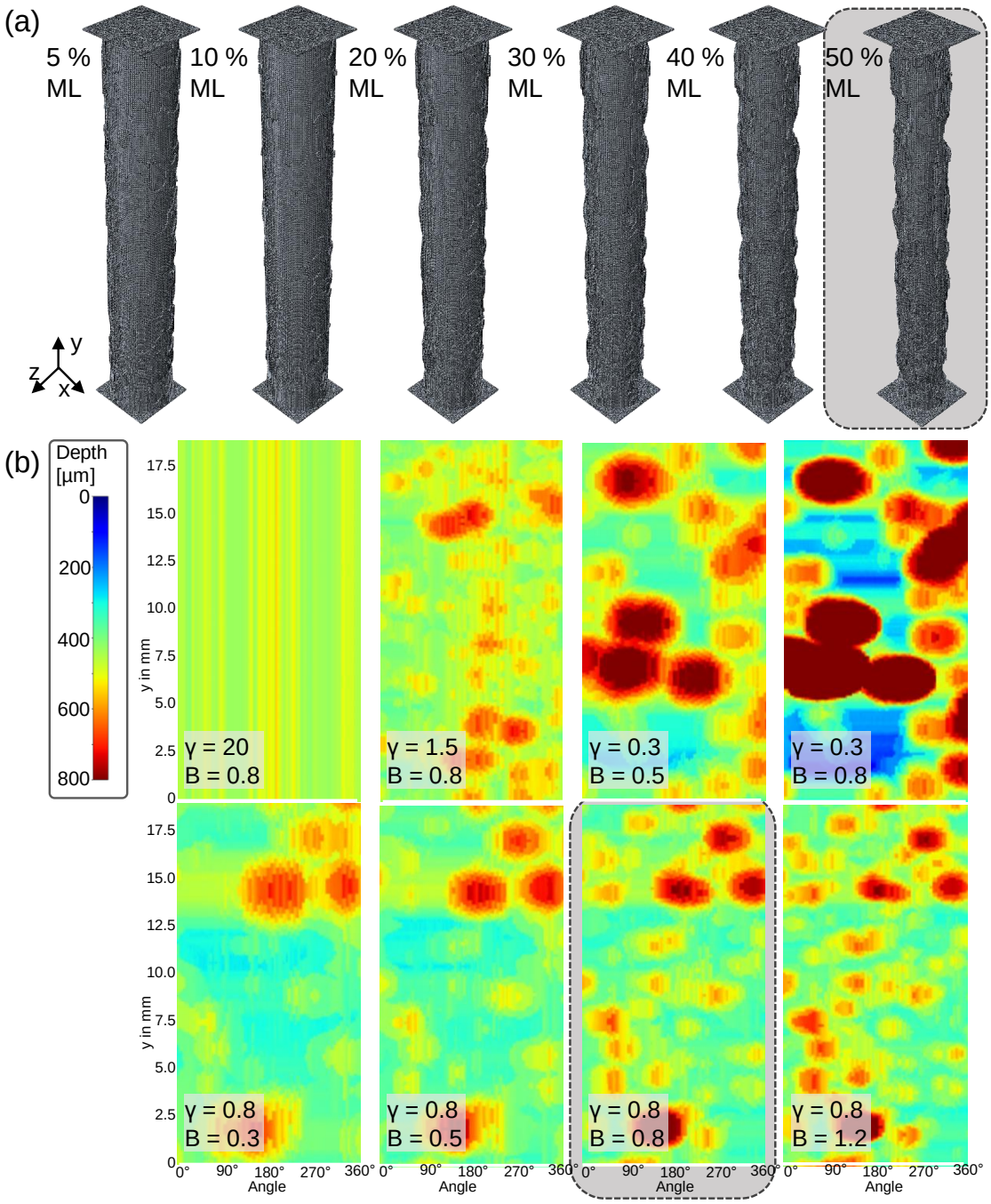

Figure 5.4: (a) Final 3D finite element models after degradation for different mass loss (ML) for one input set ($\gamma = 0.8$, $B = 0.8$); (b) Contour plots at 50 % mass loss for the eight different corrosion scenarios of the 3D circular gauge section (r_0=1.5 mm) by adapting the input values (γ, B) of the degradation model; grey highlighted figure shows the same model.

effects due to its influence on the initial random numbers.

Figure 5.5 shows the probability density functions that quantify the detected pit depths for all scenarios. Here, the experimental data from Chapter 4 are included as red lines, where suitable mass losses were available [33]. In the early stages of corrosion, the distributions for all corrosion scenarios are tight as small single pits develop. Over time, these pits evolve and coalesce to form larger pits that results in wider distribution functions. Interestingly, the experimental data showed close correlation to several of the simulated pitting profiles, in particular for the scenario that had parameters of $\gamma = 0.8$ and $B = 0.8$ or $B = 0.5$.

PitScan was used to quantify pitting parameters across all scenarios. Figure 5.6 shows this quantitative information, whereby various pitting parameters are plotted as a function of mass loss. These curves show the evolution of pitting features as corrosion progressed for each

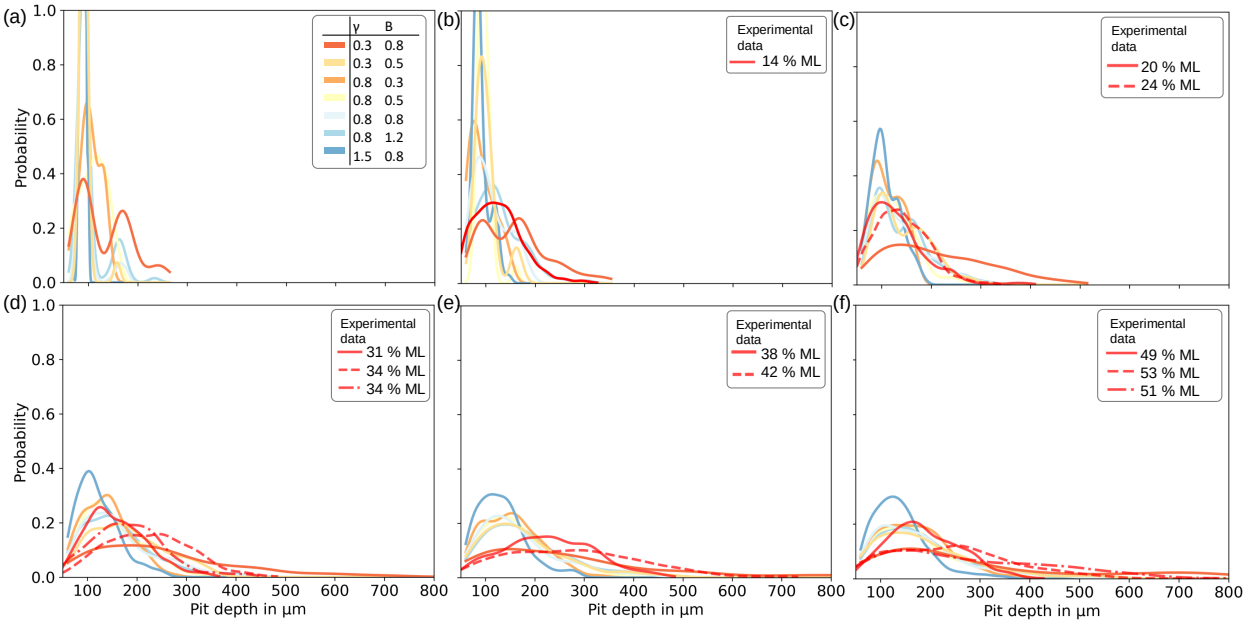

Figure 5.5: Pit depth distribution for seven localised corrosion profiles including similar experimental examined mass losses (a) 5 % (no similar experimental sample available), (b) 10 %, (c) 20 %. (d) 30 %, (e) 40 %. (f) 50 % Mass loss. (Legend for all given in (a))

simulated corrosion scenario. It must be noted that features relating to the evolution of pits (Figure 5.6 (a–d)) cannot be calculated for the uniform corrosion model ($\gamma = 20$, $B = 0.8$). This quantitative information shows the evolution of key pitting parameters in many cases to the non-uniformity of prescribed corrosion model parameters. For example, features such

as pitting factor (Figure 5.6 (a), average of 10 deepest pits Figure 5.6 (b), volume of all pits Figure 5.6 (d)), show the largest increases for ($\gamma = 0.3$, $B = 0.8$), with these changes becoming more modest as the corrosion scenario is more uniform. This is particularly true in the case of pitting factor [35], whereby values close to 1 depict more uniform formation, while higher values are attributed to more pitted profiles (Figure 5.6 (a)). Profiles with the same initial shape parameter of the Weibull-curve ($\gamma = 0.8$) resulted in similar trends in average radius loss (Figure 5.6 (e)), minimum width (Figure 5.6 (g)) and maximal detected area loss (Figure 5.6 (h)) across all pit parameter (B) values. For almost all parameters, the experimental data is distributed throughout the simulated corrosion scenarios indicating that the corrosion model is quite effective in replicating the spatial phenomenology of surface-based corrosion. The only exception here is the corrosion model's capacity to predict the pit density (see Figure 5.6 (c)), which is limited due to the finite mesh dimensions of an element size of 80 µm.

5.3.2 Mechanical modelling

5.3.2.1 Model calibration

Model parameter fitting was carried out by calibrating the mechanical model to experimental data through an axisymmetric model of the tensile dog bone specimens and the results of this process are shown in Figure 5.3 (b). This model accurately captures key features of the nominal stress/strain response determined from experiments, with the hardening and ultimate tensile strength of the magnesium correctly predicted by the model. Furthermore, the contour plots of these simulations (Figure 5.3 (a)) demonstrate that the ultimate tensile strength is reached due the predicted necking behaviour of the ductile magnesium alloy, which was also observed in experiments. The Considère criterion says that necking occurs when true stress reaches the strain hardening rate [53], whereby $\frac{d\sigma_{true}}{d\epsilon_{true}} = \sigma_{true}$. Prior to necking, the effect of strain-hardening is stronger than the effect of the area reduction. With

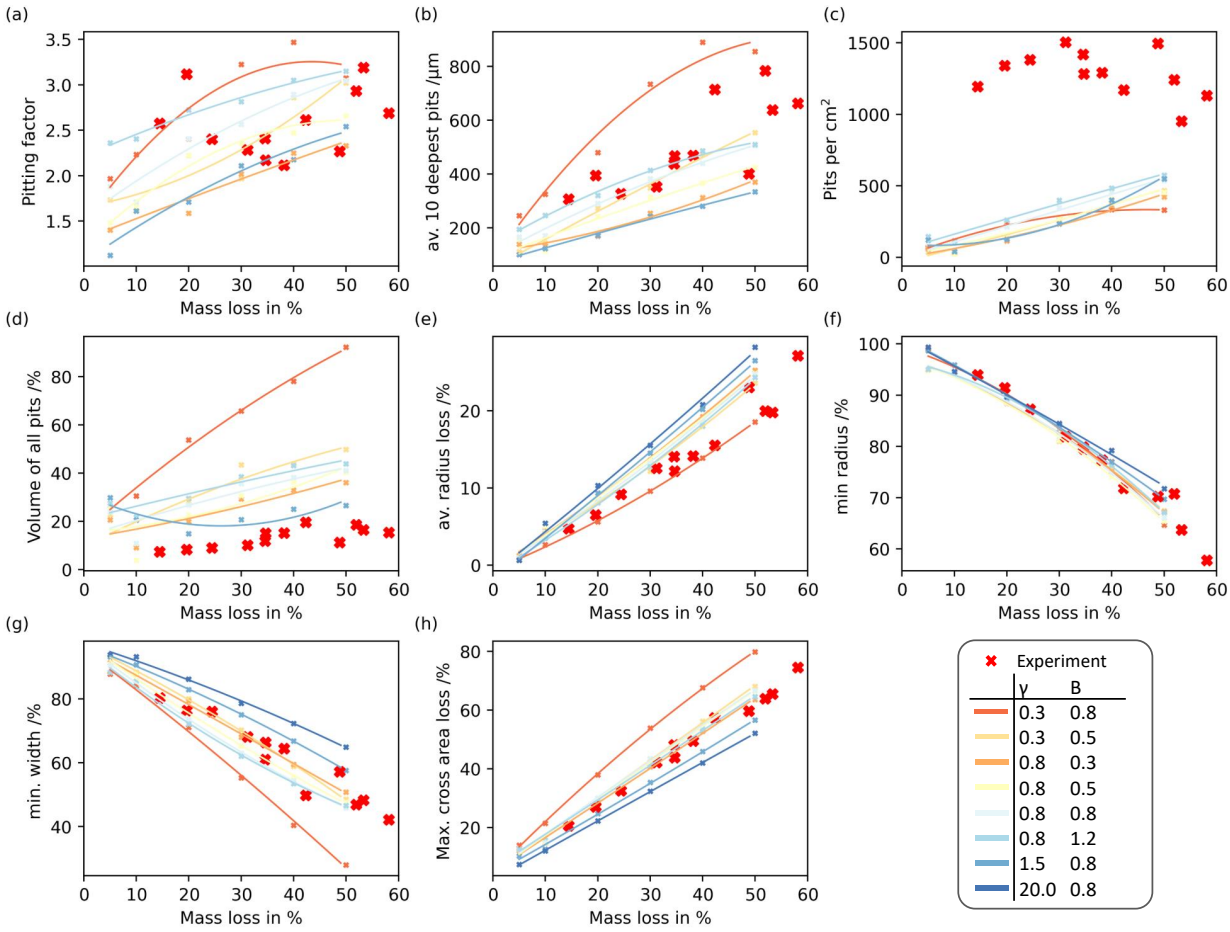

Figure 5.6: Most relevant phenomenological corrosion features vs. detected mass loss. (Plots with features related to localised corrosion are plotted without the uniform corrosion profiles (a–d)).

an increase in strain this phenomenon reverses, which leads to the formation of necking. This phenomenon in perfect models was also reported by Joun et al. in detail [54]. The behaviour was demonstrated to be independent of mesh sensitivity effects, whereby both 200 and 50 µm element size showed similar responses (see Figure 5.3 (b)).

Figure 5.7 (a) shows the results of the calibrated model, which has been extended to three dimensions. For the uncorroded sample (0 % mass loss) there is only a slightly higher elongation compared to the axisymmetric model used for the fitting process, with the stress-strain response of the WE43MEO alloy is still fully captured.

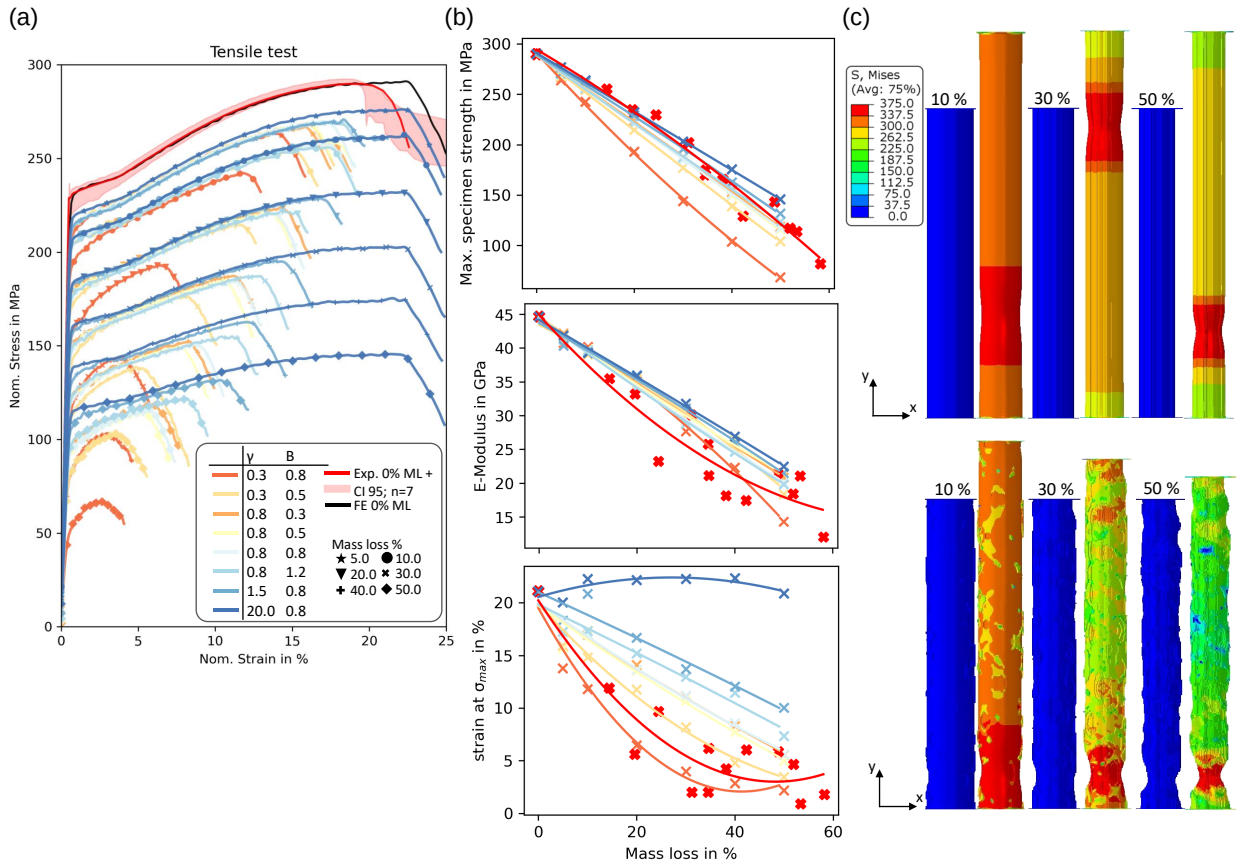

Figure 5.7: (a) Uniaxial tensile tests: experimental data (red area: Confidence Interval (CI) for n = 7 of undegraded samples) vs. simulated data (including data for several mass losses and the eight pit scenarios); (b) Maximum specimen strength (σ_{max}), Elongation at σ_{max} and effective E-Modulus over Mass loss for the eight corrosion scenarios and the experimental data set; lines are second degree polynomial fits for each scenario; (c) contour plots showing Von Mises stress distribution for two different model input parameters (on top: $\gamma = 20, B = 0.8$; bottom: $\gamma = 0.8$, $B = 0.8$) at three different mass losses each unloaded and maximal loaded under uniaxial tension.

5.3.2.2 Mechanical performance of corroding samples

Figure 5.7 (a) shows the simulated uniaxial tensile response for the corroding samples of all considered scenarios. In general, the specimen strength and elongation decrease for higher mass loss percentages. However, for the uniform model ($\gamma = 20.0$, $B = 0.8$), there is no reduction in the strain at σ_{max} as corrosion progressed. Figure 5.7 (b) shows that there is a strong relationship between specimen strength (σ_{max}) and mass loss for all computational scenarios considered, with many of these capturing the trend observed experimentally. σ_{max} is mostly taken as the relevant factor for calibrating a degradation model to an experimental

data set [19, 20]. The relationship between strain at σ_{max} (Figure 5.7 (b) bottom) shows greater variation in the predicted results across different corrosion scenarios. This clearly demonstrates that uniform corrosion is not suitable as a corrosion model for the examined WE43MEO alloy, as it does not capture any reduction in strain at σ_{max}. The effective Young's Modulus over mass loss (Figure 5.7 (b) middle) follows largely similar behaviour to the trends seen for specimen strength (σ_{max}). Overall, the severely pitted models ($\gamma = 0.3$, $B = 0.8$ or 0.5) showed the best agreement with the properties determined experimentally. Contour plots of the Von Mises stress are presented in Figure 5.7 (c) for the unloaded and maximal loaded step, respectively. Exemplarily, the uniform model and a pitted profile is taken with different mass losses. All models show the necking behaviour, which is also observed within the tested dog bones.

5.3.3 Correlations

Having proved the suitability of the corrosion model in capturing the phenomenology of corrosion (Section 5.3.1), as well as the mechanical mechanistic (Section 5.3.2), relations between key pitting parameters and the mechanical integrity can be established. Figure 5.8 (a–c) shows correlation plots that establish quantitative relationships between the pitting parameters calculated by *PitScan* and the predicted mechanical parameters (σ_{max}, strain at σ_{max}, and the effective Young's Modulus). Furthermore, included here are the experimental results from Chapter 4 [33]. Again, it must be noted that the uniform model ($\gamma = 20.0$, $B = 0.8$) was excluded for features which are related to the formation of pits (pit depth, pit density, pitting factor, etc.). The parameters described in ASTM G46-94 [35] for evaluating pitting corrosion were taken as a starting point for this analysis and extended by several more suitable features, which potentially are linked to the mechanical integrity. A coefficient of determination was calculated for all plots by including all data presented. Features with high R^2 values are considered to be independent of the profile formation, while features with

low R^2 values are highly dependent on the corrosion profile. In Figure 5.8 (a), there is a clear correlation between features linked to the reduction of the cross-sectional area and the specimen strength (σ_{max}), with minimum radius, minimum width and maximal cross-sectional area loss all having $R^2 > 0.9$. It is important to note that these pitting parameters are independently correlated to specimen strength (σ_{max}) across all simulated scenarios and the available experimental data. Potential scenario-based features can be also identified in Figure 5.8 like the pitting factor ($R^2 = 0.53$), volume loss by pits ($R^2 = 0.27$) and the average radius loss ($R^2 = 0.82$). On the other hand, the detected maximal cross-sectional area loss shows an almost linear correlation to the remaining specimen strength, and no distinguishable trends for the profiles are visible. No correlation was observed for pit density, which was again likely due to the finite mesh dimensions used in the computational model (80 µm). The strain at maximum specimen strength (Figure 5.8 (b)) shows for all features distinguishable trends between the tested scenarios. Even features which are scenario-independent for σ_{max} and the effective Young's modulus are scenario-dependent for the maximum strain (like minimum width, max. cross-sectional area loss, minimum fitted radius). This behaviour underlines the importance of considering the strain value for calibrating degradation models. The manner of the formation of pits seems to highly dictate the strain response, and a uniform model is not suitable as a degradation model, because of the non-reduction in strain over several mass losses. Figure 5.8 (c) shows the relationship between the pitting features and the effective Young's modulus. In general, a similar response compared to σ_{max} is visible, however the dependence of effective Young's modulus on the maximal cross-sectional area loss is not as clear as it was observed for σ_{max}.

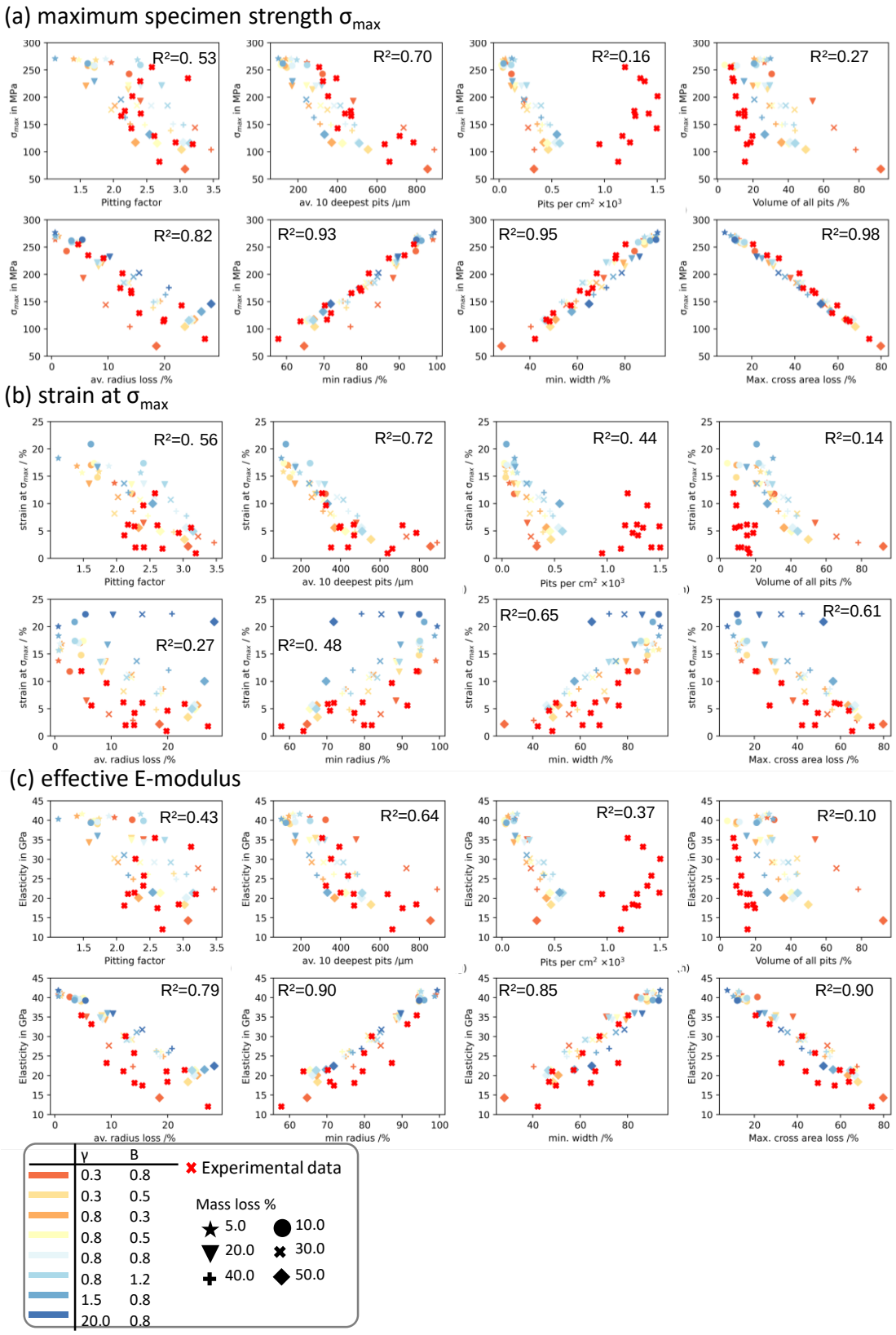

Figure 5.8: Correlation plots of eight most important phenomenological corrosion features over (a) remaining specimen strength σ_{max}, (b) strain at σ_{max}, (c) effective E-modulus. First row each, are features belonging to the formation of pits, so the uniform model ($\gamma = 20.0$) was excluded.

5.4 Discussion

In this study, a computational framework was developed to establish mechanistic relationships between the localised corrosion and mechanical performance of a magnesium-based alloy. A finite element-based corrosion model [20] was used to generate corrosion profiles, with subsequent uniaxial tensile test simulations to track the mechanical integrity. The Python-based detection framework *PitScan* provide detailed quantification of the phenomenological features of corrosion, including a full spatial tracking of surface-based corrosion. Through this approach, this study is the first to quantitatively demonstrate that a surface-based non-uniform corrosion model can capture both the geometrical and mechanical features of a magnesium alloy undergoing corrosion by comparing to experimental data [33]. Using this verified corrosion modelling approach, this study evaluated a wide range of corrosion scenarios and enabled quantitative relationships to be established between the mechanical integrity and key phenomenological corrosion features. In particular, it was demonstrated that parameters that were directly linked to the reduction of the cross-sectional area of the specimen were the best predictors of mechanical performance.

Rapid mechanical deterioration of magnesium-based medical implants has limited their implementation in load-bearing applications [55, 56]. While the accelerated loss of mechanical integrity of specimens undergoing corrosion has previously been linked to pitting corrosion through qualitative means [19, 20], there has been a lack of understanding mechanistic relationships between corrosion and mechanical performance. Here, it was clearly demonstrated that the deterioration in mechanical performance of corroding specimens is directly linked to localised corrosion and a comprehensive set of quantitative relationships between surface-based pit formation and the mechanical performance, described by specimen strength (σ_{max}), strain at maximum strength (ϵ at σ_{max}) and Young's modulus (E), is provided. The current data set shows that the minimal cross-sectional area is the strongest predictor of the remaining mechanical strength ($R^2 = 0.98$), and this parameter is independent of the severity or

spatial features of localised surface corrosion. Interestingly, however, minimal cross-sectional area was not predictive of the failure strain of the specimen, whereby there was substantial variation of this parameter with the various profiles simulated, particularly when uniform corrosion scenarios were considered. Instead, it was found that parameters relating to the deepest pits better correlated with strain at failure. From experimental data, there is a clear reduction of the strain-to-failure in corroding specimens [19, 20, 33, 37], which is likely a result of localised corrosion providing suitable imperfection(s) that allow damage to localise. On the other hand, minimal cross-sectional area did show good correlation with the reducing remaining elastic modulus ($R^2 = 0.98$), which was again independent of the corroding profile considered. Interestingly, the analysis demonstrated that parameters described in ASTM G46-94 (e.g. pitting factor, average of ten deepest pits) showed weaker correlations to the mechanical integrity of corroding specimens, highlighting the importance of considering the other parameters detailed here (e.g. minimum cross-sectional area).

This study quantitatively demonstrates that a finite element-based corrosion model can capture both the geometrical and mechanical features of a magnesium alloy undergoing corrosion. Until now, many other corrosion-based models have assumed uniform corrosion [38–42], or have implemented non-uniform surface-based corrosion through stochastic approaches, but have not presented any validation of in capturing geometric features of corrosion, or associated implications on mechanical performance. Instead, there has tended to be calibration of model parameters to fit the bulk mechanical performance over time [19, 20, 43, 44]. The current study has shown that it is possible to control the geometrical formation of localised corrosion features by two factors (γ and B) of the corrosion model. This corrosion model framework has the potential to be used for any metal type that undergoes surface-based corrosion, and is not limited to magnesium-based alloys. Furthermore, the corrosion model presented here not only enables control of the severity of pitting, but it is also possible to adjust the width, depth and density of pits evolving. Plotting corrosion features over the predefined mass loss resulted in clear trends for each profile (Figure 5.6), so that each set

is clearly distinguishable from each other. Pitting factor described in ASTM G46-94 [35] follows this trend and the calculated values show that a pitting factor of 1 describes a uniform behaviour, while higher values are related to more pitted profiles. An increasing pitting factor with an increase in mass loss in all scenarios was observed. Importantly, the findings demonstrated that a uniform degradation model is not suitable to predict the mechanical response for magnesium alloys that are undergoing corrosion, i.e., degrading in the human body. Uniform corrosion models have two major failings in that the predicted reduction in specimen strength is proportional to the mass loss and the strain at failure remains largely constant for all simulated mass losses (see Figure 5.8). Although it was not the initial goal of the study, a combination of γ and B was identified, which tend to fit best the experimental data in terms of both geometric and mechanical performance.

In addressing the limitations of the current study, it should be noted that the corrosion model fails to replicate the pit density that was observed experimentally, which is a direct result of the limited element size within the finite element mesh. However, this is necessary to achieve simulated results within an appropriate computational time. These plots clearly show the limits of the finite element model in predicting the pit density (Pits per cm^2). Here, all models weaken to replicate the experimental data due to the limits of the mesh size. Nevertheless, a mesh sensitivity analysis examining smaller element sizes was not conducted to confirm whether smaller elements would yield more accurate results. Also, the used threshold of 50 µm as the minimum depth to be accounted as pit, has a potential influence on the measured pit density. However, it was found experimentally that this feature does not have a strong correlation with mechanical parameters and, instead, the corrosion features that dominate the mechanical response are related to larger scale parameters (e.g. minimum radius), which are represented quite well in the model meaning that the mechanical response can still be captured. Additionally, the used phenomenological degradation model neglects the formation of the outer degradation layer with its ion compositions. However, to include its effect on the overall degradation with a sufficient mesh sensitive with subsequent

uniaxial tensile test requires a massive computational power. Further, it must be noted that stress corrosion cracking effects were fully neglected, which could accelerate degradation [20, 57, 58]. Furthermore, using in-vitro tests as a benchmark can lead to different corrosion performance compared to the corrosion mechanism in the human body. Nevertheless, the focus of the current study is on the correlation between any pit formation and the relating mechanical response, independently of how and where it evolves. Often lower degradation rates in-vivo were reported than in in-vitro tests (especially for TRIS- or HEPES-buffered media) [59, 60]. Here, an accelerated degradation rate is favourable to achieve reasonable mass losses within an appropriate time period.

5.5 Conclusion

This study demonstrated that a surface-based non-uniform corrosion model can capture both the geometrical and mechanical features of a magnesium alloy undergoing corrosion by comparing to experimental data. Using this verified corrosion modelling approach, this study demonstrated that the minimal cross-sectional area parameter was the strongest predictor of the remaining mechanical strength ($R^2 = 0.98$), with this relationship being independent of the severity or spatial features of localised surface corrosion. Findings demonstrated that a uniform degradation model is not suitable for simulating the mechanical response for magnesium alloys that are undergoing corrosion. Interestingly, the current analysis demonstrated that parameters described in ASTM G46-94 showed weaker correlations to the mechanical integrity of corroding specimens, compared to parameters determined by *PitScan*. This study establishes new mechanistic insight into the performance of the magnesium-based materials undergoing corrosion within biological environments.

References

[1] H. Nygren, P. Malmberg, and Y. Liu, "MgO Implanted in Rat Tibia Bone Marrow is Osteoinductive through the Formation of a Matrix, Containing Hydroxyapatite," in *Materials Science Forum*, vol. 879, pp. 1404–1407, ISBN: 1662-9752. DOI: 10.4028/www.scientific.net/MSF.879.1404.

[2] A. Burmester, R. Willumeit-Romer, and F. Feyerabend, "Behavior of bone cells in contact with magnesium implant material," *J Biomed Mater Res B Appl Biomater*, vol. 105, no. 1, pp. 165–179, 2017, ISSN: 1552-4981 (Electronic) 1552-4973 (Linking). DOI: 10.1002/jbm.b.33542. [Online]. Available: https://www.ncbi.nlm.nih.gov/pubmed/26448207.

[3] L. Wu, F. Feyerabend, A. F. Schilling, R. Willumeit-Romer, and B. J. C. Luthringer, "Effects of extracellular magnesium extract on the proliferation and differentiation of human osteoblasts and osteoclasts in coculture," *Acta Biomater*, vol. 27, pp. 294–304, 2015, ISSN: 1878-7568 (Electronic) 1742-7061 (Linking). DOI: 10.1016/j.actbio.2015.08.042. [Online]. Available: https://www.ncbi.nlm.nih.gov/pubmed/26318802.

[4] F. Witte, H. Ulrich, C. Palm, and E. Willbold, "Biodegradable magnesium scaffolds: Part II: peri-implant bone remodeling," *J Biomed Mater Res A*, vol. 81, no. 3, pp. 757–765, 2007, ISSN: 1549-3296 (Print) 1549-3296 (Linking). DOI: 10.1002/jbm.a.31293. [Online]. Available: https://www.ncbi.nlm.nih.gov/pubmed/17390322.

[5] N. Kawamura, Y. Nakao, R. Ishikawa, D. Tsuchida, and M. Iijima, "Degradation and Biocompatibility of AZ31 Magnesium Alloy Implants In Vitro and In Vivo: A Micro-Computed Tomography Study in Rats," *Materials (Basel)*, vol. 13, no. 2, 2020, ISSN: 1996-1944 (Print) 1996-1944 (Linking). DOI: 10.3390/ma13020473. [Online]. Available: https://www.ncbi.nlm.nih.gov/pubmed/31963840.

[6] T. Kraus, S. F. Fischerauer, A. C. Hanzi, P. J. Uggowitzer, J. F. Loffler, and A. M. Weinberg, "Magnesium alloys for temporary implants in osteosynthesis: in vivo studies of their degradation and interaction with bone," *Acta Biomater*, vol. 8, no. 3, pp. 1230–8, 2012, ISSN: 1878-7568 (Electronic) 1742-7061 (Linking). DOI: 10.1016/j.actbio.2011.11.008. [Online]. Available: https://www.ncbi.nlm.nih.gov/pubmed/22107870.

[7] D. Sumner, "Long-term implant fixation and stress-shielding in total hip replacement," *Journal of Biomechanics*, vol. 48, no. 5, pp. 797–800, 2015, ISSN: 0021-9290.

[8] S. Agarwal, J. Curtin, B. Duffy, and S. Jaiswal, "Biodegradable magnesium alloys for orthopaedic applications: A review on corrosion, biocompatibility and surface modifications," *Mater Sci Eng C Mater Biol Appl*, vol. 68, pp. 948–963, 2016, ISSN: 1873-0191 (Electronic) 0928-4931 (Linking). DOI: 10.1016/j.msec.2016.06.020. [Online]. Available: https://www.ncbi.nlm.nih.gov/pubmed/27524097.

[9] Y. Chen, Z. Xu, C. Smith, and J. Sankar, "Recent advances on the development of magnesium alloys for biodegradable implants," *Acta Biomater*, vol. 10, no. 11, pp. 4561–4573, 2014, ISSN: 1878-7568 (Electronic) 1742-7061 (Linking). DOI: 10.1016/j.actbio.2014.07.005. [Online]. Available: https://www.ncbi.nlm.nih.gov/pubmed/25034646.

[10] G. B. Darband, M Aliofkhazraei, P Hamghalam, and N Valizade, "Plasma electrolytic oxidation of magnesium and its alloys: Mechanism, properties and applications," *Journal of Magnesium and Alloys*, vol. 5, no. 1, pp. 74–132, 2017, ISSN: 2213-9567. DOI: 10.1016/j.jma.2017.02.004.

[11] A. Kopp, T. Derra, M. Muther, L. Jauer, J. H. Schleifenbaum, M. Voshage, O. Jung, R. Smeets, and N. Kroger, "Influence of design and postprocessing parameters on the degradation behavior and mechanical properties of additively manufactured magnesium scaffolds," *Acta Biomater*, vol. 98, pp. 23–35, 2019, ISSN: 1878-7568 (Electronic) 1742-7061 (Linking). DOI: 10.1016/j.actbio.2019.04.012. [Online]. Available: https://www.ncbi.nlm.nih.gov/pubmed/30959185.

[12] H. M. Wong, K. W. Yeung, K. O. Lam, V. Tam, P. K. Chu, K. D. Luk, and K. M. Cheung, "A biodegradable polymer-based coating to control the performance of magnesium alloy orthopaedic implants," *Biomaterials*, vol. 31, no. 8, pp. 2084–96, 2010, ISSN: 1878-5905 (Electronic) 0142-9612 (Linking). DOI: 10.1016/j.biomaterials.2009.11.111. [Online]. Available: https://www.ncbi.nlm.nih.gov/pubmed/20031201.

[13] M. Abdalla, A. Joplin, M. Elahinia, and H. Ibrahim, "Corrosion Modeling of Magnesium and Its Alloys for Biomedical Applications: Review," *Corrosion and Materials Degradation*, vol. 1, no. 2, pp. 219–248, 2020, ISSN: 2624-5558. DOI: 10.3390/cmd1020011.

[14] M. F. Montemor, "Corrosion issues in joining lightweight materials: A review of the latest achievements," *Physical Sciences Reviews*, vol. 1, no. 2, 2016, ISSN: 2365-659X. DOI: 10.1515/psr-2015-0011.

[15] H. Xu, T. Hu, M. Wang, Y. Zheng, H. Qin, H. Cao, and Z. An, "Degradability and biocompatibility of magnesium-MAO: The consistency and contradiction between in-vitro and in-vivo outcomes," *Arabian Journal of Chemistry*, vol. 13, no. 1, pp. 2795–2805, 2020, ISSN: 18785352. DOI: 10.1016/j.arabjc.2018.07.010.

[16] Y. Koo, H. B. Lee, Z. Dong, R. Kotoka, J. Sankar, N. Huang, and Y. Yun, "The Effects of Static and Dynamic Loading on Biodegradable Magnesium Pins In Vitro and In Vivo," *Sci Rep*, vol. 7, no. 1, p. 14 710, 2017, ISSN: 2045-2322 (Electronic) 2045-2322 (Linking). DOI: 10.1038/s41598-017-14836-5. [Online]. Available: https://www.ncbi.nlm.nih.gov/pubmed/29089642.

[17] Y. Xu, H. Meng, H. Yin, Z. Sun, J. Peng, X. Xu, Q. Guo, W. Xu, X. Yu, Z. Yuan, B. Xiao, C. Wang, Y. Wang, S. Liu, S. Lu, Z. Wang, and A. Wang, "Quantifying the degradation of degradable implants and bone formation in the femoral condyle

using micro-CT 3D reconstruction," *Exp Ther Med*, vol. 15, no. 1, pp. 93–102, 2018, ISSN: 1792-0981 (Print) 1792-0981 (Linking). DOI: 10.3892/etm.2017.5389. [Online]. Available: https://www.ncbi.nlm.nih.gov/pubmed/29375677.

[18] O. Jung, R. Smeets, P. Hartjen, R. Schnettler, F. Feyerabend, M. Klein, N. Wegner, F. Walther, D. Stangier, A. Henningsen, C. Rendenbach, M. Heiland, M. Barbeck, and A. Kopp, "Improved In Vitro Test Procedure for Full Assessment of the Cytocompatibility of Degradable Magnesium Based on ISO 10993-5/-12," *Int J Mol Sci*, vol. 20, no. 2, 2019, ISSN: 1422-0067 (Electronic) 1422-0067 (Linking). DOI: 10.3390/ijms20020255. [Online]. Available: https://www.ncbi.nlm.nih.gov/pubmed/30634646.

[19] E. L. Boland, R. N. Shirazi, J. A. Grogan, and P. E. McHugh, "Mechanical and Corrosion Testing of Magnesium WE43 Specimens for Pitting Corrosion Model Calibration," *Advanced Engineering Materials*, vol. 20, no. 10, 2018, ISSN: 14381656. DOI: 10.1002/adem.201800656.

[20] J. A. Grogan, B. J. O'Brien, S. B. Leen, and P. E. McHugh, "A corrosion model for bioabsorbable metallic stents," *Acta Biomater*, vol. 7, no. 9, pp. 3523–33, 2011, ISSN: 1878-7568 (Electronic) 1742-7061 (Linking). DOI: 10.1016/j.actbio.2011.05.032. [Online]. Available: https://www.ncbi.nlm.nih.gov/pubmed/21664498.

[21] G. Song, A. Atrens, and D. StJohn, "An Hydrogen Evolution Method for the Estimation of the Corrosion Rate of Magnesium Alloys," in *Essential Readings in Magnesium Technology*, S. N. Mathaudhu, A. A. Luo, N. R. Neelameggham, E. A. Nyberg, and W. H. Sillekens, Eds. Cham: Springer International Publishing, 2001, pp. 565–572, ISBN: 978-3-319-48099-2. DOI: 10.1007/978-3-319-48099-2_90.

[22] M. Li, Y. Cheng, Y. F. Zheng, X. Zhang, T. F. Xi, and S. C. Wei, "Surface characteristics and corrosion behaviour of WE43 magnesium alloy coated by SiC film," *Applied Surface Science*, vol. 258, no. 7, pp. 3074–3081, 2012, ISSN: 01694332. DOI: 10.1016/j.apsusc.2011.11.040.

[23] D. Mei, S. V. Lamaka, J. Gonzalez, F. Feyerabend, R. Willumeit-Römer, and M. L. Zheludkevich, "The role of individual components of simulated body fluid on the corrosion behavior of commercially pure Mg," *Corrosion Science*, vol. 147, pp. 81–93, 2019, ISSN: 0010938X. DOI: 10.1016/j.corsci.2018.11.011.

[24] I. Marco, F. Feyerabend, R. Willumeit-Romer, and O. Van der Biest, "Degradation testing of Mg alloys in Dulbecco's modified eagle medium: Influence of medium sterilization," *Mater Sci Eng C Mater Biol Appl*, vol. 62, pp. 68–78, 2016, ISSN: 1873-0191 (Electronic) 0928-4931 (Linking). DOI: 10.1016/j.msec.2016.01.039. [Online]. Available: https://www.ncbi.nlm.nih.gov/pubmed/26952399.

[25] X. Gu, Y. Zheng, Y. Cheng, S. Zhong, and T. Xi, "In vitro corrosion and biocompatibility of binary magnesium alloys," *Biomaterials*, vol. 30, no. 4, pp. 484–498, 2009, ISSN: 0142-9612. DOI: 10.1016/j.biomaterials.2008.10.021.

[26] E Angelini, S Grassini, F Rosalbino, F Fracassi, and R d'Agostino, "Electrochemical impedance spectroscopy evaluation of the corrosion behaviour of Mg alloy coated with PECVD organosilicon thin film," *Progress in Organic Coatings*, vol. 46, no. 2, pp. 107–111, 2003, ISSN: 0300-9440. DOI: 10.1016/S0300-9440(02)00217-5.

[27] B. Zhang, Y. Hou, X. Wang, Y. Wang, and L. Geng, "Mechanical properties, degradation performance and cytotoxicity of Mg–Zn–Ca biomedical alloys with different compositions," *Materials Science and Engineering: C*, vol. 31, no. 8, pp. 1667–1673, 2011, ISSN: 09284931. DOI: 10.1016/j.msec.2011.07.015.

[28] A. M. Lafront, W. Zhang, S. Jin, R. Tremblay, D. Dubé, and E. Ghali, "Pitting corrosion of AZ91D and AJ62x magnesium alloys in alkaline chloride medium using electrochemical techniques," *Electrochimica Acta*, vol. 51, no. 3, pp. 489–501, 2005, ISSN: 00134686. DOI: 10.1016/j.electacta.2005.05.013.

[29] J. Harmuth, B. Wiese, J. Bohlen, T. Ebel, and R. Willumeit-Römer, "Wide Range Mechanical Customization of Mg-Gd Alloys With Low Degradation Rates by Extrusion," *Frontiers in Materials*, vol. 6, 2019, ISSN: 2296-8016. DOI: 10.3389/fmats.2019.00201.

[30] N. A. Agha, F. Feyerabend, B. Mihailova, S. Heidrich, U. Bismayer, and R. Willumeit-Romer, "Magnesium degradation influenced by buffering salts in concentrations typical of in vitro and in vivo models," *Mater Sci Eng C Mater Biol Appl*, vol. 58, pp. 817–25, 2016, ISSN: 1873-0191 (Electronic) 0928-4931 (Linking). DOI: 10.1016/j.msec.2015.09.067. [Online]. Available: https://www.ncbi.nlm.nih.gov/pubmed/26478376.

[31] J. Walker, S. Shadanbaz, N. T. Kirkland, E. Stace, T. Woodfield, M. P. Staiger, and G. J. Dias, "Magnesium alloys: predicting in vivo corrosion with in vitro immersion testing," *J Biomed Mater Res B Appl Biomater*, vol. 100, no. 4, pp. 1134–41, 2012, ISSN: 1552-4981 (Electronic) 1552-4973 (Linking). DOI: 10.1002/jbm.b.32680.

[32] F. Witte, J. Fischer, J. Nellesen, C. Vogt, J. Vogt, T. Donath, and F. Beckmann, "In vivo corrosion and corrosion protection of magnesium alloy LAE442," *Acta Biomater*, vol. 6, no. 5, pp. 1792–9, 2010, ISSN: 1878-7568 (Electronic) 1742-7061 (Linking). DOI: 10.1016/j.actbio.2009.10.012. [Online]. Available: https://www.ncbi.nlm.nih.gov/pubmed/19822226.

[33] K. van Gaalen, F. Gremse, F. Benn, P. E. McHugh, A. Kopp, and T. J. Vaughan, "Automated ex-situ detection of pitting corrosion and its effect on the mechanical integrity of rare earth magnesium alloy - WE43," *Bioactive Materials*, 2022, ISSN: 2452199X. DOI: 10.1016/j.bioactmat.2021.06.024.

[34] S. Meyer, A. Wolf, D. Sanders, K. Iskhakova, H. Ćwieka, S. Bruns, S. Flenner, I. Greving, J. Hagemann, R. Willumeit-Römer, B. Wiese, and B. Zeller-Plumhoff, "Degradation Analysis of Thin Mg-xAg Wires Using X-ray Near-Field Holotomography," *Metals*, vol. 11, no. 9, 2021, ISSN: 2075-4701. DOI: 10.3390/met11091422.

[35] ASTM G46-94, *Standard Guide for Examination and Evaluation of Pitting Corrosion*. PA: ASTM International West Conshohocken, 2005. DOI: 10.1520/g0046-94r18.

[36] A. Krause, N. von der Höh, D. Bormann, C. Krause, F.-W. Bach, H. Windhagen, and A. Meyer-Lindenberg, "Degradation behaviour and mechanical properties of magnesium implants in rabbit tibiae," *Journal of Materials Science*, vol. 45, no. 3, pp. 624–632, 2010, ISSN: 0022-2461. DOI: 10.1007/s10853-009-3936-3.

[37] I. Adekanmbi, C. Z. Mosher, H. H. Lu, M. Riehle, H. Kubba, and K. E. Tanner, "Mechanical behaviour of biodegradable AZ31 magnesium alloy after long term in vitro degradation," *Mater Sci Eng C Mater Biol Appl*, vol. 77, pp. 1135–1144, 2017, ISSN: 1873-0191 (Electronic). DOI: 10.1016/j.msec.2017.03.216. [Online]. Available: https://www.ncbi.nlm.nih.gov/pubmed/28531989.

[38] J. A. Grogan, S. B. Leen, and P. E. McHugh, "A physical corrosion model for bioabsorbable metal stents," *Acta Biomater*, vol. 10, no. 5, pp. 2313–22, 2014, ISSN: 1878-7568 (Electronic). DOI: 10.1016/j.actbio.2013.12.059. [Online]. Available: https://www.ncbi.nlm.nih.gov/pubmed/24412771.

[39] P. Bajger, J. M. A. Ashbourn, V. Manhas, Y. Guyot, K. Lietaert, and L. Geris, "Mathematical modelling of the degradation behaviour of biodegradable metals," *Biomech Model Mechanobiol*, vol. 16, no. 1, pp. 227–238, 2017, ISSN: 1617-7940 (Electronic) 1617-7940 (Linking). DOI: 10.1007/s10237-016-0812-3. [Online]. Available: https://www.ncbi.nlm.nih.gov/pubmed/27502687.

[40] A. K. Gartzke, S. Julmi, C. Klose, A. C. Waselau, A. Meyer-Lindenberg, H. J. Maier, S. Besdo, and P. Wriggers, "A simulation model for the degradation of magnesium-based bone implants," *J Mech Behav Biomed Mater*, vol. 101, p. 103 411, 2020, ISSN: 1878-0180 (Electronic) 1878-0180 (Linking). DOI: 10.1016/j.jmbbm.2019.103411. [Online]. Available: https://www.ncbi.nlm.nih.gov/pubmed/31546176.

[41] W. Wu, D. Gastaldi, K. Yang, L. Tan, L. Petrini, and F. Migliavacca, "Finite element analyses for design evaluation of biodegradable magnesium alloy stents in arterial vessels," *Materials Science and Engineering: B*, vol. 176, no. 20, pp. 1733–1740, 2011, ISSN: 09215107. DOI: 10.1016/j.mseb.2011.03.013.

[42] D. Gastaldi, V. Sassi, L. Petrini, M. Vedani, S. Trasatti, and F. Migliavacca, "Continuum damage model for bioresorbable magnesium alloy devices - Application to coronary stents," *J Mech Behav Biomed Mater*, vol. 4, no. 3, pp. 352–65, 2011, ISSN: 1878-0180 (Electronic) 1878-0180 (Linking). DOI: 10.1016/j.jmbbm.2010.11.003. [Online]. Available: https://www.ncbi.nlm.nih.gov/pubmed/21316623.

[43] N. Debusschere, P. Segers, P. Dubruel, B. Verhegghe, and M. De Beule, "A Computational Framework to Model Degradation of Biocorrodible Metal Stents Using an Implicit Finite Element Solver," *Ann Biomed Eng*, vol. 44, no. 2, pp. 382–90, 2016, ISSN: 1573-9686 (Electronic). DOI: 10.1007/s10439-015-1530-1. [Online]. Available: https://www.ncbi.nlm.nih.gov/pubmed/26703421.

[44] S. Ma, B. Zhou, and B. Markert, "Numerical simulation of the tissue differentiation and corrosion process of biodegradable magnesium implants during bone fracture healing," *ZAMM - Journal of Applied Mathematics and Mechanics / Zeitschrift für Angewandte Mathematik und Mechanik*, vol. 98, no. 12, pp. 2223–2238, 2018, ISSN: 0044-2267 1521-4001. DOI: 10.1002/zamm.201700314.

[45] A. Amerinatanzi, R. Mehrabi, H. Ibrahim, A. Dehghan, N. Shayesteh Moghaddam, and M. Elahinia, "Predicting the Biodegradation of Magnesium Alloy Implants: Modeling, Parameter Identification, and Validation," *Bioengineering (Basel)*, vol. 5, no. 4, 2018, ISSN: 2306-5354 (Print). DOI: 10.3390/bioengineering5040105. [Online]. Available: https://www.ncbi.nlm.nih.gov/pubmed/30501102.

[46] A. Oyane, H. Kim, T. Furuya, T. Kokubo, T. Miyazaki, and T. Nakamura, "Preparation and assessment of revised simulated body fluids," *J. Biomed. Mater. Res.*, vol. 65A, no. 2, pp. 188–195, 2003, ISSN: 1549-3296. DOI: 10.1002/jbm.a.10482.

[47] C. Quinn, K. van Gaalen, P. E. McHugh, A. Kopp, and T. J. Vaughan, "An enhanced phenomenological model to predict surface-based localised corrosion of magnesium alloys for medical use," *Journal of the Mechanical Behavior of Biomedical Materials*, p. 105 637, 2022, ISSN: 1751-6161. DOI: https://doi.org/10.1016/j.jmbbm.2022.105637. [Online]. Available: https://www.sciencedirect.com/science/article/pii/S1751616122005422.

[48] G. Bradski, "The openCV library," *Dr. Dobb's Journal: Software Tools for the Professional Programmer*, vol. 25, no. 11, pp. 120–123, 2000, ISSN: 1044-789X.

[49] J. Lemaitre and R. Desmorat, *Engineering damage mechanics: ductile, creep, fatigue and brittle failures*. Springer Science & Business Media, 2006, ISBN: 3540272933.

[50] Y. Gao, L. Wang, X. Gu, Z. Chu, M. Guo, and Y. Fan, "A quantitative study on magnesium alloy stent biodegradation," *Journal of Biomechanics*, vol. 74, pp. 98–105, 2018, ISSN: 1873-2380 (Electronic) 0021-9290 (Linking). DOI: 10.1016/j.jbiomech.2018.04.027. [Online]. Available: https://www.ncbi.nlm.nih.gov/pubmed/29735265.

[51] M. Smith, *ABAQUS/Standard User's Manual, Version 6.9*. Dassault Systèmes Simulia Corp., 2009.

[52] W. Wu, L. Petrini, D. Gastaldi, T. Villa, M. Vedani, E. Lesma, B. Previtali, and F. Migliavacca, "Finite element shape optimization for biodegradable magnesium alloy stents," *Ann Biomed Eng*, vol. 38, no. 9, pp. 2829–40, 2010, ISSN: 1573-9686 (Electronic). DOI: 10.1007/s10439-010-0057-8. [Online]. Available: https://www.ncbi.nlm.nih.gov/pubmed/20446037.

[53] A. Considère, *Annales des Ponts et Chaussées 9*, pp. 574–775, 1885.

[54] M. Joun, I. Choi, J. Eom, and M. Lee, "Finite element analysis of tensile testing with emphasis on necking," *Computational Materials Science*, vol. 41, no. 1, pp. 63–69, 2007, ISSN: 09270256. DOI: 10.1016/j.commatsci.2007.03.002.

[55] X. Gu, F. Wang, X. Xie, M. Zheng, P. Li, Y. Zheng, L. Qin, and Y. Fan, "In vitro and in vivo studies on as-extruded Mg- 5.2 wt.%Zn- 0.6 wt.%Ca alloy as biodegradable metal," *Science China Materials*, vol. 61, no. 4, pp. 619–628, 2018, ISSN: 2095-8226 2199-4501. DOI: 10.1007/s40843-017-9205-x.

[56] Y. Liu, Y. Zheng, X. Chen, J. Yang, H. Pan, D. Chen, L. Wang, J. Zhang, D. Zhu, S. Wu, K. W. K. Yeung, R. Zeng, Y. Han, and S. Guan, "Fundamental Theory of Biodegradable Metals - Definition, Criteria, and Design," *Advanced Functional Materials*, vol. 29, no. 18, 2019, ISSN: 1616-301X 1616-3028. DOI: 10.1002/adfm.201805402.

[57] N Winzer, A Atrens, W Dietzel, V. Raja, G Song, and K. Kainer, "Characterisation of stress corrosion cracking (SCC) of Mg–Al alloys," *Materials Science and Engineering: A*, vol. 488, no. 1-2, pp. 339–351, 2008, ISSN: 0921-5093.

[58] M. B. Kannan, W Dietzel, C Blawert, A Atrens, and P Lyon, "Stress corrosion cracking of rare-earth containing magnesium alloys ZE41, QE22 and Elektron 21 (EV31A) compared with AZ80," *Materials Science and Engineering: A*, vol. 480, no. 1-2, pp. 529–539, 2008, ISSN: 0921-5093.

[59] E. Lukyanova, N. Anisimova, N. Martynenko, M. Kiselevsky, S. Dobatkin, and Y. Estrin, "Features of in vitro and in vivo behaviour of magnesium alloy WE43," *Materials Letters*, vol. 215, pp. 308–311, 2018, ISSN: 0167577X. DOI: 10.1016/j.matlet.2017.12.125.

[60] M. Schinhammer, J. Hofstetter, C. Wegmann, F. Moszner, J. F. Löffler, and P. J. Uggowitzer, "On the Immersion Testing of Degradable Implant Materials in Simulated Body Fluid: Active pH Regulation Using CO2," *Advanced Engineering Materials*, vol. 15, no. 6, pp. 434–441, 2013, ISSN: 14381656. DOI: 10.1002/adem.201200218.

Chapter 6

Predicting localised corrosion and mechanical performance of PEO surface modified rare earth Magnesium alloys for implant use through in-silico modelling

6.1 Introduction

Magnesium-based medical implants have the potential to overcome several complications that arise with permanent metallic implants. Implants made from magnesium are biodegradable such that they can undergo absorption once their load-bearing function has been completed, thereby avoiding a secondary removal surgery typically associated with permanent metallic implants [1–3]. Furthermore, magnesium alloys are osteostimulative, which makes them attractive in orthopaedic applications [4–9], and have similar mechanical properties to native bone, which means they could avoid stress shielding effects that are commonly encountered for titanium and stainless steel implants [10]. However, major challenges remain in the widespread implementation of magnesium-based alloys for implant applications due to the rather fast degradation rate and their inherent non-uniform surface corrosion mechanisms that result in localised material loss from the corroding surface [11].

In magnesium-based alloys, surface-based corrosion is governed by the accumulation of secondary cathodic phases, which are influenced by the density and distribution of intermetallic

precipitations as well impurities. These are practically unavoidable due to the manufacturing process, and the breakdown of the protective corrosion layer through the presence of chloride-Ions [12]. Recent efforts to improve performance have sought to decelerate the corrosion rate of magnesium through different alloy compositions or through the application of protective surface coatings and modifications [13–17]. Despite these approaches, non-uniform surface corrosion is still prevalent to some extent and the localised removal of bulk material during degradation can result in early loss of mechanical performance [18–21]. However, the majority of in-vitro studies on magnesium corrosion do not consider the mechanical performance of immersed specimens, and have instead simply evaluated corrosion based on bulk measurements through techniques such as electrochemical tests [22–25], hydrogen evolution [16, 18, 19, 24, 26–30], mass loss measurements [31–33] or micro-CT volume-based measurements [20, 34]. Recent efforts have been made to enable better understanding of how local corrosion mechanisms impact mechanical performance, with initial studies quantifying the non-uniform relationship between mass loss and specimen strength [18, 19]. More recently, studies have sought to provide a quantitative understanding on how the severity and spatial distribution of surface corrosion affects overall mechanical performance (Chapter 5) [35]. Through this most recent approach [35], in Chapter 5 it was demonstrated that tracking mass loss alone provides limited information on the mechanical performance of magnesium alloys undergoing corrosion. In fact, this study and others have even identified challenges in correctly determining mass loss from corroding specimens, with substantial differences observed in mass loss estimated using hydrogen evolution and micro-CT based approaches [20, 30, 34, 36, 37]. Through a more robust micro-CT based approach, several surface-based geometric features were identified (such as minimal cross-sectional area or average pit depth), which provide a mechanistic link between the severity of localised corrosion and the remaining mechanical strength [35] and are therefore more useful than bulk mass loss measurements alone.

Surface modifications like etching, ceramic coatings through plasma-electrolytic oxidation or

the application of polymer coatings on magnesium alloys all aim to decelerate the degradation process and make surface corrosion more uniform [38]. While the application of distinct coating materials, such as polymers, to magnesium substrates can effectively reduce corrosion rates, the presence of a separate material layer on a base alloy can result in low adhesion strength, with separation observed in the early stages of the corrosion process [39]. On the contrary, plasma electrolytic oxidation (PEO) surface modification converts the exposed surface into a homogeneously integrated surface layer without a distinct interface [13, 40, 41], thereby avoiding adhesion issues. In addition, the modified layer has high hardness, which makes it suitable in applications where high contact stresses are encountered [42, 43]. The influence of PEO surface treatment on different geometries like coins or scaffolds has been examined within several studies [16, 26, 44–46] that have demonstrated that PEO surface treatment can decelerate corrosion, with bulk measurements in mass loss significantly lower compared to unmodified specimens. It has been also shown that PEO surface treatment results in a better biocompatibility, enhanced osteostimulation and improved osseointegration compared to unmodified samples [44, 46, 47]. While this highlights the potential for PEO surface treatments, few studies to date have robustly quantified their effect on the mechanical integrity of specimens undergoing corrosion. Furthermore, while bulk corrosion rates are slowed with PEO modified specimens, it is not clear how this surface modifications affects the progression of localised corrosion features on the surface of the alloys. To further improve the corrosion performance of magnesium-based implants through approaches such as alloying or surface coating and modification, a more detailed understanding how these strategies alter the localised corrosion mechanisms, and ultimately mechanical performance is required.

In advancing medical implants towards clinical application, predictive models are becoming more widespread to simulate aspects of the physical, mechanical or biological performance of devices. For robust predictions of the performance of bioabsorbable implants, computational models should consider the degradation process in terms of both the geometric changes

due to surface mass loss and the resulting decline in mechanical performance. While several surface-based corrosion models have been able to reproduce bulk degradation rates of corroding specimens and have provided reasonable predictions of the overall mechanical response [18, 19, 48], these studies tend not predict the morphological features of corrosion that are observed physically.Instead, these models implement non-uniform corrosion by assuming some form of random distribution function, which produces corrosion profiles that might not truly capture the extent and severity of localised corrosion taking place. Furthermore, few studies have compared the predicted morphology of the corroding surface to experimental specimens. Studies that have compared their predictions to experiments have only done so through qualitative means through visual comparison [49, 50]. Further adaptations for the enhanced surface-based phenomenological model were proposed for magnesium corrosion [51], showing in Chapter 5 the potential to capture key geometrical features, as well as the mechanical response for an unmodified WE43 medical grade alloy [35]. To further elaborate on the performance of this model, and for the first time ever to include simulation and prediction of PEO surface modified specimens, there is a distinct need to ensure that both phenomenological aspects of corrosion and mechanical performance are robustly captured.
The objective of this study is to investigate the phenomenological differences of surface corrosion and mechanical performance of unmodified (WE43) and plasma-electrolytically oxidised (WE43-PEO) medical grade magnesium alloy. An extensive experimental in-vitro immersion study to characterise the degradation performance and mechanical integrity of tensile specimens from medical grade WE43 magnesium alloy was conducted. This experimental data was then used to calibrate the model parameters of a finite element-based surface corrosion model for both the unmodified WE43 and WE43-PEO groups [18, 51, 52].

6.2 Material and Methods

6.2.1 Study design

In-vitro immersion testing was conducted on axial tensile test specimens of both groups (WE43, WE43-PEO) up to 12 weeks, with mass loss evaluated through three different approaches including (i) hydrogen evolution, (ii) segmentation of micro-CT scans and analysis through a commercially available software and through our in-house *PitScan* code [20], and (iii) gravimetric methods following ultrasonic cleaning. Micro-CT imaging was used to quantify surface corrosion of each specimen at pre-defined time points, with mechanical testing subsequently carried out to characterise the uniaxial tensile response of both groups. Based on the findings, the surface-based corrosion model was calibrated to predict the geometrical and mechanical features of both groups in-silico.

6.2.2 Sample preparation

A total of 55 tensile specimens were manufactured by SWISS-type turning from chill-casted and extruded magnesium WE43MEO alloy rods with an initial diameter of 6.5 mm and a nominal composition of 1.4 - 4.2 % Y, 2.5 - 3.5 % Nd, < 1 % (Al, Fe, Cu, Ni, Mn, Zn, Zr) balance Mg (in wt %) (Meotec GmbH, Germany). The manufacturers' specification of the chemical composition was confirmed using inductively coupled plasma atomic emission spectroscopy (ICP-OES) measurements (Varian 720-ES, Agilent Technologies, CA, USA). The dimensions of the uniaxial tensile specimen dimensions are provided in Figure 6.1 (a). Following turning, 30 of the specimens underwent PEO treatment [16], while the other 25 remained untreated. Plasma-electrolytic oxidation, also referred as micro-arc oxidation (MAO), is a high-voltage anodising procedure using plasma discharges on the metallic sample surface leading to the formation of an outer porous oxide film [53]. For the surface treatment,

a phosphate-based electrolyte (Kermasorb®, Meotec GmbH, Germany) was used together with a pulsed rectifier set (M-PEO A1, Meotec GmbH, Germany) and process parameters were chosen to target a surface thickness of $\sim 15\,\mu m$. The full surface modification process is described in further detail in Kopp et al. [16]. Images of the WE43 and WE43-PEO samples prior to immersion testing are provided in Figure 6.1 (b).

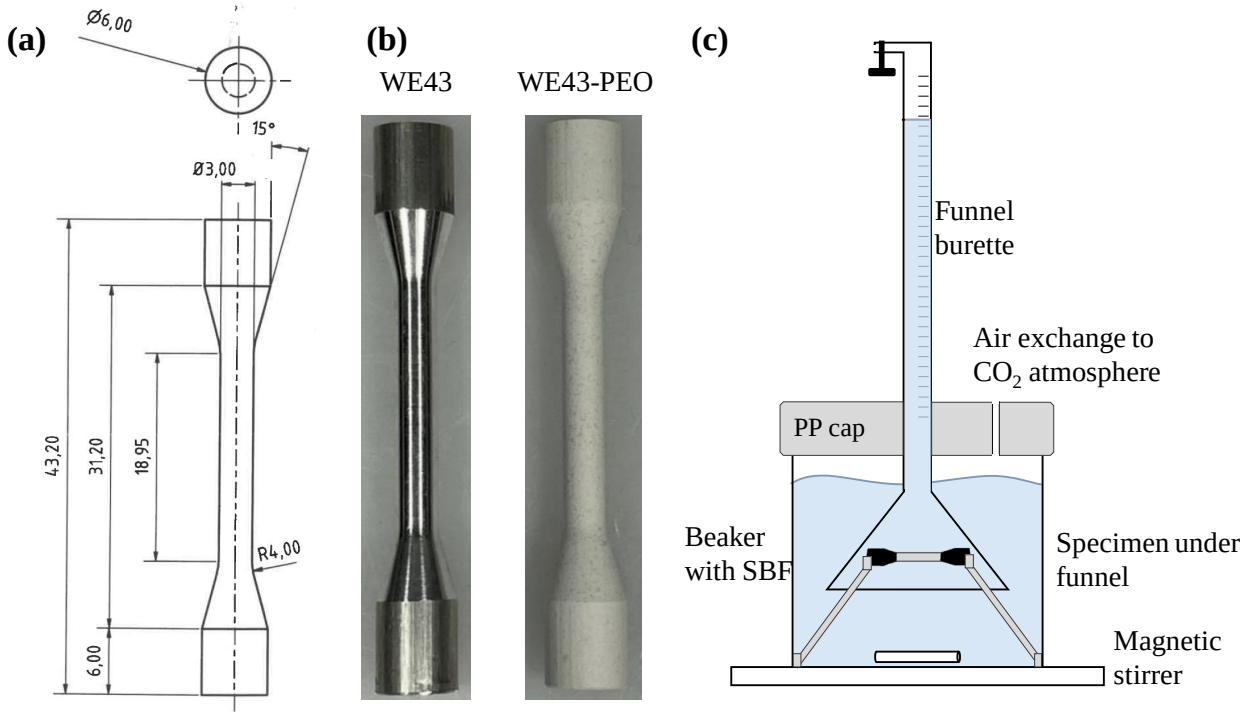

Figure 6.1: (a) Dimensions of tensile specimens; (b) images of WE43 and WE43-PEO modified samples; (c) schematic setup of immersion testing for one tensile specimen.

6.2.3 Experimental in-vitro testing

Immersion testing was carried out over a six-week period, with time points at 1, 2, 3, 4 and 6 weeks ($n = 5$ specimens for each time point) for both groups. The PEO-modified group was extended by an additional time point at 12 weeks ($n = 5$) to achieve a comparable amount of mass loss compared to the faster degrading unmodified group. Prior to testing, and for further measurements after the distinct time points, the weight of the samples was

determined with a balance (Kern ABJ-NM/ABS-N, e = 0.001 g, KERN & SOHN GmbH, Germany). Clamping ends of the tensile specimens were coated with liquid rubber PUR (mibenco GmbH, Germany) so that only the gauge sections undergo in-vitro corrosion. The immersion testing followed a similar protocol to previous studies [16, 20, 54, 55]. Briefly, the current study used glass funnel burettes as well as glass beakers to immerse samples, as shown in Figure 6.1 (c). The immersion media was conventional simulated body fluid (c-SBF) with a chemical composition taken from Oyane et al. [56]. C-SBF was chosen to avoid contamination over the long test period and due to its well-established accelerated degradation rate, which enables sufficient mass loss in a reasonable timeframe. Beakers were filled with 500 mL c-SBF each, which resulted in a high volume to surface area ratio ($V/S = 2.80\,mL/mm^2$) in accordance with ASTM G31-21 (minimum of $0.2\,mL/mm^2$ [57]). Testing was performed in an incubator under cell culture conditions (CellXpert C170i, Eppendorf AG, Hamburg, Germany) at $37\,°C \pm 1\,°C$ with a constant CO_2 atmosphere of 1.5 % to buffer a physiological pH of 7.4 in the medium, despite alkaline corrosion products. The amount of CO_2 was determined through pre-tests where the pH was monitored daily over a period of two weeks to ensure sufficient buffer capacity of the medium and environment in the incubator. pH measurements of the immersion media were taken after specimen removal at each time point (FiveEasy F20, Mettler-Toledo GmbH, Germany). After removal, specimens were rinsed with deionized water and pure ethanol before full drying. A reference was included in the incubator with the same test setup but without any sample to eliminate the influence of the environment. Micro-CT scanning for spatial reconstruction of the gauge section was performed following immersion testing at each time point using X-ray with emission parameters of 100 kV and 100 µA, which provided a pixel size of 15 µm (Skyscan 1272, Bruker Corporation, Billerica, MA, USA). For the 1-, 2- and 3-week time points in the WE43-PEO group, only one specimen was scanned as only minimal surface corrosion could be detected, thus preventing quantitative geometric information to be obtained.

Following micro-CT scanning, cross-sectional images were transformed to binary images and

the inner magnesium core was detected, since it was assumed that only the remaining metallic core contributes to the load bearing of the pre-corroded parts. *PitScan*, a Python-based detection framework developed in Chapter 4 [20], was used to quantitatively evaluate the geometrical features of the samples. Several predefined and surface-based phenomenological features to describe the progression of corrosion, including pit size, pit density, pit depth, average radius loss and minimum cross-sectional area loss were retrieved by calculation. Further details of the *PitScan* framework may be found in [20].

Following µCT-scanning, specimens also underwent uniaxial tensile tests at a constant velocity of 1.0 mm/min until failure (10 kN load cell, ZwickRoell GmbH & Co. KG, Germany). Displacement of the gauge length was tracked through an extensometer (makroXtens, ZwickRoell GmbH & Co. KG, Germany). To determine the nominal stress, the initial theoretical cross-sectional area was taken ($A = \pi r^2 = \pi 1.5^2\,\mathrm{mm}^2 = 7.07\,\mathrm{mm}^2$) for all time points, irrespective of how far corrosion had already progressed.

To calculate the actual mass loss of tested specimens, a total of three different methods were considered including (i) hydrogen evolution, (ii) weight measurement following ultrasonic cleaning (following ASTM G1–03 [58]), (iii) volume loss calculation through µCT scanning, whereby a 3D reconstruction of the gauge section was conducted with Imalytics Preclinical 3.0 (Gremse-IT GmbH, Germany) [59] as well as the *PitScan* framework [20]. For the hydrogen method, mass loss was derived through measurement of hydrogen gas evolution collected in burettes, using the following chemical reaction in which 1 mol of released magnesium corresponds to 1 mol hydrogen:

$$\mathrm{Mg} + 2\mathrm{H_2O} \rightarrow \mathrm{Mg(OH)_2} + \mathrm{H_2} \tag{6.1}$$

For gravimetric measurements, all samples underwent repeated ultrasonic cleaning (following ASTM G1–03 [58]) in deionized water and ethanol to remove the corrosion layer while avoiding the potentially hazardous use of chromic acid. Furthermore, chromic acid showed in

pre-experiments to have adverse effects on the PEO modified samples, making this treatment unusable for the current study.

6.2.4 Surface-based corrosion and mechanical modelling

An enhanced surface-based corrosion model [51] was used to calibrate a set of model parameters to the corroding specimens. This model was calibrated by replicating the experimental procedure through simulation, whereby (i) surface corrosion was simulated on the cylindrical gauge sections, (ii) cross-sectional analysis carried out using *PitScan* and (iii) simulated tensile testing was conducted on the corroded model and compared to experiments. The enhanced surface-based corrosion model was built on the initially published version from Gastaldi et al. and Grogan et al. [18, 52] where a scalar damage factor (D) is introduced to initialise damage on corroding elements with the effective stress tensor ($\widetilde{\sigma}_{ij}$):

$$\widetilde{\sigma}_{ij} = \frac{\sigma_{ij}}{1 - D} \tag{6.2}$$

Within this study, the enhanced model proposed by Quinn et al. [51] was used to achieve more realistic surface corrosion features. This model uses a damage increment (dD_e) for each element that is calculated by:

$$\frac{dD_e}{dt} = k_u \lambda_{e_{norm}} L_{active} \tag{6.3}$$

where k_u is a kinetic parameter, and L_{active} is the ratio of the exposed active surface area to the respective element volume. Here, $\lambda_{e_{norm}}$ is the normalised (summation of all random number equals 1) set of random numbers, which is represented by a Weibull-shape function (Equation (6.4)) to control the severity of localised corrosion (Figure 6.2 (d)).

$$f(x) = \gamma\,(x)^{\gamma-1}\, e^{-(x)^{\gamma}} \tag{6.4}$$

In Figure 6.2 (e) a sample finite element mesh is shown with different values for $\lambda_{e_{norm}}$

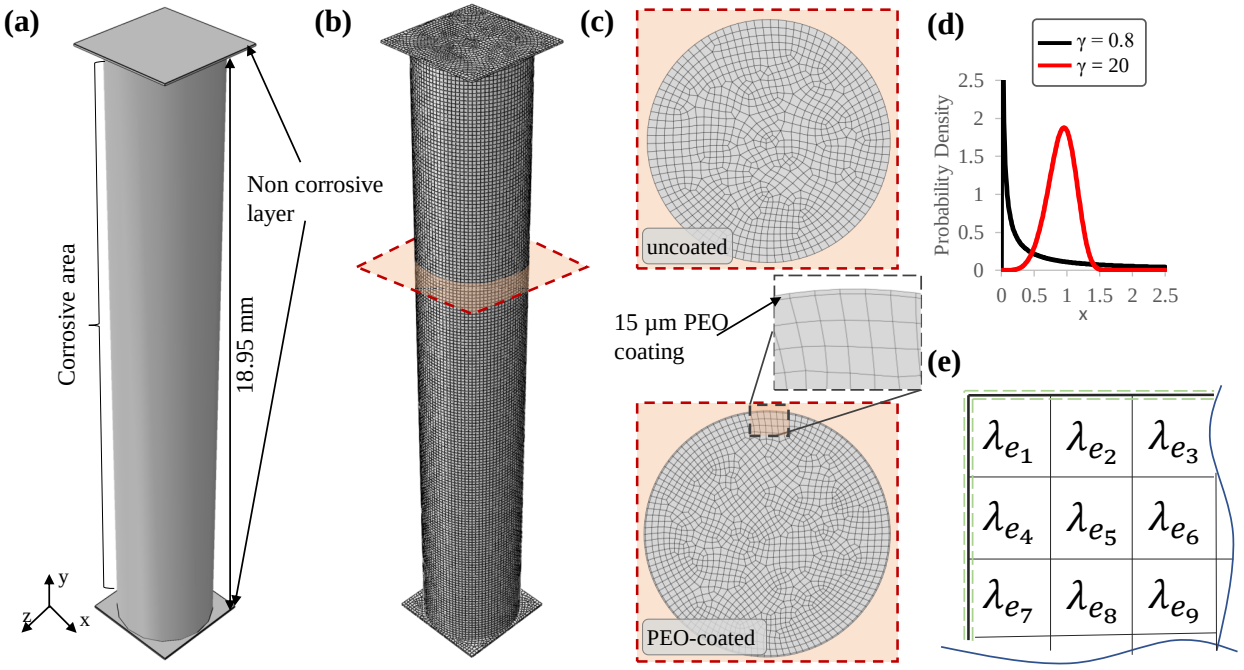

Figure 6.2: (a) Gauge section model geometry undegraded (b) FE-mesh of the model (c) cross-section image of the undegraded unmodified model and PEO-modified model (additional 15 µm solid element layer on the outer surface) (d) Probability density function for a standard Weibull-Curve for pitting ($\gamma = 0.8$) and uniform corrosion ($\gamma = 20.0$) (e) random numbers with green dashed lines marking the exposed surface.

for each element. If $D_{ecritical}$ exceeded a value of 0.5 for at least one element the kinetic parameter k_u is then recalculated for all elements within the current time increment (i) to:

$$k_{ui+1} = k_{ui} \frac{0.5}{D_{ecritical}} \tag{6.5}$$

PEO modified models were adapted by adding a thin surface layer of solid elements with a thickness of 15 µm (see Figure 6.2 (c) bottom). Further, the degradation code was adapted so that these new outer surface elements got a deceleration factor (f_{PEO}) for each damage increment. The damage increment for the outer layer is expressed as:

$$\frac{dD_e}{dt} = f_{PEO} k_u \lambda_{e_{norm}} L_{active} \tag{6.6}$$

Table 6.1 Input parameters used for the degradation model for WE43 alloy and WE43-PEO modified.

Parameter	WE43	WE43-PEO
k_u	0.05	0.0025
γ	0.6	0.6
β	1.0	1.0
B	3.0	3.0
f_{PEO}	-	0.0015

Degradation simulations were implemented using a Python-based code, which enabled efficient computation of corrosion and high mesh density. The previous determined relationship between mass loss versus time of the experimental data set (Section 6.2.3) provided the basis for the final mass loss points of the degradation simulations for both WE43 and WE43-PEO models. Table 6.1 shows the input parameters that were identified through an iterative procedure until they matched the phenomenological experimental results, while tensile test simulations were performed afterwards. No adaptation loop of the input data was performed after identifying first mechanical features. After the corrosion simulations, cross-sectional images every 80 µm (e.g. the size of an element layer) along the gauge section were generated for all simulated mass losses and were then processed by *PitScan* for geometric evaluation of the surface profile.

To simulate tensile testing, finite element models were created in Abaqus/CAE (Dassault Systèmes Simulia Corp., RI, USA), whereby only the gauge section of the dog bone geometry was modelled to save computational time. These geometries had a top and bottom layer of undegradable elements where the boundary conditions were applied for the final uniaxial tensile test simulation (Figure 6.2). A mesh sensitivity study was conducted to establish a suitable mesh size to capture key geometrical corrosion features and ensuring an appropriate execution time, which resulted in a final characteristic element length of ~ 80 µm. This resulted in a total of 340,000 three-dimensional reduced integration brick elements (C3D8R) in the models, with a slightly higher number in the WE43-PEO models due to the extra surface layer of solid elements (Figure 6.2 (c)). An elastic-plastic constitutive material model that

was previously calibrated to WE43, as described in van Gaalen et al. [35], was used. It was found that the WE43-PEO samples also had a similar mechanical response prior to corrosion (see Figure 6.7), so same material parameters were used in both, unmodified WE43 and WE43-PEO groups. Uniaxial tensile test simulations were performed using Abaqus/Explicit (Dassault Systèmes Simulia Corp., RI, USA).

6.3 Results

6.3.1 Experimental in-vitro testing

Figure 6.3 shows images of the surface corrosion on immersed dog bone specimens from the first and last time point for (a) unmodified WE43 and (b) WE43-PEO modified groups. Top images show the dried samples after immersion, while the bottom images show specimens following tensile testing and ultrasonic cleaning. The middle images show the predicted corrosion profile of the gauge section of the corresponding computational corrosion simulation (as not stretched by tensile testing). The complete set of images for all specimens across all time points is shown in Appendix B in Figure B.1.

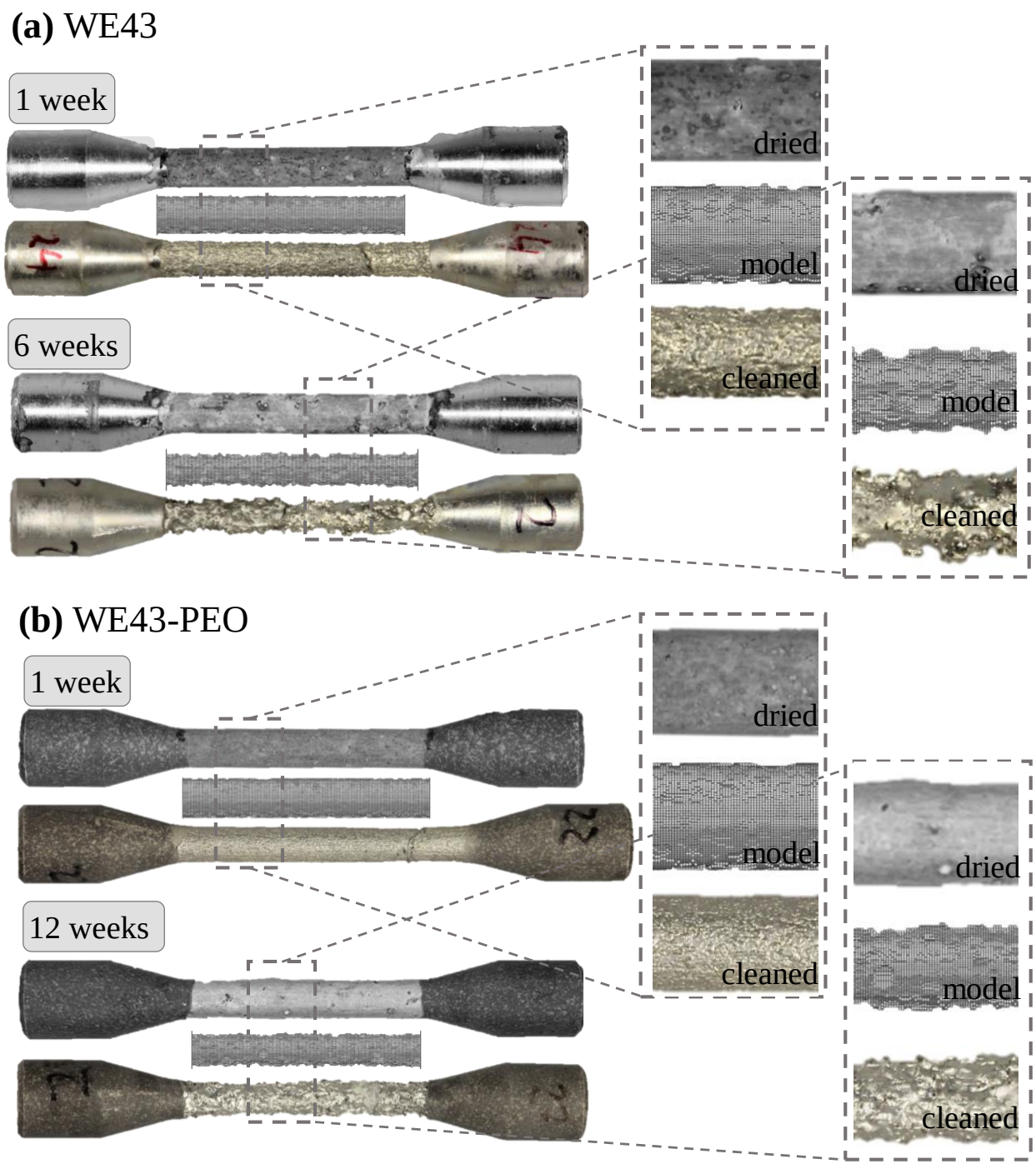

Figure 6.3: Images of dog bone samples after immersion, after tensile testing and ultrasonic cleaning, with the two separated ends after tensile testing being glued together for (a) WE43 1 and 6 weeks and (b) WE43-PEO 1 and 12 weeks. Corresponding simulated gauge section for the respective time are included (in the middle).

Figure 6.4 (a) and (b) show the mean hydrogen gas evolution and corresponding mass

loss over the respective test periods of WE43 and WE43-PEO specimens. The mean values up to one week were derived from the full set of samples in each group (e.g. n = 25 for WE43 and n = 30 for WE43-PEO). For each subsequent time point, the sample number reduced by n = 5 for each group due to the destructive characterisation that took place for weight loss measurements. This scheme was enforced until only five samples remained for the WE43 group after 6 weeks and five samples for the WE43-PEO group after 12 weeks. There was a substantial difference in mass loss between WE43 and WE43-PEO groups, with

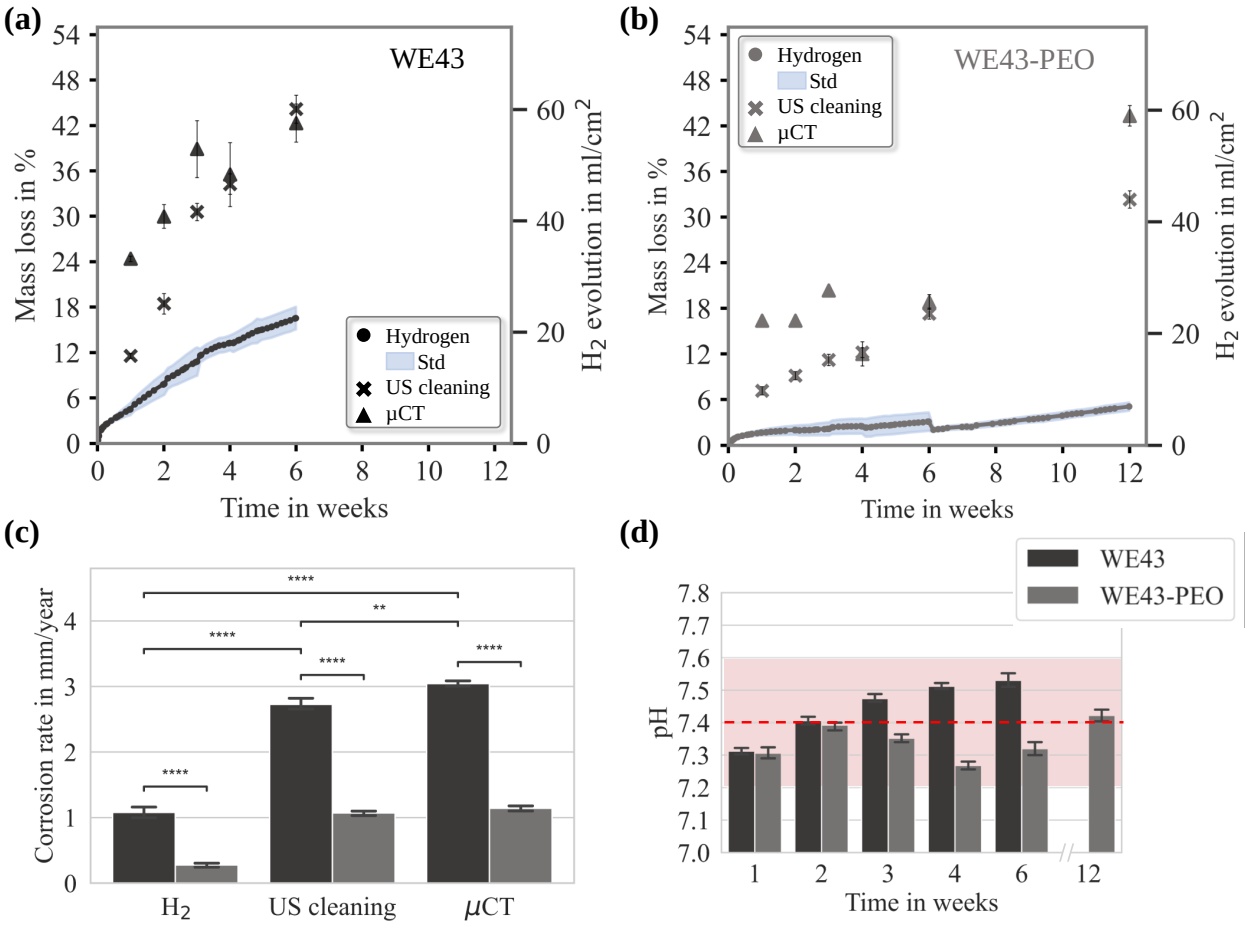

Figure 6.4: (a) WE43, (b) WE43-PEO Mass loss determined by (i) hydrogen gas evolution (ii) gravimetric weight loss using ultrasonic (US) cleaning (iii) µCT evaluation with *PitScan* (c) corresponding corrosion rates [60] after an immersion time of 6 weeks for WE43 and WE43-PEO; p-value annotation legend: ns: $5.00e-02 < p \leq 1.00e+00$; *: $1.00e-02 < p <= 5.00e-02$; **: $1.00e-03 < p \leq 1.00e-02$; ***: $1.00e-04 < p \leq 1.00e-03$; ****: $p \leq 1.00e-04$; (d) pH values of the solution with standard deviation after immersion. (Legend in (a) applies to all images)

the corrosion taking place at a much slower rate for WE43-PEO samples. In both groups,

an initial steep mass loss was observed in the first days by hydrogen gas evolution, while the WE43 group already showed approximately 17 % mass loss after 6 weeks as compared the WE43-PEO group only had approximately 5 % mass loss up to 12 weeks. For clarity on the difference of testing methods, Figure 6.4 (a) and (b) show deviations of the three methods used to determine overall mass loss of unmodified WE43 and WE43-PEO groups. The results labelled in Figure 6.4 as mass loss derived from µCT, are related to the calculation through *PitScan*. These results agreed with the calculations through the commercially available Imalytics software. In general, there was an average deviation of 1.2 % between those two µCT image evaluation methods. From this, it can be concluded that *PitScan* is able to generate reliable results in terms of calculating the volume loss.

Across all methods and despite of single differences, the rate of mass loss was substantially lower in the WE43-PEO group as compared to the WE43 specimens. However, significant differences were observed in the detected mass loss when comparing measurements by hydrogen gas evolution and all other methods. It also became evident that the differences between hydrogen evolution and other mass loss measurements became greater as the experiment continued. At 12 weeks, mass loss in the WE43-PEO group determined by hydrogen gas evolution was more than 7 times lower than that measured by µCT. Considering the µCT results, mass loss is considerably slower in the WE43-PEO group, with similar mass loss observed at 12 weeks, compared to the unmodified WE43 at 6 weeks. In general, lower values are reported through the gravimetric method (cross markers) compared to the evaluation through µCT scanning, the difference in average was found to be $\sim 8\,\%$.

The corrosion rates from the different methods of the six-week immersed samples are provided in Figure 6.4 (c). P-values were calculated through t-tests to show whether there were significant differences (i) between the methods and (ii) between unmodified WE43 and WE43-PEO modified groups. P-values showed highly significant differences in corrosion rates between the unmodified and PEO modified groups. Furthermore, highly significant differences are also present in mass loss determined from hydrogen evolution and the other two

methods across unmodified WE43. Differences among the methods are also highly significant for WE43-PEO, but not shown in the figure, to ensure easier interpretation. Additionally, the pH value over time is plotted in Figure 6.4 (d). In general, all pH values were within the specification of ASTM F3268-18a accounting to 7.4 ± 0.2 [60]. While the unmodified WE43 group showed a steady increase in the pH with time, the pH in the WE43-PEO group decreased after 2 weeks, and subsequently increased after 4 weeks. Standard deviations were low for both groups.

6.3.2 Phenomenological corrosion tracking

PitScan provides a three-dimensional reconstruction of the processed µCT scans, along the entire gauge length of the dog bone specimens. Contour plots for one degraded sample per group and time increment are shown in Figure 6.5 (a) for the unmodified WE43 groups and in (b) for the PEO modified groups. Figure 6.5 (c) shows the pit depth distribution identified through *PitScan*. From the experimental data, the distribution for both groups moves from a narrow distribution with high peaks to a broader distribution over time. This trend means that small pits initially form and gradually grow and coalesce into larger and deeper pits, which is supported by the contour plots (Figure 6.5 (a)). While for the first 3 weeks the WE43-PEO group shows only very shallow pits, the unmodified WE43 samples show much deeper pits within the same timeframe.

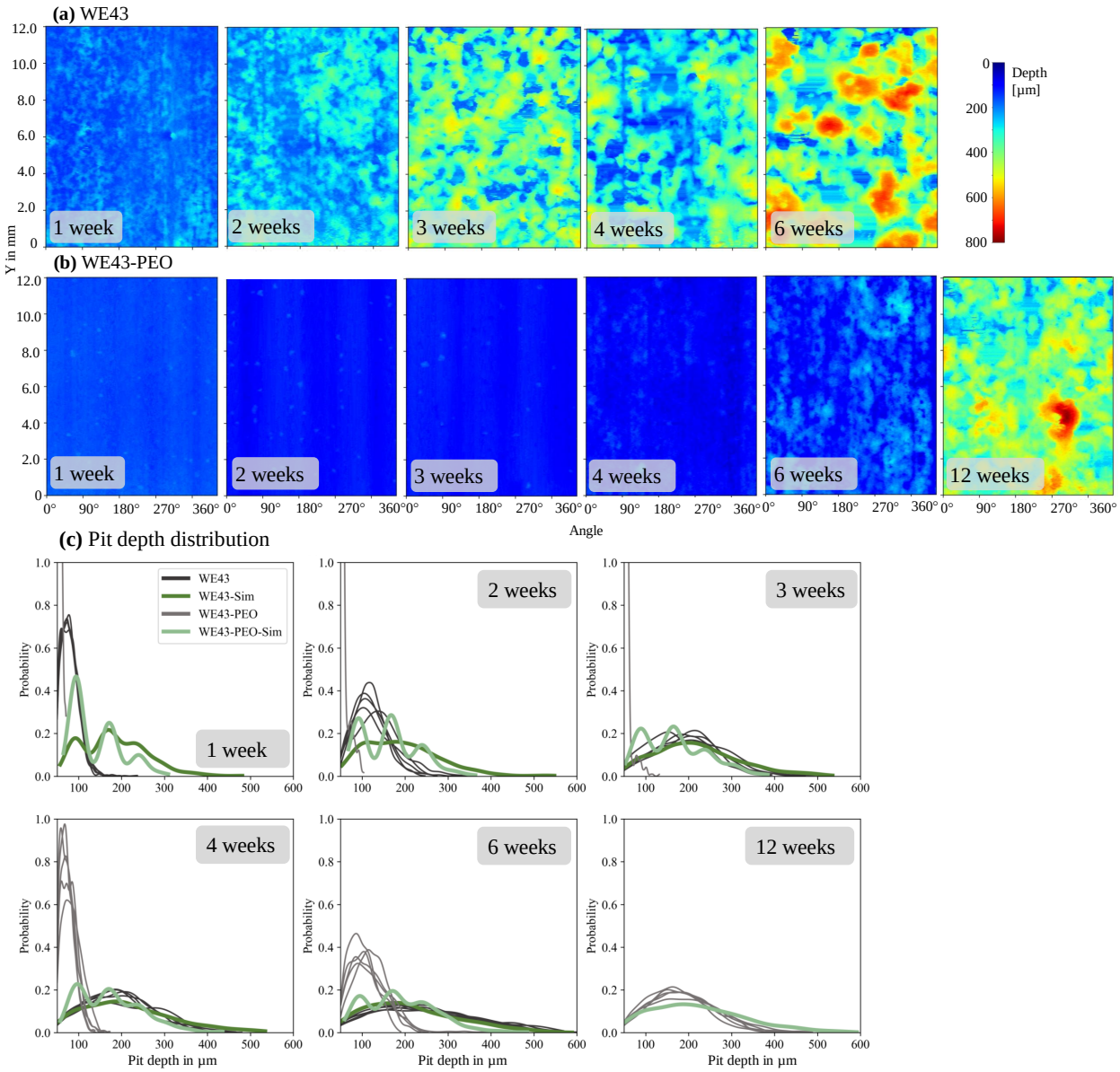

Figure 6.5: Contour plots of the gauge section of the immersed dog bones over time, representing the depth from the initial surface to the current interface surface - environment. Only one sample per time step is shown (a) WE43 unmodified (b) WE43-PEO modified; (c) Pit depth distribution for WE43 and WE43 PEO modified magnesium WE43. Simulated data depict (a) 1 week (b) 2 weeks (c) 3 weeks (d) 4 weeks (e) 6 weeks (f) 12 weeks (only PEO modified) immersion time.

Figure 6.6 shows the evolution of key geometrical features over the testing time for unmodified WE43 and WE43-PEO modified groups. Statistical significance facilitating t-tests were calculated only from week 4 onwards, where n=5 samples of WE43-PEO were available from µCT scanning (as there was minimal corrosion at the earlier time points). Figure 6.6 (a)

shows the measure of pitting factor (PF) for both groups during corrosion, which is defined by ASTM G46-94 [61] as the ratio of the deepest pit depth to the average pit depth. Pit-

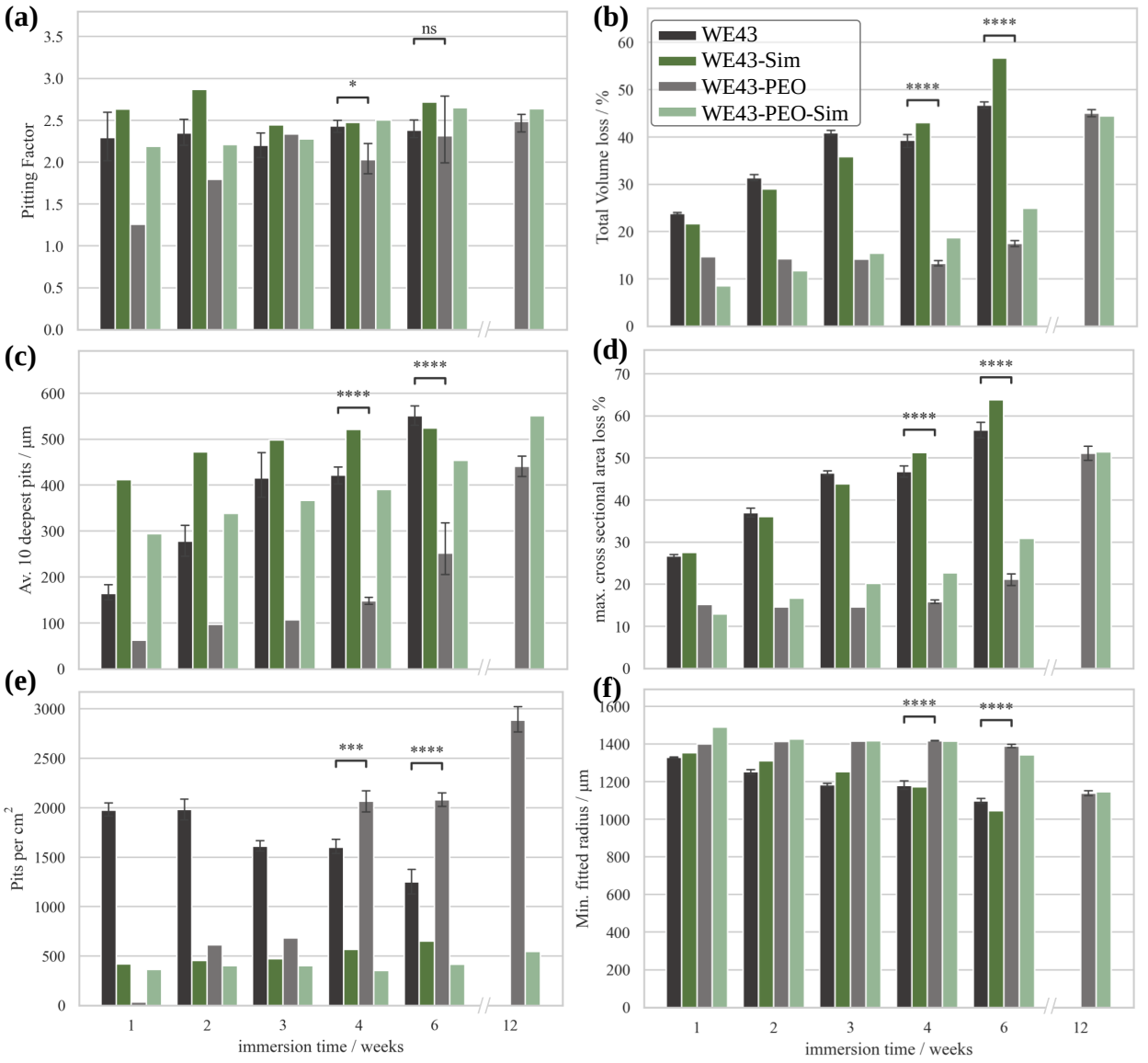

Figure 6.6: Evolution of key phenomenological corrosion features over time for WE43 and WE43 PEO-treated samples including simulated data from degradation models; t-test; p-value annotation legend: ns: $5.00e-02 < p \leq 1.00e+00$; *: $1.00e-02 < p <= 5.00e-02$; **: $1.00e-03 < p \leq 1.00e-02$; ***: $1.00e-04 < p \leq 1.00e-03$; ****: $p \leq 1.00e-04$. (Legend in (b) applies to all plots)

ting factor does not change substantially over time for unmodified WE43 and measures are between PF = 2.2-2.4 for all time points. For the WE43-PEO modified group, the pitting factor was just above 1 in the earliest time point (as there was minimal corrosion) and

gradually increased until there was a non-significant difference with the WE43 unmodified group at week 5. Interestingly, this suggests that while the rate of corrosion was slowed for the WE43-PEO modified samples, the surface features, and how corrosion progressed spatially was similar. Figure 6.6 (c) compared the average depth of the ten deepest pits, which is also a metric proposed in ASTM G46-94 to evaluate localised corrosion [61]. Here, for both groups, the average depth steadily increased over time and the 12-week WE43-PEO samples showed similar values to the 4-week unmodified WE43 group. For the maximum cross-sectional area loss (see Figure 6.6 (d)), there is a steady increase for unmodified WE43, while the PEO-modified group shows little change until 6 weeks. Interestingly, the pit density of the unmodified WE43 group decreases over time (as pits merge together to wider and deeper pits), while the WE43-PEO samples show an increase in the pit density while corrosion progresses (Figure 6.6 (e)). For unmodified WE43 samples, many small pits instantly evolve and merge together over time, while the PEO treatment slows initial pit evolution and by week 12, many small pits have formed by the effect of these merging into larger pits is not yet visible. The minimum fitted radius (see Figure 6.6 (f)) constantly decreases in the unmodified WE43 group, while in the PEO-treated group this feature stays almost constant until the final time step where it decreases.

P-values demonstrate highly significant differences between the two groups for most features. While for pitting factor, the level of significance decreases over time, which demonstrates again that PEO surface modification decelerates the corrosion process but does not influence the surface morphology once corrosion progresses. This is evident when two separate time points from each group with similar mass loss are compared. In general, the features in the 12-week WE43-PEO group show similar values as the 6-week group of WE43, which is in accordance with the mass loss measure, where 6 week WE43 (46 %) samples have a similar mass loss as 12-weeks WE43-PEO (45 %).

6.3.3 Mechanical testing

Figure 6.7 (a) shows the uniaxial tensile test responses for the experimental (thin lines) and the respective simulated data (bold lines). WE43-PEO modified specimens are more effective in retaining their mechanical properties compared to WE43 specimens during corrosion. Specimens of both groups show a steady decrease in the specimen strength and strain-at-failure as the corrosion period progressed. Interestingly, there were large variations in the measured strain-to-failure (ε_f) for unmodified WE43 (Figure 6.7 (a) left) for the uncorroded specimens at week zero. However, this wide variation reduced once corrosion had started. The general mechanical behaviour of WE43-PEO modified specimens at week 0 is similar to the unmodified group. Again, there was a steady decrease in the specimen strength and strain-at-failure for the WE43-PEO-modified specimens as the corrosion period progressed. However, the WE43-PEO specimens showed smaller levels of reduction in mechanical properties compared to the WE43 specimens. Figure 6.7 (b) shows the mechanical parameters determined from each timepoint, whereby maximum specimen strength ($\sigma_{\max}$), strain at $\sigma_{\max}$ and effective Young's modulus are plotted. Specimen strength ($\sigma_{\max}$) shows a clear decrease over time for both groups. There was a significant difference in specimen strength between WE43 and WE43-PEO, with $p < 1.00e\text{-}04$ once corrosion had started. At time zero, a p-value of 4.5e-03 was calculated which indicate minor differences in specimen strength between WE43 and WE43-PEO. However, any variation was within the manufacturer's specification for the base alloy. At 12 weeks, the WE43-PEO group had similar specimen strengths as the WE43 unmodified after only 4 weeks. Figure 6.7 (b) shows the strain at $\sigma_{\max}$, where a continuous reduction was found as corrosion progressed. Significant differences between unmodified WE43 and the PEO surface treated groups arise from week 4 onwards, with standard deviations being higher compared to the measured maximum specimen strength among all groups and time points. Once more, the 12-week WE43-PEO modified group shows a similar mechanical behaviour as between the 4-week unmodified WE43 group. The

effective Young's modulus (Figure 6.7 (b) bottom) shows a decrease during corrosion, where there is little change in the WE43-PEO modified samples between two- and four-weeks immersion time. Here, differences between the unmodified and PEO-modified group became more pronounced from week 3 onwards. Again, the 12 weeks WE43-PEO group showed similar mechanical properties to the 4 weeks unmodified group.

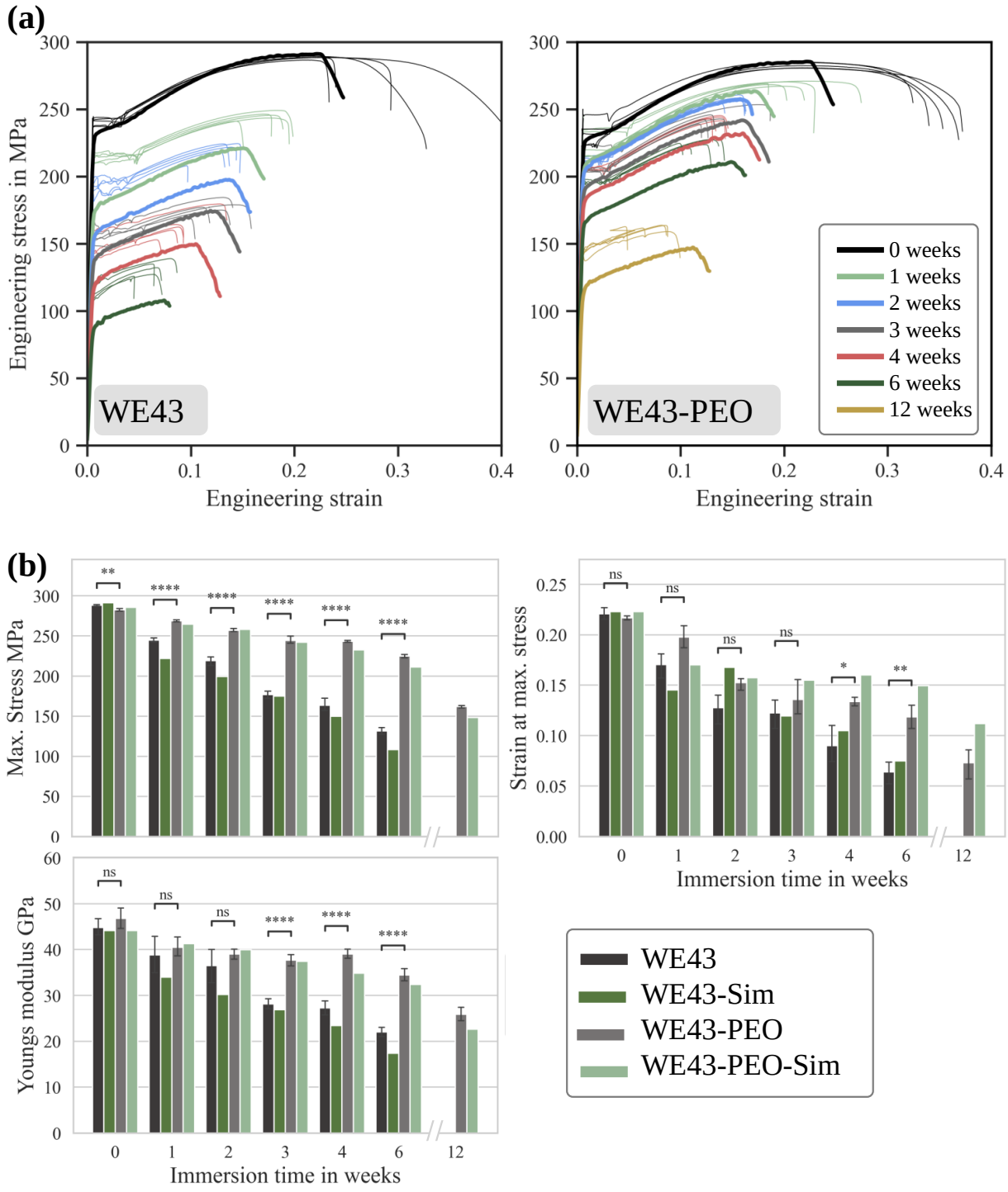

Figure 6.7: (a) Results from uniaxial tensile testing for experimental data (thin lines) and simulated data (thick line) for different time points left: WE43 unmodified and right WE43-PEO. (b) Mechanical parameter evolution over time including experimental and simulated data (a) maximum specimen strength ($\sigma_{\max}$); (b) strain at $\sigma_{\max}$; (c) effective Young's modulus; t-test; p-value annotation legend: ns: $5.00e-02 < p \leq 1.00e+00$; *: $1.00e-02 < p <= 5.00e-02$; **: $1.00e-03 < p \leq 1.00e-02$; ***: $1.00e-04 < p \leq 1.00e-03$; ****: $p \leq 1.00e-04$.

6.3.4 Model fitting

To support the findings on the influence of PEO surface modification on the degradation and mechanical properties of WE43, the numerical model was fitted to the experimental results to describe surface corrosion formation and the mechanical integrity over time. Therefore, two different models were calibrated with different input parameters (Table 6.1). To capture

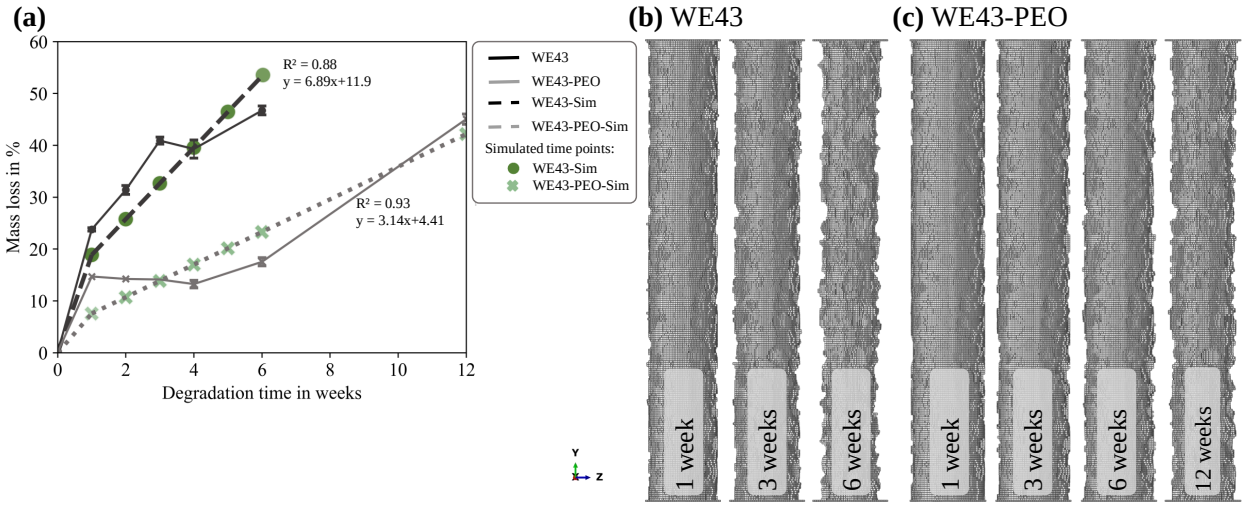

Figure 6.8: (a) Mass loss over degradation time derived from experimental data using immersion in c-SBF. Linear regression for WE43 (dark grey dashed line) and for WE43-PEO (light grey dotted line). Green dots correspond to the predefined mass loss for degradation simulation for WE43 and light green crosses correspond to the mass loss input data for WE43 PEO; (b) and (c) show the surface evolution of the gauge section of simulated WE43 and WE43-PEO over time.

the true corrosion rate of the WE43-PEO group, a deceleration factor was implemented to slow down the initial corrosion on the exposed surface elements (which measured 15 µm), and the kinetic parameter k_u of the core WE43 material was 2 times lower in the WE43-PEO modified model than the unmodified WE43 model. This parameter fitting demonstrates that the protection provided by the PEO treatment continues to protect the sample from surface corrosion throughout the entire examined corrosion period. To identify target mass losses for the degradation simulations, correlations between time and the mass loss were calculated for WE43 and WE43-PEO specimens, respectively (Figure 6.8 (a)). Mass loss values were determined through *PitScan* with the µCT images (see Section 3.1). The green dots and

light green crosses mark the target values for the final degradation simulations, respectively. Figure 6.8 (b) and (c) show the predicted surface corrosion on gauge section for few time steps from the two models and compares them to the experimentally tested samples. In Appendix B in Figure B.1, the images from all time points are provided next to the experimentally tested samples.

Contour plots of the degradation models for both groups and each time are given In Appendix B in Figure B.2. Figure 6.5 shows a quantitative comparison of the pit depth distribution predicted by the surface-based corrosion model and experiments, where both unmodified WE43 and WE43-PEO modified capture similar behaviour to the experimental data. In particular, from week 3 for the unmodified WE43 and for the 12 weeks WE43-PEO group a good agreement was reached with the models.

It was found that the surface-based corrosion models replicated similar trends in geometrical features, which are included and compared to experimental data in Figure 6.6. In particular, there is good agreement in model predictions of the minimum fitted radius (Figure 6.6 (f)) and maximum cross-sectional area loss (Figure 6.6 (d)). Factors related to the loss of the cross-sectional area are highly correlated to the loss of the overall specimen's strength, so a good fit here is indispensable [20]. However, the WE43-PEO model did not capture the average pit depth for early time steps (Figure 6.6 (c)), which derives from the selected mesh density of 80 µm [35]. Only for the 12-week group the results agree, which agrees with the results from Figure 6.5.

Following the corrosion simulation for each group, uniaxial tensile test simulations were conducted, without any adaptation of the previously identified model input parameters through the phenomenological alignment. Figure 6.7 (a) shows the predictions of the tensile test response for WE43 unmodified and WE43-PEO. Firstly, a good fit for the uncorroded response was possible (black curves). Once corrosion initiate, the corrosion model predicts mechanical responses that are just slightly lower than the experimentally measured mechanical response (except for the 3 weeks group). Both corrosion models correctly predict the

decreasing trends across the mechanical parameters as corrosion progressed. For most time steps, the predictions from the corrosion models were slightly lower than the $\sigma_{\max}$ values measured by experiments (see Figure 6.7 (b) top left). Figure 6.7 (b) the right plot shows the detected strain at $\sigma_{\max}$, where a good match was generally achieved. For the effective Young's modulus (Figure 6.7 (b) bottom) a similar a good fit was achieved for both groups.

6.4 Discussion

This study presented a combined experimental-computational investigation that characterised the corrosion behaviour of a medical grade WE43 alloy, which had undergone surface modification through plasma electrolytic oxidation. A 12 week in-vitro immersion study was carried out using tensile test specimens from both non-modified and WE43-PEO modified groups. It was found that the WE43-PEO modified group had a significantly lower corrosion rate and significantly higher mechanical properties than the WE43 unmodified specimens throughout the test period. It was also found that, while corrosion was slowed in the WE43-PEO modified specimens, the local geometric features and characteristics of corroding surfaces were very similar to the WE43 unmodified specimens, which were evaluated through a quantitative phenomenological tracking of the surface formation. The experimental data were used to successfully calibrate the parameters of a finite element-based surface corrosion model, whereby for the first time the PEO layer was considered as well. Through this testing framework, this study is the first to quantitatively demonstrate that the PEO surface treatment on WE43-based alloy protects the samples from corrosion throughout the entire examined corrosion period here, and not just in the early stages of corrosion.

A major disadvantage of magnesium-based medical implants is their unpredictable and often rapid mechanical deterioration, which has limited their use in load-bearing applications to date [62, 63]. Different strategies have been used to control the corrosion rate, which have included optimising the alloy composition, coating technologies or surface modifications.

While other studies have examined the effect of PEO modification on bulk mass loss, biocompatibility and osseointegration of magnesium alloys [16, 26, 44–47], this study is the first to quantitatively investigate localised aspects of surface corrosion and relate these features to the resulting mechanical performance. Here, the experimental evaluation showed that PEO modification provided significant enhancement of the corrosion performance. Overall, the in-vitro corrosion rate of PEO modified samples within the experimental framework used in this study was 1.5 mm/year, which was only 40 % of the unmodified samples and similar to those found in [45]. Furthermore, the corrosion process in the early weeks was extremely low in the WE43-PEO modified samples, with geometric quantification showing largely uniform features and very few localised pits forming at that stage. Beyond this timeframe, and up to six weeks, it was found that the severity of the surface corrosion features of the WE43-PEO modified samples were less pronounced with minimum cross-sectional area loss, pit depth and pitting factors lower than the unmodified WE43. As a result, the mechanical strength of the WE43-PEO modified specimens was significantly higher than the unmodified WE43 at all these time points. However, significant differences in Young's Modulus and strain at maximum strength only arose after 3 and 4 weeks, respectively. Interestingly, it was found that, while corrosion was slowed in the WE43-PEO modified group, the surface features of corrosion eventually progressed in a similar way to the WE43 unmodified samples. By comparing time points that showed similar levels of mass loss, it was found that similar surface features were present in the WE43-PEO modified group at 12 weeks, compared to WE43 unmodified samples at 6 weeks. Similarly, the mechanical response of the WE43-PEO modified group at 12 weeks was very similar to the mechanical response of the WE43 unmodified group at 4 and 6 weeks. Rendenbach et al. [44] determined a similar relative differences in an in-vivo study with a WE43MEO screw-plate system after 6 months implantation in Göttingen Miniature Pigs, where double the amount of SV/TV (screw volume/total volume) was present in the PEO treated group compared to the unmodified group. The halving of the volume reduction through the PEO treatment was also confirmed within the current

study through both experimentally and the numerical degradation model.

Furthermore, this study calibrated model parameters for a surface-based corrosion model for both the unmodified WE43 and WE43-PEO modified group. This surface-based corrosion model has been shown to be effective in capturing non-uniform and localised aspects of magnesium corrosion, with details reported previously [18, 19, 35, 64]. While many other surface-based corrosion models have been calibrated to predict specimen strength as a function of mass loss [18, 19, 48, 52, 64, 65], there is no existing model implementation that captures the actual geometric surface features of corrosion. In this respect, the model was calibrated until there was good agreement between the model prediction of average pit depth, pitting factor and maximum detected cross-sectional area loss (see Figure 6.6). Based on this calibration, it was found that the corrosion model independently provided a good match for the mechanical response, as well, with key mechanical parameters (i) specimen strength ($\sigma_{\max}$), (ii) strain at maximum strength (ε at $\sigma_{\max}$) and the (iii) effective Young's modulus (E). This study is the first to date to simulate corrosion of PEO modified samples through a phenomenological surface-based degradation model, whereby a discrete outer layer of elements was introduced and a deceleration factor (f_{PEO}) prescribed to this surface region. However, through this implementation of f_{PEO}, it was found that the kinetic parameter k_u for the WE43 core in the PEO modified group was two-times smaller than the unmodified group. This calibrated set of parameters highlights the fact that PEO modification protects the core material during the later stages of corrosion. While in the model this surface layer is removed, in the experiments it is likely that the outer surface is transformed to degradation products, which possibly persists on the material throughout the process and hence has a beneficial effect on the degradation within the PEO modified group.

This study also investigated three separate strategies to evaluate mass loss from corroding specimens. When determining mass loss by the hydrogen evolution method, there is already evidence that it is subject to error, mainly because of the difficulty in fully tracking the evolved hydrogen, which can migrate through the equipment due to its molecular size, and

the lack of understanding of the full corrosion reaction of magnesium in aqueous solution [66]. The previous experimental study from Chapter 4 [20] as well as other studies by Liu et al. [34], Denkena et al. [67] and Marco et al. [30] have already found significant differences in mass loss measurements between the hydrogen method and µCT evaluation or gravimetric measurements, whereby up to three times higher mass loss values were reported [67]. In the current study, the largest discrepancy was found at 12 weeks of immersion (WE43-PEO), where a 7-fold difference was found in the mass losses calculated from hydrogen evolution than evaluated from µCT. Thus, it seems that measurements of the mass loss through hydrogen evolution are constantly underestimated in this testing setup, with an increase in the difference to µCT values over time. However, through hydrogen tracking, it is possible to monitor mass loss values over time without removing samples, over the full immersion time. Additionally, it was demonstrated that gravimetric evaluation using ultrasonic cleaning was easy to implement and a safe method compared to other approaches that use hazardous chromic acid for cleaning of specimens [27, 30, 33, 68].

In addressing the limitations of the current study, it must be emphasized that all experimental data are based on in-vitro immersion tests in c-SBF buffered with Tris and CO_2. However, it is known that other corrosion media such as Dulbecco's Modified Eagle's Medium (DMEM) for immersion might be closer to physiological composition of interstitial body fluids and hence might reflect the in-vivo behaviour in terms of both corrosion rate and degradation layer formation. However, by using c-SBF, it was possible to avoid contamination of the used test setup during the long immersion time of 12 weeks, and due to the accelerated degradation was more favourable to achieve reasonable mass loss during the chosen testing time. Furthermore, the experimental data only delivered mass losses of up to 50 %, so further data would be necessary to capture the full degradation profile until most core material is degraded. However, the selected immersion time of 6-12 weeks roughly corresponds to a time of 15-30 weeks in-vivo [69], which covers the normal healing timeframe of a bone fracture, where these magnesium-based implants are used. Finally, despite the good pre-

diction of several geometrical corrosion features using the surface-based degradation model, it was noticeable that it does not correctly capture the pit density, which arises due to the chosen element size (80 µm). However, these models were sufficiently large so that results were calculable within a reasonable time, both for degradation simulation and the structural mechanical analysis. Furthermore, the approach of simulating the PEO surface layer by a one element layer, should investigated in more detail by implementing more surface elements representing, since currently the removal of the PEO layer only depends on the one element at the interface. In addition, the current approach of representing the PEO surface with a single element layer should be further investigated. Specifically, the accuracy of this approach could be potentially improved by implementing multiple surface elements to better capture the characteristics of the layer. Currently, the removal of the PEO layer is solely determined by the one element at the interface, which may not fully capture the complexity of the layer.

6.5 Conclusion

This study demonstrated that PEO surface modification significantly enhanced the corrosion performance of a medical grade WE43 magnesium alloy. It was found that the WE43-PEO modified specimens had corrosion rates that were two times lower than the WE43 unmodified group, with significantly higher mechanical properties in the PEO modified group throughout the whole test period. Our study demonstrated that PEO surface treatment on medical grade magnesium alloys can provide samples with protection from corrosion throughout the entire corrosion process, and not just in the early stages of corrosion. It was also found that, while corrosion was slowed in the WE43-PEO modified specimens, the general local geometric features and morphology of corroding surfaces were still very similar to the WE43 unmodified specimens but took place on a different timescale. This study also presented a numerical degradation model, which was calibrated through fitting with phenomenological

corrosion features detected with *PitScan*. This enabled, for the first time, in-silico prediction of both the physical features of corrosion and the resulting mechanical performance of both unmodified and PEO modified magnesium specimens. This simulation framework can enable future in-silico design and optimisation of bioabsorbable magnesium devices for load-bearing medical applications.

References

[1] M. P. Staiger, A. M. Pietak, J. Huadmai, and G. Dias, "Magnesium and its alloys as orthopedic biomaterials: a review," *J Biomaterials*, vol. 27, no. 9, pp. 1728–1734, 2006, ISSN: 0142-9612. DOI: 10.1016/j.biomaterials.2005.10.003..

[2] J. J. Jacobs, J. L. Gilbert, and R. M. Urban, "Current Concepts Review - Corrosion of Metal Orthopaedic Implants," *The Journal of Bone & Joint Surgery*, vol. 80, no. 2, pp. 268–82, 1998, ISSN: 0021-9355. [Online]. Available: https://journals.lww.com/jbjsjournal/Fulltext/1998/02000/Current_Concepts_Review___Corrosion_of_Metal.15.aspx.

[3] D. A. Puleo and W. W. Huh, "Acute toxicity of metal ions in cultures of osteogenic cells derived from bone marrow stromal cells," *Journal of Applied Biomaterials*, vol. 6, no. 2, pp. 109–116, 1995, ISSN: 1045-4861. DOI: /10.1002/jab.770060205.

[4] D. Sumner, "Long-term implant fixation and stress-shielding in total hip replacement," *Journal of Biomechanics*, vol. 48, no. 5, pp. 797–800, 2015, ISSN: 0021-9290.

[5] A. Burmester, R. Willumeit-Romer, and F. Feyerabend, "Behavior of bone cells in contact with magnesium implant material," *J Biomed Mater Res B Appl Biomater*, vol. 105, no. 1, pp. 165–179, 2017, ISSN: 1552-4981 (Electronic) 1552-4973 (Linking). DOI: 10.1002/jbm.b.33542. [Online]. Available: https://www.ncbi.nlm.nih.gov/pubmed/26448207.

[6] L. Wu, F. Feyerabend, A. F. Schilling, R. Willumeit-Romer, and B. J. C. Luthringer, "Effects of extracellular magnesium extract on the proliferation and differentiation of human osteoblasts and osteoclasts in coculture," *Acta Biomater*, vol. 27, pp. 294–304, 2015, ISSN: 1878-7568 (Electronic) 1742-7061 (Linking). DOI: 10.1016/j.actbio.2015.08.042. [Online]. Available: https://www.ncbi.nlm.nih.gov/pubmed/26318802.

[7] F. Witte, H. Ulrich, C. Palm, and E. Willbold, "Biodegradable magnesium scaffolds: Part II: peri-implant bone remodeling," *J Biomed Mater Res A*, vol. 81, no. 3, pp. 757–765, 2007, ISSN: 1549-3296 (Print) 1549-3296 (Linking). DOI: 10.1002/jbm.a.31293. [Online]. Available: https://www.ncbi.nlm.nih.gov/pubmed/17390322.

[8] N. Kawamura, Y. Nakao, R. Ishikawa, D. Tsuchida, and M. Iijima, "Degradation and Biocompatibility of AZ31 Magnesium Alloy Implants In Vitro and In Vivo: A Micro-Computed Tomography Study in Rats," *Materials (Basel)*, vol. 13, no. 2, 2020, ISSN: 1996-1944 (Print) 1996-1944 (Linking). DOI: 10.3390/ma13020473. [Online]. Available: https://www.ncbi.nlm.nih.gov/pubmed/31963840.

[9] T. Kraus, S. F. Fischerauer, A. C. Hanzi, P. J. Uggowitzer, J. F. Loffler, and A. M. Weinberg, "Magnesium alloys for temporary implants in osteosynthesis: in vivo studies of their degradation and interaction with bone," *Acta Biomater*, vol. 8, no. 3,

pp. 1230–8, 2012, ISSN: 1878-7568 (Electronic) 1742-7061 (Linking). DOI: 10.1016/j.actbio.2011.11.008. [Online]. Available: https://www.ncbi.nlm.nih.gov/pubmed/22107870.

[10] H. Nygren, P. Malmberg, and Y. Liu, "MgO Implanted in Rat Tibia Bone Marrow is Osteoinductive through the Formation of a Matrix, Containing Hydroxyapatite," in *Materials Science Forum*, vol. 879, pp. 1404–1407, ISBN: 1662-9752. DOI: 10.4028/www.scientific.net/MSF.879.1404.

[11] A. Atrens, G. Song, Z. Shi, A. Soltan, S. Johnston, and M. Dargusch, "Understanding the Corrosion of Mg and Mg Alloys," *Encyclopedia of Interfacial Chemistry*, pp. 515–534, 2018. DOI: https://doi.org/10.1016/B978-0-12-409547-2.13426-2.

[12] G. Song and A. Atrens, "Understanding Magnesium Corrosion - A Framework for Improved Alloy Performance," *Advanced Engineering Materials*, vol. 5, no. 12, pp. 837–858, 2003, ISSN: 1438-1656 1527-2648. DOI: 10.1002/adem.200310405.

[13] S. Agarwal, J. Curtin, B. Duffy, and S. Jaiswal, "Biodegradable magnesium alloys for orthopaedic applications: A review on corrosion, biocompatibility and surface modifications," *Mater Sci Eng C Mater Biol Appl*, vol. 68, pp. 948–963, 2016, ISSN: 1873-0191 (Electronic) 0928-4931 (Linking). DOI: 10.1016/j.msec.2016.06.020. [Online]. Available: https://www.ncbi.nlm.nih.gov/pubmed/27524097.

[14] Y. Chen, Z. Xu, C. Smith, and J. Sankar, "Recent advances on the development of magnesium alloys for biodegradable implants," *Acta Biomater*, vol. 10, no. 11, pp. 4561–4573, 2014, ISSN: 1878-7568 (Electronic) 1742-7061 (Linking). DOI: 10.1016/j.actbio.2014.07.005. [Online]. Available: https://www.ncbi.nlm.nih.gov/pubmed/25034646.

[15] G. B. Darband, M Aliofkhazraei, P Hamghalam, and N Valizade, "Plasma electrolytic oxidation of magnesium and its alloys: Mechanism, properties and applications," *Journal of Magnesium and Alloys*, vol. 5, no. 1, pp. 74–132, 2017, ISSN: 2213-9567. DOI: 10.1016/j.jma.2017.02.004.

[16] A. Kopp, T. Derra, M. Muther, L. Jauer, J. H. Schleifenbaum, M. Voshage, O. Jung, R. Smeets, and N. Kroger, "Influence of design and postprocessing parameters on the degradation behavior and mechanical properties of additively manufactured magnesium scaffolds," *Acta Biomater*, vol. 98, pp. 23–35, 2019, ISSN: 1878-7568 (Electronic) 1742-7061 (Linking). DOI: 10.1016/j.actbio.2019.04.012. [Online]. Available: https://www.ncbi.nlm.nih.gov/pubmed/30959185.

[17] H. M. Wong, K. W. Yeung, K. O. Lam, V. Tam, P. K. Chu, K. D. Luk, and K. M. Cheung, "A biodegradable polymer-based coating to control the performance of magnesium alloy orthopaedic implants," *Biomaterials*, vol. 31, no. 8, pp. 2084–96, 2010, ISSN: 1878-5905 (Electronic) 0142-9612 (Linking). DOI: 10.1016/j.biomaterials.2009.11.111. [Online]. Available: https://www.ncbi.nlm.nih.gov/pubmed/20031201.

[18] J. A. Grogan, B. J. O'Brien, S. B. Leen, and P. E. McHugh, "A corrosion model for bioabsorbable metallic stents," *Acta Biomater*, vol. 7, no. 9, pp. 3523–33, 2011, ISSN: 1878-7568 (Electronic) 1742-7061 (Linking). DOI: 10.1016/j.actbio.2011.05.032. [Online]. Available: https://www.ncbi.nlm.nih.gov/pubmed/21664498.

[19] E. L. Boland, R. N. Shirazi, J. A. Grogan, and P. E. McHugh, "Mechanical and Corrosion Testing of Magnesium WE43 Specimens for Pitting Corrosion Model Calibration," *Advanced Engineering Materials*, vol. 20, no. 10, 2018, ISSN: 14381656. DOI: 10.1002/adem.201800656.

[20] K. van Gaalen, F. Gremse, F. Benn, P. E. McHugh, A. Kopp, and T. J. Vaughan, "Automated ex-situ detection of pitting corrosion and its effect on the mechanical integrity of rare earth magnesium alloy - WE43," *Bioactive Materials*, 2022, ISSN: 2452199X. DOI: 10.1016/j.bioactmat.2021.06.024.

[21] I. Adekanmbi, C. Z. Mosher, H. H. Lu, M. Riehle, H. Kubba, and K. E. Tanner, "Mechanical behaviour of biodegradable AZ31 magnesium alloy after long term in vitro degradation," *Mater Sci Eng C Mater Biol Appl*, vol. 77, pp. 1135–1144, 2017, ISSN: 1873-0191 (Electronic). DOI: 10.1016/j.msec.2017.03.216. [Online]. Available: https://www.ncbi.nlm.nih.gov/pubmed/28531989.

[22] E Angelini, S Grassini, F Rosalbino, F Fracassi, and R d'Agostino, "Electrochemical impedance spectroscopy evaluation of the corrosion behaviour of Mg alloy coated with PECVD organosilicon thin film," *Progress in Organic Coatings*, vol. 46, no. 2, pp. 107–111, 2003, ISSN: 0300-9440. DOI: 10.1016/S0300-9440(02)00217-5.

[23] B. Zhang, Y. Hou, X. Wang, Y. Wang, and L. Geng, "Mechanical properties, degradation performance and cytotoxicity of Mg–Zn–Ca biomedical alloys with different compositions," *Materials Science and Engineering: C*, vol. 31, no. 8, pp. 1667–1673, 2011, ISSN: 09284931. DOI: 10.1016/j.msec.2011.07.015.

[24] X. Gu, Y. Zheng, Y. Cheng, S. Zhong, and T. Xi, "In vitro corrosion and biocompatibility of binary magnesium alloys," *Biomaterials*, vol. 30, no. 4, pp. 484–498, 2009, ISSN: 0142-9612. DOI: 10.1016/j.biomaterials.2008.10.021.

[25] A. M. Lafront, W. Zhang, S. Jin, R. Tremblay, D. Dubé, and E. Ghali, "Pitting corrosion of AZ91D and AJ62x magnesium alloys in alkaline chloride medium using electrochemical techniques," *Electrochimica Acta*, vol. 51, no. 3, pp. 489–501, 2005, ISSN: 00134686. DOI: 10.1016/j.electacta.2005.05.013.

[26] O. Jung, R. Smeets, P. Hartjen, R. Schnettler, F. Feyerabend, M. Klein, N. Wegner, F. Walther, D. Stangier, A. Henningsen, C. Rendenbach, M. Heiland, M. Barbeck, and A. Kopp, "Improved In Vitro Test Procedure for Full Assessment of the Cytocompatibility of Degradable Magnesium Based on ISO 10993-5/-12," *Int J Mol Sci*, vol. 20, no. 2, 2019, ISSN: 1422-0067 (Electronic) 1422-0067 (Linking). DOI: 10.3390/ijms20020255. [Online]. Available: https://www.ncbi.nlm.nih.gov/pubmed/30634646.

[27] G. Song, A. Atrens, and D. StJohn, "An Hydrogen Evolution Method for the Estimation of the Corrosion Rate of Magnesium Alloys," in *Essential Readings in Magnesium Technology*, S. N. Mathaudhu, A. A. Luo, N. R. Neelameggham, E. A. Nyberg, and W. H. Sillekens, Eds. Cham: Springer International Publishing, 2001, pp. 565–572, ISBN: 978-3-319-48099-2. DOI: 10.1007/978-3-319-48099-2_90.

[28] M. Li, Y. Cheng, Y. F. Zheng, X. Zhang, T. F. Xi, and S. C. Wei, "Surface characteristics and corrosion behaviour of WE43 magnesium alloy coated by SiC film," *Applied Surface Science*, vol. 258, no. 7, pp. 3074–3081, 2012, ISSN: 01694332. DOI: 10.1016/j.apsusc.2011.11.040.

[29] D. Mei, S. V. Lamaka, J. Gonzalez, F. Feyerabend, R. Willumeit-Römer, and M. L. Zheludkevich, "The role of individual components of simulated body fluid on the corrosion behavior of commercially pure Mg," *Corrosion Science*, vol. 147, pp. 81–93, 2019, ISSN: 0010938X. DOI: 10.1016/j.corsci.2018.11.011.

[30] I. Marco, F. Feyerabend, R. Willumeit-Romer, and O. Van der Biest, "Degradation testing of Mg alloys in Dulbecco's modified eagle medium: Influence of medium sterilization," *Mater Sci Eng C Mater Biol Appl*, vol. 62, pp. 68–78, 2016, ISSN: 1873-0191 (Electronic) 0928-4931 (Linking). DOI: 10.1016/j.msec.2016.01.039. [Online]. Available: https://www.ncbi.nlm.nih.gov/pubmed/26952399.

[31] J. Harmuth, B. Wiese, J. Bohlen, T. Ebel, and R. Willumeit-Römer, "Wide Range Mechanical Customization of Mg-Gd Alloys With Low Degradation Rates by Extrusion," *Frontiers in Materials*, vol. 6, 2019, ISSN: 2296-8016. DOI: 10.3389/fmats.2019.00201.

[32] N. A. Agha, F. Feyerabend, B. Mihailova, S. Heidrich, U. Bismayer, and R. Willumeit-Romer, "Magnesium degradation influenced by buffering salts in concentrations typical of in vitro and in vivo models," *Mater Sci Eng C Mater Biol Appl*, vol. 58, pp. 817–25, 2016, ISSN: 1873-0191 (Electronic) 0928-4931 (Linking). DOI: 10.1016/j.msec.2015.09.067. [Online]. Available: https://www.ncbi.nlm.nih.gov/pubmed/26478376.

[33] J. Walker, S. Shadanbaz, N. T. Kirkland, E. Stace, T. Woodfield, M. P. Staiger, and G. J. Dias, "Magnesium alloys: predicting in vivo corrosion with in vitro immersion testing," *J Biomed Mater Res B Appl Biomater*, vol. 100, no. 4, pp. 1134–41, 2012, ISSN: 1552-4981 (Electronic) 1552-4973 (Linking). DOI: 10.1002/jbm.b.32680.

[34] L. Liu, K. Gebresellasie, B. Collins, H. Zhang, Z. Xu, J. Sankar, Y.-C. Lee, and Y. Yun, "Degradation Rates of Pure Zinc, Magnesium, and Magnesium Alloys Measured by Volume Loss, Mass Loss, and Hydrogen Evolution," *Applied Sciences*, vol. 8, no. 9, 2018, ISSN: 2076-3417. DOI: 10.3390/app8091459.

[35] K. van Gaalen, C. Quinn, F. Benn, P. E. McHugh, A. Kopp, and T. J. Vaughan, "Linking the effect of localised pitting corrosion with mechanical integrity of a rare

earth magnesium alloy for implant use," *Bioactive Materials*, vol. 21, pp. 32–43, 2023, ISSN: 2452199X. DOI: 10.1016/j.bioactmat.2022.08.004.

[36] N. T. Kirkland, N. Birbilis, and M. P. Staiger, "Assessing the corrosion of biodegradable magnesium implants: a critical review of current methodologies and their limitations," *Acta Biomater*, vol. 8, no. 3, pp. 925–36, 2012, ISSN: 1878-7568 (Electronic) 1742-7061 (Linking). DOI: 10.1016/j.actbio.2011.11.014. [Online]. Available: https://www.ncbi.nlm.nih.gov/pubmed/22134164.

[37] Y. B. Ren, H. Wang, J. J. Huang, B. C. Zhang, and K. Yang, "Study of Biodegradation of Pure Magnesium," *Key Engineering Materials*, vol. 342, pp. 601–604, 2007. DOI: 10.4028/www.scientific.net/KEM.342-343.601.

[38] H. Hornberger, S. Virtanen, and A. R. Boccaccini, "Biomedical coatings on magnesium alloys - a review," *Acta Biomater*, vol. 8, no. 7, pp. 2442–55, 2012, ISSN: 1878-7568 (Electronic) 1742-7061 (Linking). DOI: 10.1016/j.actbio.2012.04.012. [Online]. Available: https://www.ncbi.nlm.nih.gov/pubmed/22510401.

[39] X. Li, X. Liu, S. Wu, K. W. K. Yeung, Y. Zheng, and P. K. Chu, "Design of magnesium alloys with controllable degradation for biomedical implants: From bulk to surface," *Acta Biomater*, vol. 45, pp. 2–30, 2016. DOI: 10.1016/j.actbio.2016.09.005. [Online]. Available: https://www.ncbi.nlm.nih.gov/pubmed/27612959.

[40] P. Wan, L. Tan, and K. Yang, "Surface Modification on Biodegradable Magnesium Alloys as Orthopedic Implant Materials to Improve the Bio-adaptability: A Review," *Journal of Materials Science & Technology*, vol. 32, no. 9, pp. 827–834, 2016, ISSN: 10050302. DOI: 10.1016/j.jmst.2016.05.003.

[41] L. Y. Li, L. Y. Cui, R. C. Zeng, S. Q. Li, X. B. Chen, Y. Zheng, and M. B. Kannan, "Advances in functionalized polymer coatings on biodegradable magnesium alloys - A review," *Acta Biomater*, vol. 79, pp. 23–36, 2018, ISSN: 1878-7568 (Electronic) 1742-7061 (Linking). DOI: 10.1016/j.actbio.2018.08.030. [Online]. Available: https://www.ncbi.nlm.nih.gov/pubmed/30149212.

[42] L. Pezzato, L. B. Coelho, R. Bertolini, A. G. Settimi, K. Brunelli, M. Olivier, and M. Dabalà, "Corrosion and mechanical properties of plasma electrolytic oxidation-coated AZ80 magnesium alloy," *Materials and Corrosion*, vol. 70, no. 11, pp. 2103–2112, 2019. DOI: 10.1002/maco.201910847.

[43] L. White, Y. Koo, S. Neralla, J. Sankar, and Y. Yun, "Enhanced mechanical properties and increased corrosion resistance of a biodegradable magnesium alloy by plasma electrolytic oxidation (PEO)," *Mater Sci Eng B Solid State Mater Adv Technol*, vol. 208, pp. 39–46, 2016, ISSN: 0921-5107 (Print). DOI: 10.1016/j.mseb.2016.02.005. [Online]. Available: https://www.ncbi.nlm.nih.gov/pubmed/28603382.

[44] C. Rendenbach, H. Fischer, A. Kopp, K. Schmidt-Bleek, H. Kreiker, S. Stumpp, M. Thiele, G. Duda, H. Hanken, B. Beck-Broichsitter, O. Jung, N. Kroger, R. Smeets,

and M. Heiland, "Improved in vivo osseointegration and degradation behavior of PEO surface-modified WE43 magnesium plates and screws after 6 and 12 months," *Mater Sci Eng C Mater Biol Appl*, vol. 129, p. 112 380, 2021, ISSN: 1873-0191 (Electronic) 0928-4931 (Linking). DOI: 10.1016/j.msec.2021.112380. [Online]. Available: https://www.ncbi.nlm.nih.gov/pubmed/34579899.

[45] H. R. Bakhsheshi-Rad, E. Hamzah, A. F. Ismail, M. Aziz, A. Najafinezhad, and M. Daroonparvar, "Synthesis and in-vitro performance of nanostructured monticellite coating on magnesium alloy for biomedical applications," *Journal of Alloys and Compounds*, vol. 773, pp. 180–193, 2019, ISSN: 09258388. DOI: 10.1016/j.jallcom.2018.08.310.

[46] O. Jung, D. Porchetta, M. L. Schroeder, M. Klein, N. Wegner, F. Walther, F. Feyerabend, M. Barbeck, and A. Kopp, "In Vivo Simulation of Magnesium Degradability Using a New Fluid Dynamic Bench Testing Approach," *Int J Mol Sci*, vol. 20, no. 19, 2019, ISSN: 1422-0067 (Electronic) 1422-0067 (Linking). DOI: 10.3390/ijms20194859. [Online]. Available: https://www.ncbi.nlm.nih.gov/pubmed/31574947.

[47] H. Xu, T. Hu, M. Wang, Y. Zheng, H. Qin, H. Cao, and Z. An, "Degradability and biocompatibility of magnesium-MAO: The consistency and contradiction between in-vitro and in-vivo outcomes," *Arabian Journal of Chemistry*, vol. 13, no. 1, pp. 2795–2805, 2020, ISSN: 18785352. DOI: 10.1016/j.arabjc.2018.07.010.

[48] S. Ma, B. Zhou, and B. Markert, "Numerical simulation of the tissue differentiation and corrosion process of biodegradable magnesium implants during bone fracture healing," *ZAMM - Journal of Applied Mathematics and Mechanics / Zeitschrift für Angewandte Mathematik und Mechanik*, vol. 98, no. 12, pp. 2223–2238, 2018, ISSN: 0044-2267 1521-4001. DOI: 10.1002/zamm.201700314.

[49] A. K. Gartzke, S. Julmi, C. Klose, A. C. Waselau, A. Meyer-Lindenberg, H. J. Maier, S. Besdo, and P. Wriggers, "A simulation model for the degradation of magnesium-based bone implants," *J Mech Behav Biomed Mater*, vol. 101, p. 103 411, 2020, ISSN: 1878-0180 (Electronic) 1878-0180 (Linking). DOI: 10.1016/j.jmbbm.2019.103411. [Online]. Available: https://www.ncbi.nlm.nih.gov/pubmed/31546176.

[50] M. Marvi-Mashhadi, W. Ali, M. Li, C. Gonzalez, and L. L. J, "Simulation of corrosion and mechanical degradation of additively manufactured Mg scaffolds in simulated body fluid," *J Mech Behav Biomed Mater*, vol. 126, p. 104 881, 2022, ISSN: 1878-0180 (Electronic). DOI: 10.1016/j.jmbbm.2021.104881. [Online]. Available: https://www.ncbi.nlm.nih.gov/pubmed/34702672.

[51] C. Quinn, K. van Gaalen, P. E. McHugh, A. Kopp, and T. J. Vaughan, "An enhanced phenomenological model to predict surface-based localised corrosion of magnesium alloys for medical use," *Journal of the Mechanical Behavior of Biomedical Materials*, p. 105 637, 2022, ISSN: 1751-6161. DOI: https://doi.org/10.1016/j.jmbbm.2022.105637. [Online]. Available: https://www.sciencedirect.com/science/article/pii/S1751616122005422.

[52] D. Gastaldi, V. Sassi, L. Petrini, M. Vedani, S. Trasatti, and F. Migliavacca, "Continuum damage model for bioresorbable magnesium alloy devices - Application to coronary stents," *J Mech Behav Biomed Mater*, vol. 4, no. 3, pp. 352–65, 2011, ISSN: 1878-0180 (Electronic) 1878-0180 (Linking). DOI: 10.1016/j.jmbbm.2010.11.003. [Online]. Available: https://www.ncbi.nlm.nih.gov/pubmed/21316623.

[53] C. Blawert and P. Bala Srinivasan, "Plasma electrolytic oxidation treatment of magnesium alloys," in *Surface Engineering of Light Alloys*. Elsevier, 2010, pp. 155–183, ISBN: 9781845695378. DOI: 10.1533/9781845699451.2.155.

[54] F. Benn, F. D'Elia, K. van Gaalen, M. Li, S. Malinov, and A. Kopp, "Printability, mechanical and degradation properties of Mg-(x)Zn elemental powder mixes processed by laser powder bed fusion," *Additive Manufacturing Letters*, vol. 2, 2022, ISSN: 27723690. DOI: 10.1016/j.addlet.2021.100025.

[55] F. Benn, N. Kroger, M. Zinser, K. van Gaalen, T. J. Vaughan, M. Yan, R. Smeets, E. Bibiza, S. Malinov, F. Buchanan, and A. Kopp, "Influence of surface condition on the degradation behaviour and biocompatibility of additively manufactured WE43," *Mater Sci Eng C Mater Biol Appl*, vol. 124, p. 112 016, 2021, ISSN: 1873-0191 (Electronic) 0928-4931 (Linking). DOI: 10.1016/j.msec.2021.112016. [Online]. Available: https://www.ncbi.nlm.nih.gov/pubmed/33947530.

[56] A. Oyane, H. Kim, T. Furuya, T. Kokubo, T. Miyazaki, and T. Nakamura, "Preparation and assessment of revised simulated body fluids," *J. Biomed. Mater. Res.*, vol. 65A, no. 2, pp. 188–195, 2003, ISSN: 1549-3296. DOI: 10.1002/jbm.a.10482.

[57] ASTM NACE G31-12a, *Standard Guide for Laboratory Immersion Corrosion Testing of Metals*. PA: ASTM International West Conshohocken, 2012. DOI: 10.1520/G0031-21.

[58] ASTM G1-03 (Reapproved 2017), *Standard Practice for Preparing, Cleaning, and Evaluating Corrosion Test Specimens*. PA: ASTM International West Conshohocken, 2017. DOI: 10.1520/g0001-03r17e01.

[59] F. Gremse, M. Stärk, J. Ehling, J. R. Menzel, T. Lammers, and F. Kiessling, "Imalytics preclinical: interactive analysis of biomedical volume data," *Theranostics*, vol. 6, no. 3, pp. 328–341, 2016. DOI: 10.7150/thno.13624.

[60] ASTM F3268-18a, *Standard Guide for in vitro Degradation Testing of Absorbable Metals*. PA: ASTM International West Conshohocken, 2018. DOI: 10.1520/f3268-18a.

[61] ASTM G46-94, *Standard Guide for Examination and Evaluation of Pitting Corrosion*. PA: ASTM International West Conshohocken, 2005. DOI: 10.1520/g0046-94r18.

[62] X. Gu, F. Wang, X. Xie, M. Zheng, P. Li, Y. Zheng, L. Qin, and Y. Fan, "In vitro and in vivo studies on as-extruded Mg- 5.2 wt.%Zn- 0.6 wt.%Ca alloy as biodegradable

metal," *Science China Materials*, vol. 61, no. 4, pp. 619–628, 2018, ISSN: 2095-8226 2199-4501. DOI: 10.1007/s40843-017-9205-x.

[63] Y. Liu, Y. Zheng, X. Chen, J. Yang, H. Pan, D. Chen, L. Wang, J. Zhang, D. Zhu, S. Wu, K. W. K. Yeung, R. Zeng, Y. Han, and S. Guan, "Fundamental Theory of Biodegradable Metals - Definition, Criteria, and Design," *Advanced Functional Materials*, vol. 29, no. 18, 2019, ISSN: 1616-301X 1616-3028. DOI: 10.1002/adfm.201805402.

[64] A. Amerinatanzi, R. Mehrabi, H. Ibrahim, A. Dehghan, N. Shayesteh Moghaddam, and M. Elahinia, "Predicting the Biodegradation of Magnesium Alloy Implants: Modeling, Parameter Identification, and Validation," *Bioengineering (Basel)*, vol. 5, no. 4, 2018, ISSN: 2306-5354 (Print). DOI: 10.3390/bioengineering5040105. [Online]. Available: https://www.ncbi.nlm.nih.gov/pubmed/30501102.

[65] Z. Shen, M. Zhao, X. Zhou, H. Yang, J. Liu, H. Guo, Y. Zheng, and J.-A. Yang, "A numerical corrosion-fatigue model for biodegradable Mg alloy stents," *Acta Biomaterialia*, vol. 97, pp. 671–680, 2019, ISSN: 17427061. DOI: 10.1016/j.actbio.2019.08.004.

[66] E. L. Silva, S. V. Lamaka, D. Mei, and M. L. Zheludkevich, "The Reduction of Dissolved Oxygen During Magnesium Corrosion," *ChemistryOpen*, vol. 7, no. 8, pp. 664–668, 2018, ISSN: 2191-1363 (Print) 2191-1363 (Linking). DOI: 10.1002/open.201800076. [Online]. Available: https://www.ncbi.nlm.nih.gov/pubmed/30181945.

[67] B. Denkena and A. Lucas, "Biocompatible Magnesium Alloys as Absorbable Implant Materials – Adjusted Surface and Subsurface Properties by Machining Processes," *CIRP Annals*, vol. 56, no. 1, pp. 113–116, 2007, ISSN: 00078506. DOI: 10.1016/j.cirp.2007.05.029.

[68] E. Galvin, S. Jaiswal, C. Lally, B. MacDonald, and B. Duffy, "In Vitro Corrosion and Biological Assessment of Bioabsorbable WE43 Mg Alloy Specimens," *Journal of Manufacturing and Materials Processing*, vol. 1, no. 1, 2017, ISSN: 2504-4494. DOI: 10.3390/jmmp1010008.

[69] M. Schinhammer, J. Hofstetter, C. Wegmann, F. Moszner, J. F. Löffler, and P. J. Uggowitzer, "On the Immersion Testing of Degradable Implant Materials in Simulated Body Fluid: Active pH Regulation Using CO2," *Advanced Engineering Materials*, vol. 15, no. 6, pp. 434–441, 2013, ISSN: 14381656. DOI: 10.1002/adem.201200218.

Chapter 7

Predicting in-vitro corrosion performance and mechanical integrity of WE43 Magnesium bone plate designs through in-silico modelling

7.1 Introduction

Bioabsorbable magnesium-based implants have the potential to overcome certain complications that arise with permanent metallic implants, as they are completely absorbed by the human body once the surrounded tissue is fully healed. Magnesium alloys have excellent mechanical properties, good biocompatibility and show both osseointegration and osteoconductive effects [1–5]. However, challenges still remain with magnesium-based implants and rapid corrosion rates can lead to early failure of implants. Furthermore, hydrogen formation during the corrosion process can also cause necrotic cell death of the surrounding tissue [6]. To control the degradation process, two main approaches are used, whereby (i) alloy composition is optimised or (ii) surface treatments are used to provide a protective layer against corrosion. Through the in-vitro study in Chapter 6, it has been shown that plasma electrolytical oxidation (PEO) surface modification decelerates the overall corrosion rate of magnesium WE43 significantly. However, localised corrosion is still unavoidable due to impurities in the alloy through the manufacturing process and the presence of Chloride ions, which break down the protective degradation layer [7, 8]. From the experimental work conducted in Chapters 4 and 6, it has been shown that degradation proceeds through a non-

uniform surface-based corrosion process, which presents certain challenges when designing load-bearing orthopaedic implants.

Bioabsorbable magnesium-based implants have a range of potential orthopaedic applications, with several fixation and interference screws having already achieved clinical success and are available on the market. There is further potential to develop magnesium-based bone plates for fracture fixation in either foot or hand reconstructions [9]. However, the development of these devices presents some further challenges, as the required material volume is much higher compared to individual fixation screws. This implies that the overall amount of hydrogen released by the implant during the corrosion process will be greater, which could lead to complications in the implanted region. In designing these implants, design optimisation and the minimisation of material usage becomes increasingly important. This is particularly relevant as, while baseline alloy compositions might be similar, magnesium-based implants can be produced through a range of different production processes, which could result in different surface structures, provoking differences in corrosion rates and mechanisms [10].

The target functional properties of magnesium-based orthopaedic implants are that they should provide enough structural support in the first number of months, while minimizing the amount of material used to limit the overall amount of hydrogen that is released during degradation. To streamline the development process of biodegradable implants, degradation models can be beneficial to optimise the corrosion performance. In Chapter 6, a phenomenological surface-based finite element degradation model was calibrated to a WE43 medical grade magnesium alloy, in both unmodified and PEO surface modified conditions. This was based on an extensive in-vitro immersion study of uniaxial tensile test specimens that identified input parameters of the corrosion models to match the morphological features of surface-based corrosion and the resulting mechanical integrity. While this surface-based degradation model has shown an excellent match following model calibration in this previous study, further independent validation of the model parameters is required to demonstrate the functionality of the degradation model in the design optimisation of orthopaedic implants.

In this study, the predictive power of a calibrated surface-based corrosion model was evaluated through a case study that uses orthopaedic bone plates manufactured from magnesium WE43. Both unmodified and PEO-modified bone plates were designed and manufactured, with in-vitro immersion testing conducted under the same testing conditions that were described in Chapter 6. After immersion, four-point bending tests were conducted to evaluate the mechanical response of the plate designs during the corrosion process. In parallel, finite element models of the bone plates were generated, with degradation models used to simulate the corrosion process based on the previously calibrated model parameters. The performance of these models was assessed by simulating the resulting four-point bend behaviour and comparing to the experimental data. In addition, a simulated design study was carried out to adapt the design of the bone plates to enable a reduced material volume, without reducing the mechanical performance.

7.2 Material and Methods

7.2.1 Sample preparation

A total of 14 generic 8-hole bone plates were manufactured from WE43MEO (Meotec GmbH, Aachen Germany, chill-casted and extruded) in accordance to ASTM F382-17 minimal specification [11]. WE43MEO is the same magnesium alloy as the tensile specimens from Chapter 6 and material composition was tested through inductively coupled plasma atomic emission spectroscopy (ISC-OES) measurements, to confirm the specification. Bone plates were manufactured from an 8 mm diameter rod (Swiss GT 13, Tornos, Switzerland) until the plates had a thickness of 1.8 mm. A final thickness of 1.6 mm was achieved by manual sanding using 120 and 320 grit silicon carbide sandpaper. Holes were initially machined with a diameter of 2 mm and then finally increased to 3.2 mm with a drill press. The final geometry of the plates is shown in Figure 7.1 (a), with these designs having similar dimensions within

the range of orthopaedic plates for the foot [12, 13].

Prior to immersion testing, one sample group underwent plasma electrolytic oxidation surface modification following the same protocol as described in [14] and employed in Chapter 6. Briefly, a pulsed rectifier set (M-PEO A1, Meotec GmbH, Germany) and phosphate-based electrolyte (Kermasorb®, Meotec GmbH, Germany) were utilized, while process parameters were chosen to achieve a target surface thickness of 15 µm. Prior to immersion, all samples were weighed using a precision balance (Kern ABJ-NM/ABS-N, $e = 0.001\,g$, KERN & SOHN GmbH, Germany).

7.2.2 Immersion testing

Immersion testing was carried out over a 28-day period, with an intermediate time step defined at 14 days, whereby $n = 3$ plates were used at each time point for both the unmodified and PEO-modified groups. Testing followed the same protocol as described in Chapter 6, whereby samples were immersed in a 500 mL c-SBF filled glass beaker [15]. This resulted in a volume (V) to surface (S) ratio of $V/S = 0.594\,\mathrm{mL/mm^2}$, which was above the minimum of $0.2\,\mathrm{mL/mm^2}$ required by ASTM G31-21 [16]. Hydrogen evolution was measured by capturing hydrogen gas in an inverted funnel burette, with readings taken twice a day, whereby 1 mol of magnesium corresponds to 1 mol of evolved hydrogen [17]:

$$\mathrm{Mg} + 2\mathrm{H_2O} \rightarrow \mathrm{Mg(OH)_2} + \mathrm{H_2} \uparrow \tag{7.1}$$

Immersion testing was performed under cell culture conditions in an incubator (CellXpert C170i, Eppendorf AG, Hamburg, Germany) at $37\,^{\circ}\mathrm{C} \pm 1\,^{\circ}\mathrm{C}$ with a constant CO_2 atmosphere of 1.5 % to maintain a physiological pH of 7.4. After removal, the pH of each solution was measured (FiveEasy F20, Mettler-Toledo GmbH, Germany) and samples were rinsed with deionized water and ethanol before they were fully dried.

Based on the findings from Chapter 6, measurements of mass loss from hydrogen evolution

method are generally underestimated [18–22]. Therefore, all plates underwent several ultrasonic cleaning cycles after mechanical testing to obtain accurate measurements of mass loss through weighing. To remove brittle particles, the samples were first cleaned with a brush and then immersed for ten minutes in a deionized water ultrasonic bath (Emmi 20 with 45 kHz, EMAG AG, Germany), cleaned for ten seconds in pure ethanol, and dried for five minutes at 70 °C in an oven (UNB 100, 14 L, Memmert GmbH + Co. KG, Germany). Samples were weighed every fourth loop using a balance (Kern ABJ-NM/ABS-N, e = 0.001 g, KERN & SOHN GmbH, Germany). The cycle restarted from the beginning until the mass difference between four cycles was less than 0.5 %.

7.2.3 Four-point bend testing

Static four-point bending tests were performed in accordance to ASTM F382-17 [11] using an uniaxial testing machine (DYNA-MESS TP 5 kN HF, DYNA-MESS Prüfsysteme GmbH, Germany). A schematic of the four-point bend configuration and the corresponding test set-up is provided in Figure 7.1 (b) and (c), respectively. The machine was equipped with supports/rollers that were custom-made from PLA, which had a diameter of 6 mm and had stainless steel rods that were fixed with a rubber band to serve as support points on the plate. An even force distribution on the panel was achieved by placing the rollers at equal distances from each other, with a span of 12 mm used between each roller/support. Uniaxial displacement loading was applied with a constant velocity of 0.1 mm/s up to a displacement of 12 mm.

7.2.4 Finite element modelling – validation

A finite element model with the same geometry as the tested bone plates was built in Abaqus/CAE (Dassault Systèmes Simulia Corp., RI, USA), as shown in Figure 7.2 (b) de-

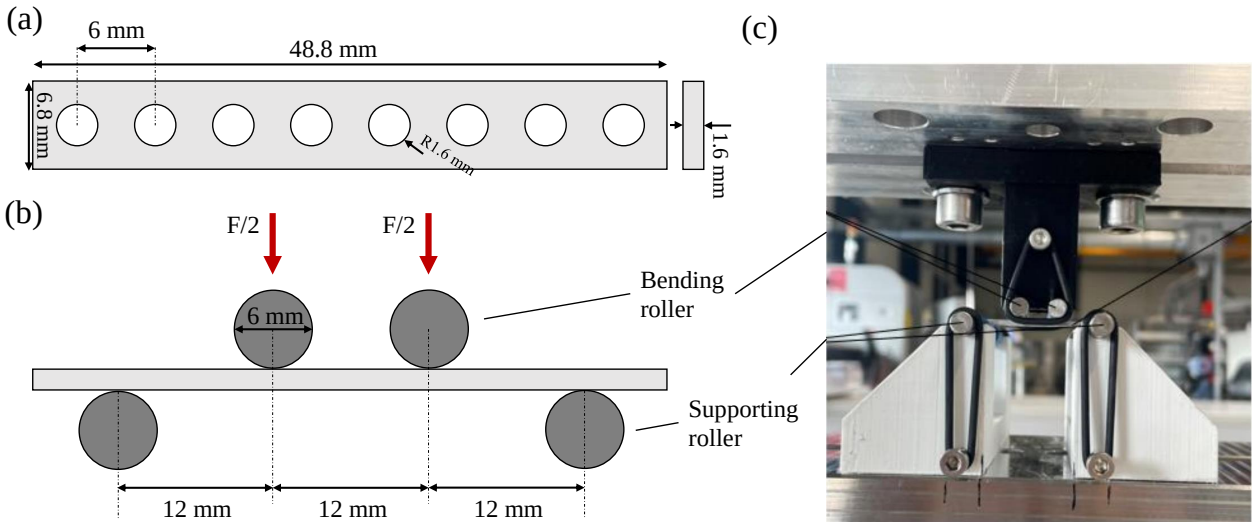

Figure 7.1: (a) Dimensions bone plate (b) Schematic overview of the four-point bending test setup (c) corresponding photograph of the four-point bending test setup.

sign A. A characteristic element size of 80 µm was used (similar to the tensile specimens in Chapter 5 and 6), which resulted in a total of 1.03 million three-dimensional reduced integration brick elements (C3D8R) for the unmodified WE43 samples. For the WE43-PEO surface modified sample, an additional surface layer of solid elements was included on the surface of the model that had a thickness of 15 µm and resulted in a total of 1.17 million C3D8R elements.

A calibrated elastic-plastic constitutive material model was chosen to predict the mechanical response of the WE43 material, which used the same parameters as those described in Chapter 5 and 6 and shown in Table 7.1 (b) [23]. Corrosion simulations were carried out using Python, by exporting nodal and element data from Abaqus. This enabled larger models to be simulated ($>$100,000) in a lower amount of computational time. The script returned a list of the elements to Abaqus to remove those elements from the initial finite element mesh. Similar to Chapter 5 and 6, the enhanced surface-based corrosion model was used to predict the corrosion performance of the bone plates. This is explained in detail in Sections 5.2.2 and 6.2.4. Briefly, this enhanced surface-based corrosion model used a continuum damage mechanics approach described by Quinn et al. [24] to achieve realistic spatial progression of corrosion. Non-uniform corrosion was governed by assigning a random number distribution

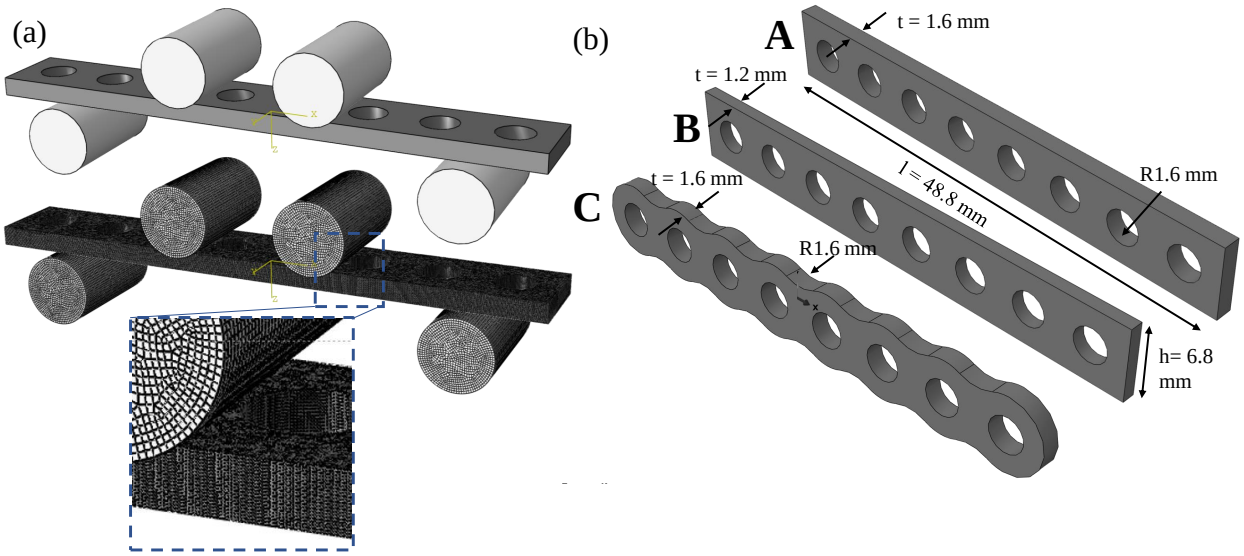

Figure 7.2: (a) four-point bending simulation set-up, (b) Dimension of the three generic bone plate designs.

to all elements, which is represented by a standard Weibull shape function, which controlled the severity of localised corrosion. Following the calibration process in Section 6.2.4, this bone plate models used an identical set of parameters for corrosion simulations here. These are summarised below in Table 7.1 (a).

Surface-based corrosion was simulated for both the unmodified WE43 and WE43-PEO modified groups for the same 28-day time period. Four-point bend testing was simulated at the same time points as the experimental tests (day 0, 14 and 28). For these simulations, the rollers/supports were assumed as discrete rigid bodies, which were represented in Abaqus as R3D4 elements. Figure 7.2 (a) shows the four-point bending simulation setup. The general contact algorithm in Abaqus was used, whereby a friction coefficient of 0.3 in the tangential direction was assumed between the plate and the rollers.

7.2.5 Design optimisation

To optimise the plate design, two other geometries were simulated for both the unmodified WE43 and WE43-PEO modified materials, as shown in Figure 7.2 (b). Plate design B had

Table 7.1 Input parameters of the degradation simulations for WE43 alloy and WE43-PEO

(a) Input parameters degradation model

Parameter	WE43	WE43-PEO
k_u	0.05	0.0025
γ	0.6	0.6
β	1.0	1.0
B	3.0	3.0
f_{PEO}	-	0.0015

(b) Elastic-plastic material parameters for WE43 and WE43-PEO

Parameter	Value
Young's modulus (E)	44.703 GPa
Density (ρ)	1.84 g/cm^3
Poisson ratio (ν)	0.3
Yield stress (MPa)	**True Plastic strain**
230.04	0.
229.59	0.00029
235.40	0.00643
247.92	0.02990
265.67	0.05166
284.68	0.07424
302.16	0.09617
317.50	0.11763
330.60	0.13883
341.29	0.15982
349.00	0.1793
355.00	0.19422
357.00	0.1985

a reduced thickness of $t = 1.2$ mm compared to the initial geometry (t_0 =1.6 mm). Plate design C retained the original thickness and considered round cut-outs from each screw holes to maintain the minimum characteristics of the initial plate. Both design adaptations were developed for WE43 and WE43-PEO with the same element size (80 µm) as the initial design, which resulted in approximately 1 million C3D8R elements. Again, surface-based corrosion was simulated for both the unmodified WE43 and WE43-PEO modified groups for both design B and design C over the 28 day time period. Four-point bend testing was simulated, as before, with the maximum bending force compared across each group (unmodified WE43 and PEO modified WE43).

7.3 Results

7.3.1 Immersion testing and four-point bending testing

Figure 7.3 shows images from one bone plate from the (a) unmodified WE43 and (b) WE43-PEO modified group after each time point. Here, the as-manufactured day 0 samples are shown, while the corroded and dried samples are shown at 14 and 28 days after removal from immersion media, with additional samples shown after mechanical testing and ultrasonic cleaning. It was found that as soon as samples were immersed, a thick degradation layer started to evolve on the plate surface in c-SBF [25], which meant that it was difficult to quantify the local severity of corrosion without removing the degradation products. However, after ultrasonic cleaning, differences between the unmodified WE43 group and the WE43-PEO modified group become visible across both time points.

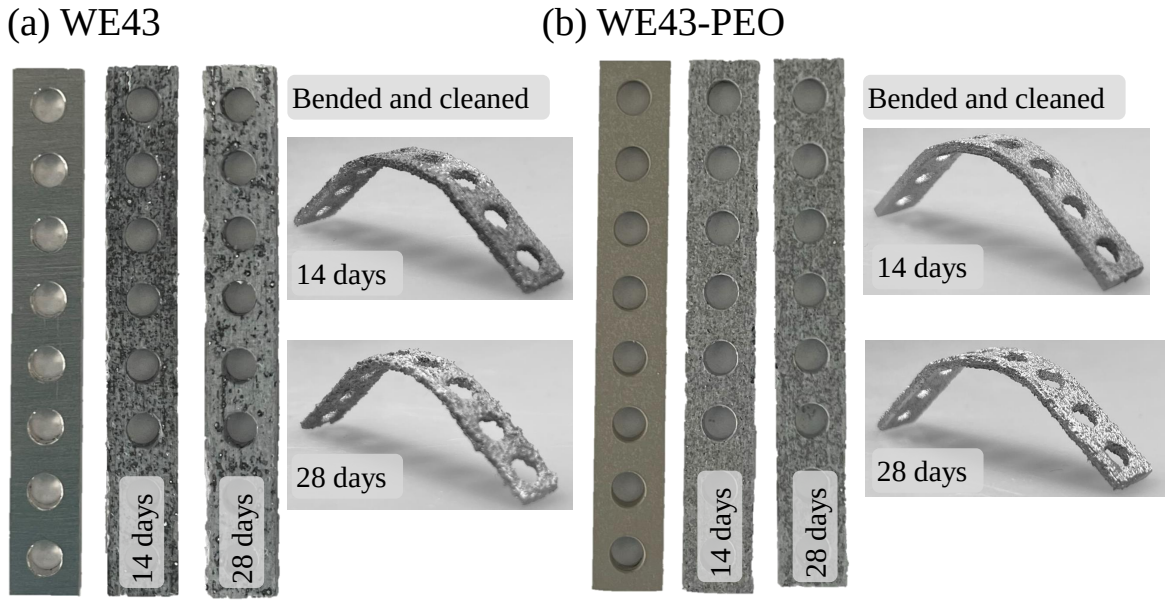

Figure 7.3: Images of the undegraded, degraded, four-point bending tested and ultrasonic cleaned samples (a) WE43 (b) WE43-PEO.

Figure 7.4 (a) shows the hydrogen evolution in mL/cm^2 (secondary y-axis) and corresponding

mass loss calculated through Equation (7.1) with the chemical reaction of magnesium in aqueous solutions. Across both the unmodified WE43 and WE43-PEO modified groups, hydrogen evolution showed an initial steep increase, followed by a more constant evolution. Moreover, the detected standard deviation for both groups was low, which is represented by shaded areas around the mean values (n=3 per group).

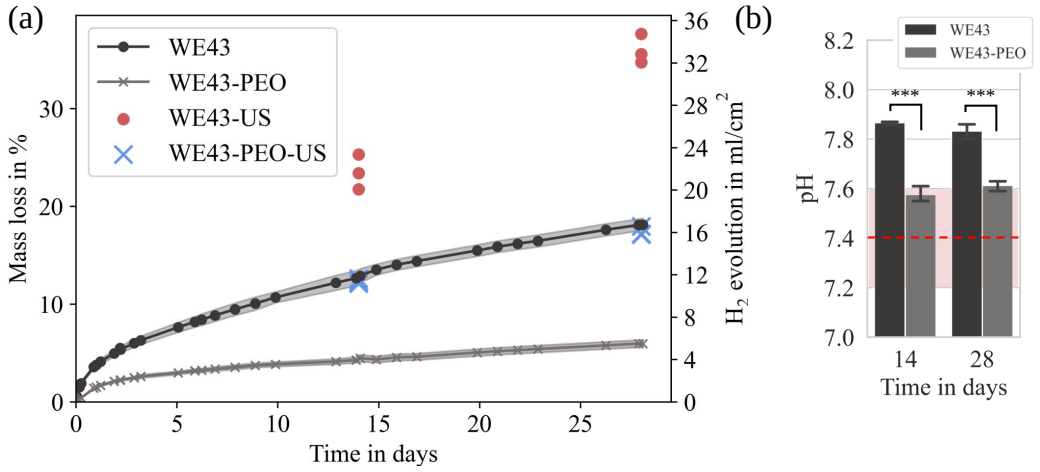

Figure 7.4: (a) Determined mass loss from evolved hydrogen and determined mass loss through gravimetric measurements by ultrasonic cleaning (b) detected pH in the immersion solution after sample removal.

Figure 7.4 (a) also provides the mass loss of both groups at each time point (14 and 28 days), derived through gravimetric methods with ultrasonic cleaning. As before, hydrogen evolution underestimated the overall mass loss by a factor of ~ 2 compared to the ultrasonic cleaning. Here, the total mass loss of the WE43-PEO modified plates was almost half of the unmodified WE43 at both time points considered. Additionally, pH values are shown in Figure 7.4 (b), whereby a significantly lower pH was observed for the PEO modified WE43 group compared to unmodified WE43. Thus, the pH values for both time points of the unmodified WE43 group exceeded the specification of ASTM F3268-18a (7.4 ± 0.2) [26], due to the high absolute amount of corrosion products that were presented. However, the same testing conditions as in Chapter 6 were required to avoid any differences in performance.

Figure 7.5 shows the force-deflection curves from the experimental four-point bend testing for all samples. Both the stiffness and peak loads for both WE43 and WE43-PEO groups at

day 0 were similar. As corrosion proceeded, there was a general reduction in the peak force

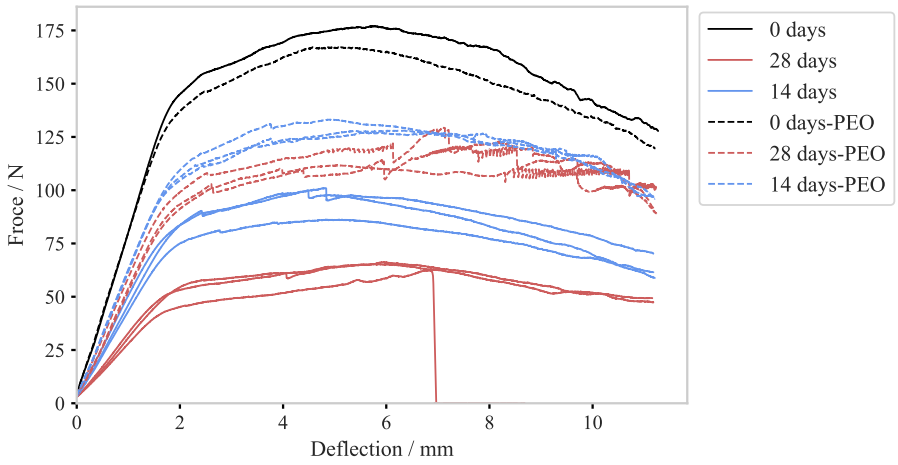

Figure 7.5: Force deflection curves for WE43 and WE43-PEO, undegraded, 14 and 28 day degraded from four-point bending testing. For clarity, only one representative curve is shown for day 0 samples.

achieved across all corroding samples, with the unmodified WE43 having a lower stiffness and peak force compared to WE43-PEO modified group at each time point. After 14 days, the peak force of the WE43-PEO modified samples was 35 % higher than the unmodified WE43 group at this time point. At 28 days, the WE43-PEO modified samples were 66 % higher than the unmodified WE43 group. At both time points, these higher peak forces corresponded to a lower mass loss of the WE43-PEO modified group compared to the unmodified WE43 group. It should also be noted that at 28 days, one of the unmodified WE43 samples failed at a deflection of just 7 mm, which may have been a result of highly localised corrosion in areas under bending.

7.3.2 Degradation and four-point bending simulations

Figure 7.6 (a) shows the corrosion rate, which is plotted as mass loss over immersion time, from both the experiments, shown as data points, and the computational simulations of corrosion on the generic bone plates. Here, the experimental corrosion rates were lower than those initially predicted by the calibrated models from Chapter 6 for both groups (solid

lines). As a consequence of the predicted corrosion rate being higher than experimental

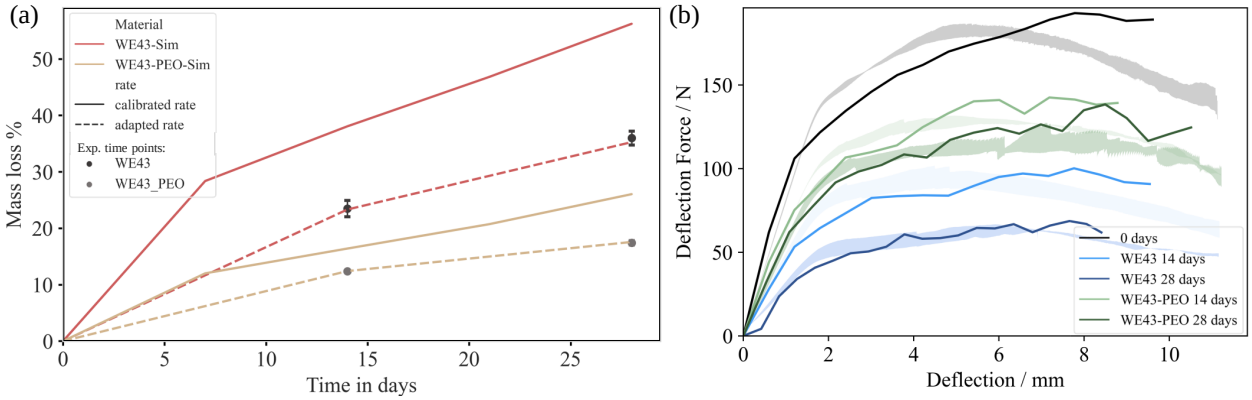

Figure 7.6: (a) Calibrated degradation rate identified in Chapter 6 and the adapted rate used for the simulations to fit experimentally tested plates. (b) Force-deflection response of the simulation (solid lines) compared to the experimental response (shaded areas).

values, a further calibration was carried out, whereby the identified mass loss values for the two time points (14 and 28 days) were used as target values for the respective degradation models. This ensured the same corrosion formation as the experiments and enabled mechanical responses to be compared and further design optimisation to be carried out. It is important to note that the kinetic parameter presented in Table 7.1 (a) was not modified in this study. Instead, the conversion of the accumulated damage increment from the number of loops was adjusted to align with the time points of 14 and 28 days, respectively. Based on this adapted rate, the simulated degradation models are shown in Figure 7.8 and the corresponding force-deflection curves derived from the four-point bending simulations are shown in Figure 7.6 (b). Here, the resulting force-deflection curves from the simulations generally show good agreement with the experimental data across the various time points, with a general reduction in stiffness and peak forces captured by the model as corrosion progressed. Furthermore, the relative differences between the unmodified WE43 and the WE43-PEO modified was captured. However, the simulations slightly over-predicted the response after a peak force and did not quite capture a drop in force that occurred in the experiments.

Figure 7.7 shows the peak deflection force over mass loss for all experimentally tested bone plates and the respective simulated data points. Results show, for the WE43-PEO modified

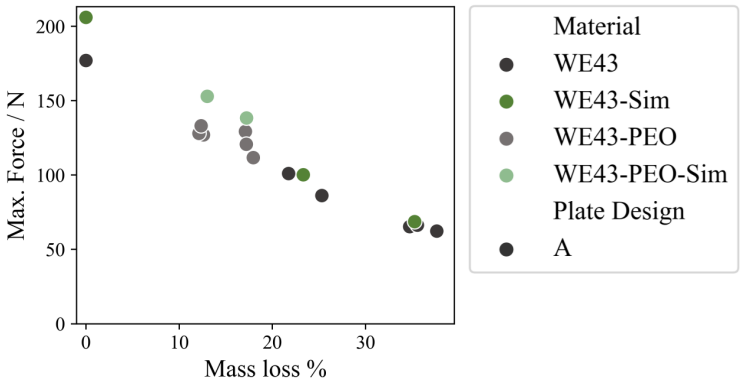

Figure 7.7: Peak deflection force over mass loss for all experimentally tested bone plates and the respective simulated data points. (Mass loss values here were taken from the gravimetric measurements with ultrasonic cleaning.)

group, absolute differences between the simulated and experimental values of 23 N (14 %) for 14 days and 17 N (12 %) for 28 days. For WE43 unmodified, the differences between the average maximum force and the simulated results are for both time points almost negligible with 4 N. In general, for unmodified WE43, a greater consistency of the simulations with the experimental data is visible, compared to the PEO surface modified models. Interestingly, all data points in Figure 7.7 are almost linearly correlated, within the examined range of mass loss values, independent of the surface treatment.

Figure 7.9 shows the Von Mises stress distribution for the last time increment of the four-point bending simulations of the previous corroded models of both groups, unmodified WE43 and WE43-PEO modified. Peak stresses always occurred around the holes, where the highest deflections were also detected. Although, the stress distribution around each hole is not the same, which can be attributed to the occurrence of localised corrosion. Thus, areas with more localised corrosion are more highly stressed compared to less corroded areas. It should be noted that some simulations had convergence issues and weren't able to reach the full predefined deflection of 12 mm.

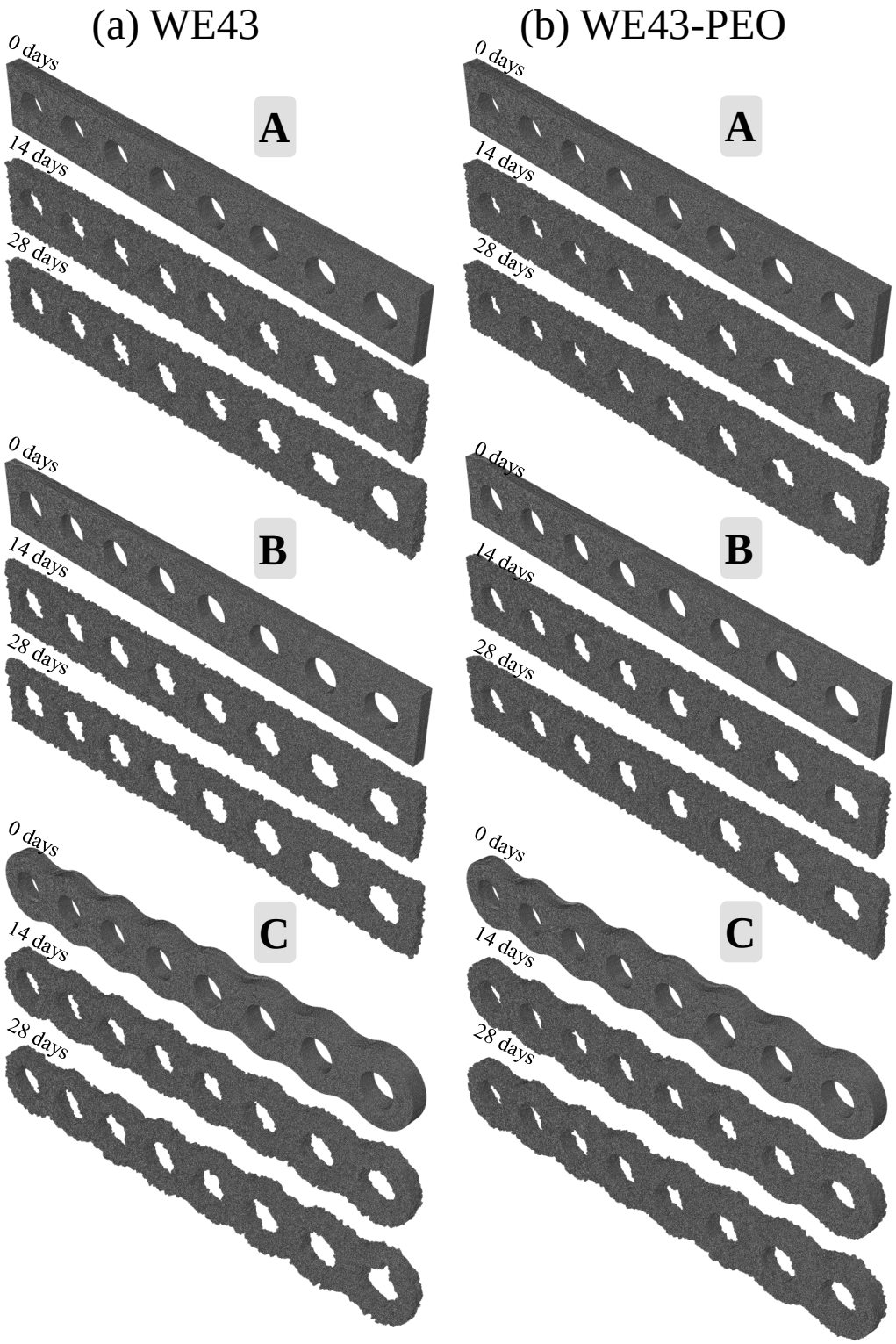

Figure 7.8: Finite element models of designs A, B, C after the respective degradation simulations for 14 and 28 days for WE43 and WE43-PEO.

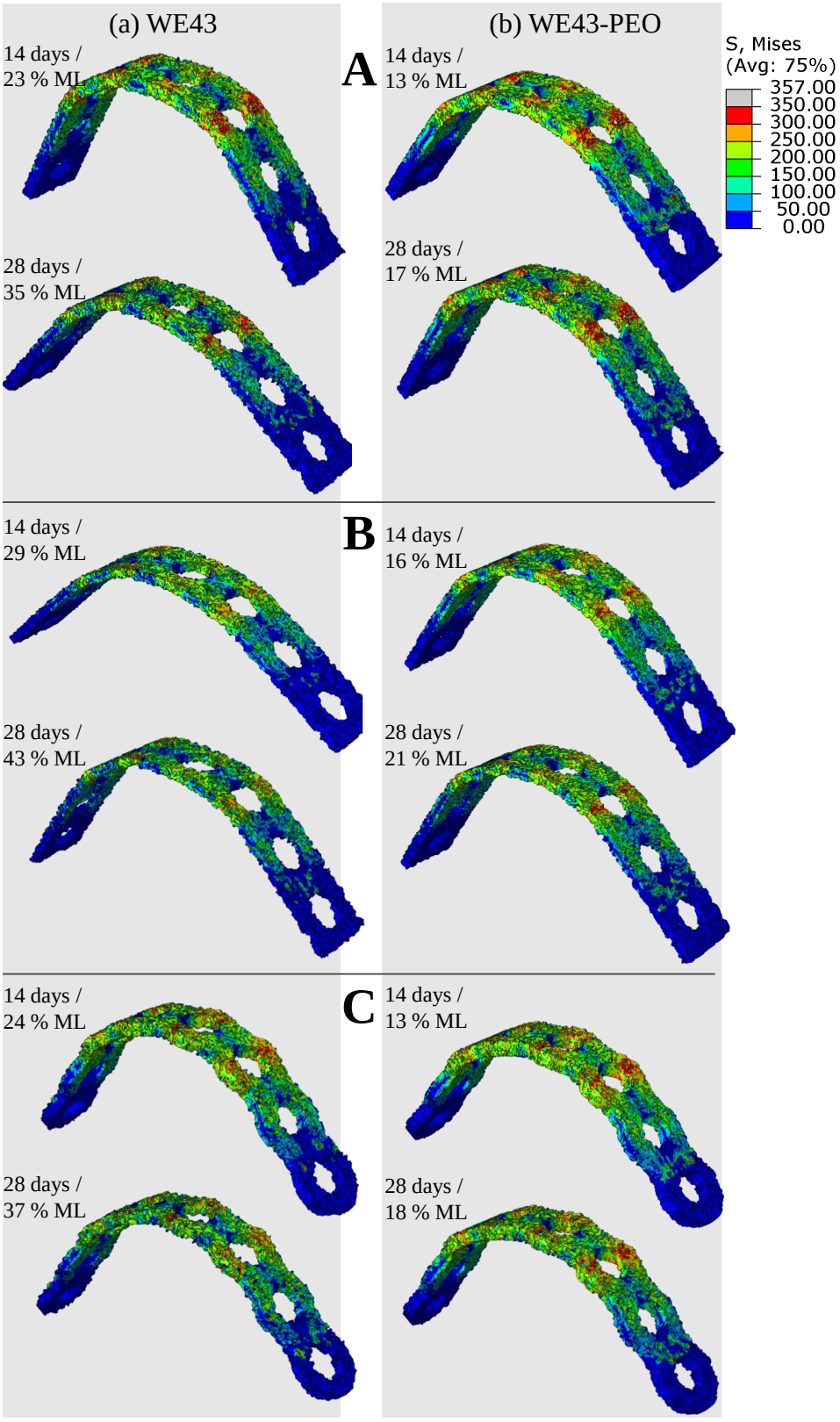

Figure 7.9: Von Mises stress distribution for models degraded for 14 and 28 days for WE43 and WE43-PEO. Some simulations ran into convergence before reaching the final deflection of 12 mm. (Mass loss is abbreviated as ML).

7.3.3 Design comparison

Additionally, two other plate geometries were simulated, to examine the influence of the plate design on the resulting mass loss and remaining deflection force during corrosion. Figure 7.8 shows the predicted corrosion in the unmodified WE43 and WE43-PEO models for all designs, respectively. Here, design B is 0.4 mm thinner compared to design A, while C was equipped with circular shaped cut-outs, to keep the minimum characteristics of the initial plate. The full simulated force deflection response of the four-point bending tests of design B and C are shown in Figure 7.10. In general, also design B and C do not show a clear

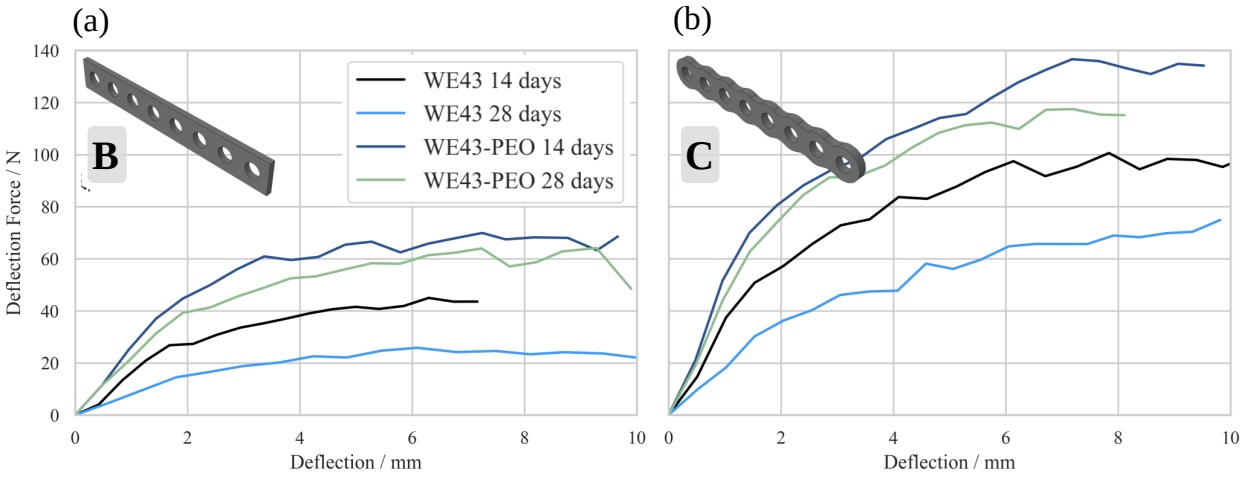

Figure 7.10: Full force deflection response of four-point bending testing of (a) plate design B and (b) plate design C. (Legend in (a) applies also to (b)).

drop once the peak force is reached for all conducted simulations. The thinner plate design B showed a lower deflection force compared to design C at all time points for both groups, unmodified WE43 and WE43-PEO. Including the force deflection curves from Figure 7.6 (b) for the initial design A, a similar force deflection response over the time points was found for design C for both groups, shown in Figure 7.10 (b).

Measurements of the material loss and the corresponding peak deflection force, and immersion time are plotted among each other in Figure 7.11. For unmodified WE43, Figure 7.11 (c) shows that, due to its thinner profile, plate B has substantially lower peak forces at 14

and 28 days compared to plate design A. However, Figure 7.11 (a) shows that the difference in the absolute material loss between design A and B is almost zero for the two time points. While PEO modification slows the corrosion rate of plate B, there is still a lower remaining peak deflection force compared to unmodified plate A. Considering design C (triangle shaped markers in Figure 7.11), there is $\sim 10\,\%$ less material loss taking place compared to design A. While at early time points, plate C achieves a slightly lower peak force compared to plate A, both designs achieve almost the same force at 28 days for the unmodified samples. In the PEO modified samples, the slightly lower peak force in design C compared to design A is still evident at 28 days, although these properties are achieved with less material loss. The difference between the unmodified WE43 and WE43-PEO group might be related to the overall less degraded PEO modified group, which induces the need for more data. With design C, the absolute amount of material loss is reduced, while providing similar mechanical stability as with design A. Design C is therefore favourable due to less amount of accompanied hydrogen release.

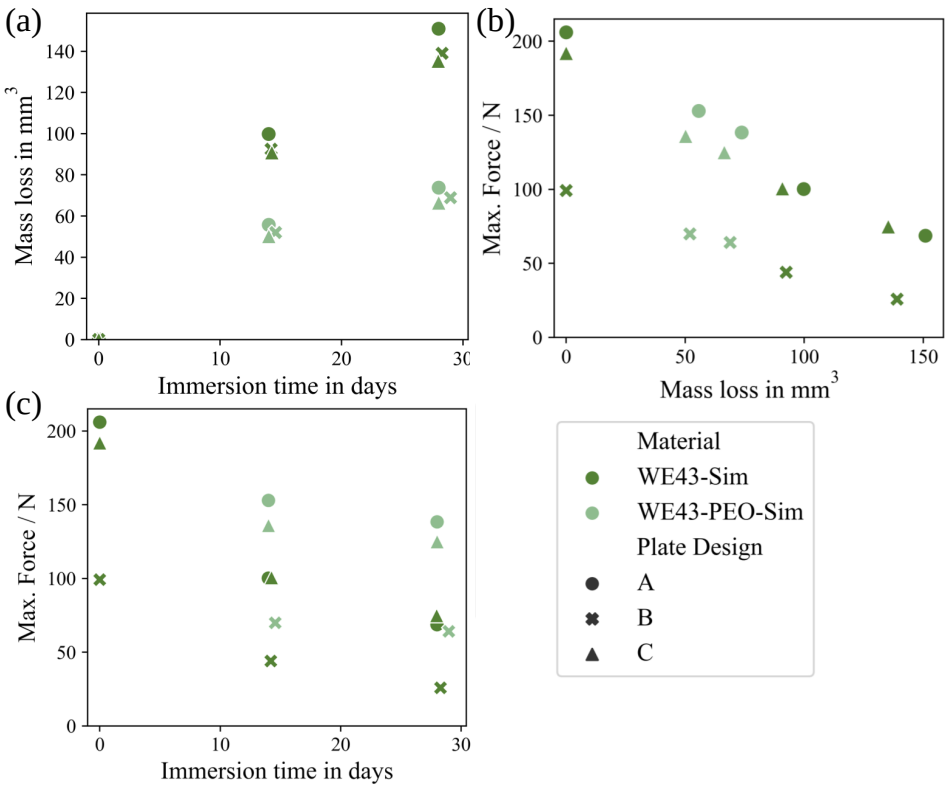

Figure 7.11: Simulation results of the plate designs A,B and C. (a) Total material loss over immersion time; (b) Peak deflection force over total material loss; (c) Peak deflection force over immersion time.

7.4 Discussion

In this study, a finite element phenomenological based degradation model [24, 27], which was calibrated in Chapter 6 to tensile test specimens, was assessed to predict the degradation performance for different bone plate designs. Here, again two groups were examined: (i) unmodified WE43 and (ii) WE43-PEO which underwent PEO surface modification. Using the same testing conditions as the in-vitro immersion tests in Chapter 6, a total of 12 generic bone plates were degraded for 14 and 28 days for both groups. Mechanical testing was performed through four-point bending testing. Additionally, two other plate designs were examined through degradation simulations, followed by structural mechanical finite element analysis.

It was found that the corrosion model parameters that were calibrated in Chapter 6, related to the corrosion rate, did not capture the experimental degradation rates of the bone plates. Model parameters dictating the severity of localised corrosion were not adapted and were taken from Chapter 6. With the adapted lower rate, the corrosion models were able to reproduce the mechanical response of the plates undergoing corrosion within in-vitro immersion testing over the two time steps. In the current study, it was again shown that PEO surface modification on the WE43 magnesium alloy was effective in reducing the corrosion rate. Furthermore, it was shown that relatively simple design changes can be used to enhance the performance of the bone plates during the corrosion process. If the corrosion process is known, design adaptation might be different to those made to conventional implants made from Titanium or Stainless Steel.

In this study, the performance of the calibrated surface-based corrosion model was evaluated through a case study of an orthopaedic bone plate manufactured from magnesium WE43. Here, it was found that the calibrated model parameters from Chapter 6 did not correctly predict the degradation rates of the bone plate during the corrosion experiments. Thus, an adapted rate had to be chosen within the current study, to match the mass loss values from

the degradation simulations with the experimentally immersed plates. These differences may arise from difficulties in the reproducibility of the experimental in-vitro immersion testing, with different specimen geometries [10, 21]. While this study used an identical test setup Chapter 6, there are several potential reasons for differences in the measured rates. Firstly, the geometric features of the plates were substantially different and had a surface area that was four times greater than the exposed gauge section area of the tensile test specimens in Chapter 6. Under immersion, this meant that more corrosion products arise, which resulted in high pH values (WE43 $>$ 7.8; WE43-PEO $>$ 7.55). These values were too high for unmodified WE43 and at the limit of the permissible (7.4 ± 0.2) for WE43-PEO, according ASTM F3268-18a [26]. These higher pH values could be a reason for the lower degradation rates, since it is known that higher pH values will protect specimens from corrosion [28]. Additionally, for the dog bone samples from Chapter 6 the mass loss values were derived from µCT scans, while within the current study µCT scans were not available and gravimetric measurements with ultrasonic cleaning were used. In Chapter 6 in Figure 6.4 (c) it was shown that these gravimetric measurements resulted in a 10 % lower rate for unmodified WE43 and a 6 % lower rate for WE43-PEO. While the bone plate used the identical alloy, the semi-finished product for the bone plate had a larger diameter (8 mm) than the semi-finished product from which the tensile specimens were made (6.5 mm). Furthermore, the bone plates were manually ground to their final thickness of 1.6 mm. Finally, all the above described points influenced in certain degree the corrosion rate, which highlights the challenges in achieving comparable, reproducible results among different test series. Although, with the adapted rates, both degradation models (WE43 and WE43-PEO) were able to follow the same trends as the experimental data, in terms of the rate, as well as the mechanical response for the two examined time points.

The use of magnesium-based implants in load-bearing applications remains limited due to their relatively fast corrosion rates [29, 30] and unavoidable localised corrosion effects. Few in-vivo studies tested magnesium-based bone plates up to date [3, 31–35], with each study

examined only one design. Mostly a generic bone plate design was used, or the same design as conventional bone plates, which induces the need for an additional testing approach to assess several designs to avoid cost-extensive in-vitro or even in-vivo testing, in terms of their mechanical integrity while corrosion progresses. Considering the results from the two design adaptations, highlighted that even simple geometric adjustments can lead to a reduction in the total material loss while maintaining the same mechanical support. With the thinner plate design B, only a minor total material loss was achieved, while a massive reduction of 53 and 66 % deflection force was observed at 28 days for the unmodified WE43 and WE43-PEO group, respectively. Design C, on the other hand, had the same thickness as design A with round cut-outs, which kept the minimum characteristics of the initial plate. For WE43-PEO at 28 days, a total of 10 % less mass loss is detected with 9.4 % less corresponding deflection force. Interestingly, with WE43 at 28 days, also 10 % less total mass loss is detected while a 9 % higher peak force was reached with design C. This is attributed to the localised corrosion effect. Consequently, design C is favourable compared to design A.

In addressing the limitations of the current study, it should be noted that same material properties were assumed for the bone plate designs as for the tensile specimens in Chapter 6, even though the plates were manufactured from a 8.0 mm rod while the initial samples were turned from 6.5 mm rods. Additionally, variations in the mechanical properties of the magnesium alloy are unavoidable along the full length of the final extruded rod, which could result in variations in mechanical properties of the undegraded samples already. Furthermore, four-point bending testing of localised corroded samples can result in a different response if highly attacked areas of corrosion are in the high stressed areas or if they are located in the minor stressed areas. Consequently, different force deflection responses will arise.

Comparing the identified in-vitro corrosion rates to in-vivo data, might be challenging, since it is known, that higher corrosion rates with in-vitro testing in c-SBF are reached compared to in-vivo [21]. Nevertheless, an accelerated degradation performance is favourable in this context to achieve reasonable mass loss within a shorter testing period. Additionally, in the

used in-vitro setup, the hydrogen evolution method is vulnerable to errors due to leakage through the equipment. Further it is known that the evolved hydrogen is also built in the degradation layer itself, and up to date the full reaction of magnesium alloys in aqueous solution is not fully understood [18, 22, 36]. A correct determination of the final mass loss values is crucial for the later degradation model. Within this study, those values were taken from gravimetric measurements by ultrasonic cleaning of the degradation products. In Chapter 6, it was shown that those results show only slightly lower mass loss values compared to the determination through µCT-scans. For a sufficient validation of the degradation models and therefore a definition of the full degradation process of an implant, more in-vitro data is necessary, with a wider sample set, as well as, more time points with a longer immersion time. Additional in-vitro testing of design B and C would be beneficial to support the outcomes of the degradation models.

7.5 Conclusion

In this study, degradation models, which were calibrated through initial in-vitro testing of tensile test specimens, were applied to different generic bone plate models. Whereby, one design was additionally manufactured from the same WE43 magnesium alloy and were subjected to the same test cycle as the tensile specimens, but mechanical testing was conducted through four-point bending tests. Two groups were examined, the WE43 base alloy and a PEO surface modified group. Through in-vitro testing, as well as the degradation model, the decelerating effect of the PEO modification was demonstrated and resulted in general up to 50 % less total mass loss within the same degradation time. However, no agreement in terms of the degradation rate was reached due to inconsistencies within the experimental in-vitro testing. Though, the degradation model was able to predict the same force-deflection response with an adapted degradation rate for unmodified WE43 and PEO modified WE43. Furthermore, it was shown that with biodegradable materials within the design development,

the degradation behaviour should be considered, whereby degradation models have the potential to safe cost-intensive in-vitro and in-vivo tests. It should be carefully considered how long implants have to support the fractured tissue, to be able to save as much material as possible and thus reducing hydrogen formation to a minimum, which might avoid complications at a later stage. Here, the bending force of plate C with round cut-outs to keep minimum characteristics of the initial plate design, resulted in the same values as the initial plate, but with a reduction of 10 % total mass loss.

References

[1] G. B. Darband, M Aliofkhazraei, P Hamghalam, and N Valizade, "Plasma electrolytic oxidation of magnesium and its alloys: Mechanism, properties and applications," *Journal of Magnesium and Alloys*, vol. 5, no. 1, pp. 74–132, 2017, ISSN: 2213-9567. DOI: 10.1016/j.jma.2017.02.004.

[2] L. White, Y. Koo, S. Neralla, J. Sankar, and Y. Yun, "Enhanced mechanical properties and increased corrosion resistance of a biodegradable magnesium alloy by plasma electrolytic oxidation (PEO)," *Mater Sci Eng B Solid State Mater Adv Technol*, vol. 208, pp. 39–46, 2016, ISSN: 0921-5107 (Print). DOI: 10.1016/j.mseb.2016.02.005. [Online]. Available: https://www.ncbi.nlm.nih.gov/pubmed/28603382.

[3] C. Rendenbach, H. Fischer, A. Kopp, K. Schmidt-Bleek, H. Kreiker, S. Stumpp, M. Thiele, G. Duda, H. Hanken, B. Beck-Broichsitter, O. Jung, N. Kroger, R. Smeets, and M. Heiland, "Improved in vivo osseointegration and degradation behavior of PEO surface-modified WE43 magnesium plates and screws after 6 and 12 months," *Mater Sci Eng C Mater Biol Appl*, vol. 129, p. 112 380, 2021, ISSN: 1873-0191 (Electronic) 0928-4931 (Linking). DOI: 10.1016/j.msec.2021.112380. [Online]. Available: https://www.ncbi.nlm.nih.gov/pubmed/34579899.

[4] O. Jung, D. Porchetta, M. L. Schroeder, M. Klein, N. Wegner, F. Walther, F. Feyerabend, M. Barbeck, and A. Kopp, "In Vivo Simulation of Magnesium Degradability Using a New Fluid Dynamic Bench Testing Approach," *Int J Mol Sci*, vol. 20, no. 19, 2019, ISSN: 1422-0067 (Electronic) 1422-0067 (Linking). DOI: 10.3390/ijms20194859. [Online]. Available: https://www.ncbi.nlm.nih.gov/pubmed/31574947.

[5] H. Xu, T. Hu, M. Wang, Y. Zheng, H. Qin, H. Cao, and Z. An, "Degradability and biocompatibility of magnesium-MAO: The consistency and contradiction between in-vitro and in-vivo outcomes," *Arabian Journal of Chemistry*, vol. 13, no. 1, pp. 2795–2805, 2020, ISSN: 18785352. DOI: 10.1016/j.arabjc.2018.07.010.

[6] R. Zan, H. Wang, W. Cai, J. Ni, B. J. C. Luthringer-Feyerabend, W. Wang, H. Peng, W. Ji, J. Yan, J. Xia, Y. Song, and X. Zhang, "Controlled release of hydrogen by implantation of magnesium induces P53-mediated tumor cells apoptosis," *Bioact Mater*, vol. 9, pp. 385–396, 2022, ISSN: 2452-199X (Electronic) 2452-199X (Linking). DOI: 10.1016/j.bioactmat.2021.07.026. [Online]. Available: https://www.ncbi.nlm.nih.gov/pubmed/34820578.

[7] S. Agarwal, J. Curtin, B. Duffy, and S. Jaiswal, "Biodegradable magnesium alloys for orthopaedic applications: A review on corrosion, biocompatibility and surface modifications," *Mater Sci Eng C Mater Biol Appl*, vol. 68, pp. 948–963, 2016, ISSN: 1873-0191 (Electronic) 0928-4931 (Linking). DOI: 10.1016/j.msec.2016.06.020. [Online]. Available: https://www.ncbi.nlm.nih.gov/pubmed/27524097.

[8] G. Song and A. Atrens, "Understanding Magnesium Corrosion - A Framework for Improved Alloy Performance," *Advanced Engineering Materials*, vol. 5, no. 12, pp. 837–858, 2003, ISSN: 1438-1656 1527-2648. DOI: 10.1002/adem.200310405.

[9] J. Wang, J. Dou, Z. Wang, C. Hu, H. Yu, and C. Chen, "Research progress of biodegradable magnesium-based biomedical materials: A review," *Journal of Alloys and Compounds*, vol. 923, p. 166 377, 2022, ISSN: 0925-8388. DOI: https://doi.org/10.1016/j.jallcom.2022.166377. [Online]. Available: https://www.sciencedirect.com/science/article/pii/S0925838822027682.

[10] E. L. Boland, R. N. Shirazi, J. A. Grogan, and P. E. McHugh, "Mechanical and Corrosion Testing of Magnesium WE43 Specimens for Pitting Corrosion Model Calibration," *Advanced Engineering Materials*, vol. 20, no. 10, 2018, ISSN: 14381656. DOI: 10.1002/adem.201800656.

[11] ASTM F382-17, *Standard Specification and Test Method for Metallic Bone Plates*. PA: ASTM International West Conshohocken, 2017. DOI: 10.1520/f0382-17.

[12] Novastep, *Comprehensive platform-Plates & screws*, Web Page, Accessed: 20/12/2022. [Online]. Available: https://www.novastep-ortho.com/en/foot-ankle-surgery-products/airlock-plating-system/.

[13] Medartis AG, *Fore- and Midfoot System 2.0 / 2.3, 2.8*, Web Page, Accessed: 20/12/2022. [Online]. Available: https://www.medartis.com/downloadcenter_brochures/product_brochures/EN_UK/FOOT-01000001_fore_midfoot_system_2.0-2.8_product_information.pdf.

[14] A. Kopp, T. Derra, M. Muther, L. Jauer, J. H. Schleifenbaum, M. Voshage, O. Jung, R. Smeets, and N. Kroger, "Influence of design and postprocessing parameters on the degradation behavior and mechanical properties of additively manufactured magnesium scaffolds," *Acta Biomater*, vol. 98, pp. 23–35, 2019, ISSN: 1878-7568 (Electronic) 1742-7061 (Linking). DOI: 10.1016/j.actbio.2019.04.012. [Online]. Available: https://www.ncbi.nlm.nih.gov/pubmed/30959185.

[15] A. Oyane, H. Kim, T. Furuya, T. Kokubo, T. Miyazaki, and T. Nakamura, "Preparation and assessment of revised simulated body fluids," *J. Biomed. Mater. Res.*, vol. 65A, no. 2, pp. 188–195, 2003, ISSN: 1549-3296. DOI: 10.1002/jbm.a.10482.

[16] ASTM NACE TM0169/G31-21, *Standard guide for laboratory immersion corrosion testing of metals*, Standard, 2021.

[17] G. Song, A. Atrens, and D. StJohn, "An Hydrogen Evolution Method for the Estimation of the Corrosion Rate of Magnesium Alloys," in *Essential Readings in Magnesium Technology*, S. N. Mathaudhu, A. A. Luo, N. R. Neelameggham, E. A. Nyberg, and W. H. Sillekens, Eds. Cham: Springer International Publishing, 2001, pp. 565–572, ISBN: 978-3-319-48099-2. DOI: 10.1007/978-3-319-48099-2_90.

[18] L. Liu, K. Gebresellasie, B. Collins, H. Zhang, Z. Xu, J. Sankar, Y.-C. Lee, and Y. Yun, "Degradation Rates of Pure Zinc, Magnesium, and Magnesium Alloys Measured by Volume Loss, Mass Loss, and Hydrogen Evolution," *Applied Sciences*, vol. 8, no. 9, 2018, ISSN: 2076-3417. DOI: 10.3390/app8091459.

[19] N. T. Kirkland, N. Birbilis, and M. P. Staiger, "Assessing the corrosion of biodegradable magnesium implants: a critical review of current methodologies and their limitations," *Acta Biomater*, vol. 8, no. 3, pp. 925–36, 2012, ISSN: 1878-7568 (Electronic) 1742-7061 (Linking). DOI: 10.1016/j.actbio.2011.11.014. [Online]. Available: https://www.ncbi.nlm.nih.gov/pubmed/22134164.

[20] Y. B. Ren, H. Wang, J. J. Huang, B. C. Zhang, and K. Yang, "Study of Biodegradation of Pure Magnesium," *Key Engineering Materials*, vol. 342, pp. 601–604, 2007. DOI: 10.4028/www.scientific.net/KEM.342-343.601.

[21] N. T. Kirkland and N. Birbilis, *Magnesium Biomaterials* (SpringerBriefs in Materials). Springer, 2014, ISBN: 978-3-319-02122-5 978-3-319-02123-2. DOI: 10.1007/978-3-319-02123-2.

[22] K. van Gaalen, F. Gremse, F. Benn, P. E. McHugh, A. Kopp, and T. J. Vaughan, "Automated ex-situ detection of pitting corrosion and its effect on the mechanical integrity of rare earth magnesium alloy - WE43," *Bioactive Materials*, 2022, ISSN: 2452199X. DOI: 10.1016/j.bioactmat.2021.06.024.

[23] K. van Gaalen, C. Quinn, F. Benn, P. E. McHugh, A. Kopp, and T. J. Vaughan, "Linking the effect of localised pitting corrosion with mechanical integrity of a rare earth magnesium alloy for implant use," *Bioactive Materials*, vol. 21, pp. 32–43, 2023, ISSN: 2452199X. DOI: 10.1016/j.bioactmat.2022.08.004.

[24] C. Quinn, K. van Gaalen, P. E. McHugh, A. Kopp, and T. J. Vaughan, "An enhanced phenomenological model to predict surface-based localised corrosion of magnesium alloys for medical use," *Journal of the Mechanical Behavior of Biomedical Materials*, p. 105 637, 2022, ISSN: 1751-6161. DOI: https://doi.org/10.1016/j.jmbbm.2022.105637. [Online]. Available: https://www.sciencedirect.com/science/article/pii/S1751616122005422.

[25] M. I. Jamesh, G. Wu, Y. Zhao, D. R. McKenzie, M. M. M. Bilek, and P. K. Chu, "Electrochemical corrosion behavior of biodegradable Mg–Y–RE and Mg–Zn–Zr alloys in Ringer's solution and simulated body fluid," *Corrosion Science*, vol. 91, pp. 160–184, 2015, ISSN: 0010938X. DOI: 10.1016/j.corsci.2014.11.015.

[26] ASTM F3268-18a, *Standard Guide for in vitro Degradation Testing of Absorbable Metals*. PA: ASTM International West Conshohocken, 2018. DOI: 10.1520/f3268-18a.

[27] J. A. Grogan, S. B. Leen, and P. E. McHugh, "A physical corrosion model for bioabsorbable metal stents," *Acta Biomater*, vol. 10, no. 5, pp. 2313–22, 2014, ISSN: 1878-

7568 (Electronic). DOI: 10.1016/j.actbio.2013.12.059. [Online]. Available: https://www.ncbi.nlm.nih.gov/pubmed/24412771.

[28] W. F. Ng, K. Y. Chiu, and F. T. Cheng, "Effect of pH on the in vitro corrosion rate of magnesium degradable implant material," *Materials Science and Engineering: C*, vol. 30, no. 6, pp. 898–903, 2010, ISSN: 09284931. DOI: 10.1016/j.msec.2010.04.003.

[29] X. Gu, F. Wang, X. Xie, M. Zheng, P. Li, Y. Zheng, L. Qin, and Y. Fan, "In vitro and in vivo studies on as-extruded Mg- 5.2 wt.%Zn- 0.6 wt.%Ca alloy as biodegradable metal," *Science China Materials*, vol. 61, no. 4, pp. 619–628, 2018, ISSN: 2095-8226 2199-4501. DOI: 10.1007/s40843-017-9205-x.

[30] Y. Liu, Y. Zheng, X. Chen, J. Yang, H. Pan, D. Chen, L. Wang, J. Zhang, D. Zhu, S. Wu, K. W. K. Yeung, R. Zeng, Y. Han, and S. Guan, "Fundamental Theory of Biodegradable Metals - Definition, Criteria, and Design," *Advanced Functional Materials*, vol. 29, no. 18, 2019, ISSN: 1616-301X 1616-3028. DOI: 10.1002/adfm.201805402.

[31] A. Chaya, S. Yoshizawa, K. Verdelis, N. Myers, B. J. Costello, D. T. Chou, S. Pal, S. Maiti, P. N. Kumta, and C. Sfeir, "In vivo study of magnesium plate and screw degradation and bone fracture healing," *Acta Biomater*, vol. 18, pp. 262–9, 2015, ISSN: 1878-7568 (Electronic) 1742-7061 (Linking). DOI: 10.1016/j.actbio.2015.02.010. [Online]. Available: https://www.ncbi.nlm.nih.gov/pubmed/25712384.

[32] H. Wu, C. Zhang, T. Lou, B. Chen, R. Yi, W. Wang, R. Zhang, M. Zuo, H. Xu, P. Han, S. Zhang, J. Ni, and X. Zhang, "Crevice corrosion - A newly observed mechanism of degradation in biomedical magnesium," *Acta Biomater*, vol. 98, pp. 152–159, 2019, ISSN: 1878-7568 (Electronic) 1742-7061 (Linking). DOI: 10.1016/j.actbio.2019.06.013. [Online]. Available: https://www.ncbi.nlm.nih.gov/pubmed/31201866.

[33] H. Naujokat, C. B. Ruff, T. Kluter, J. M. Seitz, Y. Acil, and J. Wiltfang, "Influence of surface modifications on the degradation of standard-sized magnesium plates and healing of mandibular osteotomies in miniature pigs," *Int J Oral Maxillofac Surg*, vol. 49, no. 2, pp. 272–283, 2020, ISSN: 1399-0020 (Electronic) 0901-5027 (Linking). DOI: 10.1016/j.ijom.2019.03.966. [Online]. Available: https://www.ncbi.nlm.nih.gov/pubmed/31227276.

[34] T. Imwinkelried, S. Beck, T. Iizuka, and B. Schaller, "Effect of a plasmaelectrolytic coating on the strength retention of in vivo and in vitro degraded magnesium implants," *Acta Biomater*, vol. 9, no. 10, pp. 8643–9, 2013, ISSN: 1878-7568 (Electronic) 1742-7061 (Linking). DOI: 10.1016/j.actbio.2012.08.047. [Online]. Available: https://www.ncbi.nlm.nih.gov/pubmed/22963846.

[35] B. Schaller, N. Saulacic, T. Imwinkelried, S. Beck, E. W. Liu, J. Gralla, K. Nakahara, W. Hofstetter, and T. Iizuka, "In vivo degradation of magnesium plate/screw osteosynthesis implant systems: Soft and hard tissue response in a calvarial model in miniature pigs," *J Craniomaxillofac Surg*, vol. 44, no. 3, pp. 309–17, 2016, ISSN:

1878-4119 (Electronic) 1010-5182 (Linking). DOI: 10.1016/j.jcms.2015.12.009. [Online]. Available: https://www.ncbi.nlm.nih.gov/pubmed/26805919.

[36] E. L. Silva, S. V. Lamaka, D. Mei, and M. L. Zheludkevich, "The Reduction of Dissolved Oxygen During Magnesium Corrosion," *ChemistryOpen*, vol. 7, no. 8, pp. 664–668, 2018, ISSN: 2191-1363 (Print) 2191-1363 (Linking). DOI: 10.1002/open.201800076. [Online]. Available: https://www.ncbi.nlm.nih.gov/pubmed/30181945.

Chapter 8

Concluding Remarks and Future Perspectives

8.1 Summary of Key Contributions

For the treatment of bone fractures, a wide variety of orthopaedic fixation implants are available, including screws, plates, nails and wires, with the vast majority of these implants made from titanium or stainless Steel. However, the presence of these permanent metallic implants can cause complications in certain indications, such as the occurrence of stress shielding, which requires implant removal through a second surgery exposing patients to further risk and subjecting them to an additional recovery period [1, 2]. Recently, bioabsorbable magnesium-based implants are receiving increasing attention due to their excellent biocompatibility, osteoconductive properties and their similar mechanical properties to native bone [3–5]. However, there are still key issues to be addressed in the field of magnesium-based implants due to non-uniform and localised corrosion mechanisms that take place, which presents significant challenges during the design and development process in both characterising and predicting the degradation of these devices.

This thesis has provided substantial technical and scientific contributions that address some of the key challenges in understanding and predicting corrosion in magnesium-based materials. The key technical contribution has been to develop a Python-based automated detection framework that quantifies the spatial features of surface-based corrosion formation of magnesium specimens through cross-sectional images derived from either micro-computed tomography (µCT) or simulated models. This framework, *PitScan*, quantifies surface-based corrosion, not only in terms of overall mass loss, but also in terms of the key morphological pa-

rameters that describe both the extent and distribution of non-uniform corrosion. In parallel, the thesis also implemented an enhanced surface-based corrosion model through a combined Python-based finite element framework to enable robust predictions of both the geometrical features and mechanical integrity of corroding specimens. The key scientific contributions have been, for the first time, to establish quantitative correlations between the extent and distribution of surface-based corrosion and the mechanical strength of magnesium specimens through an in-vitro immersion study. Based on these, several new surface-based corrosion parameters were proposed that provided a better mechanistic link with the mechanical performance of specimens. Furthermore, the thesis identified that plasma electrolytic oxidation surface modification, not only significantly reduces the corrosion rate, but also reduces the rate of the mechanical deterioration. This information has the potential to streamline the design development of magnesium-based implants. In the following, further details of the key contributions and main findings from each study are outlined.

In Chapter 4, the automated Python-based detection framework *PitScan* was developed to systematically assess the spatial formation of corrosion. This framework used binary cross-sectional images of circular shaped tensile specimens to identify the current surface profile through edge detection, whereby local minima and maxima were identified through micro-CT scanning. Several parameters describing the geometrical features were quantified, including pit density, pit size, pit depth, and pitting factor as per ASTM G46-94 [6]. Through an in-vitro immersion study of tensile specimens, it was demonstrated that several of these features from ASTM G46-94 showed little correlation to the mechanical strength of specimens undergoing corrosion. However, several new parameters were proposed that provided meaningful correlation to the specimen strength. Typically, these tended to be directly related to the specimen's cross-sectional area. Until now, the vast majority of studies have not considered quantitative measurements of localised corrosion, and instead rely on bulk measurements of mass loss through a range of techniques [7–15]. Studies that have assessed the effects of localised corrosion have typically only done so through qualitative visual inspection of

surfaces or cross-sections [16–20]. However, these techniques provide limited information on the important features of corrosion, which is critical considering their detrimental impact on the mechanical performance of magnesium-based implants. The development of *PitScan* provides a reliable method of tracking surface-based corrosion and could be adopted as a standard for corrosion measurements throughout the research community.

In Chapter 5, a computational model was implemented to further explore the correlations between the severity and distribution of localised corrosion with the mechanical integrity. This framework uses an enhanced surface-based finite element corrosion model to simulate the formation of a wide variety of corrosion morphologies, varying from fully uniform to severe localised corrosion. Using this computational approach, corrosion formation was systematically tracked through the *PitScan* framework. By simulating uniaxial tensile testing, the mechanical response of each corrosion scenario was determined and quantitative relationships were demonstrated between corrosion formation and key mechanical parameters, including specimen strength, strain at maximum strength and the effective Young's modulus. Again, it was found that the minimal cross-sectional area parameter was the strongest predictor of the remaining mechanical strength, with this study showing that this relationship was independent of the severity of localised surface corrosion. Furthermore, it was found that uniform degradation models failed to fully capture the mechanical response of corroding magnesium especially in terms of predicting the remaining strain of samples undergoing corrosion. Importantly, this study was the first to show that a surface-based corrosion model could capture both geometrical features of corrosion and the resulting mechanical performance of a magnesium-based alloy undergoing corrosion.

Chapter 6 examined the influence of a plasma electrolytic oxidation (PEO) surface treatment on a WE43 medical grade magnesium alloy, in terms of the phenomenology of surface corrosion and the mechanical integrity. Testing followed a similar protocol as in Chapter 4, although with a higher amount of samples and a longer testing time. This investigation indicated that PEO treatment significantly decelerated the corrosion rate of the WE43 alloy

compared to unmodified controls. While results showed a deceleration by half in terms of the overall mass loss, mechanical parameters, as well as the phenomenological surface features (calculated through *PitScan*), it was also found that surface corrosion spatially proceeded in a very similar manner in the PEO modified group. This highlights that PEO modification decelerates the progression of corrosion, but does not impact the extent or morphological features of localised corrosion compared to the unmodified WE43 specimens. Calibration of the degradation model was performed on the phenomenological corrosion features, while mechanical parameters followed and no additional adaptation of the model input parameter was conducted. Thus, both models for unmodified WE43 and PEO-modified WE43 can not only capture key geometrical corrosion features, describing the accuracy of the surface morphology under corrosion, but also these models can predict the current mechanical integrity. Finally, in Chapter 7, the performance of the surface-based corrosion model was investigated by applying the model to a generic bone plate geometry for unmodified and PEO-modified WE43 magnesium alloys under four-point bending loading. To validate the results, an experimental in-vitro immersion study was conducted using this bone plate design, followed by four-point bending testing. The simulated results of the corrosion model generally showed good agreement with the in-vitro study. However, the degradation rate of the models had to be adapted compared to the results from Chapter 6. To highlight the potential of the degradation model in the design development chain of degradable implants, two other bone plate designs were simulated. It was found that thinning the plate by 25 % resulted in an insufficient saving of the overall material loss of 7.3 %, but led to drastic reductions in the corresponding deflection force of ∼66 % compared to the initial design. On the other hand, using a design with round cut-outs, which kept the minimum characteristics of the initial plate, resulted in an overall reduction in the amount of degraded material of ∼10 %, with no reduction in the deflection force. This model analysis provides a practical example of how the corrosion model could be used to optimise the design of magnesium-based devices and potentially reduce the amount of material while maintaining mechanical support, thus

avoiding high amounts of hydrogen released during the corrosion process.

8.2 Future Recommendations

This thesis provides a quantitative understanding of the relationship between surface-based corrosion and the mechanical integrity of a WE43 medical grade magnesium alloy. In particular, the development of the *PitScan* automated detection framework provides a method to systematically track the spatial formation of corrosion of cylindrical specimens during immersion testing. This tracking framework, in combination with an extensive in-vitro immersion testing with uniaxial tensile tests over several time steps, enabled a full characterisation of the raw WE43 magnesium alloy and an extensive investigation on the influence of a plasma electrolytic oxidation surface treatment. However, there are several areas for future improvements and following limitations should be mentioned.

A general drawback to date, is that strict guidelines for in-vitro testing of absorbable metals are not available. Currently, an ASTM committee (WK72897) is working on a standardized setup to guide the quantification of degradation properties of absorbable metals [21]. The results from this thesis highlight perfectly the challenges in this area, whereby the corrosion testing from Chapter 7 resulted in a different corrosion rate compared to the initial testing in Chapter 6, which was conducted using the same testing procedures. More generally, these issues make it extremely difficult to (i) compare the corrosion data from different research groups [22, 23] and (ii) to predict how in-vitro corrosion performance would compare to in-vivo conditions. For example, in this thesis, all experimental data were derived from in-vitro immersion testing with c-SBF media, which was chosen to lower the risk of contamination for long-term testing ($>$ 1 week). However, c-SBF accelerates the corrosion process, which is favourable in that it reduces the overall testing time, although the evolving degradation layer that forms is different compared to in-vivo tested samples [24, 25]. Variations in the ion composition of the media will result in a different degradation layer composition, and

also the evolving thickness varies with the selected media. However, within in-vivo tests or in the final later application, implants themselves can be subject to different corrosion rates depending on the implant location [24]. Alternatively, other cell-culture media (e.g. DMEM) could provide more comparable performance when compared to in-vivo data. However, the high tendency for contamination and the longer immersion time to get reasonable mass loss measurements could have led to other challenges. It is still challenging to provide a quantitative correlation between data of in-vitro and in-vivo corrosion tests. Several studies have already identified initial correlation [19, 26–31], although results are not in agreement with one another, with in-vitro rates being reported as between 1-4 times higher than in-vivo. Differences between these rates arise mainly due to difficulties in replicating the complex physiological conditions [32]. One of the major contributions of this thesis was to provide an automated detection framework to evaluate the extent and morphology of local surface-based corrosion. One of the key future recommendations would be to apply this framework to an in-vivo study on corrosion performance of similar specimens, which would enable a correlation between corrosion rates and also the phenomenology of surface corrosion in-vivo. In this thesis, the surface-based corrosion model was calibrated for one specific material in both unmodified and PEO modified conditions. There is potential to apply this surface-based corrosion model to other alloy composition(s), different coating technologies, or materials produced through other manufacturing processes, such as 3D-printed samples using Laser Powder Bed Fusion [33]. In doing this, the *PitScan* framework helps to detail quantification of corrosion across such specimens, although currently it is limited to cylindrical-shaped specimens. Extending the framework to other regular geometries, or even more complex ones to quantify corrosion across screws and plates features would be beneficial to gain more understanding of corrosion formation across samples. With characterisation of other materials, there is the potential to calibrate a specific set of model parameters to predict the corrosion process.

Currently, the medical device industry relies almost completely on experimental testing dur-

ing the development phase of new medical implants. The model framework presented here, shows that predictive tools could provide insights into performance of implants during the design process to reduce the amount of design iterations required during physical prototyping and testing. However, to maximize their use, robust validation approaches are required. Recently, the ASME published a guideline Assessing Credibility of Computational Modeling through Verification & Validation: Application to Medical Devices (ASME V&V40-2018), in which the level of model credibility is evaluated using data from in-vitro testing and any other relevant supporting data in accordance with a predetermined set of credibility parameters. Nevertheless, the calibration of corrosion model parameters from in-vitro data for absorbable metals is subject to substantial variation depending on testing conditions (e.g. aqueous solution, buffer system, flow conditions, etc.). To advance the use of computational corrosion models, rigorous efforts and verification, validation and uncertainty quantification are required. Again, this would benefit from standardised in-vitro setups, but also more data being available from in-vivo corrosion testing. This would maximise the potential for computational approach to optimize designs early in the design process, with time and costs potentially being saved during the development process.

References

[1] S. Agarwal, J. Curtin, B. Duffy, and S. Jaiswal, "Biodegradable magnesium alloys for orthopaedic applications: A review on corrosion, biocompatibility and surface modifications," *Mater Sci Eng C Mater Biol Appl*, vol. 68, pp. 948–963, 2016, ISSN: 1873-0191 (Electronic) 0928-4931 (Linking). DOI: 10.1016/j.msec.2016.06.020. [Online]. Available: https://www.ncbi.nlm.nih.gov/pubmed/27524097.

[2] D. Sumner, "Long-term implant fixation and stress-shielding in total hip replacement," *Journal of Biomechanics*, vol. 48, no. 5, pp. 797–800, 2015, ISSN: 0021-9290.

[3] D. F. Williams, "On the mechanisms of biocompatibility," *Biomaterials*, vol. 29, no. 20, pp. 2941–53, 2008. DOI: 10.1016/j.biomaterials.2008.04.023.

[4] H. Nygren, P. Malmberg, and Y. Liu, "MgO Implanted in Rat Tibia Bone Marrow is Osteoinductive through the Formation of a Matrix, Containing Hydroxyapatite," in *Materials Science Forum*, vol. 879, pp. 1404–1407, ISBN: 1662-9752. DOI: 10.4028/www.scientific.net/MSF.879.1404.

[5] J. B. Park and J. D. Bronzino, *Biomaterials : Principles and Applications*. Baton Rouge, UNITED STATES: Taylor & Francis Group, 2002, ISBN: 9781420040036. [Online]. Available: http://ebookcentral.proquest.com/lib/nuig/detail.action?docID=262228.

[6] ASTM G46-94, *Standard Guide for Examination and Evaluation of Pitting Corrosion*. PA: ASTM International West Conshohocken, 2005. DOI: 10.1520/g0046-94r18.

[7] E. L. Boland, R. N. Shirazi, J. A. Grogan, and P. E. McHugh, "Mechanical and Corrosion Testing of Magnesium WE43 Specimens for Pitting Corrosion Model Calibration," *Advanced Engineering Materials*, vol. 20, no. 10, 2018, ISSN: 14381656. DOI: 10.1002/adem.201800656.

[8] J. A. Grogan, B. J. O'Brien, S. B. Leen, and P. E. McHugh, "A corrosion model for bioabsorbable metallic stents," *Acta Biomater*, vol. 7, no. 9, pp. 3523–33, 2011, ISSN: 1878-7568 (Electronic) 1742-7061 (Linking). DOI: 10.1016/j.actbio.2011.05.032. [Online]. Available: https://www.ncbi.nlm.nih.gov/pubmed/21664498.

[9] A. Kopp, T. Derra, M. Muther, L. Jauer, J. H. Schleifenbaum, M. Voshage, O. Jung, R. Smeets, and N. Kroger, "Influence of design and postprocessing parameters on the degradation behavior and mechanical properties of additively manufactured magnesium scaffolds," *Acta Biomater*, vol. 98, pp. 23–35, 2019, ISSN: 1878-7568 (Electronic) 1742-7061 (Linking). DOI: 10.1016/j.actbio.2019.04.012. [Online]. Available: https://www.ncbi.nlm.nih.gov/pubmed/30959185.

[10] X. Gu, Y. Zheng, Y. Cheng, S. Zhong, and T. Xi, "In vitro corrosion and biocompatibility of binary magnesium alloys," *Biomaterials*, vol. 30, no. 4, pp. 484–498, 2009, ISSN: 0142-9612. DOI: 10.1016/j.biomaterials.2008.10.021.

[11] O. Jung, R. Smeets, P. Hartjen, R. Schnettler, F. Feyerabend, M. Klein, N. Wegner, F. Walther, D. Stangier, A. Henningsen, C. Rendenbach, M. Heiland, M. Barbeck, and A. Kopp, "Improved In Vitro Test Procedure for Full Assessment of the Cytocompatibility of Degradable Magnesium Based on ISO 10993-5/-12," *Int J Mol Sci*, vol. 20, no. 2, 2019, ISSN: 1422-0067 (Electronic) 1422-0067 (Linking). DOI: 10.3390/ijms20020255. [Online]. Available: https://www.ncbi.nlm.nih.gov/pubmed/30634646.

[12] G. Song, A. Atrens, and D. StJohn, "An Hydrogen Evolution Method for the Estimation of the Corrosion Rate of Magnesium Alloys," in *Essential Readings in Magnesium Technology*, S. N. Mathaudhu, A. A. Luo, N. R. Neelameggham, E. A. Nyberg, and W. H. Sillekens, Eds. Cham: Springer International Publishing, 2001, pp. 565–572, ISBN: 978-3-319-48099-2. DOI: 10.1007/978-3-319-48099-2_90.

[13] M. Li, Y. Cheng, Y. F. Zheng, X. Zhang, T. F. Xi, and S. C. Wei, "Surface characteristics and corrosion behaviour of WE43 magnesium alloy coated by SiC film," *Applied Surface Science*, vol. 258, no. 7, pp. 3074–3081, 2012, ISSN: 01694332. DOI: 10.1016/j.apsusc.2011.11.040.

[14] D. Mei, S. V. Lamaka, J. Gonzalez, F. Feyerabend, R. Willumeit-Römer, and M. L. Zheludkevich, "The role of individual components of simulated body fluid on the corrosion behavior of commercially pure Mg," *Corrosion Science*, vol. 147, pp. 81–93, 2019, ISSN: 0010938X. DOI: 10.1016/j.corsci.2018.11.011.

[15] I. Marco, F. Feyerabend, R. Willumeit-Romer, and O. Van der Biest, "Degradation testing of Mg alloys in Dulbecco's modified eagle medium: Influence of medium sterilization," *Mater Sci Eng C Mater Biol Appl*, vol. 62, pp. 68–78, 2016, ISSN: 1873-0191 (Electronic) 0928-4931 (Linking). DOI: 10.1016/j.msec.2016.01.039. [Online]. Available: https://www.ncbi.nlm.nih.gov/pubmed/26952399.

[16] T. Kraus, S. F. Fischerauer, A. C. Hanzi, P. J. Uggowitzer, J. F. Loffler, and A. M. Weinberg, "Magnesium alloys for temporary implants in osteosynthesis: in vivo studies of their degradation and interaction with bone," *Acta Biomater*, vol. 8, no. 3, pp. 1230–8, 2012, ISSN: 1878-7568 (Electronic) 1742-7061 (Linking). DOI: 10.1016/j.actbio.2011.11.008. [Online]. Available: https://www.ncbi.nlm.nih.gov/pubmed/22107870.

[17] T. A. Huehnerschulte, N. Angrisani, D. Rittershaus, D. Bormann, H. Windhagen, and A. Meyer-Lindenberg, "In Vivo Corrosion of Two Novel Magnesium Alloys ZEK100 and AX30 and Their Mechanical Suitability as Biodegradable Implants," *Materials (Basel)*, vol. 4, no. 6, pp. 1144–1167, 2011, ISSN: 1996-1944 (Print) 1996-1944 (Linking). DOI: 10.3390/ma4061144. [Online]. Available: https://www.ncbi.nlm.nih.gov/pubmed/28879972.

[18] Y. Koo, H. B. Lee, Z. Dong, R. Kotoka, J. Sankar, N. Huang, and Y. Yun, "The Effects of Static and Dynamic Loading on Biodegradable Magnesium Pins In Vitro and In Vivo," *Sci Rep*, vol. 7, no. 1, p. 14 710, 2017, ISSN: 2045-2322 (Electronic) 2045-

2322 (Linking). DOI: 10.1038/s41598-017-14836-5. [Online]. Available: https://www.ncbi.nlm.nih.gov/pubmed/29089642.

[19] H. M. Wong, K. W. Yeung, K. O. Lam, V. Tam, P. K. Chu, K. D. Luk, and K. M. Cheung, "A biodegradable polymer-based coating to control the performance of magnesium alloy orthopaedic implants," *Biomaterials*, vol. 31, no. 8, pp. 2084–96, 2010, ISSN: 1878-5905 (Electronic) 0142-9612 (Linking). DOI: 10.1016/j.biomaterials.2009.11.111. [Online]. Available: https://www.ncbi.nlm.nih.gov/pubmed/20031201.

[20] L. Liu, K. Gebresellasie, B. Collins, H. Zhang, Z. Xu, J. Sankar, Y.-C. Lee, and Y. Yun, "Degradation Rates of Pure Zinc, Magnesium, and Magnesium Alloys Measured by Volume Loss, Mass Loss, and Hydrogen Evolution," *Applied Sciences*, vol. 8, no. 9, 2018, ISSN: 2076-3417. DOI: 10.3390/app8091459.

[21] *ASTM WK72897 - New Guide for Quantification of Degradation Properties of Absorbable Metals*, https://www.astm.org/workitem-wk72897, Accessed: 14/09/2022.

[22] ASTM F3268-18a, *Standard Guide for in vitro Degradation Testing of Absorbable Metals*. PA: ASTM International West Conshohocken, 2018. DOI: 10.1520/f3268-18a.

[23] ASTM NACE G31-12a, *Standard Guide for Laboratory Immersion Corrosion Testing of Metals*. PA: ASTM International West Conshohocken, 2012. DOI: 10.1520/G0031-21.

[24] I. Marco, A. Myrissa, E. Martinelli, F. Feyerabend, R. Willumeit-Romer, A. M. Weinberg, and O. Van der Biest, "In vivo and in vitro degradation comparison of pure Mg, Mg-10Gd and Mg-2Ag: a short term study," *Eur Cell Mater*, vol. 33, pp. 90–104, 2017, ISSN: 1473-2262 (Electronic) 1473-2262 (Linking). DOI: 10.22203/eCM.v033a07. [Online]. Available: https://www.ncbi.nlm.nih.gov/pubmed/28197988.

[25] D. Mei, S. V. Lamaka, X. Lu, and M. L. Zheludkevich, "Selecting medium for corrosion testing of bioabsorbable magnesium and other metals – A critical review," *Corrosion Science*, vol. 171, 2020, ISSN: 0010938X. DOI: 10.1016/j.corsci.2020.108722.

[26] F. Witte, J. Fischer, J. Nellesen, H. A. Crostack, V. Kaese, A. Pisch, F. Beckmann, and H. Windhagen, "In vitro and in vivo corrosion measurements of magnesium alloys," *Biomaterials*, vol. 27, no. 7, pp. 1013–8, 2006, ISSN: 0142-9612 (Print) 0142-9612 (Linking). DOI: 10.1016/j.biomaterials.2005.07.037. [Online]. Available: https://www.ncbi.nlm.nih.gov/pubmed/16122786.

[27] Y. B. Ren, H. Wang, J. J. Huang, B. C. Zhang, and K. Yang, "Study of Biodegradation of Pure Magnesium," *Key Engineering Materials*, vol. 342, pp. 601–604, 2007. DOI: 10.4028/www.scientific.net/KEM.342-343.601.

[28] Z. Li, X. Gu, S. Lou, and Y. Zheng, "The development of binary Mg-Ca alloys for use as biodegradable materials within bone," *Biomaterials*, vol. 29, no. 10, pp. 1329–44, 2008, ISSN: 0142-9612 (Print) 0142-9612 (Linking). DOI: 10.1016/j.biomaterials.

2007.12.021. [Online]. Available: https://www.ncbi.nlm.nih.gov/pubmed/18191191.

[29] Y. Ren, J. Huang, B. Zhang, and K. Yang, "Preliminary study of biodegradation of AZ31B magnesium alloy, journal = Frontiers of Materials Science in China," vol. 1, no. 4, pp. 401–404, 2007, ISSN: 1673-7377 1673-7482. DOI: 10.1007/s11706-007-0073-2.

[30] L. Xu, F. Pan, G. Yu, L. Yang, E. Zhang, and K. Yang, "In vitro and in vivo evaluation of the surface bioactivity of a calcium phosphate coated magnesium alloy," *Biomaterials*, vol. 30, no. 8, pp. 1512–23, 2009, ISSN: 1878-5905 (Electronic) 0142-9612 (Linking). DOI: 10.1016/j.biomaterials.2008.12.001. [Online]. Available: https://www.ncbi.nlm.nih.gov/pubmed/19111896.

[31] N. Kawamura, Y. Nakao, R. Ishikawa, D. Tsuchida, and M. Iijima, "Degradation and Biocompatibility of AZ31 Magnesium Alloy Implants In Vitro and In Vivo: A Micro-Computed Tomography Study in Rats," *Materials (Basel)*, vol. 13, no. 2, 2020, ISSN: 1996-1944 (Print) 1996-1944 (Linking). DOI: 10.3390/ma13020473. [Online]. Available: https://www.ncbi.nlm.nih.gov/pubmed/31963840.

[32] A. H. Martinez Sanchez, B. J. Luthringer, F. Feyerabend, and R. Willumeit, "Mg and mg alloys: How comparable are in vitro and in vivo corrosion rates? a review," *Acta Biomater*, vol. 13, pp. 16–31, 2015, ISSN: 1878-7568 (Electronic) 1742-7061 (Linking). DOI: 10.1016/j.actbio.2014.11.048. [Online]. Available: https://www.ncbi.nlm.nih.gov/pubmed/25484334.

[33] F. Benn, F. D'Elia, K. van Gaalen, M. Li, S. Malinov, and A. Kopp, "Printability, mechanical and degradation properties of Mg-(x)Zn elemental powder mixes processed by laser powder bed fusion," *Additive Manufacturing Letters*, vol. 2, 2022, ISSN: 27723690. DOI: 10.1016/j.addlet.2021.100025.

A. Appendix

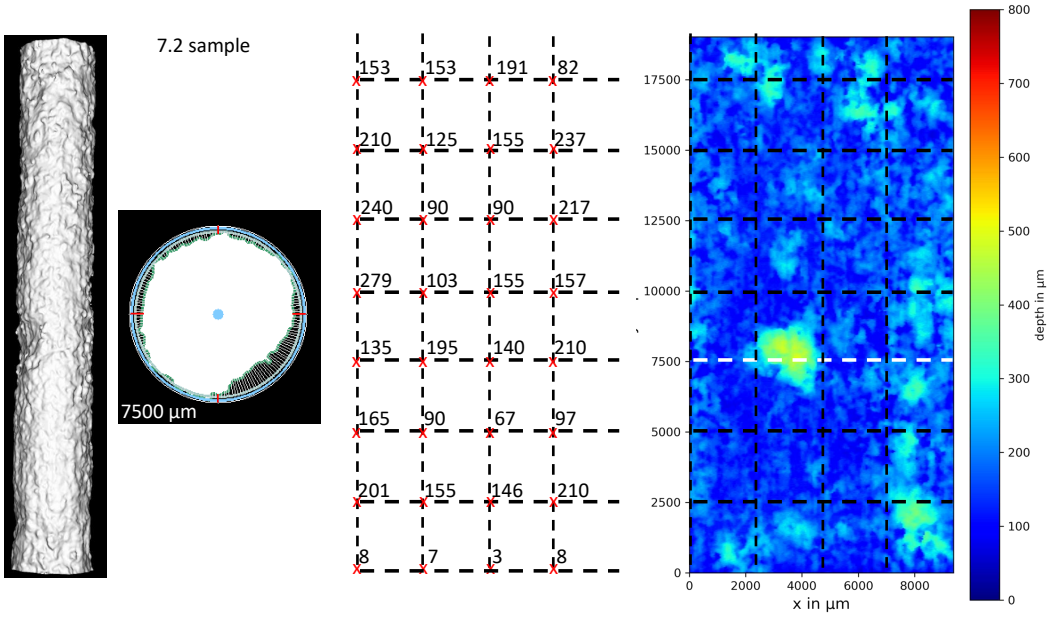

Figure A.1: 7 days sample 2.

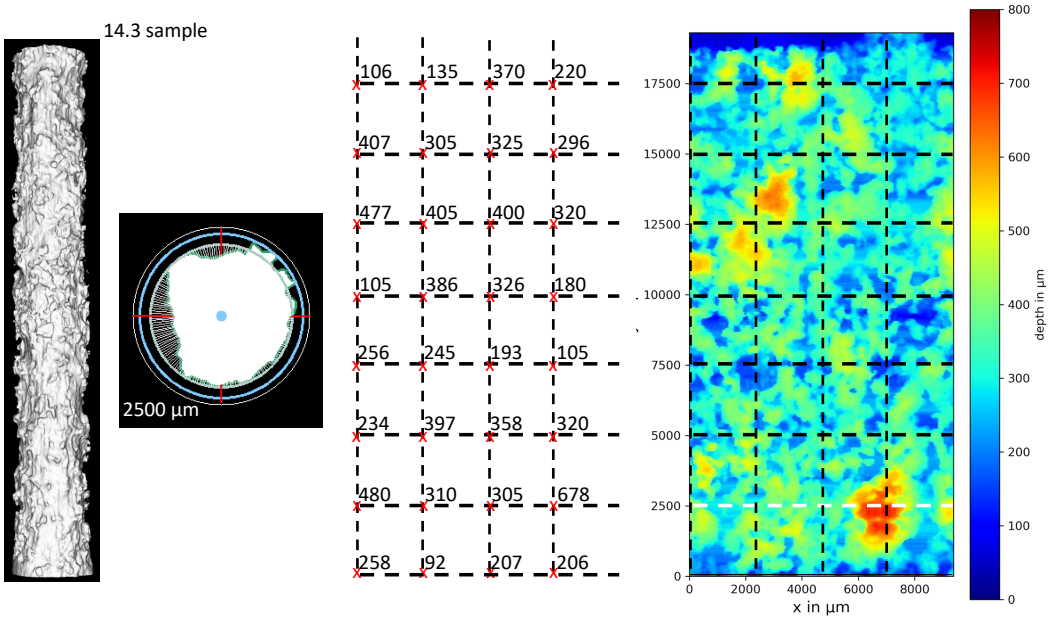

Figure A.2: 14 days sample 3.

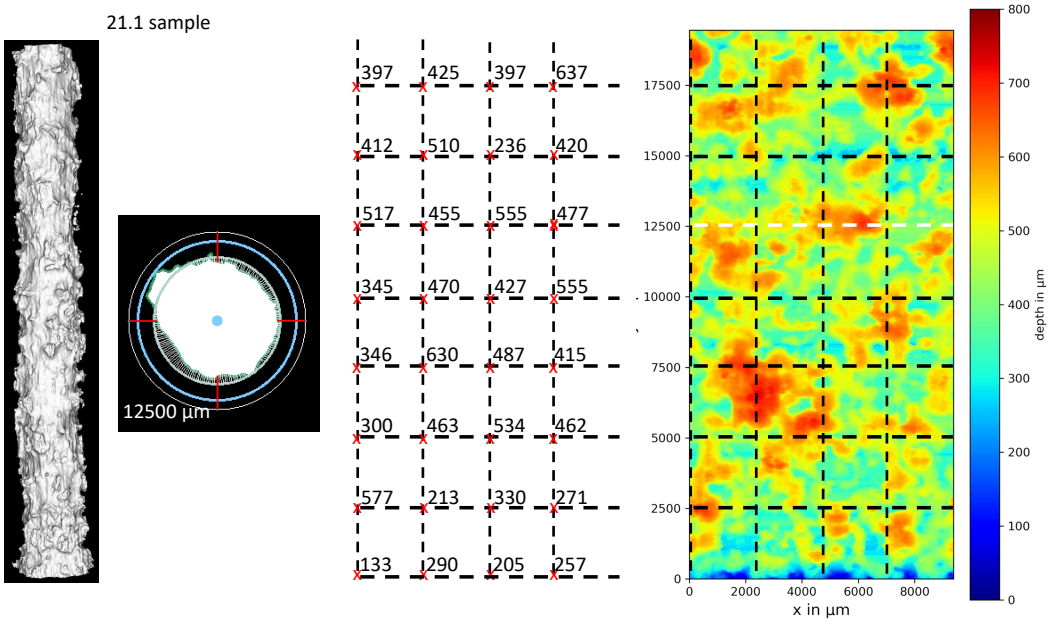

Figure A.3: 21 days sample 1.

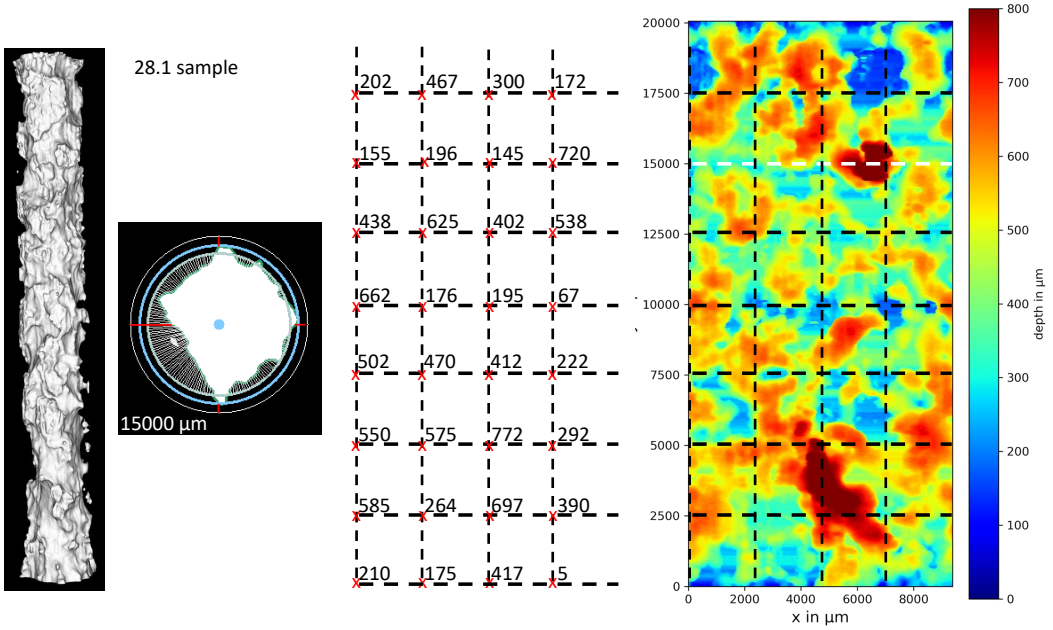

Figure A.4: 28 days sample 1.

B. Appendix

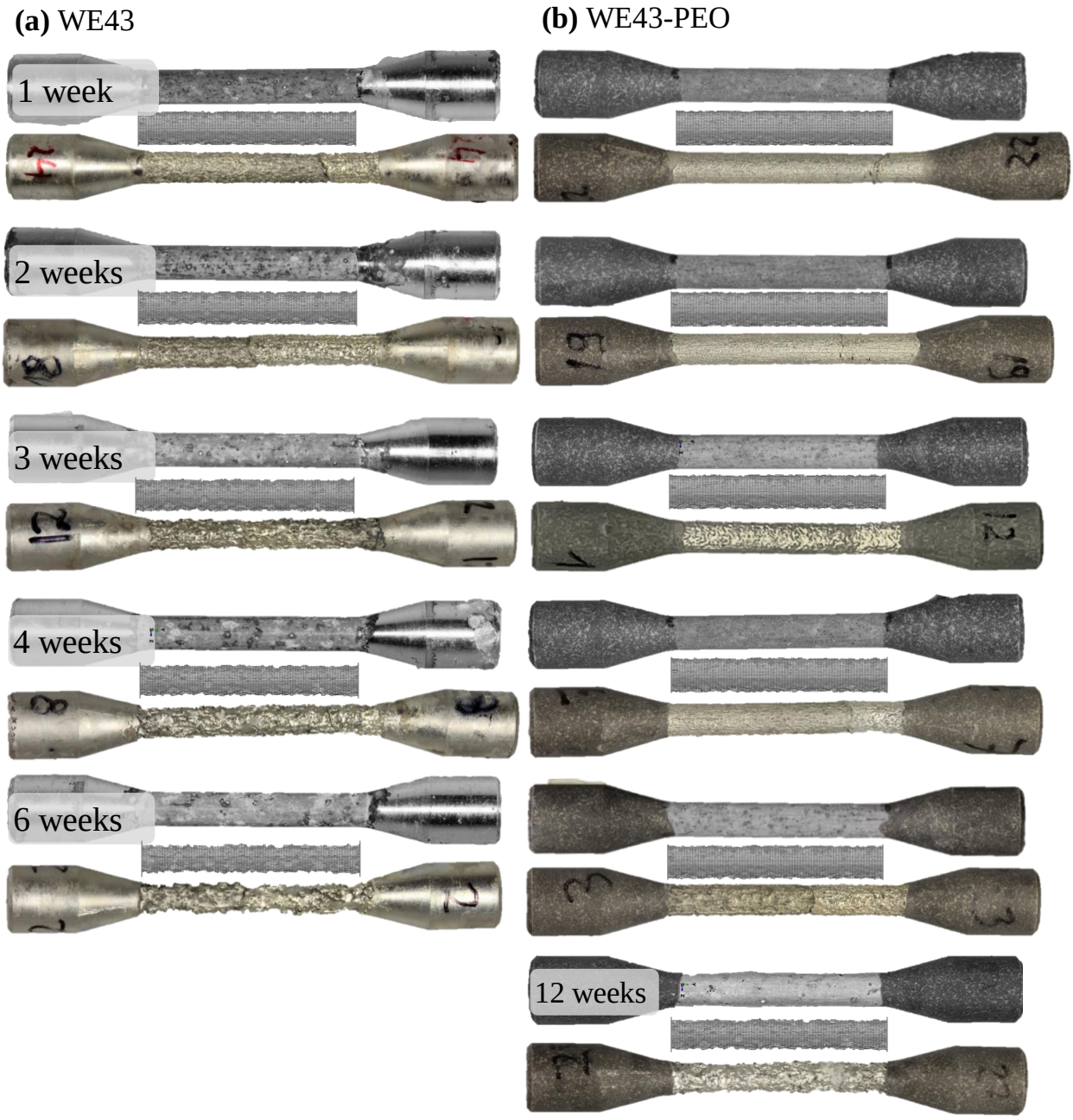

Figure B.1: Images (i) degraded samples pre cleaning (ii) corresponding simulated gauge section for the respective time step and (iii) after ultrasonic cleaning (please note that cleaning was performed after tensile testing which results in stretched specimens, the halves were glued together for the photographs) (a) WE43 Magnesium alloy (b) WE43-PEO coated Magnesium alloy.

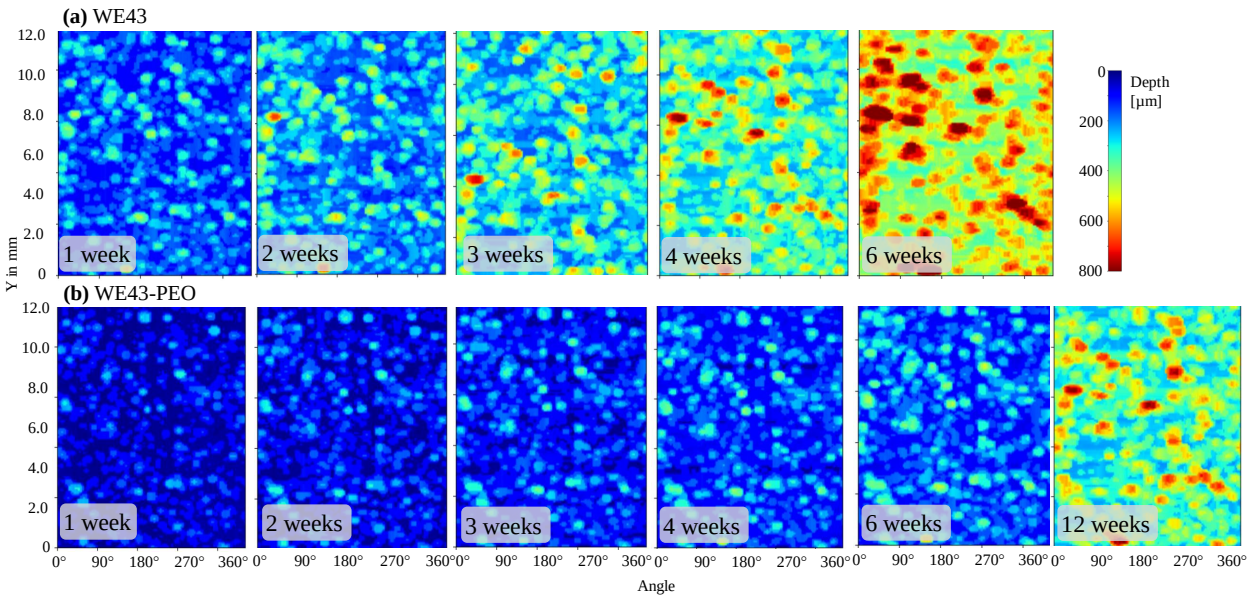

Figure B.2: Contour plots of the gauge section of the simulated dog bones over time, representing the depth from the initial surface to the current interface surface – environment (a) WE43 unmodified (b) WE43-PEO modified